GAS LOSS AND DURABILITY OF EVA FOAMS USED IN RUNNING SHOES

by

RAQUEL VERDEJO

A thesis submitted to

The University of Birmingham

for the degree of

DOCTOR OF PHILOSOPHY

School of Engineering
Metallurgy and Materials
The University of Birmingham
October 2003

Abstract

Ageing mechanisms affect the thermal properties and creep response of polymeric foams. This research analyses the effects of gas diffusion on the mechanical response of polymeric foams subjected to periodic loads and studies their durability.

A repeat impact machine was developed to analyse changes in the mechanical response of ethylene vinyl acetate copolymer foams used in running shoes. The equipment showed some advantages compared to the standard method used in running shoes and produced reproducible results. The softening of the material with the distance run and the reduction in the cushioning properties are mainly due to the yielding and unyielding of the cellular structure and not to a change in the air content.

Midsole deterioration in running shoes was measured in controlled running tests. These confirmed the deterioration of the midsole foam, with an increase of the peak plantar pressure and structural damage in the foam after a long run.

The diffusion coefficients of Ethylene-Vinyl Acetate (EVA) foams were measured using a microbalance where the pressure and the temperature were controlled. Theoretical analysis of gas diffusion in foams subjected to repeat impact was carried out and confirmed a negligible gas loss due to diffusion in foams under cyclic loads.

To Javi

And to my family:
Mum, Isabel, Luis
And Dad
I hope he would be proud of his youngest daughter.

Acknowledgements

Firstly, I would like to thank Dr. Nigel Mills for giving me the opportunity of carring out this research. I really appreciate the discussions we had about the research; his advice and knowledge have been invaluable.

From my previous university, I would like to thank Dr. Miguel Angel Rodríguez Pérez for introducing me into research and into the world of foams. I am really grateful for his comments and discussions. Also, to Prof. José Antonio de Saja for his keen interest in my progress and to Blanca Calvo for her comments on the gold coating settings and for carrying out a few DSC on my samples.

I would like to thank Nike for providing the samples for this study. And specially to John Yu for his comments along this research.

When I first came I felt a friendly welcome from people around me. Such feeling has never abandon me. I would like to mention my research group Adam, Catherine, Iona, Stephanie and Yago. It has been great working and discussing our research problems at the weekly meetings. Finally, I would like to thank Dr. Adam Gilchrist for mending the computers I have never broken.

Two different groups of the department have also been very helpful and from here I would like to thank Prof. Jim Hay and Prof. Rex Harris for letting me use the DSC and the IGA microbalance. Also, to Frank Biddlestone and Dr. Alan Walton for carrying those experiments for me. And from the workshop of this school, I am particularly indebted to Derek Boole for his help building the impact test rig developed in this research.

Also, I would like to thank the runners who took part in the experiments. Without them a very important part of this research would have not been possible.

Contents

List of Tables

List of Figures

Chapter 1

Introduction

Foams are very versatile materials, as they extend the range of properties of the materials they are made of, hence extending the number of applications. Two major applications of closed cell polymeric foams are as thermal insulators and shock absorbers. However, ageing mechanisms affect the thermal insulation properties of foams, due to the outward diffusion of the low conductivity blowing agent and the inward diffusion of air constituents. Furthermore, two previous studies [Mills and Gilchrist (1997a) and Mills and Rodríguez-Pérez (2001)] suggest that the diffusion also affects the mechanical behaviour, in particular the creep response, of foams.

The aim of this research was to analyse the effects of gas diffusion on the mechanical response of polymeric foams subjected to periodic loads and to study their durability. These analyses aim to determine the mechanisms which cause the foam fatigue. The research was carried out keeping in mind a system where a change in the response can have harmful consequences: the midsole of running shoes.

Running shoes have experienced major developments over the years, from simple and uniform designs to the highly specialised products of today [Cheskin et al. (1987); Frederick (1989)]. In the late 1970s, running underwent the so-called "Running Boom" coinciding with the first running shoe incorporating cushioned soles

[Shorten (2000)]. Since then, extended research has been carried out on the biomechanics of running and the injuries associated with it and some major books [Nigg and Kerr (1983); Frederick (1984); Nigg (1986b); Cavanagh (1990)] have been produced on the subject. However, not much published information is available on tests of the durability of running shoes and in some cases there is a lack of information on the characteristics of the foam. Prior research has fatigued shoe foams under uniform uniaxial compression [Misevich and Cavanagh (1984); Cook et al. (1985)]. However, both such studies were carried out nearly 20 years ago and foam types have changed in this period; hence, it is unclear how the results apply nowadays.
In running shoes, periodic impact loads are applied to midsole foam. Most runners, in particular long-distance runners, land heel first. This landing technique generates 2 to 3 times normal body weight [Cavanagh and Lafortune (1980); Cook and Kester (1985); Miller (1990)]. The repeated high forces could cause lower leg injuries [Shorten (2000)] if they were not adequately attenuated. Running shoe midsoles, by deforming and absorbing energy, limit the peak force in the heel-strike. However, in the course of a long run, there is an increase of the peak pressures registered at the foot/shoe interface, implying a reduction of the cushioning [Misevich and Cavanagh (1984); Cook et al. (1985)]. Furthermore, the foam does not appear to recover fully after a run.

The present research concentrates on the foamed copolymer of ethylene and vinyl acetate (EVA), of density in the range 100 to 250 kg m^{-3} from which most running shoe midsoles are made. In order to achieve the goals of this research, the following factors were identified. Firstly, to obtain a clear picture of the foams under study, their microscopic aspects, such as chemical composition and cellular structure, and macroscopic aspects, such as their mechanical response, need to be characterised. Secondly, the effects of the gas diffusion from the cells needed to be addressed both experimentally and theoretically. The latter had to consider the application conditions under which the foams are used. Thirdly, the durability of the foams had to be analysed both in the field and in the lab, which required the development of a new test rig which simulated heel strikes.

The thesis is divided into five main chapters,

1. Literature review
2. Experimental techniques
3. Results
4. Gas diffusion in foams
5. Midsole durability

In Chapter 2, a review of the current state of knowledge of the areas under study is detailed. The aim of this chapter is to present a general study of both materials and running fields involved in the research.

Chapter 3 explains the experimental techniques used to characterise the different aspects of the foams, such as structure, mechanical response and chemical composition. The characterisation is divided into two sections where the foam is studied at the microscopic and macroscopic level. The microscopic aspects of the foam are assessed through its cellular structure and chemical composition using Scanning Electron Microscopy (SEM), Differential Scanning Calorimetry (DSC), Attenuated Total Reflectance (ATR), which is an infrared (IR) reflection technique, and X-Ray diffraction. Meanwhile, the macroscopic aspects analysed the mechanical properties through Dynamic Mechanical Thermal Analysis (DMTA), creep and impact behaviour.

In Chapter 4, the results obtained from the previous characterisation of the foams are analysed and discussed.

Chapter 5 analyses the diffusion process in foams and it explains both the empirical and theoretical approach to the subject. The diffusion experiment was based on

sorption techniques; meanwhile the theoretical approach was carried out analysing the mass flux through the walls of a cell subjected to periodic loads.
Finally, Chapter 6 details the durability test carried out in the field with volunteer runners.

This thesis addresses aspects related to the two phases of which foams are made, the gas and the solid structure. The solid structure is examined from the aspects of durability and foam fatigue, whereas the gas is examined from the aspects of gas diffusion and its effect on the mechanical response of foams.

Chapter 2

Literature Review

The object of this research was to analyse the effects of gas diffusion on the mechanical response of polymeric foams subjected to periodic loads and hence to study their durability. This analysis had in mind a system where such research has a particular relevance: the midsole of running shoes. Therefore, this research links two main fields: materials and human biomechanics, with particular emphasis on the material research.

To gain an understanding of the fields related to the research, a review of the current state of knowledge was necessary. Thus, the aim of this chapter is to present a general study of both the materials and the human motions involved in the current research.

The materials section entails aspects of polymeric foams and their mechanical properties, in particular their compressive behaviour, while some general properties of the polymer under study are also detailed. To conclude the materials section, the diffusion process is defined and previous studies on diffusion in closed cell foams are explained.

Meanwhile, the running section is divided into (1) an analysis of the biomechanics of running based on the parameters used for its study and (2) an analysis of the running shoe based on its components and its design.

To complete the review, the foaming process and some characteristics of the foams under study are detailed.

2.1 Foams

2.1.1 Definition and general aspects

Foams are two-phase materials: a solid matrix, with a cellular structure, in which is dispersed a fluid phase [Klempner and Frisch (1991); Mills (1993); Gibson and Ashby (1997)]. Due to their definition as two-phase materials, they have also been considered as composite materials [Brady et al. (1997); Mills et al. (2003)]. The properties of these two-phase systems, and of composites in general, depend on the properties of the materials they are made of. For example, if the modulus of the dispersed phase is lower than that of the solid matrix then the modulus of the mixture will be lower than that of the unfilled matrix; such is the case of polymeric foams with a gas dispersed in them [Nielsen (1962)].
Man-made foams are produced from different materials; the first materials to be foamed were polymers but metals, glasses and ceramics are also being used for the solid matrix. Hereafter, this study concentrates on polymeric foams where the dispersed phase is a gas.

Foams are mainly classified on the basis of two different parameters [Klempner and Frisch (1991); Cunningham and Hilyard (1994)]:

1. *Cell structure.* The cell structure may be divided into two groups: closed-cell and open-cell structures (Figure 2.1). In closed-cell foams, the gas is contained in the cells, i.e. the solid phase is a continuum whereas the gas is discretely dispersed. In open-cell foams, the cells are interconnected, i.e. the solid phase is mainly in the cell edges, and both solid and gas phases are continuous.

2. *Solid matrix.* The solid matrix or base polymer includes three types of polymer: *elastomers*, such as polybutadiene and natural rubber, *thermosets*, such

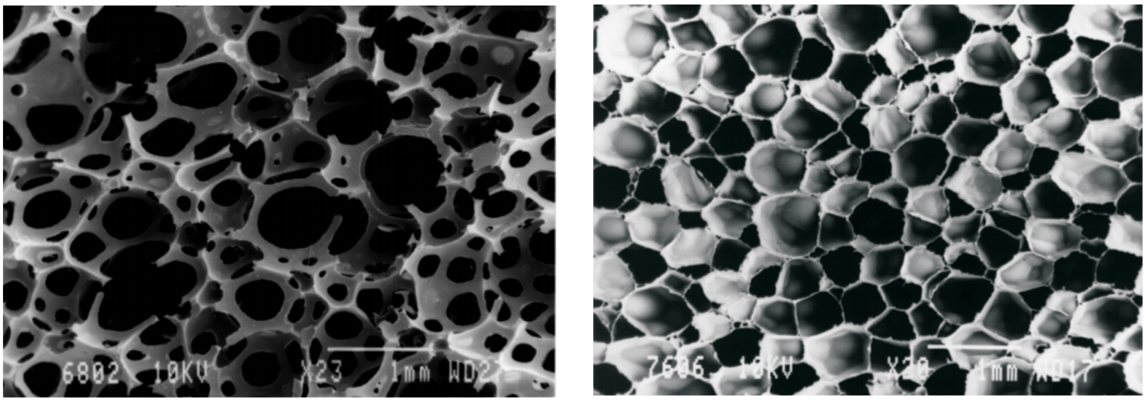

Open cell

Closed cell

Figure 2.1: Example of the cellular structure of foams. Left: Open cell structure. Right: Closed cell structure.

as polyurethane and epoxy, and *thermoplastics*, such as polyethylene and polypropylene. Thermoplastic polymers can solidify in two structures: a completely amorphous structure where the molecular chains do not have any type of regular arrangement, or a semi-crystalline structure where some molecular chains acquire an ordered arrangement [Charrier (1990); Young and Lovell (1991)].

All three base polymer have different properties, e.g. elastomers are highly elastic, they can undergo large deformations and completely recover their original shape when unloaded, whereas thermosets are rigid and intractable, i.e. once formed they do not melt nor do they dissolve in solvents [Young and Lovell (1991)].

The foaming of polymeric materials can be carried out by many different methods, depending mainly on the base polymer used, but the method most widely used involves (1) dispersing gas bubbles throughout the hot liquid polymer, (2) allowing the bubbles to grow and stabilise, and then (3) solidifying the product [Saunders (1991); Gibson and Ashby (1997)].

The gas is introduced either by mechanical agitation of the liquid or by introducing a blowing agent into the polymer. These blowing agents are classified according to the mechanism by which the gas is liberated [Shutov (1991a)]:

- chemical blowing agents (CBA), which are usually solid additives liberating gas as a result of thermal decomposition, or as a result of chemical reactions of the CBA or interaction of the CBA with other components of the formulation. They constitute the most numerous and widely used set of blowing agents because they are easy to introduce into the hot polymer and they are easy to process; and
- physical blowing agents (PBA), which do not undergo chemical reactions because they are inert gases or liquids; they produce gases as a results of physical process, evaporation or desorption, at high temperatures or low pressures.

The growth of the gas bubbles leads to the expansion of the foam and can produce either a closed or an open cell structure. Closed cell structure is the result of the first stage of foam expansion where the bubble growth forms a polyhedral structure in which the cell membrane surrounding the bubble remains intact. Closed cells became open when the growth of the bubble is allowed to continue, causing the rupture of cell membranes [Saunders (1991); Cunningham and Hilyard (1994)]. This process depends on the rheology and surface tension of the hot polymer [Gibson and Ashby (1997)].

The foaming of solids extends their range of properties (Figure 2.2), and hence increases the range of their applications [Gibson and Ashby (1997)]. These applications can be grouped into three main areas based on the physical property involved: thermal conductivity, energy absorption capabilities in static and dynamic situations, and buoyancy. Some applications are listed in Table 2.1.

Foams with an open cell structure have high levels of water, moisture and sound absorption. However, their insulation capability and shock absorption are worse than those of closed cell foams [Shutov (1991b)].

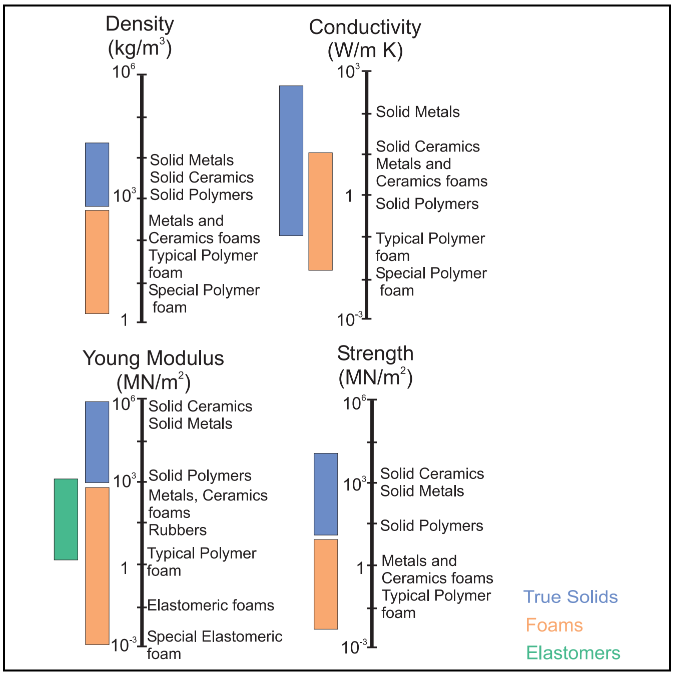

Figure 2.2: Range of properties obtained through the foaming of solids. (After Gibson and Ashby (1997))

Key Parameter	Application	Examples
Thermal conductivity	Construction	wall panelling, floor underlayment,
	Insulation	sandwich structures, imitation wood...
Energy absorption (static situations)	Automotive, Furniture	seats, mattresses...
Energy absorption (dynamic situations)	Packaging, Sports	pads, sport fences, athletic shoes...
Buoyancy	Industrial, Sports, Leisure	flotation collars, swim aids, boats...

Table 2.1: Applications of polymeric foams.

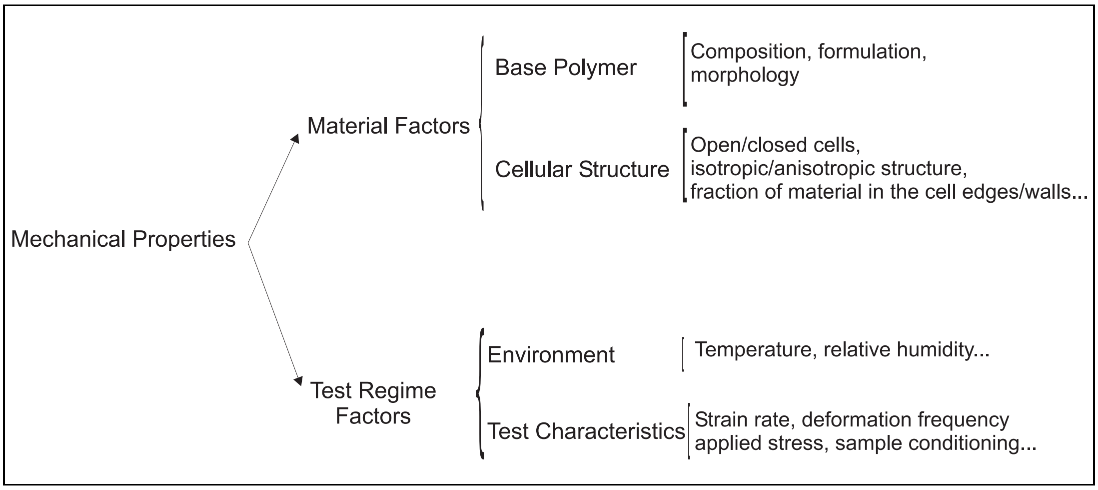

Figure 2.3: Diagram of the factors affecting the mechanical properties of foams.

2.1.2 Mechanical properties

The mechanical properties of foams depend not only on the base polymer and their cellular structure but also on factors related to the test regime (Figure 2.3).

The base polymer determines intrinsic properties such as the density, the Young's modulus, the plastic yield strength, and the fracture strength among the most important mechanical parameters [Gibson and Ashby (1997)]. Meanwhile, a foam with the same base polymer but a different cell structure would have different mechanical properties, e.g. if the structure is anisotropic, with different cell sizes along different directions, then the compressive strength [Shutov (1991b)] is different according to whether the compression is parallel or perpendicular to the direction of the largest cell orientation.

The additional factors related to the test regime in which the foams are being characterised have to be reported in order to compare the results given by different researchers [Cunningham and Hilyard (1994)]. These factors are the temperature, the strain rate, the frequency of deformation, and the conditioning of the foam test sample, among the most important. These factors are associated with the dependency of the mechanical behaviour of foams on the temperature and the rate at which they are deformed. The temperature dependency is related to the base polymer, whereas the strain rate is related to both the solid matrix and the gas. The temperature dependency is discussed below, while the strain rate dependency will only be mentioned in connection with the compressive behaviour.

Thermoplastic, thermoset and elastomer base polymers show three clear regimes as a function of the temperature (Figures 2.4): the glassy regime, the glass transition and the rubber regime [Gibson and Ashby (1997)]. Each regime has well defined characteristics for each base polymer.

> At temperatures below the glass transition temperature T_g, there is the glassy regime where the chains are impeded from sliding relative to each other. Within this regime, the increase in the temperature leads to a thermal expansion and a decrease of the modulus. This is due to relaxations in the bonds between the chains; several relaxation processes are known as β, γ and δ in order of decreasing temperature. Foams made of glassy polymers, those that have their vitreous relaxation above room temperature, are *rigid* or *brittle.*
>
> In the glass or vitreous transition, the chains are able to move and the polymer changes from glassy to a rubbery state. This transition is characterised by the gas transition temperature (T_g). Foams made of polymers with the glass transition at room temperature are *viscoelastic* or *plastic.*
>
> Finally, there is the rubbery regime, which has a lower modulus than the glassy regime. In this region, the intermolecular bonds have melted while the covalent C-C bonds and crosslinks are intact, leading to chains with a fairly large degree of freedom of movement relative to each other. Elastomers have a wide rubbery regime at room temperature; hence, foams made of elastomers are *flexible* or *elastic.*

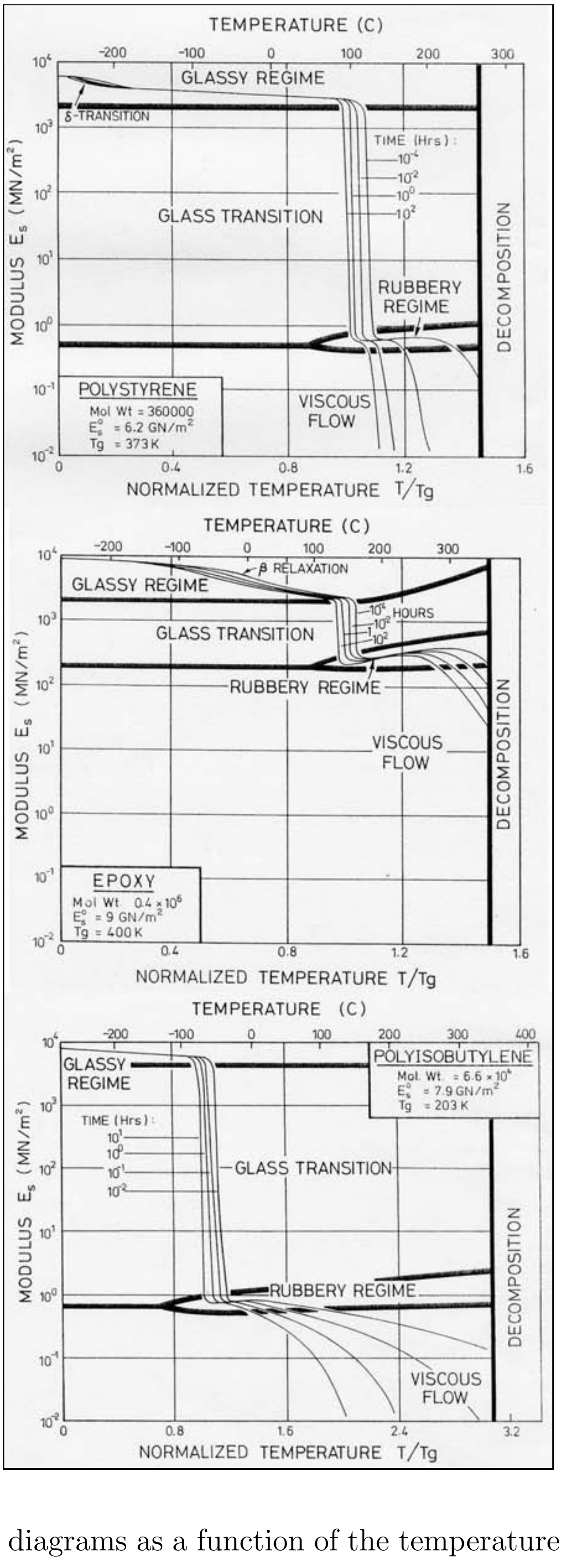

Figure 2.4: Modulus diagrams as a function of the temperature for a thermoplastic, thermoset and elastomer base polymers showing the three distinctive regimes. (From Gibson and Ashby (1997))

Due to the large range of applications, foams are used under tension, shear and mostly compression. Although extended literature is available on the modelling of the compressive behaviour [Rusch (1969, 1970b); Kraynik and Warren (1994); Throne and Proglhof (1985); Gibson and Ashby (1997); Cocks and Ashby (2000); Mills (2000)], up to date there has been no theoretical model which describes all aspects of the foam mechanics [Kraynik and Warren (1994)]. Also, most of these compression models correspond to open cell structure because models for closed cell foams have to consider the cell faces and the gas entrapped inside.

Compressive behaviour

The compressive behaviour shows three regions (Figure 2.5) [Ashby (1983)]. At low strains, the foam deforms in a linear-elastic way, i.e. the foam behaves like an elastic material. Then there is a plateau of deformation at almost constant stress; in this region the deformation is elastic but non-linear. Finally, there is a region of densification where the stress increases sharply and the foam acts as a solid polymer. These regions are governed by different deformation mechanisms [Maiti et al. (1984); Gibson and Ashby (1997)]:

- the linear region is controlled by cell wall bending (Figure 2.6), and in the case of closed cells by cell wall stretching. This deformation mechanisms is common to elastic, plastic and brittle foams

- the plateau is associated with elastic buckling in elastic foams, plastic yielding in plastic foams and by brittle crushing in brittle foams (Figure 2.7) and

- the densification is produced by the collapse of cell walls; this mechanism is common to elastic, plastic and brittle foams.

Linear region

Models of the linear region for open cell structure embody a relationship between

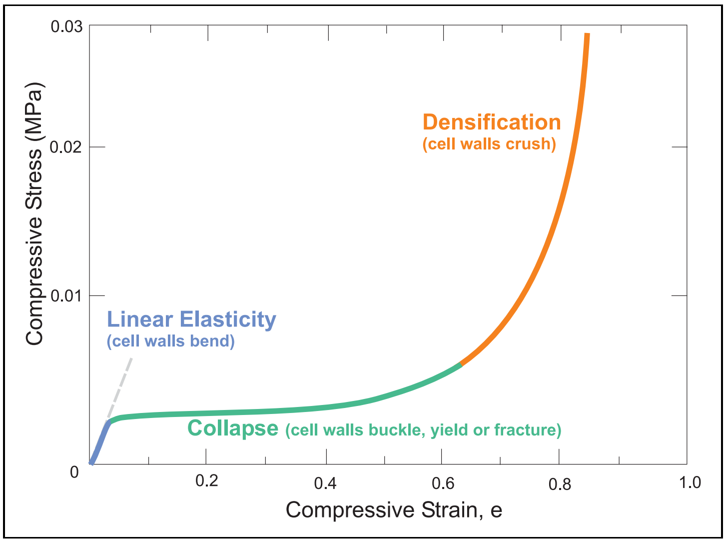

Figure 2.5: Compressive behaviour of polymeric foams showing three regions. (After Ashby (1983))

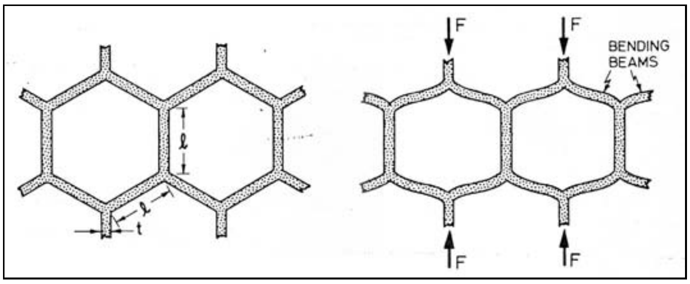

Figure 2.6: Mechanism responsible for the linear region of the compressive behaviour. Left: 2D open cell undeformed. Right: bending of the cell walls. (From Ashby (1983))

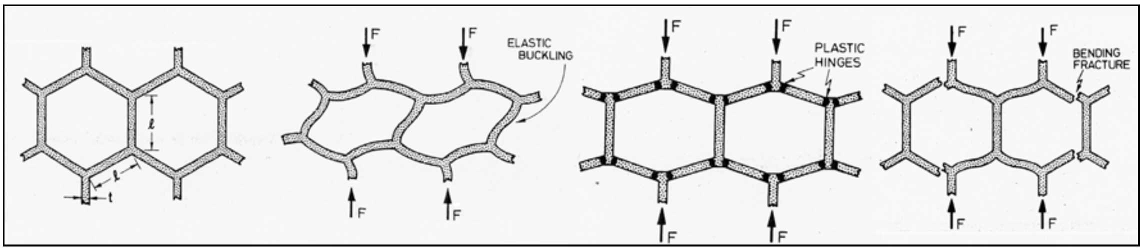

Figure 2.7: Mechanisms responsible for the collapse region of the compressive behaviour. From Left to Right: 2D undeformed cell walls, buckling of the cell walls, plastic yielding of the cell walls and brittle crushing of the cell walls. (From Ashby (1983))

the Young's modulus (E_f) and the relative density (ρ_r) of the foam, where ρ_r is the volume fraction of solid material and is calculated as the density of the foam (ρ_f) divided by the density of the solid polymer (ρ_s). However, depending on the cell shape under consideration [Kraynik and Warren (1994)], E_f has been found to be $\propto \rho_r$ or $\propto \rho_r^2$. Such difference is related to a change in the dominant deformation mechanism, which depends on the geometry of the structure and its orientation towards the strain principal axes. A more general empirical relation is also used to fit data:

$$E_f = K\,\rho_r^n \tag{2.1}$$

where K and n are empirically determined constants.

In a closed cell structure, Young's modulus has three different contributions [Gibson and Ashby (1997)]; two from the polymer, one accounting for cell-edge bending and the other one for cell-face stretching, while the third contribution corresponds to the enclosed gas:

$$E_f \approx f_s^2\,\rho_r^2 E_s + (1 - f_s)\,\rho_r E_s + \frac{\rho_g(1-2\nu_f)}{1-\rho_r} \tag{2.2}$$

where f_s is the fraction of solid in the cell edges, E_s is the Young's modulus of the solid polymer, ρ_g is the gas density and ν_f is the foam Poisson's ratio.

Plateau region

The plateau micromechanics differ according to the type of base polymer involved, and therefore there are separate models for each one. In order to keep this review relevant to the research, only references to elastic buckling will be presented.

The shape of plateau observed in this type of base polymer depends on whether the foam has an open or closed cell structure. Open cell foams collapse at almost constant load, i.e. they show a long flat plateau which is $\propto \rho_r^2$, whereas closed cell foams have a plateau of constant slope which accounts for the compression of the gas and the membrane stresses in the cell faces [Gibson and Ashby (1997)]. The uniaxial compressive stress in closed-cell foams [Rusch (1969, 1970b); Gibson and Ashby (1997)] is given by the expression:

$$\sigma = \sigma_0 + \frac{\epsilon}{1 - \epsilon - \rho_r} p_0 \tag{2.3}$$

where σ is the compressive stress, σ_0 is the initial yield stress and p_0 is the initial gas pressure in the unstressed cells which is assumed equal to the atmospheric pressure. The initial yield stress is the polymer contribution and is assumed to be constant. The term $\epsilon/(1 - \epsilon - \rho_r)$ is called the gas volumetric strain and is the contribution of the gas, which is responsible for the rise of the plateau. This equation corresponds to a foam under isothermal compression and for which the Poisson's ratio (ν_f) is assumed to be zero in the region of collapse. When the equation is rederived for $\nu_f \neq 0$ [Mills and Gilchrist (1997b)], the compressive stress is then given by:

$$\sigma = \sigma_0 + \left(\frac{1 - \rho_r}{(1 - \epsilon)(1 + \nu_f \epsilon)^2 - \rho_r} - 1 \right) p_0 \tag{2.4}$$

which produces a nearly linear graph of stress versus the gas volumetric strain with initial slope $p_0(1 - 2\nu_f)$. Thus, equation 2.4 states that there is also a contribution from the polymer to the term assumed to be the gas input by previous researchers.

Densification region

An empirical relation has been found for the densification region [Gibson and Ashby

(1997)]. This region occurs when opposite walls of the cells are crushed together and further compressed, leading to a sharp increase of stress. The limiting strain where the stress rise can be calculated as follows:

$$\epsilon_D = 1 - 1.4 \times \rho_r \tag{2.5}$$

where ϵ_D is the starting point of the densification region.

Compressive experiments involve the measurement of the deformation suffered by the foam to applied forces [Nielsen (1962)]. Among the different experiments to study this response are: creep and impact tests. The interest of these experiments is in the type of applied stress to which the foam is subjected. In creep experiments, the applied stress is constant or static [Mills (1997)]; they reveal the response of the foams to long and slow compressions. In impact tests, the applied stress is variable or dynamic; they show the response of the foams to short, rapid compressions [Mills (1994)]. Thus, the type of experiment to be performed is determined by the foam application: the creep experiments are an important characterisation for structural, cushioning and packaging applications, while the impact experiments are important for shock absorbing applications [Klempner and Frisch (1991)].

Creep response

Creep experiments consist of the measurement of the sample length over time while a constant load is being applied to it [Nielsen (1962); Williams (1980)] (Figure 2.8). Generally, the observed response to the applied load is a relative instantaneous elastic behaviour, followed by a minor strain increase as a function of time. The creep properties depend on the temperature, the stress applied and on the type of polymer studied, i.e. for a given stress and temperature a material with low modulus deforms more than a material with high modulus [Nielsen (1962)].

The compressive mechanisms seen above are valid at temperatures well below the

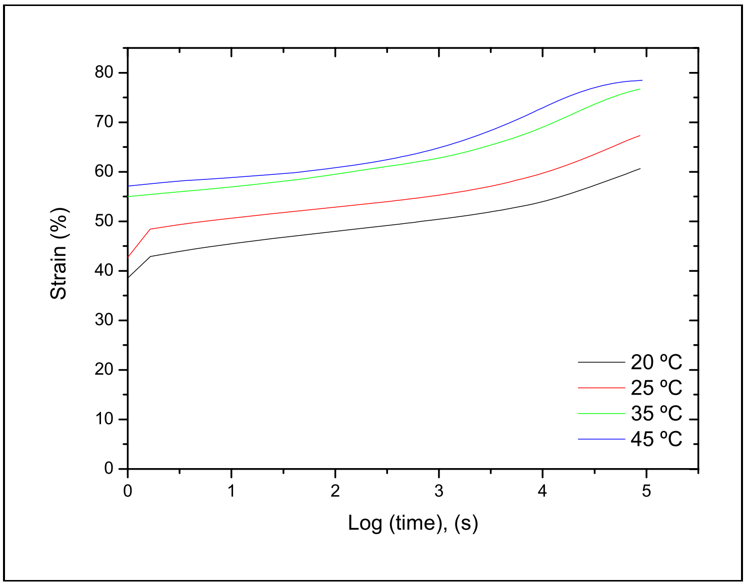

Figure 2.8: Creep response of an EVA foam to a constant load of 300 kPa at different temperatures.

melting temperature of the polymer ($T < 0.3T_m$), but at more elevated temperatures creep contributes to the deformation, which becomes time dependent [Andrews et al. (1999)].

In closed cell foams, there is also a further contribution at high strain creep [Mills (1997)] because gas escapes from the cells. This is determined by the foam density and by the polymer diffusivity to air [Mills and Gilchrist (1997a)]. A further development of the gas diffusion under creep for higher density foams [Mills and Rodríguez-Pérez (2001)] confirms the dependency of the gas diffusion rate on density, which is inversely proportional to the foam density, i.e. the higher the density the more slowly the gas escapes.

Impact response

Polymeric foams have a large number of applications as shock absorbers, from the packaging of goods to personal protection. Their function is to minimise the kinetic energy produced by an impact to non-damaging or harmless levels for the protected

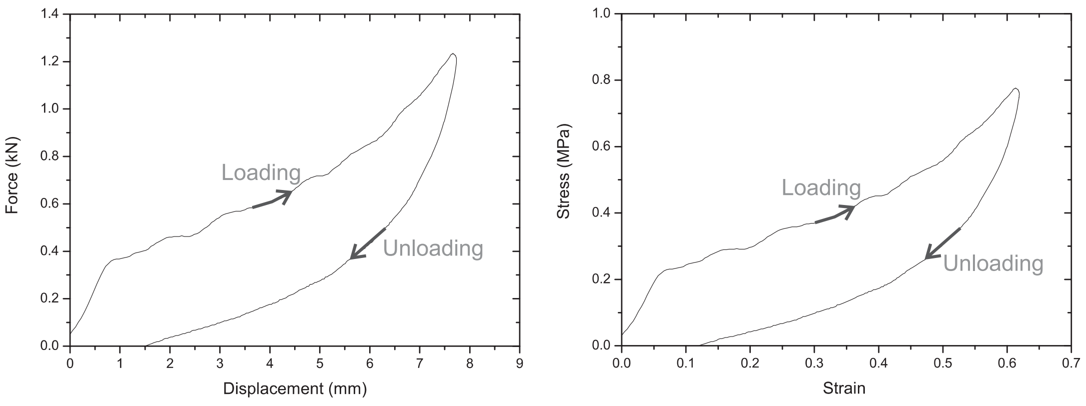

Figure 2.9: Impact response of an EVA foam at room temperature, as a force-displacement curve and as a stress-strain curve.

object or body. Therefore, the selection of a material for a particular application is based on the energy which it can absorb and the critical stress which the protected object/body can support [Maiti et al. (1984); Richardson and Nandra (1985)]. There are two types of impact tester: pendulum [Richardson and Al-Hassani (1987a,b)] and free fall tests [Richardson and Nandra (1985); Miltz and Ramon (1990); Mills (1994)]. Falling weight impact testers are the most common impact method for foams and they consist of a mass (or striker) dropping freely onto the sample from a certain height. During the impact, the striker's acceleration is measured by an accelerometer planted inside, from where the displacement of the upper surface of the sample is calculated by integrating its signal twice. The results from such experiments might be reported as force-displacement curves or as stress-strain curves and they will show a curve with the loading and unloading cycles (Figure 2.9). The absorbed energy (E_a) is then calculated as [Richardson and Nandra (1985); Cunningham and Hilyard (1994)]:

$$E_a = E_i + E_r \tag{2.6}$$

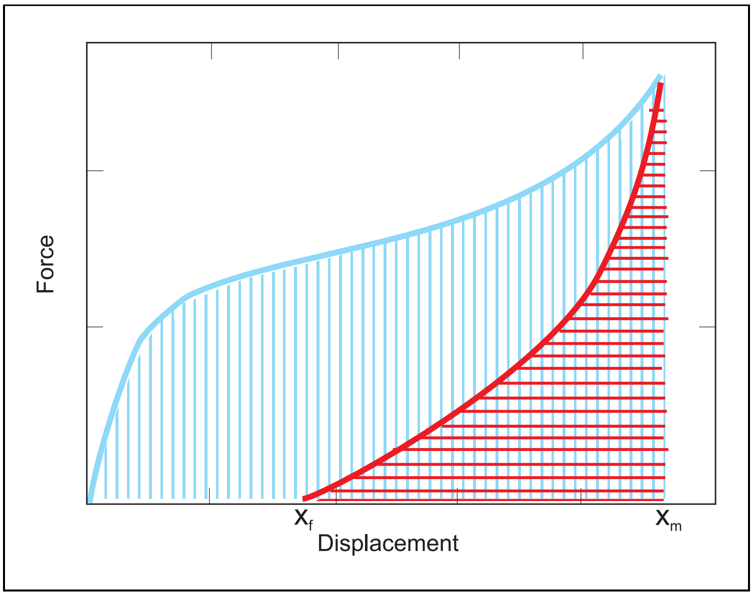

Figure 2.10: Force-displacement curve where the vertical lines correspond to E_i and the horizontal lines to E_r.

where E_i is the impact energy and E_r is the recovery energy, or the energy of the loading and unloading cycle respectively. They are calculated by integrating the force against the displacement (Figure 2.10):

$$E_i = \int_0^{x_m} F dx \tag{2.7}$$

$$E_r = \int_{x_m}^{x_f} F dx \tag{2.8}$$

where x_m is the maximum displacement and x_f is the remaining displacement of the foam once the exerted force returns to zero.

The mechanisms by which the foam absorbs energy are related to the elastic, plastic or brittle deformation of the polymer matrix and to the compression or flow of the gas within the cells [Mills (1994); Gibson and Ashby (1997)].

As mentioned above, the mechanisms causing the plateau depend on the type of base polymer, and hence result in a characteristic force-displacement curve for each type. Elastomeric foams absorb energy by the elastic buckling of their cells, and

therefore most of the impact energy is returned in the unloading cycle as rebound energy, i.e. they do not absorb very much energy. This is observed in the unloading curve by the fact that it is very close to the loading cycle. In plastic and brittle foams, energy is dissipated as plastic energy, or energy of fracture or as friction between the broken cell walls. Plastic foams exhibit a rapid increase of the load at low deformation but not as large as the increase shown by brittle foams. The plateau in these two materials differs: in plastic foams it is relatively short whereas in brittle foams it is fairly large (up to a deformation of 55-70 %) [Richardson and Nandra (1985)]. However, the recovery at the end of the impact is not complete, making these two materials good shock absorbers [Gibson and Ashby (1997)].
The gas within the cells also contributes to the impact response of foams. In open cell structures, the fluid will acquire a viscous flow causing some energy dissipation, although this effect is only significant at high strain-rates. In closed cell structures, the gas is compress as the foam deforms, storing energy which is recovered when the load is unloaded [Gibson and Ashby (1997)]. Equation 2.3 is applied in order to obtain the contribution of the gas, as gas pressure inside the cells, to the compressive stress.

Several theories have been put forward in order to predict the impact response from static and constant strain experiments [Rusch (1970a); Schwaber and Meinecke (1971); Maiti et al. (1984); Gibson and Ashby (1997); Iannace et al. (2001)]. From such theories, the stress-strain curves at any strain rate may be predicted enabling the construction of energy-absorption diagrams, which are diagrams of the absorbed energy against the peak pressure both normalised by Young's modulus.

There has not been much information published on the effects that repeat compressions or “mechanical ageing” have on foams. The literature available shows that the response depends on the type of polymer, for instance, in polystyrene foams the damage occurring in the first impact appears to be permanent and the absorbed energy is largely reduced in subsequent impacts [Mills (1994)]. Polyethylene foams show a viscoelastic recovery of the deformation after the impact and therefore the foam in multiple impacts does perform fairly well [Mills and Hwang (1989)], while flexible polyurethane suffers a loss of strength and a permanent decrease in volume [Gibson and Ashby (1997)].

2.2 EVA copolymer

Ethylene vinyl acetate (EVA) copolymer is part of the polyolefin family which is composed of thermoplastic polymers, such as low-, medium- and high-density polyethylene and polypropylene. Polyolefins are characterised by their toughness, flexibility and resistance to chemicals and abrasion [Park (1991)].

EVA is a random copolymer, obtained by the co-polymerisation of ethylene (E), particularly low density polyethylene (LDPE), with vinyl acetate (VA) under high pressure. Random copolymers are the result of a random union of their homopolymer monomers and they exhibit intermediate properties between the two homopolymers depending on the proportion of both comonomers [Young and Lovell (1991)]. Thus, each homopolymer will be briefly commented on and afterwards the properties of EVA will be described. Table 2.2 shows some properties of the homopolymers and their copolymer.

Polyethylene [Brandrup and Immergut (1975); Charrier (1990)] (PE) is a semi-crystalline thermoplastic with a melting transition which decreases from a maximum, around 135 °C, to a low of about 110 °C as the degree of crystallinity drops. It has also a very low glass transition (around −110 °C) which gives it good mechanical properties, including flexibility and impact resistance, at low temperatures.

PE has a variety of processing techniques resulting in a wide number of polymers [Charrier (1990)], e.g. low-density polyethylene (LDPE) which is produced at high pressures, high-density polyethylene (HDPE) which is made at low pressure, cross-

Property	LDPE	VA	EVA
Density (kg/m^3)	910-925	1050-1280	930-950 (9-29 % VA)
Melting point (°C)	122-124	–	47-100 (9-40 % VA)
Softening temperature (°C)	–	35-50	–
Elongation at break (%)	150-600	10-20	300-750
Tensile strength (MPa)	22-31	29.4-49.0	15-28
Thermal expansion coeff. (K^{-1})	10×10^{-5}	$7 - 22 \times 10^{-5}$	$16 - 25 \times 10^{-5}$

Table 2.2: Properties of low density polyethylene (LDPE), poly(vinyl acetate) (VA) and their copolymer ethylene-vinyl acetate (EVA).

linked polyethylene (XLPE) which is made by the introduction of chemical cross-links. Moreover, PE is suitable for co-polymerisations (EVA, EEA, E-P), and blends, increasing its range of properties.

Polyvinyl acetate [Brandrup and Immergut (1975); Charrier (1990)] (PVAc) is a non-crystallising polymer and, due to its low glass transition temperature (around 30 °C) it is not widely used as a plastic. However, as the VA units have a polar nature, it is the major ingredient of products such as adhesives and paints, e.g. white glue and latex paints.

The chemical structure of the E and the VA homopolymer is:

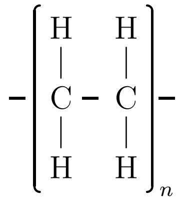

Ethylene

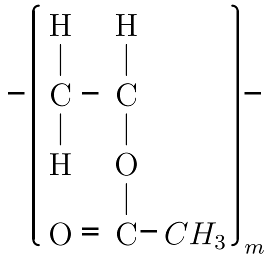

Vinyl Acetate

Therefore, the chemical structure of EVA copolymers will be a random distribution of E and VA units, where the VA units usually form the minor component. There are many different kinds of EVA commercially available because the properties of EVA are modified by the content of VA. Thus, this is a key parameter for a correct choice of the copolymer for each particular application.

The incorporation of VA reduces the crystallinity of the ethylene, because the VA units break the E segments. Therefore, the higher the percentage of VA, the lower the crystallinity of the copolymer; which becomes completely amorphous when its content is higher than 40 % [Nielsen (1960); DuPont (1997)]. This reduction of the degree of crystallinity leads to improvements in its flexibility, clarity, and impact strength and to a reduction of its hardness [Charrier (1990); Samsung (1999)]. Furthermore, the degree of VA increases the polarity of the EVA which improves its compatibility with certain types of plasticiser and blowing agents, its water vapour permeability and its oil resistance. A summary of the changes in the properties by the introduction of VA is presented in Figure 2.11

The formulation and foaming process used in EVA copolymers for footwear applications will be generally explained in section 2.5. The EVA copolymer used in the midsole of running shoes can contain between 18 % and 22 % of VA [Samsung (1999)].

2.3 Diffusion

2.3.1 Definition and general aspects

Diffusion is the movement of matter from one part of a system to another as the result of a species concentration difference [Incropera and DeWitt (1996); Masaro and Zhu (1999)], and it is mainly due to random molecular motions. Diffusion in gases has been successfully predicted by theories and it depends on temperature,

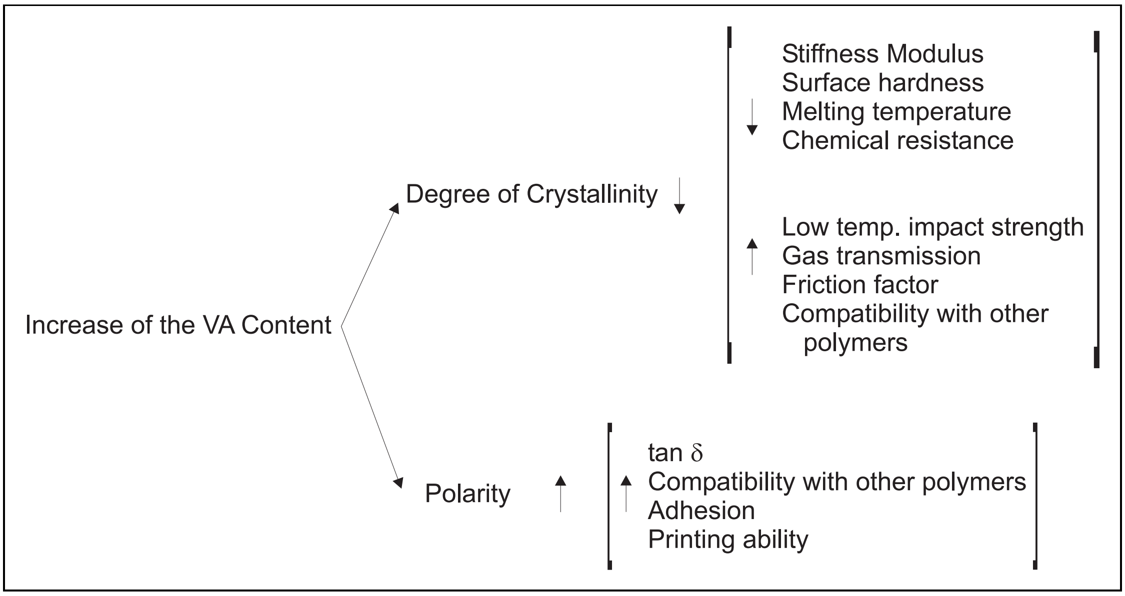

Figure 2.11: Effects of the increase of the VA content on the EVA properties.

pressure, solute size and viscosity [Masaro and Zhu (1999)]. However, diffusion in solids and liquids is difficult to predict from theories [Cussler (1975); Incropera and DeWitt (1996); Masaro and Zhu (1999)].

The first mathematical approach to mass transfer by diffusion was established by Fick who developed two equations for diffusion in one dimension. Diffusion processes assume that mass is only transported but cannot be created or destroyed, the continuity equation. Ficks law expresses that a gradient concentration leads to a flow which compensates for it. The equation states that the flux J of a diffusing substance is proportional to the concentration gradient:

$$J = -AD\frac{\partial c}{\partial x} \tag{2.9}$$

where A is the area across which diffusion occurs, D is the diffusion coefficient, c is the concentration, and $\frac{\partial c}{\partial x}$ is the gradient of the concentration along the x axis [Rabek (1980); Masaro and Zhu (1999)]. Fick's second law states that, for a constant diffusion coefficient, the rate of change in concentration with time, is proportional to the rate at which the concentration gradient changes with distance in a given direction, i.e. it describes the time-variant or non-steady state, and can be written as [Rabek (1980); Masaro and Zhu (1999)],

$$\frac{\partial c}{\partial t} = D\frac{\partial^2 c}{\partial x^2} \tag{2.10}$$

The diffusion process in polymers depends on the physical properties of the polymer network and the interactions between the polymer and the solvent [Crank and Park (1968); Rabek (1980); Vieth (1990); Masaro and Zhu (1999)]. It has been reported that the diffusion characteristics of polymers follow either a Fickian diffusion behaviour or a non-Fickian diffusion behaviour [Rabek (1980); Masaro and Zhu (1999)]. The Fickian behaviour is described by Fick's first and second laws and is characteristic of polymers well above the glass transition temperature (rubbery regime). Meanwhile, the non-Fickian diffusion behaviour is characteristic of polymers below the glass transition temperature (glassy regime) or above the glass transition temperature in cross-linked and semi-crystalline polymers. Many different diffusion models in polymers have been reported; a review of them can be found in the paper by Masaro and Zhu (1999). They concluded that, although various models have succeeded in describing the diffusion process, it is not yet possible to predict the diffusion coefficient of a given diffusant in a given system under specific conditions.

The experimental procedures for studying diffusion in polymers are based on measurements of the sorption, e.g. measuring the uptake of solute by the polymer by direct weighing, of the diffusion, e.g. following the molecular motions using NMR spectroscopy, or/and of the permeation rate, e.g. measuring the increase of pressure with time on the low-pressure side of the polymer film [Crank and Park (1968); Rabek (1980)]. The diffusion coefficients of pure oxygen (O_2) and carbon dioxide (CO_2) for EVA films with different amounts of VA have been studied by permeation measurements [Marais et al. (2002)]. The diffusion coefficient values of a film with 19 % VA were reported to be: $D_{O_2} \approx 37\times10^{-12}$ m^2/s^{-1} and $D_{CO_2} \approx 54\times10^{-12}$ m^2/s^{-1}.

2.3.2 Diffusion in foams

Theoretical models

Diffusion processes in closed-cell foams have a major effect on their thermal insulating capability and dimensional stability, as they decay significantly with time. The diffusion process in closed foams, often called *ageing*, is divided into two stages: the inward diffusion of air components and the outward diffusion of the blowing agent [Ostrogorsky and Glicksman (1988); Pilon et al. (2000)].

The rate of diffusion depends upon the partial pressures and the effective diffusion coefficients of the different gases involved [Svanström et al. (1997)]. In addition, these coefficients depend on the properties and geometrical structure of the polymer, and the properties of the gases involved. Therefore, diffusion models have to consider the effects of the solid matrix, the type of base polymer and the cellular structure, and also the effects of the gases, their properties and partial pressures. The two main approaches to the prediction of gas diffusion through closed-cell foam are: continuous models and discrete models.

Continuous diffusion models

These models consider the foam as a homogeneous and isotropic medium through which gas species i diffuses with an effective diffusion coefficient D_{eff}. This conclusion is based on the following assumptions [Hoogendoorn (1994)]:

- Diffusion processes are independent, i.e. gases do not interact between them
- The gas is only stored in the cells, there is no gas stored in the polymer and thus the gas is weakly soluble in the polymer. Hence, Henry's law is applicable
- The closed cell matrix is assumed to be continuous, i.e. there are no holes in the cell walls
- The diffusion coefficient of the different gases and blowing agent does not depend on their concentration in the foam

- The foam thickness is much larger than the average cell diameter.

The effective diffusion coefficient is found from the analytical solution of Fick's second law (2.10); which is a second order partial differential equation:

$$\frac{\partial c_i}{\partial t} = D_{eff} \nabla^2 c_i \tag{2.11}$$

where c_i is the concentration of component i, which is proportional to the partial pressure (Henry's law), and ∇^2 is the Laplacian operator. To simplify the problem, the diffusion is often consider in one direction, which allows to analytically resolve the equation,

$$\frac{\partial p_i}{\partial t} = D_{eff} \frac{\partial^2 p_i}{\partial x^2} \tag{2.12}$$

where p_i is now the partial pressure and x is the diffusion direction. The solutions of the above equation vary according to the initial and boundary conditions imposed, which depend on the system under study, e.g. two different conditions for a foam without facing can be

> (1) the initial condition is p(x,0)=0 and the boundary conditions are p(0,t)=p_1 and p(λ,t)=p_2 where p_1 and p_2 are the pressures on both sides of the foam and λ is the foam thickness [Ostrogorsky and Glicksman (1988)], i.e. the foam is subject to a pressure gradient, or
>
> (2) the initial condition is p(x,0)=p_0 and the boundary conditions are p(0,t)=p_1 and p(λ,t)=p_1 where p_0 and p_1 depends on the gas considered [Hoogendoorn (1994)].

Although some success has been reported, the main drawback of these models is that they are unable to take into account the discrete nature of the foam morphology [Alsoy (1999)], i.e. they do not consider the dependency of D_{eff} on the foam local morphology, which is reflected in the following reported results [Hoogendoorn (1994)]

- D_{eff} value varies according to the position inside the foam, cells close to the surface can be different from those in the mid-thickness,
- D_{eff} value changes according to whether the diffusion direction is parallel or perpendicular to the foaming direction.

There is also a further deviation due to the dependency of D_{eff} on the concentration of the gases and the type of gases involved, e.g. $D_{eff}^{O_2} \neq D_{eff}^{N_2}$.

Therefore, the continuous models give only minimal physical understanding of the foams' ageing behaviour.

Discrete diffusion models

These models consider the foam layer as the repetition of a unit cell, which can be characterised by its geometry (membrane thickness, cell size and shape) as well as the diffusion coefficients of the species through the condensed phase and through the gas phase [Pilon et al. (2000)]. The commonest assumptions in discrete models are:

- A steady state has been reached in the polymer membrane,
- Gases do not react with the solid phase nor between them,
- The closed cell matrix is assumed to be continuum with no holes on it,
- The diffusion coefficient of the different gases and blowing agent does not depend on their concentration in the foam,
- Cell to cell diffusion is governed by Fick's first law.

There have been two approaches depending on the physical process considered: membrane permeation [Ostrogorsky et al. (1986); Bart and du Cauzé de Nazelle (1993)] or diffusion through membrane [Pilon et al. (2000)]. Some of these models

use the analogy of an electrical resistance-capacitor RC network to describe the diffusion [Ostrogorsky et al. (1986); Pilon et al. (2000)].
Most of the available models use the permeation process of a gas through a membrane [Rabek (1980); Vieth (1990); Brandreth (1991); Bart and du Cauzé de Nazelle (1993)] which occurs in the following stages:

1. the absorption of the gas in the entering membrane due to a solubility S,
2. the diffusion through the membrane by a intrinsic diffusion coefficient D_{pol}, and
3. the desorption of the gas in the exit face of the membrane

The permeation process in stationary conditions is then given as a function of the mass flux by

$$J = P\frac{\Delta p}{\delta} \tag{2.13}$$

where J is the mass flux or the amount of the permeating component through the unit area in unit time, P is the permeation coefficient, Δp the partial pressure difference over the membrane and δ is the membrane thickness. These models also assume that Henry's law is applicable, in order to apply the following relationship between the permeation coefficient and the diffusion coefficient

$$P = SD_{pol} \tag{2.14}$$

These basic equations set up the mass balance for each cell, from where the discrete description of the diffusion in the foam is obtained [Ostrogorsky et al. (1986); Bart and du Cauzé de Nazelle (1993); Hoogendoorn (1994)]. The diffusion coefficient of the foam is found as the product of two factors: (1) a dimensionless geometrical factor, which depends on geometrical foam characteristics such as cell size, wall thickness, cell elongation, among others, and (2) the solubility and diffusivity of the polymer matrix which are material properties. Overall, these models state that the diffusion coefficient of the foam is proportional to $1/\rho_f$.

A discrete model using the diffusion process [Pilon et al. (2000)] relates the diffusion process with a geometric factor accounting for the cellular structure of the foam and the diffusion process through the solid polymer as a thermally activated process. However, this model states that the foam diffusion coefficient is proportional to ϕ/ρ_f, where ϕ is the mean cell size.

Although the discrete models express the effective diffusion coefficient in terms of parameters characterising the foam structure and composition, they have three main drawbacks [Hoogendoorn (1994); Alsoy (1999); Pilon et al. (2000)]: (1) the steady state may have not been reached, (2) the diffusion (D_{pol}) and the solubility coefficients are not always independent on the concentration of the component i solute in the polymer, and (3) Henry's law might not be applicable.

There is a third approach to this problem, where the foam is considered as a fractal-like material [Gefen et al. (1981); Kimball and Frisch (1991)]. In these theories non-uniform cell sizes could be considered, but their limitation is that the foam is not really a fractal.

The models mentioned above were developed for conditions where the foam is at rest and they were mainly established to analyse the change on the thermal properties. There has been one attempt to model the foam diffusion under compressive conditions [Mills and Gilchrist (1997a)]. The model was performed under creep in which the diffusion direction is considered perpendicular to the applied stress axis with each layer in the foam suffering the same strain. The model, using a finite-difference method, took into account that the creep stress affects the gas pressure in the cells and that the creep strain affects the diffusion coefficient. The diffusion model was treated as unidirectional and the foam was divided into vertical layers, parallel to the stress axis. The foam diffusivity was obtained by fitting the predicted creep curves to experimental data. Although the slopes of the predicted curves are close to the experimental results, there is a large separation of creep stresses in the range 100 to 200 kPa. A further analysis of the deformation suffered by the foam was performed to improve the model. For such a purpose, an SEM analysis was made after creep experiments and digital photographs were taken during a creep experiment.

> *SEM analysis*
>
> Creep experiments at 35 °C between 50 and 200 kPa were carried out in low density (50 kg/m^3) Ethylene Styrene Interpolymer samples [Ankrah et al. (2002)]. SEM analyses were made of three samples under different stress: untested, 80 kPa and 150 kPa. Both compressed samples had residual strains of 30 % and 70 %, respectively. The results showed that the foam cells close to the upper and lower surfaces are flattened after creep (Figure 2.12).
>
> *Digital photographs*
>
> Creep experiments at 35 °C with 17, 24.1 and 26.6 kPa compressions stress were carried out for low density (35 kg/m^3) EVA samples. A grid was drawn on each sample to see the deformation pattern. The first photograph was taken before the loading and then 3 photographs every 5 minutes, the next 3 photographs every 20 minutes, and then at 1 hour intervals. The last photograph was taken after 24 hours. A sequence of these photographs can be seen in Figure 2.13. The upper and lower grid squares deformed first whereas the internal grid squares remained undeformed until the experiment was almost finished.

These results suggest that the gas diffuses in the direction of the stress, so the applied stress is constant throughout the sample whilst the strain varies from cell to cell. These findings were applied to a new development of the model mentioned above, resulting in a series load transfer model [Mills and Rodríguez-Pérez (2001)]. The model takes into account the interactions between the cell strain, the gas diffusivity, the cell deformation (in particular cell face touching at high strains), and the strain rate in the polymer. The factors are considered in sequence within a short time

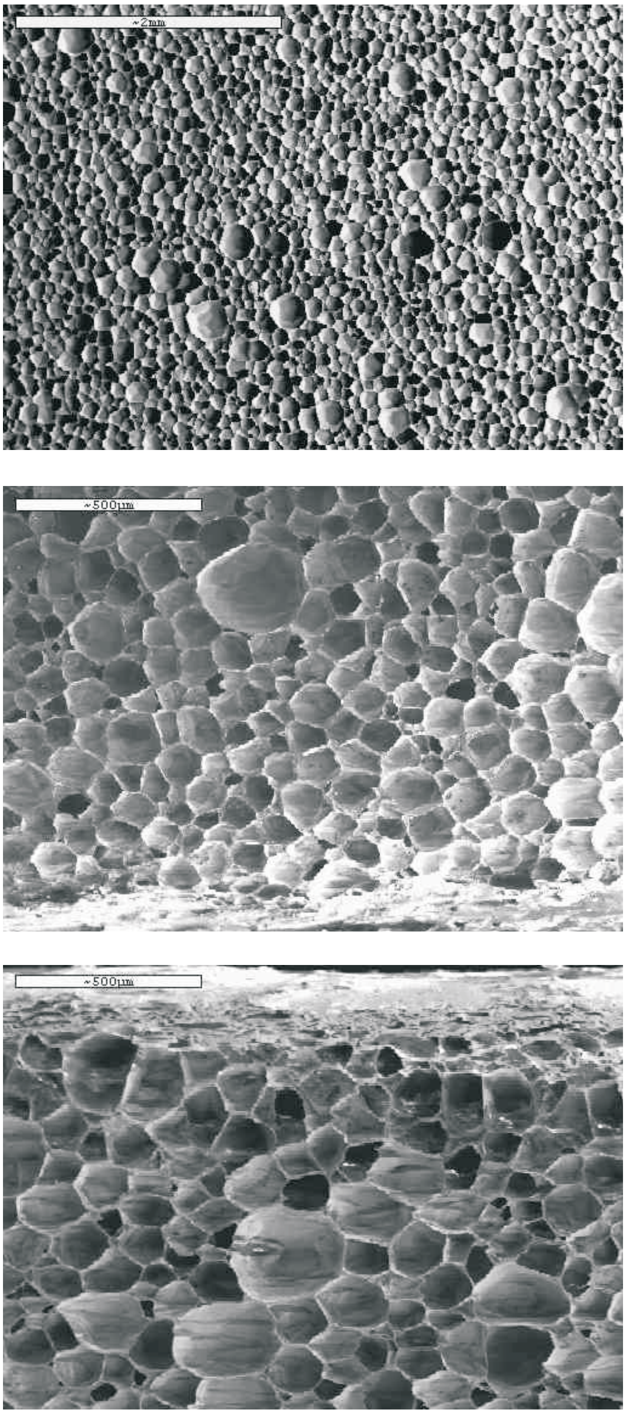

Figure 2.12: SEM photographs, the first is a general view of the uncompressed sample, the second is a lower surface view of the 80 kPa stress sample, and the third is the upper surface of the 150 kPa sample.

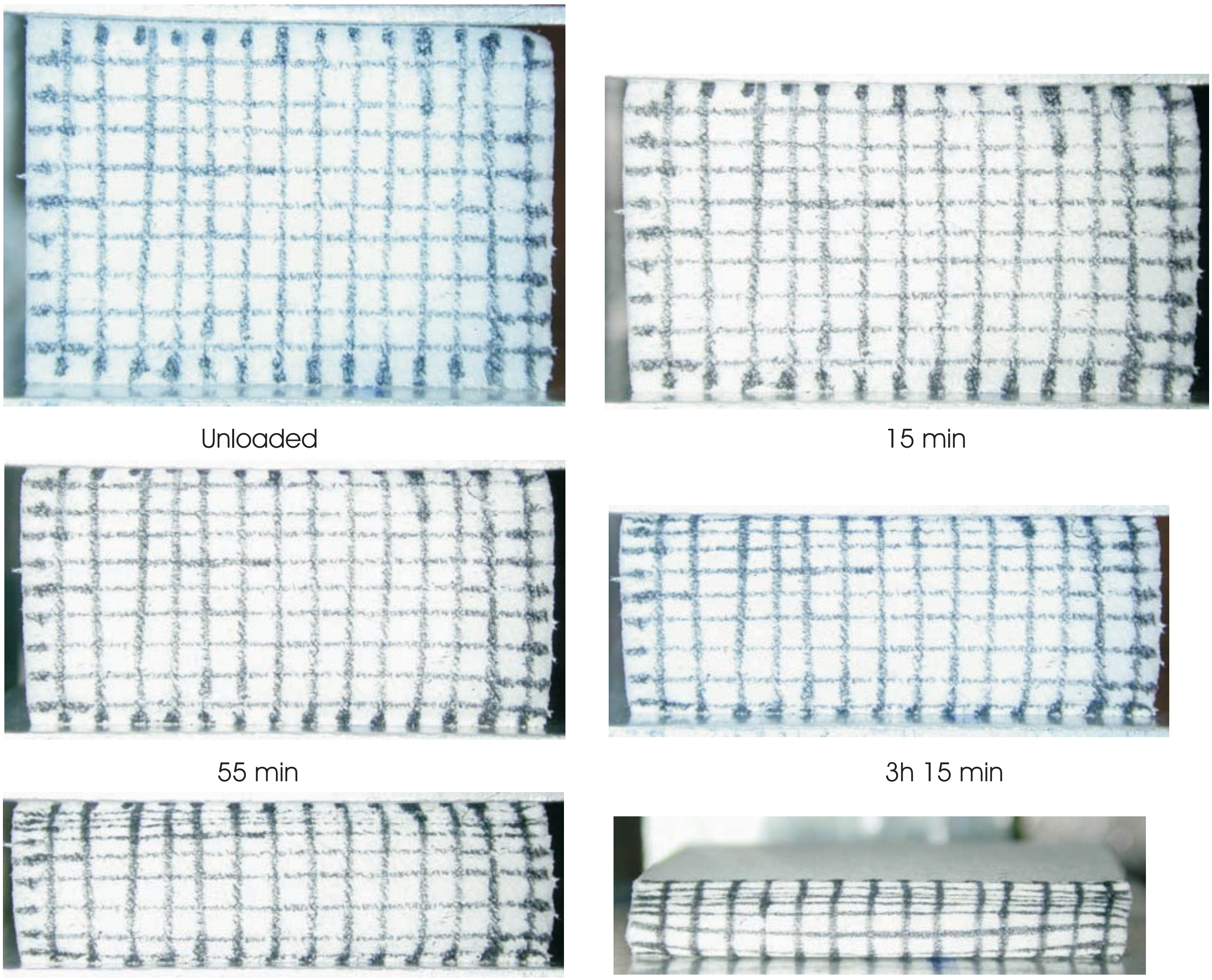

Unloaded

15 min

55 min

3h 15 min

6h 15 min

24h

Figure 2.13: Sequence of digital photographs taken during a creep experiment.

interval, and the interactions developed as the time passed. In the model, the gas flow was only impeded by the permeation through the cell faces, which do not change in thickness during compression as the faces wrinkle. The foam diffusivity was obtained by fitting the predicted creep curves to experimental data with a value of $100 \times 10^{-12}\,\mathrm{m}^2/\mathrm{s}^{-1}$. It predicted that the gas pressure changes over a short distance, from fully pressurised, near to the mid-thickness, to completely empty cells, near the surface, i.e. there has been a development of a layer of depleted cells. The prediction of the creep rate at high levels of creep strain was reasonable, but there was still a large separation between experimental and predicted creep curves in the range 100 to 200 kPa. Mills & Rodríguez-Pérez concluded that the cell gas loss was likely to cause a change in a foam response with repeated impact.

Experimental methods

The changes in the gas composition can be determined by different methods which can be divided into five [Gunn et al. (1974); Ostrogorsky et al. (1986); Ostrogorsky and Glicksman (1988); Brodt and Bart (1993); Svanström and Ramnäs (1995); Svanström et al. (1997); von Solms et al. (submitted)]:

- Variation of cell gas composition or pressure over time: this method uses gas chromatographs and a gas sampling system to determine local gas compositions at different ages. With this method part of the foam is destroyed and for fast diffusing gases a concentration profile is obtained.

- Change in thermal conductivity with time: this method measures the foam ageing and the long term thermal conductivity value is obtained. It is carried out at a raised temperature to accelerate the process.

- The rate of gas transmission through the sample: in this method a partial pressure gradient is applied across the sample and the permeation rate is measured by different methods, such as pressure measurements, gas chromatography, mass spectroscopy.

- The rate of absorption of the gases in the sample, this method is carried out with thin samples or milled samples. The gases are removed from the sample by keeping it under vacuum at 70 °C in a closed vessel. Then a gas is released into the vessel and the absorption rate is measured by monitoring the pressure as a function of time or by monitoring the mass increase if the sample is held under constant pressure and

- The rate of out-gassing from the foam sample: this method is similar to the one described above but in this case the sample is monitored while it is held in a vacuum.

2.4 Running

Running movement involves the foot contacting the ground. The first contact is made by the foot and transmitted to the rest of the body. Hence, some brief comments on the foot structure are necessary to understand the biomechanics and the role of the running shoe.

The foot plays an important role in supporting and balancing the body's weight while standing, as well as raising and moving the body forward when in motion. These functions require a high degree of stability. In addition, the foot must be flexible, so it can adapt to uneven surfaces. The multiple bones and joints of the foot give it flexibility, but these bones must form an arch to support any weight [Cheskin et al. (1987); Tortora and Grabowski (1996); Hennig (2002)]. There are three arches in the foot which are maintained by the bones, the muscles, the tendons and the ligaments (Figure 2.14),

- The foot is composed of 26 skeletal bones held together by muscles, ligaments and tendons. These bones are divided into three groups: the phalanges, the metatarsus and the tarsus [Cheskin et al. (1987); Tortora and Grabowski (1996)].

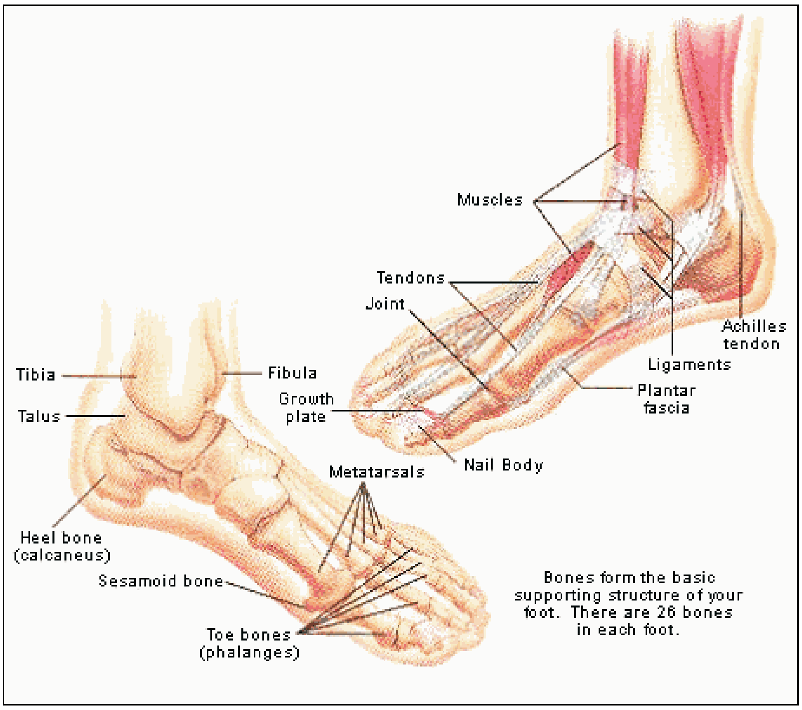

Figure 2.14: Illustration of the foot anatomy. (From FootSolutions (1999))

- The muscles of the foot are classified as either intrinsic or extrinsic. The intrinsic muscles are located within the foot and cause the movement of the toes. The extrinsic muscles have their origin in the lower leg.

- The ligaments serve as hinges to keep the bones and joints together. They are fibrous and strong but less elastic than muscles. They maintain the static form of the foot. There are 109 ligaments in the foot.

- Tendons are strong inelastic attachments between the muscles and the bones. They keep the dynamic balance and shape of the foot.

The foot is divided into three main regions [Tortora and Grabowski (1996)] (Figure 2.15):

1. Forefoot: it comprises the metatarsals and phalanges.

2. Midfoot: it contains the navicular, cuboid and cuneiform bones.

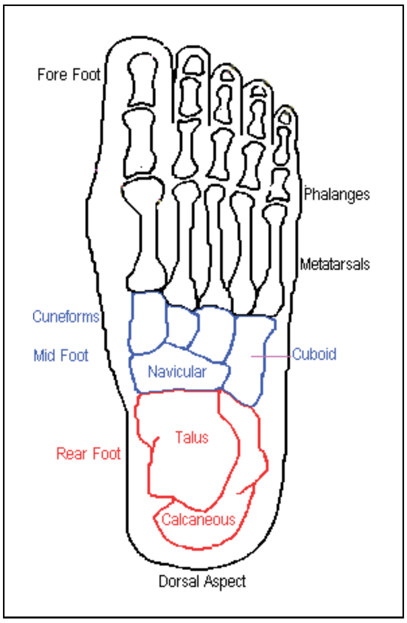

Figure 2.15: Bony structure of the foot anatomy divided into three main regions. (From Nurses Association (2003))

3. Rearfoot: it comprises the calcaneus and talus and they support the tibia.

2.4.1 Biomechanics of running

Biomechanics is the study of human motion and concentrates on three aspects of it: (1) the analysis of internal and external forces acting in and on the human body, (2) the analysis of the effects of sports shoes in such forces, and (3) the determination of stress which could cause injuries [Segesser and Nigg (1993)].

The biomechanics of running is studied by the analysis of three types of parameters,

1. kinematics parameters; the movement is studied by the use of high speed cameras without considering the forces involved [Milliron and Cavanagh (1990); Andriachi and Alexander (2000)],

2. the ground reaction forces; the forces generated during the foot-ground contacts are analysed by using force platforms [Frederick and Hagy (1986); Cavanagh and Lafortune (1980); Miller (1990)], and

3. the pressure distributions; the pressure patterns inside the running shoes are studied by inserting pressure sensitive sensors into the shoes [Henning et al. (1990); Hennig and Milani (1995, 2000); Orlin and McPoil (2000)].

Kinematics studies reveal the movement pattern of areas of the body where a reflective marker has been attached [Milliron and Cavanagh (1990)]. These skin makers are considered as an approximation of the actual movement of the bony parts of a joint. The analysis of a particular group of markers gives a good picture of the way the joints act in a coordinated manner to produce the movement under study [Andriachi and Alexander (2000)].

The kinematics analysis of running distinguish two phases in a running gait cycle, which is defined as the period from a foot contact until the following contact by the same foot [Donaghue and Veves (1997)]:

- the swing phase, which is a period where the foot has no contact with the ground and is preparing for the contact and

- the stance phase, which is the period where the foot is in contact with the ground and is divisible into three: contact, mid-stance and propulsion. During the stance phase, and in order to maintain balance, the foot contacts the ground beneath the centre of the body mass. Hence, the foot makes initial contact in a slightly supinated position (Figure 2.16), which can vary from 0 to 10 ° relative to the lower leg. As the movement continues, the foot rotates to make flat contact with the ground; this rotation is called pronation and it reaches a maximum angle (typically 10 to 20 °) within the first 50 % of foot contact. The foot then supinates until take-off [Clarke et al. (1984); Donaghue and Veves (1997)].

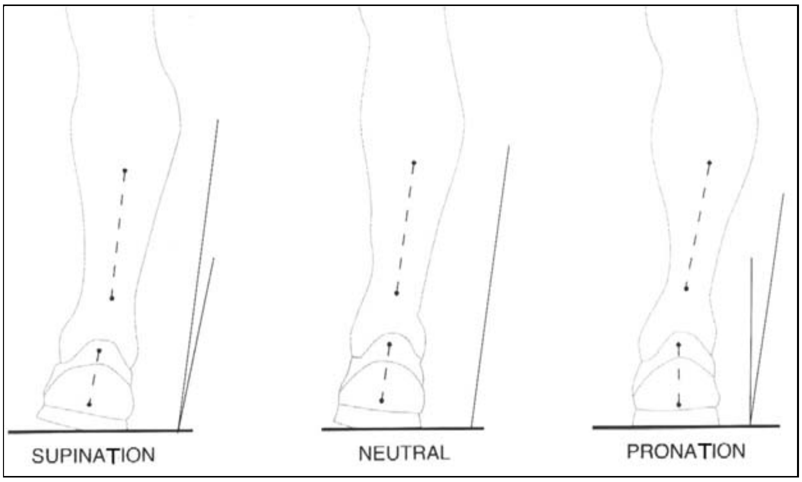

Figure 2.16: Illustration of the supinated, neutral and pronated position in running.

Although pronation is a natural movement of the foot, excessive pronation is argued to be harmful for the runner [James and Jones (1990)]; although conclusive clinical evidence for any relation between pronation and the development of specific injuries has not yet been found [Reinschmidt and Nigg (2000)]. Nevertheless, the control of pronation has been introduced into shoe design with alterations of: (1) the midsole (e.g. dual density midsoles, round and flared heels), (2) the insole (e.g. orthotics and support in the arch region), (3) the heel counter and (4) the upper (e.g. lateral reinforcements).

Force platform studies reveal the magnitude and variability of the forces generated between the runner's body and the ground under different conditions [Miller (1990)].
During the contact cycle, interactive forces are exchanged between the human body and the ground. The ground reaction force (GRF) reacts to the force of the push on the ground by the foot; this force acts over the entire contact surface [Nigg (1986c)]. By Newton's third law, it is equal in magnitude and opposite in direction to the action force. The resultant of this force consists of three orthogonal components

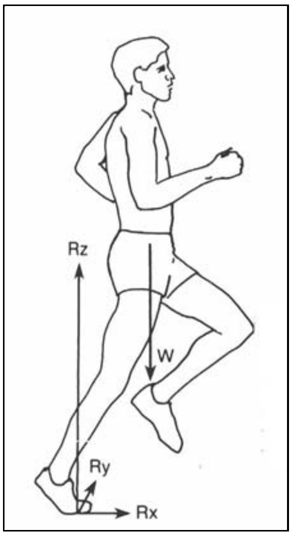

Figure 2.17: The orthogonal components of the ground reaction force. Where R_x, R_y, R_z are the ground reaction force components and W is the body weight. (From Miller (1990))

[Nigg (1986c); Miller (1990)] (Figure 2.17):

- R_x horizontal force in the movement direction, called the braking-propulsion force
- R_y horizontal force perpendicular to the movement direction, called the medial-lateral force
- R_z perpendicular to the surface platform, called the vertical force.

The vertical component is the dominant force and is used to characterise the GRF. This component has been largely studied and the curve which it describes is proved to have two peaks (Figure 2.18): an "impact" peak occurring shortly after first contact (< 50 ms) and an "active" peak occurring near the middle of the stance phase (> 50 ms); hence, the impact peak is associated with the initial contact load and the active peak is associated with the foot push-off of the stance phase [Clarke et al. (1983); Nigg (1986c)]. The impact force has been subject to extensive research

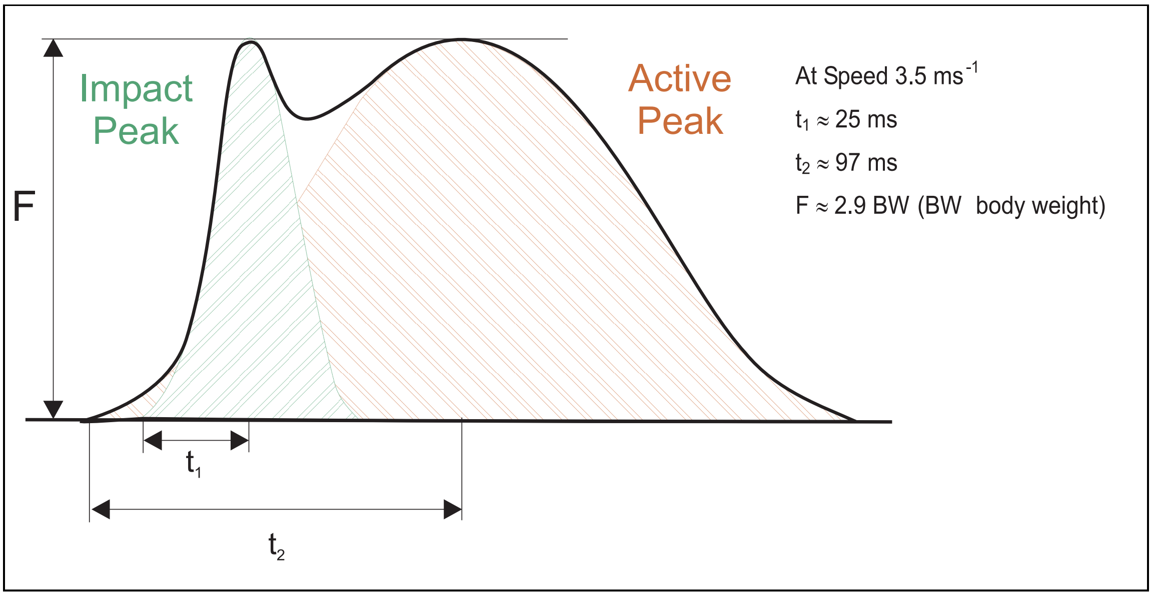

Figure 2.18: Diagram of the vertical component of the GRF as a function of time for a rearfoot striker. (After Cavanagh et al. (1984))

because is also argued that high impact forces can cause certain types of injury. The magnitude of this impact force typically is in the order of 2 to 3 kN but can go up to 5 kN (Figure 2.19) depending on the runner's body mass, running speed, running style (touchdown kinematics), shoe and surface properties and gradient [Nigg (1986c); Miller (1990); Shorten (2000)].

A further characteristic of the GRF is the centre of pressure, which is the point of application of the resultant force. This changes during the course of the stance. According to the start point of the centre of pressure, the runners are classified as rearfoot, midfoot and forefoot strikers [Cavanagh (1989)] (Figure 2.20). Most long distance runners are rearfoot or heel strikers, while sprinters are usually forefoot strikers.

The main advantage of force platforms is their ability to record all the directions of the ground reaction force. However, they are not a particularly sensitive measure because they reflect the acceleration of the body's centre of mass; hence, they pro-

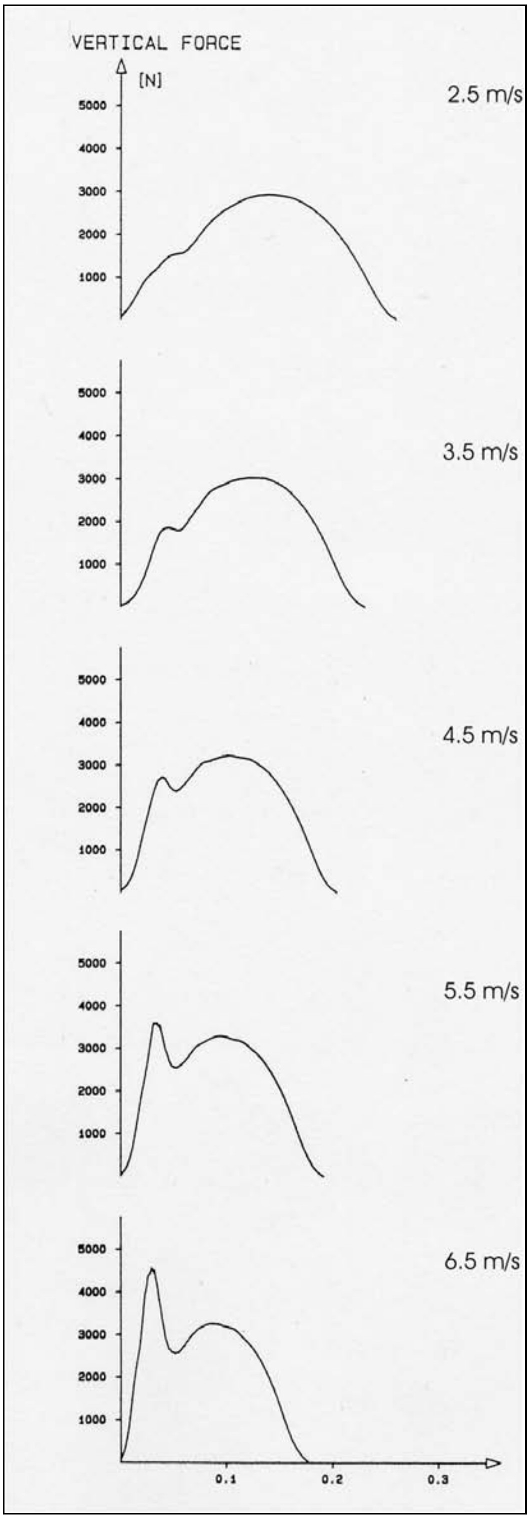

Figure 2.19: The vertical component of the GRF as a function of time for a rearfoot striker at different velocities. (From Nigg (1986a))

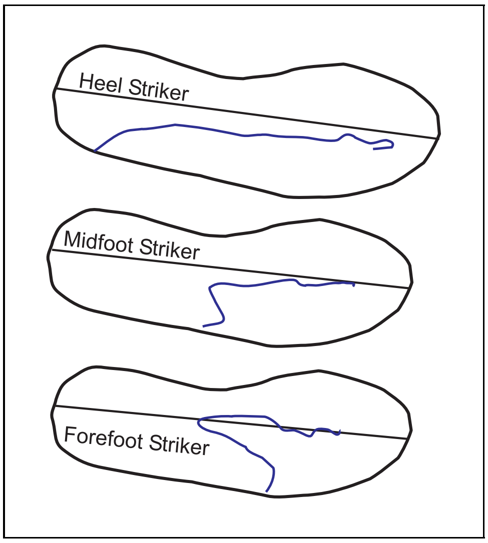

Figure 2.20: Representation of the centre of pressure patterns for three runners. (After Cavanagh et al. (1984))

vide information only about the total ground reaction force acting on the runner's body [Miller (1990)] and therefore they do not give any insight into the distribution of the load. It has been concluded that to achieve a full image of the movement under study, GRF has to be used in conjunction with in-shoe force transducers and of three-dimensional high-speed video analysis [Miller (1990); Hennig and Milani (2000)].

Pressure distribution studies provide detailed information of the distribution of the force over the sole of the foot [Cavanagh et al. (1984)]. In essence, the pressure sensors are force transducers that measure the force acting on a known surface. These sensors are electromechanical transducers which convert a mechanical event into an electrical signal. This is recorded and stored for analysis. The sensors' technology is based on piezoelectric, capacitive and resistive principles [Rosenbaum and Becker (1997); Urry (1999)],

- the piezoelectric sensors develop surface charge in an amount dependant on the magnitude and orientation of the applied stress. They are made of ceramic and polymeric materials,

- the capacitive sensors consist of two electrically conducting surfaces separated by a compressive dielectric material, and
- the resistive sensors suffer a change in resistance due to an applied stress. A standard resistive sensor uses conventional strain gauges in its design; however, resistive techniques using conductive rubber, conductive ink and conductive polymers have also been developed.

All these sensors measure the normal component of the ground reaction force and neglect the other two components of the force [Rosenbaum and Becker (1997)]. The sensors can have two configurations, (1) as a sole matrix, where each active sensor is arranged in rows and columns in the entire plantar surface of the foot [Rosenbaum and Becker (1997)], and (2) as a sole with discrete sensors at defined anatomical foot structures [Hennig and Milani (1995, 2000)]. In matrix systems, the recorded data is presented as two or three-dimensional colour coded maps at a particular moment of the foot contact or as a composition of every single map throughout the contact. In discrete systems, the data is presented as a bargraph where each sensor shows a different bar-height according to the registered pressure (Figure 2.21).

The main parameter studied is the peak pressure which is determined by the highest pressure registered in the whole plantar surface or in a selected foot region, such as the peak pressure in the heel or in the forefoot regions. The pressure distribution pattern differs for each type of runner, i.e. the distribution observed in rearfoot strikers is different from that of forefoot strikers (Figure 2.22).

In-shoe pressure distribution is used to assess the influence of footwear on foot loading characteristics [Hennig and Milani (1995, 2000)] and for clinical applications such as the evaluation of foot pathology or abnormalities [Rosenbaum and Becker (1997); Orlin and McPoil (2000)].

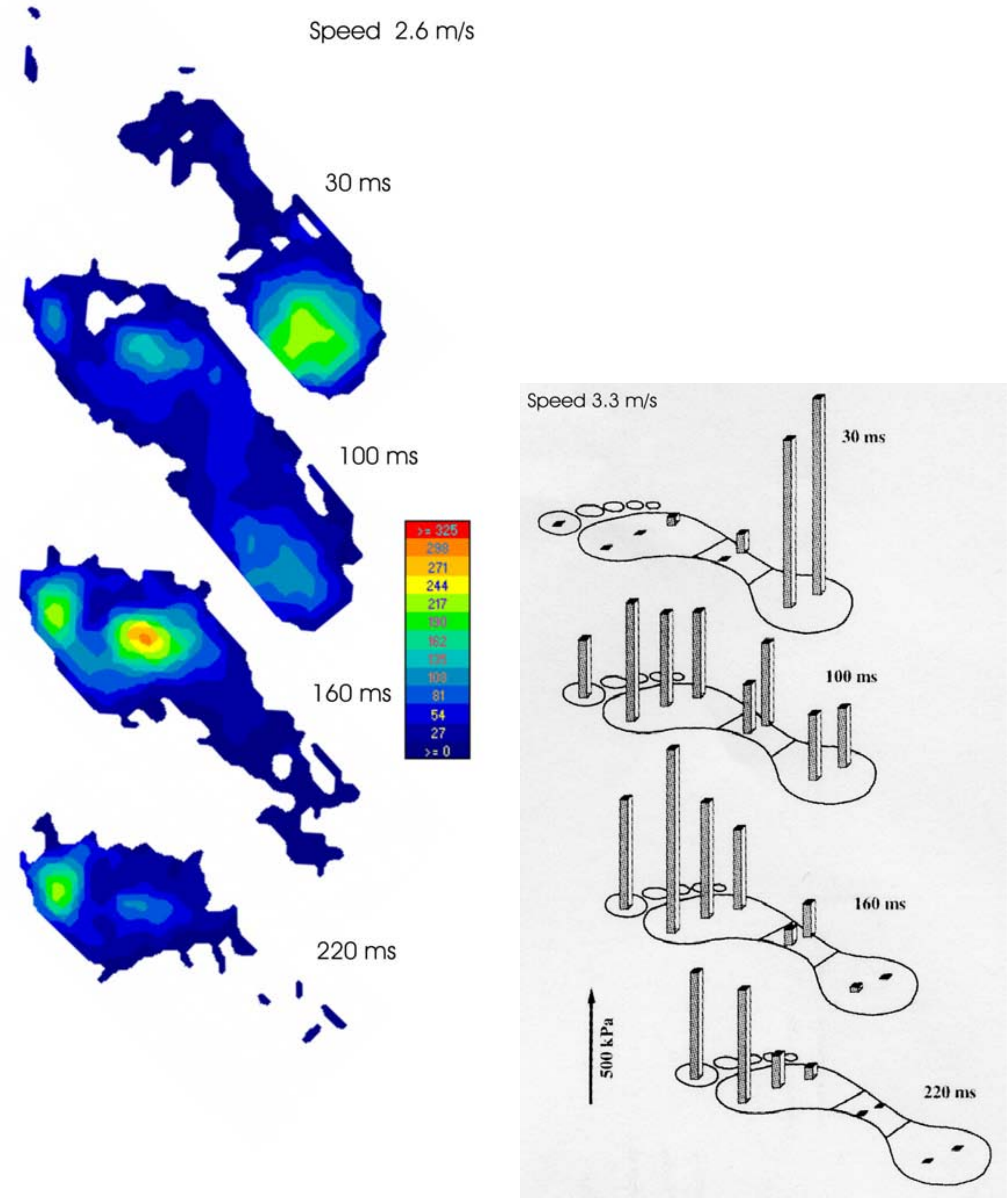

Figure 2.21: Representations of the plantar in-shoe pressures. Left: colour maps obtained with a sole matrix. Right: bargraph obtained from discrete sensor placed underneath the foot (From Hennig and Milani (2000)).

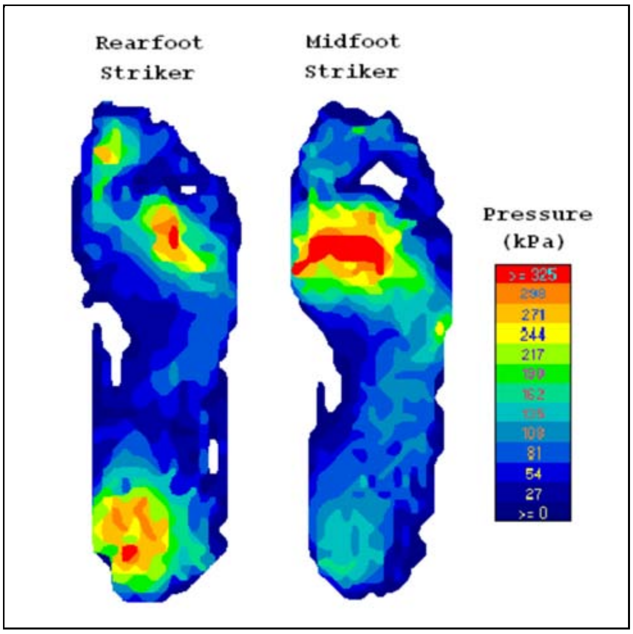

Figure 2.22: Two dimensional composite maps throughout the contact for two types of runner: rearfoot striker and midfoot striker.

Due to the nature of the biomechanics studies, the design of an experiment has to be carefully done and it would depend on whether the study is for research or for clinical proposes. Research studies have to consider that each individual chooses a certain combination of stride length and stride frequency, where the stride is defined as the period between successive contacts by the same foot [Cavanagh and Kram (1990)]. This selection has been proved to be influenced by: (1) the velocity of the experiment, (2) the footwear, (3) the properties of the surface, (4) the physical dimensions of the runners and (5) their injury history [Gross and Bunch (1989); Henning et al. (1990); Milani et al. (1997); Hennig and Milani (1995, 2000)].

There have been large efforts to model the surface-shoe-heel interaction in order to predict the generated forces by introducing changes to the midsole characteristics without the need to produce the entire shoe. However, more research has to be done because of the complexity of the system. The two reported approaches are, (a) the study of the viscoelastic characteristics by the use of springs, masses and dashpots [Shorten (1993); Nigg and Anton (1995); Nigg and Liu (1999); Liu and Nigg (2000)] and (b) the study of the pressure distributions by Finite Element Analysis (FEA) [Lemmon et al. (1996); Shiang (1997); Verdejo and Mills (2002, accepteda)].

2.4.2 Running shoes

Running shoes components

The design of running shoes, and of any sport shoe, has been deeply influenced by biomechanical and material research [Cheskin et al. (1987)]. These types of research helped identify the way the foot contacts the ground and the impact forces generated. Manufacturers introduced the findings of the researchers into their designs to improve the shoes characteristics, leading to an increase of the number of runners and joggers over the years [Shorten (2000)]. The modern design of the running shoes has three main components: the outsole, the midsole and the upper part (Figures 2.23, 2.24 and 2.26).

Outsole
The outsole is the part of the shoe that makes contact with the ground (Figure 2.23). It is mainly made of rubber, although polyurethane can also be used. The outsole is attached to the midsole and has a intricate pattern which affect its performance [Cheskin et al. (1987)].

The outsole mission is to provide [Cheskin et al. (1987)]:

- grip and traction, they are determined by the coefficient of friction between the shoe and the ground;
- flexibility, it is accomplished by the pattern design by reducing its thickness

Figure 2.23: Running shoe component: The Outsole.

in certain parts of the sole with a canal or flex path;

- durability, both by preventing the deterioration of the midsole and by providing a slow wear rate and
- shock absorption, certain patterns of the outsole provide part of the cushioning of the shoe, to some extend.

There are not many reported studies on friction characterisation of shoes [(Nigg and Kerr, 1983, pages 153–168)], most studies have concentrated on the sport surface characterisation [Nigg and Kerr (1983); Frederick (1984)]. The outsole wear tests consist on the analysis of the material loss after the shoes have been used over a period of at least four weeks [Edelmann-Nusser et al. (2002)]. However, this approach introduces difficulties to the wear analysis due to the different shoe-surface interactions of the subjects. Standardised abrasion tests have been conducted by placing a prosthetic foot-shoe system in contact with a moving abrasive belt. The areas that suffer the highest levels of wear are firstly the outside edge of the heel and secondly the centre of the forefoot.

Midsole

The midsole (Figure 2.24) is the main shock absorption system of the shoe and is

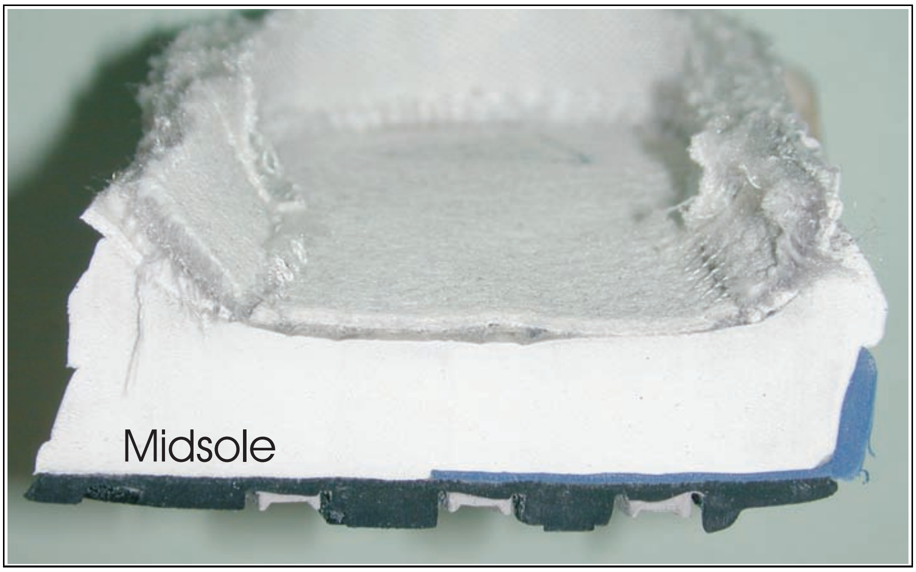

Figure 2.24: Running shoe component: The Midsole. (Transverse view)

placed between the upper part and the outsole [Cheskin et al. (1987)]. Cushioning systems can be made of different components, e.g. from a polymeric foam, from the combination of two foams with different densities, from the combination of a foam and a gel and from the combination of a foam and large air inserts.

The role of the midsole is:

- to reduce the peak forces transmitted to the body of the runner;
- to provide protection against injuries; the reduction of the impact forces is argued to reduce the risk of certain types of injury such as Achilles tendinities and heel pain; although there are no conclusive evidence for such affirmation [Reinschmidt and Nigg (2000); Shorten (2002)];
- to provide comfort; and
- to provide stability.

Running shoe midsoles are mainly made of EVA, which can be compression or injected moulded [Alley and Nichols (1999)]. The density of the midsoles varies from 150 to 250 kg/m^3, and it can go to higher density in regions intended to give extra support. The EVA copolymer used contains between 18 % to 22 % of VA [Samsung (1999)], resulting on a degree of crystallinity around 20 %.

Several materials have been suggested as an alternative to EVA, polyurethane (PU) being the most probable. PU has better cushioning and durability qualities than EVA. However, its main disadvantage is that is much dense than EVA, hence shoes made of PU are heavier than shoes made of EVA [Indesteege et al. (1998); Alley and Nichols (1999); Knoerr and Rouiller (2002)]. PU foams are used in sports which require high levels of impact absorption and where weight is not a main requirement, e.g. basketball. Recently, low density PU (*c.* 250 kg/m^3) has been processed and suggested for use in sport shoes [Sawai et al. (2000)]. Ethylene/styrene interpolymers (ESI) have also been suggested as an alternative [Dubois et al. (2002); Ankrah et al. (2002)] because they improve the impact properties although other properties such as ease of bonding to shoe components may be of critical importance [Ankrah et al. (2002)]. Nevertheless, the company has stopped the production of this material [Ankrah (2002)].

The materials testing of the midsole foams is carried out under impact conditions where the height and weight of the impact striker are adjusted to approximate the characteristics of runner impact between the shoe and the ground [Misevich and Cavanagh (1984); Cheskin et al. (1987); Alley and Nichols (1999); Knoerr and Rouiller (2002)]. The areas where the concentration of the force is significantly high are the forefoot and the heel region. Therefore, the experiments take place in these two areas and there is a specific standard method for each region [ASTMF1614-99 (1999); ASTMF1976-99 (1999)].

Another important test is the response of the foam to impacts over time, i.e. the durability of the midsole. Almost all the information available to runners [Running Magazine (2003); Pribut (2002)] suggests a shoe life of 560 to 880 km (350 to 550 miles). A figure of 805 km (500 miles) was first suggested by Peter Cavanagh's lab at University of Pennsylvania in the late 1970s [Cavanagh (1980); Cheskin et al. (1987)] and since then this information has been reinforced with experience. Analysing the comments made by runner on their internet forums, such figure seems to be widely accepted. However, there is not unanimity to what component of the shoe wears first, whether it is the outsole or the midsole. Durability tests are based on laboratory fatigue tests. Two main reported studies are:

- Uniaxial tests on EVA foam under uniform strain [Misevich and Cavanagh (1984)] at a frequency of 1 Hz with an Instron, to a constant peak compressive stress of 1.15 MPa. This research showed that the curvature of the foam force-compression relationship increased with the number of cycles, and that the input energy decreased linearly with the logarithm of the number of cycles. However, the strain rate in their test is much lower than in footstrike impacts, which may affect the viscoelastic response of the polymer.

- A prosthetic foot was used to load the heel of the shoe [Cook et al. (1985)], applying severe loads to the rear part of the heel. They only plotted the energy absorbed per cycle, and say that, after a number of cycles equivalent to 805 km of running, shoes maintained 55 ± 10 % of their initial energy absorption. They also tested shoes after 805 km of running by volunteers and say that 70 % of the initial energy absorption remained. However they did not report any details of the EVA foam.

Studies on diffusion in EVA midsole foam [Mills and Rodríguez-Pérez (2001)] under creep suggested that there is a reduction of the air content of the foam cells, hence reducing the cushioning. Finally, the cell geometry in sectioned EVA midsoles, [Bartlett (1999)] showed that cells next to the outsole became flattened after 3200 km of running.

Figure 2.25: Running shoe component: The Insole.

An additional layer of a thinner and softer foam is inserted between the midsole and the foot (Figure 2.25). This insole is introduced to improve comfort, also as an extra cushioning device, absorb perspiration and it can be design no reduce overpronation.

Upper

The upper part is the “top” of the shoe, where the foot is introduced (Figure 2.26). There is a large range of materials used in this part, from organic (e.g. leather and cotton) to synthetic (e.g. nylons and PVC coated fabrics) [Cheskin et al. (1987)] and is made of several pieces which are then sew together.

The role of the upper part is to provide [Cheskin et al. (1987)]:

- stability and protection from injuries, e.g. by the introduction of the heel counter which controls the pronation of the foot;
- support;
- flexibility;
- breathability; and
- aesthetic.

Figure 2.26: Running shoe component: The Upper part.

This part determines the foot environment which will be different from the surrounding air. The temperature and humidity inside is always greater than outside, the temperature can differ by 5 to 10 degrees from the external and road temperature [Kinoshita and Bates (1996)]. The shoe breathability and permeability are also industrially tested [Cheskin et al. (1987)], however few reported papers exist on the thermal properties of shoes [Kinoshita and Bates (1996); Covill et al. (2002)].

Running shoe design

The design of running shoes is influenced by functional (e.g. injury prevention, performance and comfort) and non-functional factors (e.g. price, fashion and durability) [Reinschmidt and Nigg (2000)]. Each functional factor is determined by different key aspects (Figure 2.27). Both injury prevention and performance might be improved by further research however the comfort factor introduces a subjective aspect to the design due to its definition [Chen et al. (1996)]. Theoretically, the best running shoe should be capable of [Frederick (1989); Robbins and Waked (1997)]

- absorbing the maximum impact forces possible
- returning the maximum energy to the runner at the forefoot during take-off

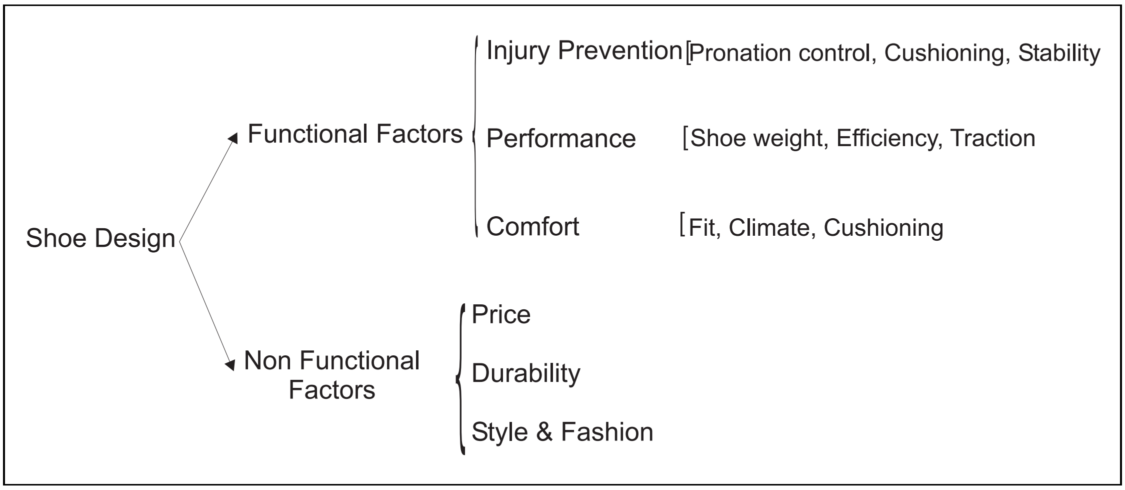

Figure 2.27: Diagram of the factors affecting the design of footwear.

[Stefanyshyn and Nigg (2000)]

- giving the maximum stability possible
- cushioning durability, that means it has to be capable of absorbing the same energy after 1000 km of running than at the start
- flexibility of the sole at a point just behind the metatarsal heads
- light weight as the addition of mass increases the runner's work [Reinschmidt and Nigg (2000)] and
- ability to control pronation.

Many of these desired qualities are mutually exclusive. Some examples are [Frederick (1989); Reinschmidt and Nigg (2000)]:

- soles that provide good traction are typically worn out quickly, i.e. they are not durable;
- harder midsoles are more stable but less flexible;
- adding cushioning decreases the stability; and

- the reduction of weight usually reduces the energy absorption and stability.

Therefore, the design of running shoes, and of any sport shoe in general, should be optimised according to the needs of each specific application, e.g. the shoe weight is a main concern to sprinters but it is not to basketball players.

2.5 Materials under study

2.5.1 Foaming process

EVA foams used in running midsoles are mainly made by two different processes: compression moulding processes and injection-moulded processes. The resulting foam from each process is called Phylon or Injection Phylon (IP) by manufacturers [Alley and Nichols (1999)]. The foams under study were made by compression moulding with a two-stage process: first, the extrusion and second, the compression moulding.

The foaming process is as follows [Park (1991); Yu (2001)]:

1. The EVA, the blowing agent, peroxide and the rest of the ingredients (Table 2.3) are mixed together and introduced into a mill to get a homogeneous mixture.
2. The extrusion stage takes place by introducing the mix into a calender, which consists of four horizontal robust counter-rotating steel rolls where the mix is formed into a sheet of uniform thickness [Powell (1983)]. The sheet is cut and pile up to a certain thickness, which depends on the volume of the cavity of the mould.
3. The slab is heated in a compression mould and expanded by a release of pressure.
4. The foam slab is moved into a cool flat place for at least three days until its dimension is stabilised.

Ingredients	Contents (*phr**)
EVA	95
Rubber	5
Crosslinking Agent	0.75
Foaming Agent	4
Stearate Acid	1
Zinc Oxide (ZnO)	1
Calcium Stearate	1
Magnesium Carbonate ($MgCO_3$)	8
Titanium dioxide (TiO_2)	1

Table 2.3: Formulation for a EVA foam with 15 to 18 % VA content. * phr denotes grams of component per 100 g of dry resin. Information from Samsung Co. [Samsung (1999)] Contents of the foams under study may vary.

5. The skin is removed and the foam slab is cut into a fixed thickness and then trim to a specific contour.
6. This preform is then heated in the mould until the surface is melted.
7. Then the foam is subjected to a change of temperature, by turning off the heat source and on a cooling system, and its dimension is stabilised.
8. The edges are trimmed to get the finished product.

2.5.2 Studied foams

The EVA foams used were provided by NIKE^{TM}, USA, with three main densities 108 kg/m^3, 150 kg/m^3, and 265 kg/m^3 (Table 2.4). Three types of medium density foams were provided, two with the same formulation but slight change in the amount of blowing agent, the cellular structure being affected by this change (referred as

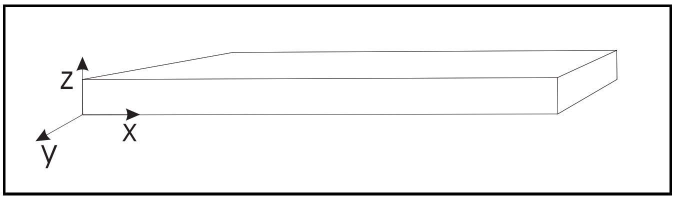

Figure 2.28: Designed axis for the study of the properties of the foams.

Used nomenclature	Measured Density (kg/m^3)
EVA108	108.4 ± 1.7
EVA146	146.6 ± 1.0
EVA151	151.3 ± 1.8
EVA152	152.3 ± 1.4
EVA265	265.2 ± 1.3

Table 2.4: Nomenclature and foam density with standard deviation.

EVA146 and EVA152), and the third was supplied for reference only (referred as EVA151) [Yu (2001)]. This foam used the same formula, but changed both the blowing agent and peroxide, its cellular structure being the coarsest one. Lower and higher density foams were made with the same formulation as EVA152 and EVA146. As some of the properties of the foams are anisotropic [Klempner and Frisch (1991); Cunningham and Hilyard (1994); Gibson and Ashby (1997)], two directions (Figure 2.28) were selected along the samples.

Chapter 3

Experimental Techniques

The mechanical behaviour of foams depends on several material factors, such as the chemical composition of the base polymer and its morphology, cellular structure and density [Cunningham and Hilyard (1994)] (Figure 2.3). Different techniques can be used to obtain a broad image of the foam characteristics. These techniques can be divided into the following areas: thermal characterisation, such as TGA and DSC; structure characterisation, as SEM and NMR; physical characterisation, such as DMTA or compression behaviour; and chemical characterisation, such as IR spectroscopy and pyrolysis-gas chromatography, etc [Craver (1983)].

In this section, the experimental procedures used in the foam characterisation are described. The chapter starts with the microscopic aspects of the material, cellular structure and chemical composition and continues with the macroscopic characterisation where the mechanical properties studied are explained.

3.1 Microscopic Characterisation

The microscopic characterisation of foams is an important aspect for understanding the sample behaviour. It allows the determination of parameters such as polymer composition, crystallinity and cellular structure, among others. Such parameters

affect the mechanical properties of foams, and in particular EVA copolymers behave differently according to the VA content or degree of crystallinity.
The experimental techniques used to perform the microscopic characterisation were SEM, for the study of the cellular structure, and DSC, ATR and X-Ray for the base polymer.

3.1.1 Cellular Structure

Scanning Electron Microscope (SEM)

The scanning electron microscope forms a sequential image of the surface of an object using a beam of electrons focused by lenses. The beam interacts with a thin layer of the surface and the detected signal is then used to form a TV-type image. Nonconductive materials require a conductive coating and the use of low accelerating voltages to prevent the sample from charging [Sawyer and Grubb (1996)].

This technique permits the determination of the cellular structure of the foams with several parameters such as type of cell (open or closed), mean cell size, cell size distribution, wall thickness and anisotropy as the most important. Qualitative and quantitative image analyses were used to assess the cellular structure of the samples. For this purpose, cross-sections of the foams were fractured at low temperature, immersing the sample in liquid nitrogen ($-169\,^{\circ}$C). A smoother surface would have been achieved by cutting the samples at low temperature but in the process the structure received damage due to the foam's density. The foam was fractured both in a plane that included the thickness direction and perpendicular to it. The samples were vacuum coated with gold and examined using JEOL JSM 5410 scanning electron microscopy (SEM). Six micrographs for the pair of directions x/z and y/z were studied, where the directions were selected as shown in Figure 2.28.

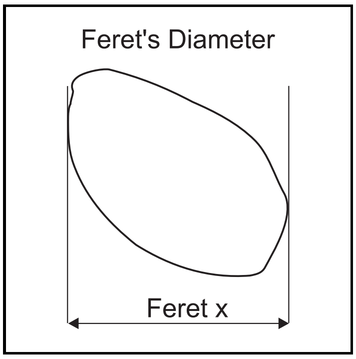

Figure 3.1: Feret's Diameter. (After Rhodes (1994)).

Image Analysis

Image analysis is a widely used technique which extracts information from a given image or a group of images. In materials science both optical and electron microscopy and X-Ray images, among others, are studied with image analysis [Rosenfeld (2001); Gonzalez and Woods (2002)].

The Image Associates KS 400 Version 3.0 software system was used. For each pair of directions, Feret x and y diameters were considered. Feret x is defined as the horizontal distance of the maximum and minimum x-coordinate for each particle, i.e. is the horizontal diameter (Figure 3.1). Thus Feret y is the vertical diameter [Rhodes (1994)]. These values are considered the apparent mean cell size. It has to be notice that, due to the orientation chosen inside the SEM chamber, for each pair of directions, Feret x will correspond to the designated z direction, and Feret y will be the defined x or y direction.

The apparent mean size results (ϕ_x, ϕ_y, ϕ_z) were multiplied by 1.62 in order to consider the relationship between the measured values, the average length of cells which were randomly truncated, and the real diameter of the cells [ASTMD3576 (1994)].

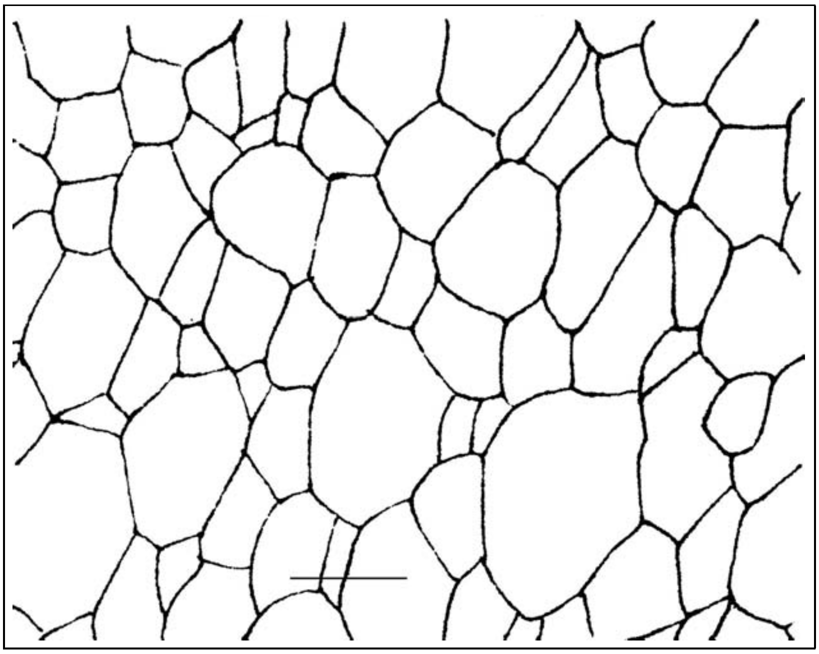

Figure 3.2: Image obtained after manual tracing and scanning. The horizontal bar in the picture represents the scale. Scale: 50 μm. (EVA152x)

The mean cell size (ϕ) was then considered as the average of the three apparent cell sizes. An anisotropy coefficient was defined as the ratio between the apparent mean cell sizes. Statistical analysis of the cell size distributions was also performed.

The wall thickness was measured over 30 randomly selected walls for the pairs x/z and y/z. Micrographs were taken of the middle of the wall where there is no effect from mass concentration due to proximity of edges. The wall thickness is considered as the average of the thicknesses obtained for the pair x/z and y/z.

Before the analysis, a manual tracing of the cell structure was performed [Sims and Khunniteekool (1994)]. A grey scaled image was obtained from scanning the reverse of the outlined cellular structure (Figure 3.2). For the analysis, a connectivity of 4 was selected to avoid ambiguity [Gonzalez and Woods (2002)] in the boundary regions of the cells, which might lead to the merging of two separate cells into one.

3.1.2 Polymer Matrix

Attenuated Total Reflectance (ATR)

Attenuated total reflectance (ATR) is an infrared (IR) reflection technique used to obtain spectra of very absorbent materials, such as polymer films, rubber, and various resins, which cannot be studied using the conventional transmission method [Stewart (1970); Ingle and Crouch (1988); Hsu (1997)]. ATR system uses a crystal of an IR transmitting material with a high refractive index (usually ZnSe crystal). The beam is directed into the crystal at an angle, which exceeds the critical angle, and internal reflection occurs. The sample is placed in optical contact with the surface of the crystal. The beam penetrates a short distance into the sample before the internal reflection occurs. The intensity of the beam is attenuated by the sample in regions of the IR spectrum where the sample absorbs.

Spectra were taken using a Nicolet Nexus FT IR spectrometer in the horizontal ATR mode, in which the crystal of transmitting material is held in a horizontal plane. The spectrum of the crystal was measured and then the sample was placed on top of the crystal and clamped. The spectrum of the sample was obtained by automatically subtracting the crystal spectrum, considered as the background, from the crystal plus the sample spectrum. Experiments were carried out between 4000 and 650 cm^{-1} with 100 iterations and 4 cm^{-1} of resolution. ATR correction was performed to increase the intensity of the absorbance of the bands toward the 4000 cm^{-1} end of the plot [Potts (1963)].

To measure the amount of VA present on the foam samples, a calibration curve had to be established. Spectra were taken from EVA films containing different VA concentrations and were used to determine the VA content of the foams. Four polymer films were pressed from 2 mg of EVA granules with 7.5, 12.5, 18, and 28 mol. % VA concentrations under high pressure (15 tons) and temperature (125 °C) for 2 minutes. A thin slice of EVA152 was cut and its spectrum measured. This sample was also pressed under the same conditions as the polymer films and a further spectrum obtained. The band intensities were larger in the case of the pressed than of the foam sample, due to the different degree of contact between the samples and the crystal. Therefore, the rest of the foam samples were pressed before IR analysis.

Later on, a Golden Gate clamp was available with the ATR facility. This clamp consists of a IIa diamond crystal brazed into a surrounding support disc of tungsten carbide with an active sampling area of 0.8 mm [User Manual (2001)]. A torque limiter screw applies a load of 36.3 kg to the sample; once this load has been achieved the screw rotates without increasing the load. This mechanism ensures the same contact pressure between all the samples and the crystal. Due to the size of the active area, the clamp allows the use of small samples. Hence foam samples were analysed without being previously compressed.

Beer-Lambert's law [Potts (1963); Mirabella (1992)] was used to analyse the results. The law states a linear relationship between the intensities of absorption bands and the concentration of each absorbing species,

$$\mathcal{A} = b \times e \times c \tag{3.1}$$

where $\mathcal{A}$ is absorbance, e is the molecular absorptivity at the frequency, b is the path length of the source beam in the sample and c is the concentration in the sample.

Differential Scanning Calorimetry (DSC)

This technique measures the energy changes by a sample during a certain heating programme by independent measurements of the heat flow in the sample and in a reference material [Craver (1983); Dodd and Tonge (1987)].

Experiments were carried out with a Perkin Elmer 2 DSC, where the energy was calibrated with indium melting energy. To be able to compare the different results, a similar mass was introduced into the calorimeters. The average weight of the samples was 3.2 ± 0.2 mg. Experiments were performed with the following heating programme:

1. Heat from 27 °C to 110 °C at 10 °C/min. The samples were maintained for 2 min at the final temperature.
2. Cool from 110 °C to 27 °C at 10 °C/min.
3. Heat from 27 °C to 110 °C at 10 °C/min.

The information from the first heating cycle reflected the state of the samples after foaming and storage. For semicrystalline materials, such as EVA, the cooling process induces crystallisation, which could be observed on subsequent heating. The purpose of this analysis was to study the melting point, the crystallinity and the thermal history of the foam. The short temperature range means that the degree of crystallinity corresponds to that at ambient temperature where the samples are used and which will affect their performance.

A DSC experiment from -40 °C to 150 °C 10 °C/min on a DSC 30 (Mettler) was performed to compare the degree of crystallinity of the samples with previous studies.

X-Ray diffraction

X-Ray diffraction techniques are widely used for the identification of the atomic structure of crystalline compounds [Ewing (1975)]. When a focused X-ray beam interacts with the atoms of the structure, part of the beam is transmitted, part is absorbed by the sample, part is refracted and scattered, and part is diffracted. X-rays are diffracted by each mineral differently, depending on the type of atom constituting the crystal and how these atoms are arranged.

In equipment for X-ray powder diffraction, X-rays are generated within a sealed

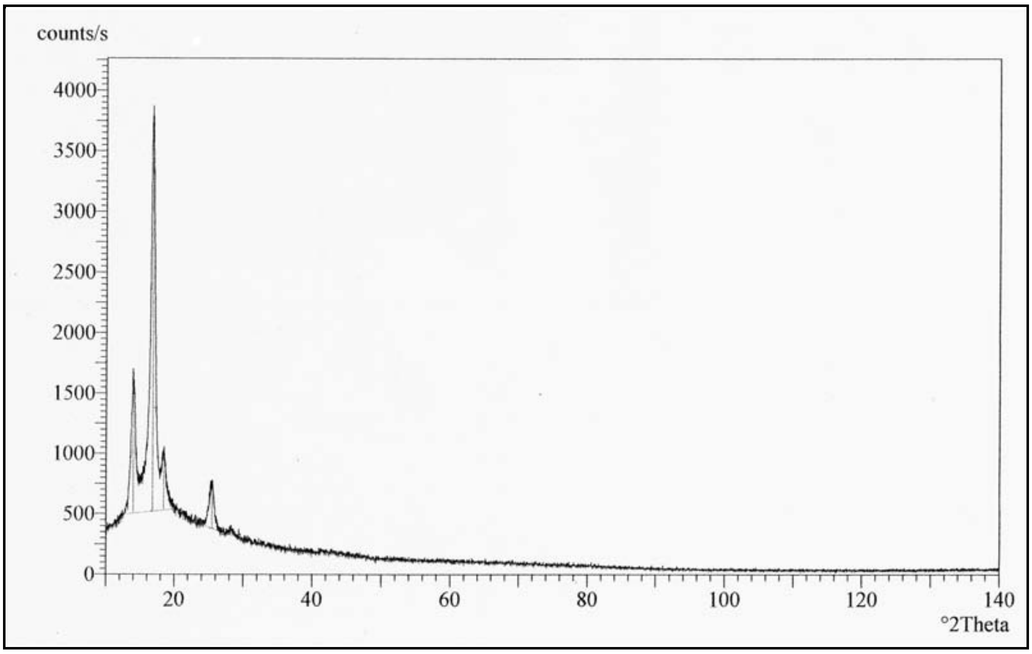

Figure 3.3: Double sided tape diffractogram.

tube that is under vacuum. A high voltage accelerates the electrons emitted by a filament, which then hit a target, commonly made of copper, generating the X-rays. These X-rays are collimated and directed onto the sample, which has been ground to a fine powder. The diffracted beam is detected and its signal converted to a count rate [Kaelble (1967); Ewing (1975)].

In order to analyse any inorganic components present in the foams, they were burned on a Pyro therm furnace at 600 °C for 10 min or until flames were extinguished. The samples were weighed before and after and the % of inorganic component calculated. Philips X'Pert was used to obtain the diffraction pattern from 0 to 140°.
The residues were mounted on a double sided tape, from which the diffraction pattern had already been obtained (Figure 3.3).

On a first stage, the Hanawalt method was used to analyse the patterns [Cullity (1956); Kaelble (1967); Diffraction Manual (1976)]. In this method, the spacing and relative intensities of the three strongest lines d_1, d_2 and d_3 are used to locate the component in the numerical index [Diffraction Manual (1976)]. Once the Hanawalt group for these 3 lines is found, the next 5 strongest lines are also compared, obtaining the component ASTM file number. Afterwards, the agreement between the component under study and the ASTM pattern is contrasted by superimposing both spectra using Philips X'Pert Graphics and Identity v.1.2d.

3.2 Macroscopic characterisation

Mechanical behaviour basically involves the deformation of a material by applied forces [Nielsen (1962)]. This behaviour in viscoelastic materials can be studied by creep, stress relaxation, stress-strain, and dynamic mechanical behaviour, the most important test methods available. The mechanical properties of the foam samples were studied by dynamic mechanical analysis, creep and impact behaviour. These two types of experiment reveal both low and high rates of deformation foam behaviour.

3.2.1 Density

The density of the foams was measured using an Electronic Densimeter (ED120T) hydrostatic balance. The balance uses Archimedes' principle, which states that a body immersed in a fluid is buoyed up by a force equal to the weight of the displaced fluid. A solid is weighed first in air and then immersed in water; the difference in the two weights is the weight of the water displaced by the volume of the solid. The density of water (ρ_w) is very nearly 1 g/cm^3, the density of any substance in g/cm^3 is almost the same numerically as its specific gravity relative to water. Then, the density is given by:

$$\rho \approx \frac{w_1}{w_1 - w_2}\rho_w + \rho_g \tag{3.2}$$

where w_1 is the weight of the solid in air, w_2 is its weight immersed in water and ρ_g (0.00129 g/cm^3) is the air density. As the density of liquids depends partly on temperature, this value was introduced into the hydrostatic equipment used. All the measurements were performed on 15 rectangular samples cut from the slabs and after 1 hour of switching on the densiometer to allow it to stabilise. This balance has a scale error of 0.001 g/cm^3.

3.2.2 Dynamic Mechanic Thermo-Analysis (DMTA)

Dynamic mechanical thermo-analysis (DMTA) is widely used on polymer characterisation [Nielsen (1960); Craver (1983)] and also polymeric foams [Rodríguez-Pérez and de Saja (2000); Rodríguez-Pérez et al. (2000, 2001)]. This technique measures the deformation of a sample by varying, usually sinusoidal, forces. From such tests it is possible to obtain simultaneously an elastic modulus and mechanical damping. The dynamic mechanical properties are described in terms of the storage modulus (E') and loss modulus (E"), which are the real and imaginary components of the complex dynamic modulus E^*, and the loss tangent (tan δ). E' is a measure of the recoverable strain energy, which for low or medium damping is the same as the Young's modulus, whereas E" is related to the dissipated energy [Nielsen (1962)]. Finally, tan δ gives the materials mechanical loss performance in relation to its stiffness.

$$E^* = \sigma/\epsilon \tag{3.3}$$

$$E' = E^* cos\delta \tag{3.4}$$

$$E'' = E^* sin\delta \tag{3.5}$$

$$tan\,\delta = E''/E' \tag{3.6}$$

Thus the stiffness and damping properties of the material can be described by any two of the quantities E', E" and tan δ. The two quantities E" and tan δ are related to the material damping. If these quantities are small at a given temperature and frequency, damping will be small, and vice versa.

The experiments were conducted using Rheometrics PL-DMTA Mk III system, from −80 °C to 110 °C at a heating rate of 5 °C/min. Foams were tested with a frequency of 1 Hz in compression with a parallel plate mode using cylindrical samples, which were 15 mm in diameter and 10 mm in height. The applied static and dynamic force were selected at the low strain range, 2% static strain and 0.11% dynamic strain.

Random copolymers have their transitions in between the positions of the same transition of the homopolymers, i.e. the melting transition of EVA should appear in between the melting point of low-density polyethylene (110-120 °C) and the softening temperature of polyvinyl acetate (35-50 °C). The main EVA transitions in the selected temperature range are [Arsac et al. (2000)]

α or melting transition

The α transition is related to the crystalline region. Its intensity increases with the amount of crystallinity and its position is mainly associated with the lamellae thickness. The melting temperature decreases with the degree of VA from over 100 °C to 0 °C for concentrations of 26.7 % VA [Nielsen (1960)].

β transition or vitreous relaxation

The β transition is related to the chain movement of the amorphous region. It appears near −25 °C and remains nearly independent of the composition until high levels of acetate content. The peak intensity increases with increasing VA content.

3.2.3 Creep

Creep is the variation on dimensions caused by constant stress [Nielsen (1960); Williams (1980); Powell (1983)], so the experiments consist on the measurement of a sample length over time while a load is being applied to it. This test can be

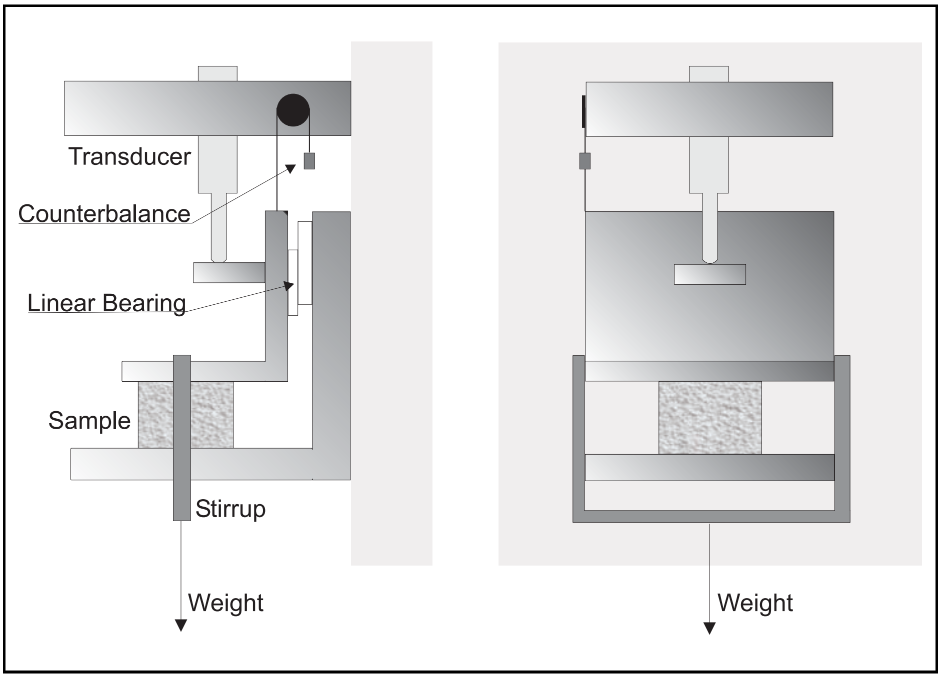

Figure 3.4: Frontal and lateral view of a creep station.

carried out in tension, compression or shear and should be studied as a function of temperature and stress to properly evaluate a material.

In the creep test rig (Figure 3.4), the thickness of the foam is monitored with a Solatron quartz-grating, which is connected to a computer via the input of an analogue to digital converter. The stress is applied by suspending a mass from the stirrup. Three creep stations are placed in a temperature-controlled environment, with recirculating air inside.

The experiments were performed on cube samples of $12 \times 12 \times 12$ mm^3, with different creep stresses, between 50 and 500 kPa, at 20, 25, 35 and 40 °C for 24 hours. The orientation of the samples was the same as its orientation in the shoe, with the compressive stress parallel to the midsole thickness or z direction (Figure 2.28). Due to the low density of EVA108, larger creep stresses (> 300 kPa) instantaneously compressed the sample, therefore creep stress for this sample was kept below 300 kPa.

Isochronous stress-strain cross-plots were obtained from these tests over a series of times. These cross-plots are obtained from each family of creep curves by representing the strain suffered by the sample at a particular time against the applied stress (Figure 3.5). Afterwards, the gas volumetric strain ($\epsilon/(1-\epsilon-\rho)$) was calculated; then the initial yield stress (σ_0) and the gas pressure in the unstressed cells (p_0) were obtained from the fitting parameters of the stress versus $\epsilon/(1-\epsilon-\rho)$ curve.

Creep recovery measurements were carried out on 400 kPa and 500 kPa samples by monitoring the length of the samples once the load had been removed.

3.2.4 Impact response

Repeat Impact based on ASTM F1614-99 Method

This test [ASTMF1614-99 (1999)] covers the measurements of shock absorbing characteristics of materials used in midsoles of athletic footwear. It is based on the use of a mass dropped from a certain height to generate peak compressive forces that are comparable to that suffered by a midsole in heel strike tests. Characterisation is done in terms of absorbed energy, peak pressure and maximum strain or displacement. The standard describes three different procedures based on three different test rigs: falling weight machines, compression force controlled rigs and compression displacement controlled equipments. The first procedure was selected to carry out the experiments.

This procedure requires a vertically-falling weight dropping a fixed distance onto the shoe midsole in the heel region with an impact kinetic energy of 5.0 J. The striker is the flat end of a steel cylinder of diameter 45 mm, with edge of 1.0 mm radius. The total drop mass of 5.9 kg fell 85 mm, guided by low friction bearings on

Selection of times

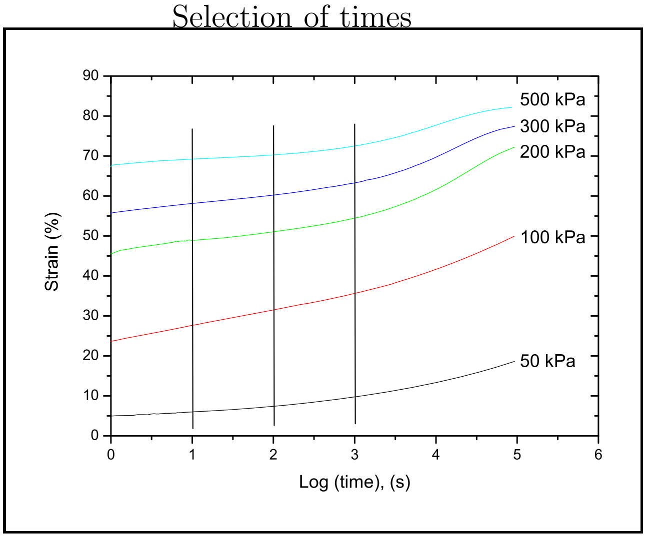

Stress-strain cross-plots

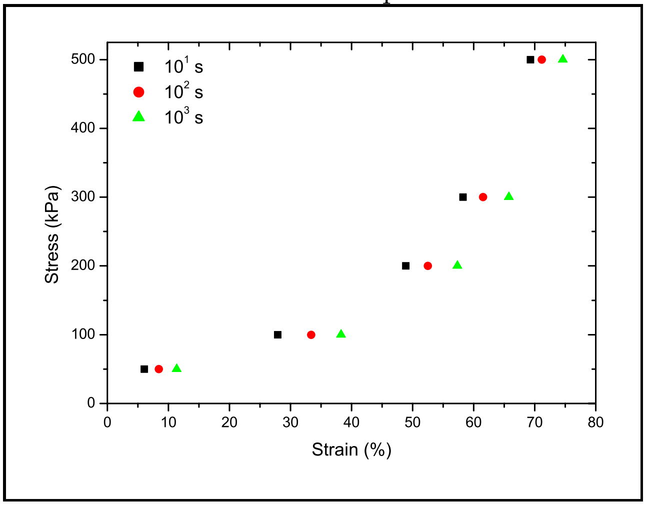

Stress-gas volumetric strain with linear fit

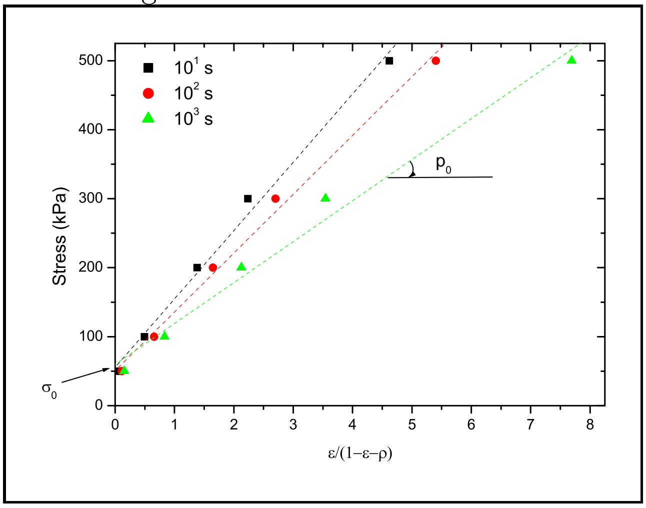

Figure 3.5: Calculation of stress-strain and stress-gas volumetric strain curves.

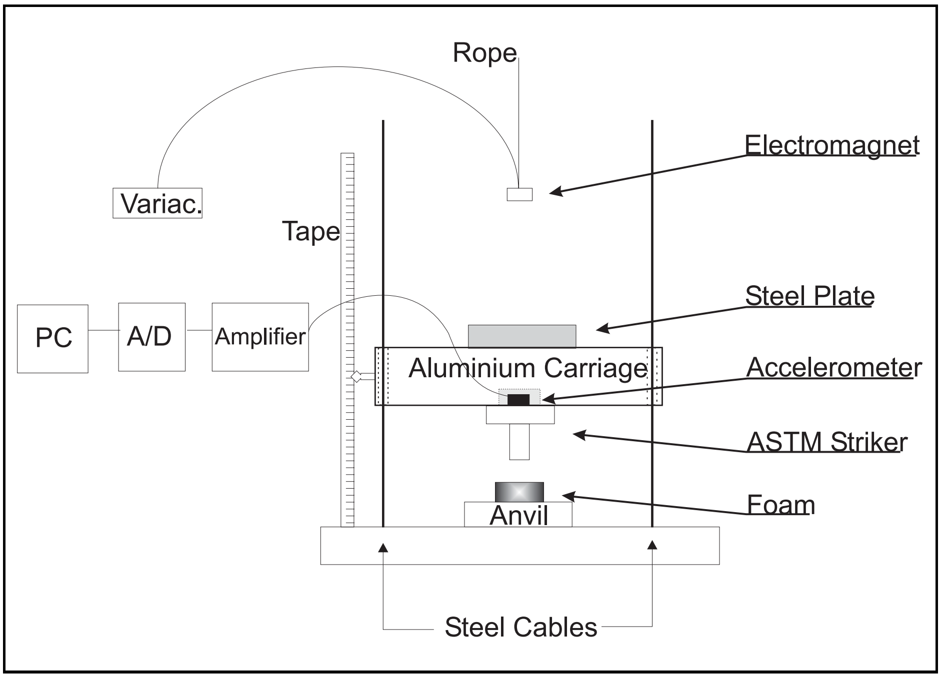

Figure 3.6: Impact test rig diagram.

two vertical cables (Figure 3.6). The signal from an accelerometer inside the striker was captured digitally and analysed by computer to give the striker force versus the deflection of the top surface of the sample [Mills (1994)].

The sample size was 75 × 75 mm^2 by 12 mm in height with the impact occurring in the middle of the area. The samples were fixed to a horizontal rigid fixed anvil and 100 cycles were performed on them. Data were collected every 25 impacts. To ensure the same drop height during the experiment, stops were fixed to the vertical cables. The foam force-deflection was studied as a function of impacts.

Repeat Impact Machine

A repeat impact machine was designed and developed to analyse changes in the mechanical response of foams under repeated impacts [Verdejo and Mills (acceptedb)]. The key parameters in the equipment design were the impact frequency and the peak pressure, which should be comparable with those measured for long-distance runners.

The human stride frequency is the reciprocal of the time interval between successive contacts [Cavanagh and Kram (1990)]. Reported stride frequencies vary from 1.36 to 1.73 Hz [Cavanagh and Kram (1990); Atwater (1990); Milani et al. (1997)]. Registered in-shoe peak pressures can reach 1 MPa [Milani et al. (1997)] for certain shoes but typically vary from 400 kPa to 700 kPa [Gross and Bunch (1989); Hennig and Milani (2000)] depending on speed.

The equipment frequency was selected to be at the upper limit of runners' frequency range, to have the worse case scenario. Therefore, a preliminary frequency range of 1.73 to 1.80 Hz was chosen. The applied force was intended to cause peak pressures of around 500 kPa, by using a peak force of about 200 N on a sample of 20 × 20 mm cross-section.

Equipment characteristics

Mechanical design

The equipment consists of three main components (Figure 1): an electric motor, a cam and an oscillating arm. The cam, connected to the motor by a belt drive, slowly depresses one end of the arm (raising the other end by a certain height), then suddenly releases it (Figures 3.7 and 3.8). The test rig baseplate is mounted on top of four anti-vibration feet (AVM Air Spring) which are clamped to a wooden table.

The friction between the cam and the arm is reduced by a nylon-coated steel roller attached to the end of the arm. The cam is made of steel with two opposite steps of the same height. The cam shape lifts the roller after the striker has rebounded from the foam for first time, avoiding secondary impacts on the foam.

The required impact frequency and motor speed determined the pulley diameters. With two impacts per cam revolution and the impact frequency in the range of 1.73 to 1.80 Hz, the angular speed of the cam should be 52 to 54 rpm. As the motor

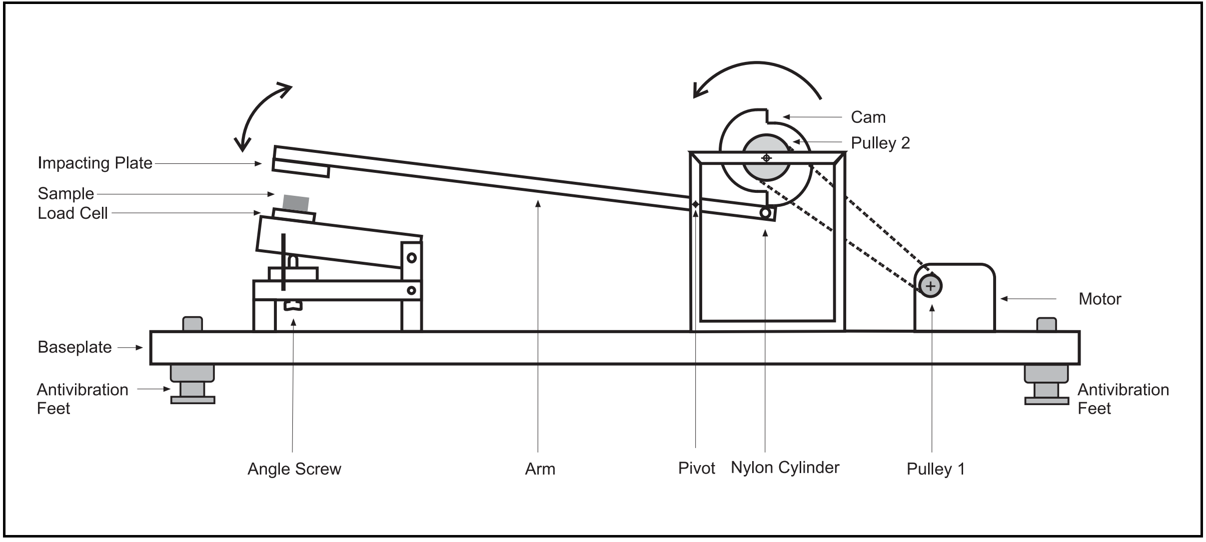

Figure 3.7: Repeat impact test rig diagram.

speed is 100 rpm, the diameters ratio should be closed to 2. The pulleys were made of steel where the drive pulley was 32.7 ± 0.2 mm and the cam pulley was 62.0 ± 0.2 mm in diameter. This ensures a impact frequency of 1.76 Hz, within the chosen range.

The impacting mass was adjusted empirically to obtain the desired maximum impact force. The arm has an aluminium impact plate of 309.4 ± 0.1 g in weight and $75 \times 75 \times 21$ mm^3 attached to one end of a T-section beam of 2071 ± 0.1 g and 583 ± 1 mm. The maximum distance between the impact plat and the load cell is 54 mm, which is reduced to 42 mm when the sample is loaded. The arm is pivoted on a shaft with roller bearings 100 mm from the cam.

Instrumentation

The dynamic force was measured with a Kistler 9321B (10 kN capacity) quartz load cell (Figure 3.9), which has a high resonant frequency of 20 kHz. There is a very slow drift of the charge output, so the zero force is taken when the striker is out of

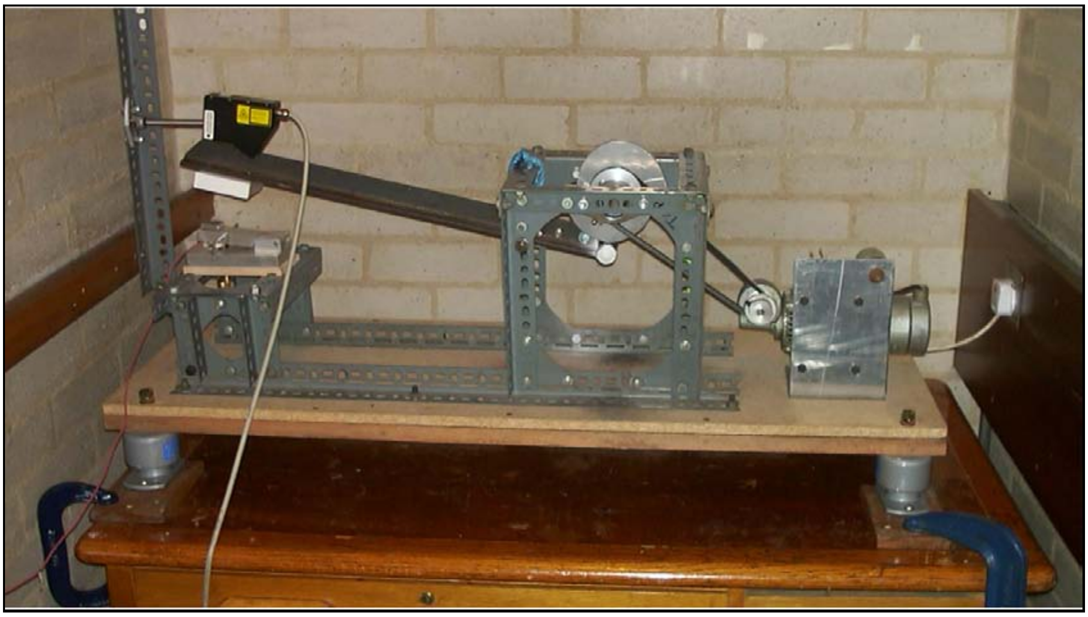

Figure 3.8: Repeat impact photo.

contact with the foam specimen. The load cell is a piezo-electric force-measuring transducer that converts the mechanical force into an electrostatic charge signal. This signal is in turn converted by a charge amplifier into electric voltage, which is then connected to one input (Channel A) of an Analogue to Digital (A/D) converter (Pico 212). The scale of the charge amplifier was set to 100 N/V. A foam sample, of 20 × 20 mm cross-section and 12 mm height, is mounted on top of a flat anvil (25.6 × 25.6 × 7.5 mm) (Figure 3.10) attached to the load cell. The angle of this plate is adjusted to be parallel to the impact plate by a screw placed underneath it.

In compressive impact testing of foams it is possible to integrate the acceleration of a vertically falling striker (or use the impact force divided by the striker mass), using the measured impact velocity, to compute the foam displacement. However, with this test rig, the effective mass of the striker plus arm is unknown, and it is not easy to measure the impact velocity. Consequently it is necessary to measure the striker displacement with a non-contact method having a fast response time.

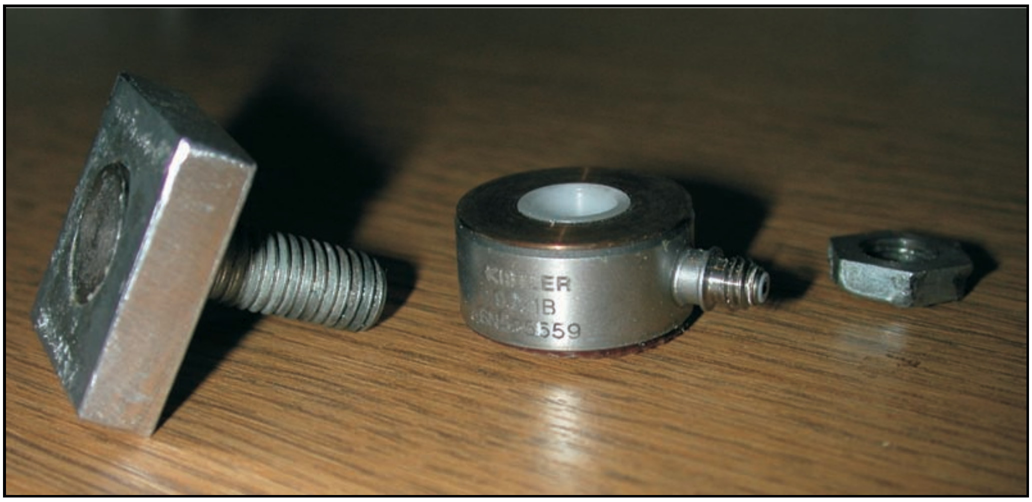

Figure 3.9: Load cell and sample holder.

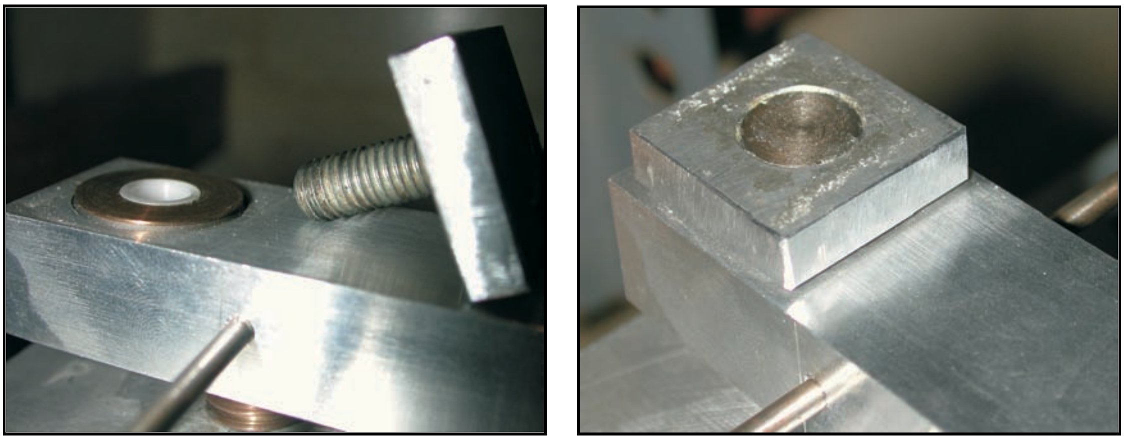

Figure 3.10: Anvil where the load cell is mounted and final set up.

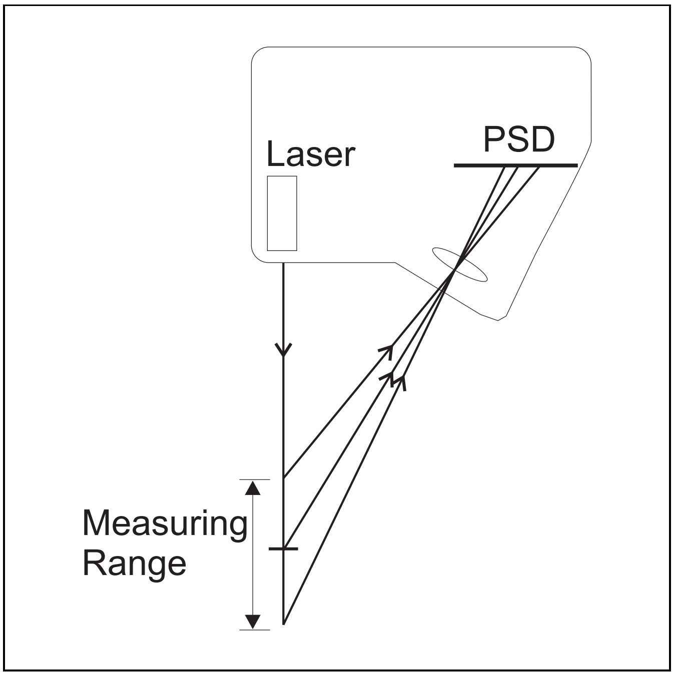

Figure 3.11: Geometry of the triangulation laser.

A Laser Displacement Sensor model LDS90/40 (LMI Sensors-95, The Netherlands) was attached to a rigid wall above the impact plate. This device consists of a triangulation laser system (Figure 3.11) which measures distance by projecting the laser beam onto a flat surface on the striker plate. The reflection off the object's surface produces diffusely scattered light. A portion of the light, after passing through an imaging optics, is focussed as a spot on a position-sensitive detector (PSD). The PSD is a photodiode with two current outputs. The ratio between the output currents is determined by the position of the light spot on the PSD. The displacement of the object changes the angle of the scattered light which in turn changes the ratio of the output currents. Integral electronics convert the output current ratio to a voltage, which is fed to the second channel (Channel B) of the A/D converter. To avoid any interference from other light sources (ambient light), the device is modulated to respond to 50 kHz frequency. The laser is powered by a 15 V power supply.

The sensor was positioned so that the laser beam was perpendicular to the impact

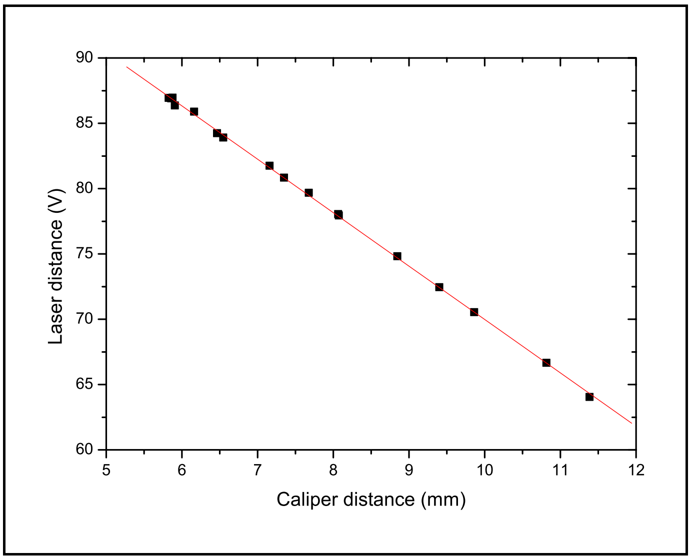

Figure 3.12: Laser calibration.

plate at the time of the impact. The sensor was calibrated by recording the output voltage as a function of the plate position measured with a digital calliper (Figure 3.12). There was a good linear fit ($R^2 = 0.999$) between the sensor output d_s (V) and the calliper distance d_c (mm),

$$d_c = -4.0877\, d_s + 110.86 \tag{3.7}$$

After calibration, the experiments were carried out without moving the sensor.

The loading direction of the foam sample was the same as in the shoe, parallel to the midsole thickness direction (Figure 3.13). This was necessary because the foam has an anisotropic cellular structure. The sample cross-section area will be referred as the “impacted area”. Impacts were monitored using PicoScope (5.06.3) software, at a frequency of 50 Hz which gave the signal from a single peak. The scales were set up at ±5 V for the force channel and ±20 V for the LDS channel. The zero position of the arm was determined with the impacting plate resting on the sample. The raw data (Figure 3.14) was converted to force and displacement with a Fortran 77 program, subtracting the baseline, then scaling the ‘load’ voltage

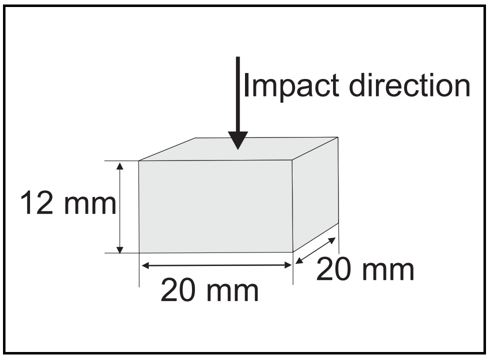

Figure 3.13: Impact direction and dimensions for repeat impact experiments.

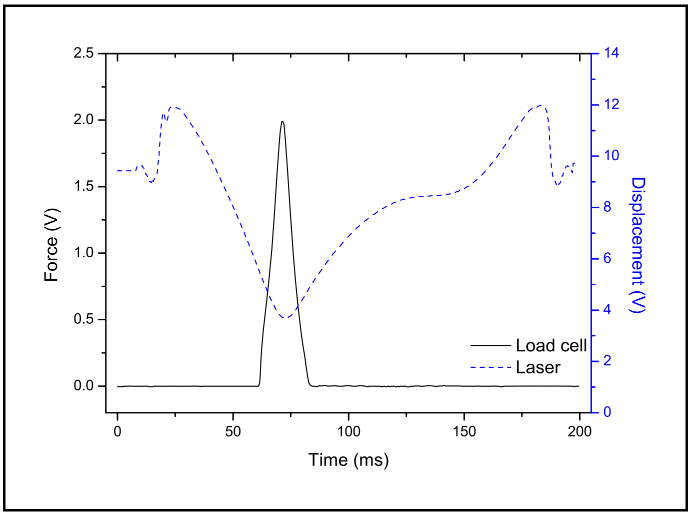

Figure 3.14: Raw data for compressive force and displacement.

by 100 N/V and the ‘displacement’ voltage by -4.0877 mm/V.

Equipment checks

Before any experiment was performed, several checks were carried out. Firstly, the impact interval was measured between two consecutive peak forces. The time between impacts was obtained as the time from maximum to maximum. The average time, from 20 measures, was 0.57 ± 0.02 s and so the equipment frequency is 1.75 Hz, that is in agreement with the theoretical calculation.

Secondly, the impact energy was calculated. As the mass of the foam ($\approx$ 0.80g) is negligible compared with the mass of the impacting arm ($\approx$ 2370 g), the force exerted by the load cell on the lower surface of the foam is equal to the force exerted by the impacting arm on the upper foam surface. The impact energy was obtained by integrating the measured force with respect to the displacement,

$$E_i = \int_0^{x_m} F dx \tag{3.8}$$

where x_m is the maximum deflection of the foam. The impact energy was on average 0.60 ± 0.03 J.

Finally, in order to establish if movement of the equipment baseplate was significant, the vertical position of the baseplate during an impact was recorded with the laser LDS. The maximum baseplate displacement (Figure 3.15 a) occurs after the impact had taken place, when the impact force had returned to zero. A comparison of the striker and baseplate displacements (Figure 3.15 b) reveals that the baseplate hardly moves while the impact force is increasing. The foam deflection should be obtained by subtracting the baseplate displacement from the striker displacement. This correction is only significant during the unloading of the foam. The uncorrected foam displacement during unloading is too large, which means that the absorbed energy is larger in reality than that suggested by the uncorrected force-displacement graphs.

And to check if every impact produces the same displacement of the equipment, the baseplate was recorded with a high speed camera (Figure 3.16) during several impacts. The camera recording frequency was set to 250 frames per second. All the movies show the same displacement.

Experiments design

To relate lab experiments with real life running, the simulated "run" distance had to be defined. For that, a relationship between human stride frequency (SF) and running velocity from different studies (Table 3.1) was established. A linear fit,

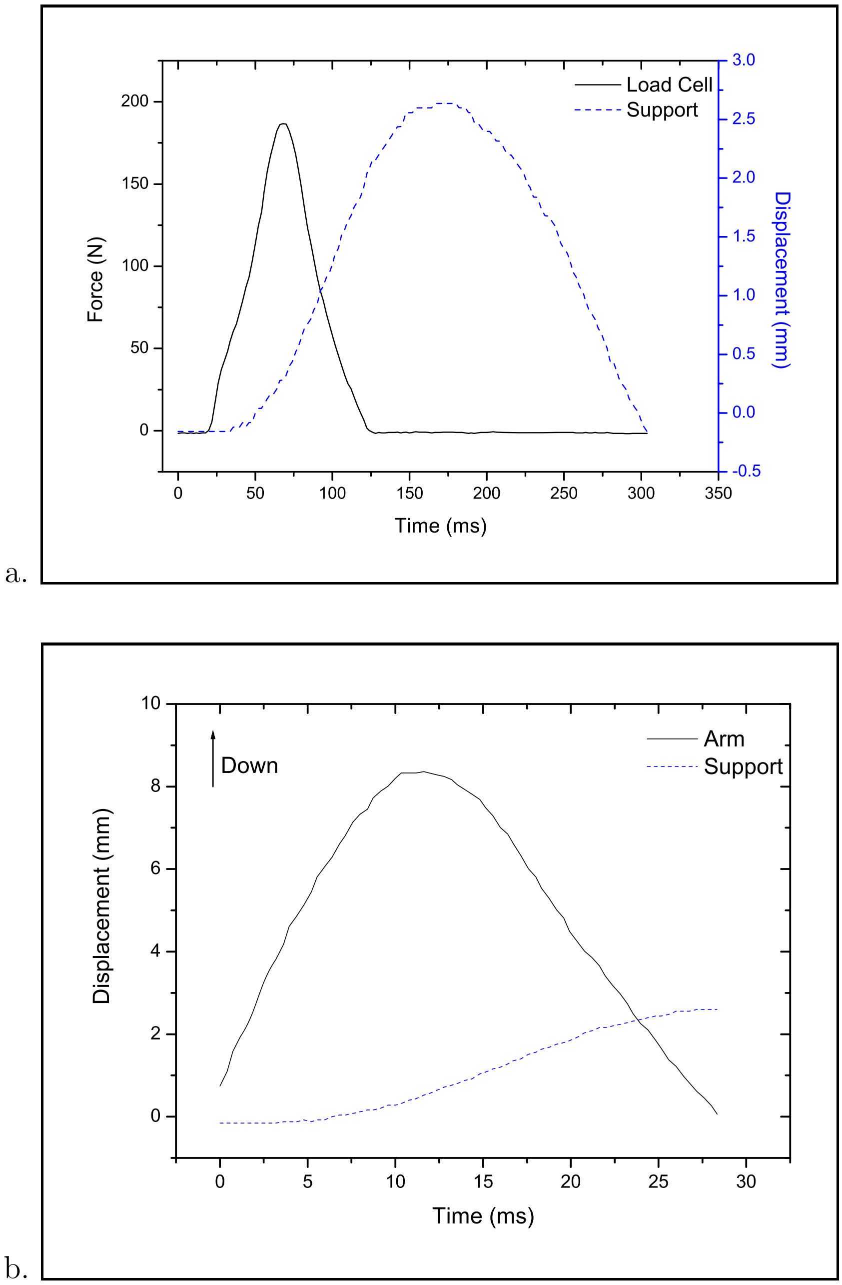

Figure 3.15: a. Variation in striker force and baseplate displacement during an impact and b. arm and support displacement.

Before Impact

During Impact

Maximum vertical displacement

Figure 3.16: Frames taken from high speed movie recorded below the load cell. Notice the equipment has moved an entire black line. Scale: Black line thickness 2.5 mm, white line thickness 0.5 mm.

Study	Stride Frequency (Hz)	Speed (m/s)
Atwater (1990)	1.36	3.50
	1.45	4.50
	1.54	5.50
	1.41	3.70
	1.52	5.41
	1.59	4.96
	1.52	4.96
Cavanagh and Kram (1990)	1.38	3.15
	1.40	3.35
	1.41	3.57
	1.42	3.83
	1.44	4.12
Verdejo (Table 6.1)	1.38	2.69

Table 3.1: Stride frequencies and velocities of male runners.

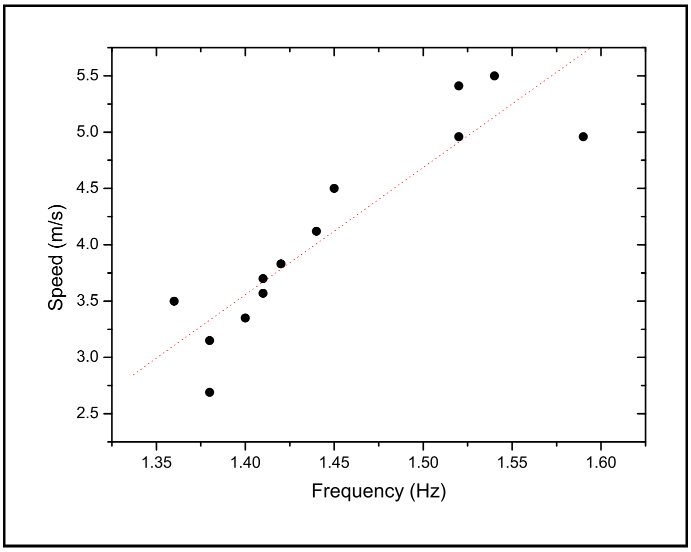

Figure 3.17: Relationship between stride frequency and speed in male long distance runners.

with $R^2 = 0.905$, was found between SF and velocity v (Figure 3.17),

$$v = 11.284\,SF - 12.241 \tag{3.9}$$

The equation can be applied to the test rig, if its impact frequency is considered as a foot strike frequency SF. The equipment has an equivalent running velocity of 7.5 m/s, which is high for marathon runners, as the Olympic world record corresponds to an average speed of 5.4 m/s. However, it gives a worse case scenario to test the durability of the foam midsoles.

Finally, the run distance per day was considered. Distance runners usually train for approximately 2 hours/day and rest at least 1 day/week [Mackenzie (2002)]. Elite runners will run a marathon just over 2 h, good club runners in around 3 h and average fun runners in about 4 hours. Taken into account these facts, two sets of experiments were carried out. Firstly, 5 samples of each foam were tested for 2 h on 5 consecutive days. Secondly, a single sample of each foam was tested for 3 h on 17 consecutive days. For the first experiment, the total distance run was 270 km while for the second it was 1377 km. In the experiments, samples were allowed to recover for 22 h or 21 h between runs. The foam density was calculated at the start and end of each experiment, from the mass measured using an Oertling NA114 balance with a scale error of $\pm\,0.00001$ g and foam dimensions measured with a Mitutoyo digital calliper with an error of $\pm\,0.02$ mm.

Chapter 4

Results

The results obtained during the study are presented in this section. For clarity of exposition, the characterisation results for all 5 samples will only be presented graphically when they differ significantly. Otherwise, a typical result will be shown to illustrate the characteristic under study. This illustrative result will correspond to any of the foams, like this a wider scope of the study is presented. Also, during the analysis exposition foam samples will be considered in three groups, EVA108, EVA150 and EVA265, where EVA150 refers to EVA146, EVA151 and EVA152. Thus, the comparison will firstly be made between these three groups and, afterwards, the EVA150 group will be studied.

4.1 Microscopic Characterisation

4.1.1 Cellular Structure

Qualitative analysis of the micrographs reveals a closed cell structure, with following characteristics:

- All the samples have flattened cells (Figure 4.1) close to the upper and lower layer. Cells close to these layers are elongated in a direction perpendicular to the thickness, giving an anisotropic structure. This is due to the moulding

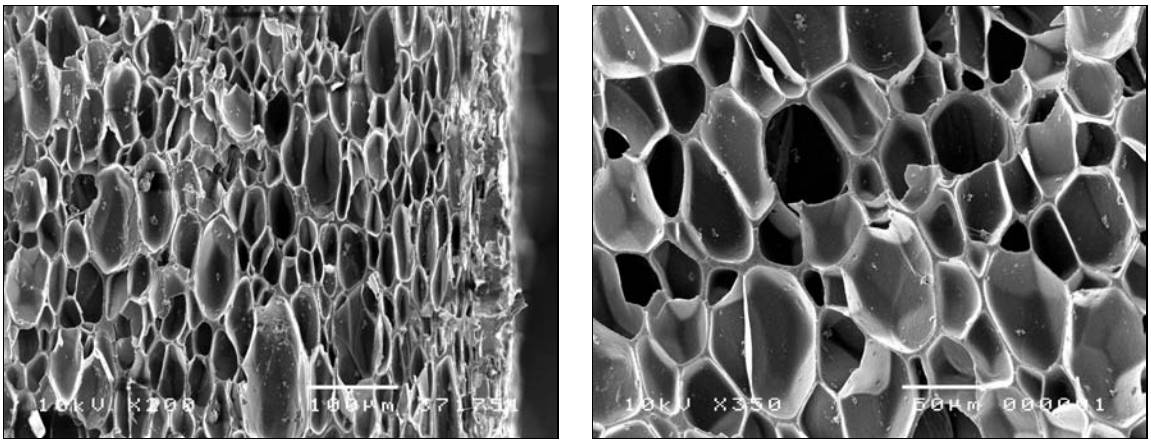

EVA152x EVA152y

Figure 4.1: Example of the samples anisotropy at the surface (left) and at the middle (right) of the samples.

process. This elongation of the cells is still observable at the mid-thickness, although is not as well defined as in the upper and lower areas (Figure 4.1).

- EVA108 has small cells within the walls of the normal cell size (Figure 4.2). These cells were considered as part of the mean cells size because they were distributed all over the sample thickness. Walls between the small cells are thicker than between larger cells.
- Presence of some abnormally large cells (Figure 4.2) in EVA150 samples. These cells were approximately concentrated along the mid-thickness. These cells were not considered in the mean cell size calculations. The sample EVA151 has the largest amount of these cells. This heterogeneity may be due to thermodynamics equilibrium of bubble growth process during the foaming. The reason why the larger cells are concentrated in the middle of the sheet thickness could be that this section is hotter than the surface for a longer period of time, allowing the cells to grow. EVA108 and EVA265 were made in a different batch and do not have this structure. Therefore, these large cells are not characteristic of the foaming process, they could be due to a heterogenic mix

Foam	$\phi_x\,(\mu\text{m})$	$\phi_y\,(\mu\text{m})$	$\phi_z\,(\mu\text{m})$	$\phi\,(\mu\text{m})$	AC_{xz}	AC_{yz}	δ
EVA108	126.29	136.08	97.90	120.09	1.29	1.39	1.9 - 5.2
EVA146	72.09	78.95	57.21	69.42	1.26	1.38	1.7
EVA151	55.26	61.49	38.92	51.89	1.42	1.58	1.7
EVA152	78.71	86.40	59.18	74.76	1.33	1.46	1.8
EVA265	315.98	339.31	212.07	289.12	1.49	1.60	15.8

Table 4.1: Apparent mean cell size, mean cell size, anisotropy coefficients and wall thickness. Values have been standardize using ASTM D3576.

of the blowing agent or due to differences on the blowing agent used.

- EVA265 has thick walls between cells and very thick edges. Visual inspection reveals the presence of small cells, although the size difference is not as large as in EVA108 case (Figure 4.2).

Image analysis

Foams cell size depends on a large number of manufacturing factors [Park (1991)], such as foaming process, nucleation density [Mahapatro et al. (1998)] and cross-linking, among others. Therefore it is hard to form a general conclusion on cell size as a function of density without explicit knowledge of the foaming process.

EVA108 and EVA265 have larger mean cell size than does EVA150 (Table 4.1). The apparent mean cell size spread over a wide range, from 38.92 μm of EVA150 foams to 339.31 μm of EVA265. All samples have both anisotropy coefficients larger than unity, i.e. cell size along the thickness direction is smaller than in the other two directions, confirming the anisotropy mentioned above. This anisotropy, due to the second stage of the foaming process where the foams are compressed, largely affects their mechanical properties and it would have to be considered in further analysis.

EVA108x

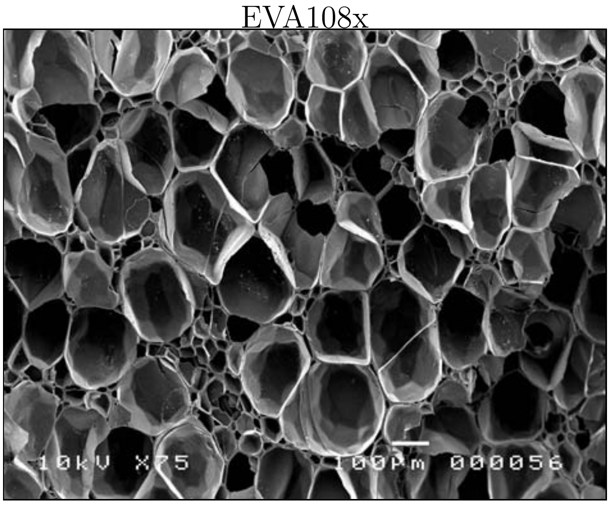

EVA151x. Sample rotated 90 ° from its position.

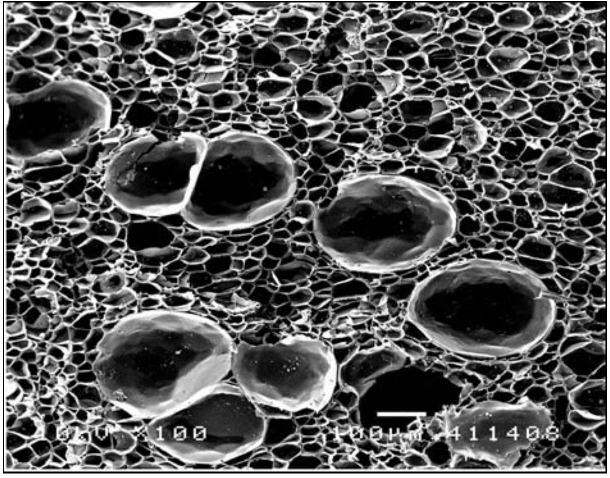

EVA265x. Where a and b represent the two type of cell.

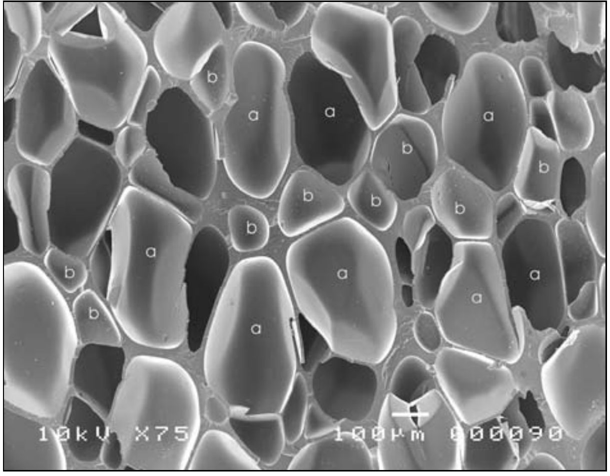

Figure 4.2: Cellular structure and heterogeneity structure observed in the foam samples.

Foam	Mean (μm)	Median (μm)	Variance	Skewness	Kurtosis
EVA108	74.13	48.99	4063.36	1.25	0.72
EVA146	42.85	39.50	451.19	0.77	0.32
EVA151	32.03	28.50	316.26	1.31	2.30
EVA152	46.15	41.85	582.72	0.94	0.68
EVA265	178.47	160.28	7826.86	0.68	-0.14

Table 4.2: Statistical distribution parameters. Values without standardize.

Cell size distributions from the apparent mean size values (ϕ_x, ϕ_y, ϕ_z) were examined to reveal more aspects of the cellular structure (Figures 4.3 and 4.4). The statistical parameters mean, median, variance, skewness and kurtosis (Table 4.2), completely characterise the cell size distribution of the samples.

High mean and median values correspond to large cells and vice-versa. Samples with high variances have a wide range of cell sizes whilst small variances show cell sizes comprised to a smaller interval. The disparity of mean and median values and the positive skewness reveals a non symmetrical distribution slightly shifted towards larger cell size values.

The negative kurtosis of EVA265, is due to the scarcity of cells similar to the mean cell size, and, as its skewness is the smallest of the group, this distribution is the one which has the highest symmetry. Meanwhile, the high kurtosis of EVA151 reveals a large number of cells close to the average value, and its large skewness relates to a highly asymmetrical distribution.

Due to the presence of two sets of cells, EVA108 and EVA265 show a bimodal distribution. In order to calculate the mean cell size of both types of cell, the distributions were separated in two sections. EVA108 histogram was divided at 120 μm obtaining two separate distributions with mean cell sizes 45.26 μm and 181.99 μm. Similarly, EVA265 was divided at 180 μm obtaining mean cell sizes of 112.73 μm and 260.27 μm.

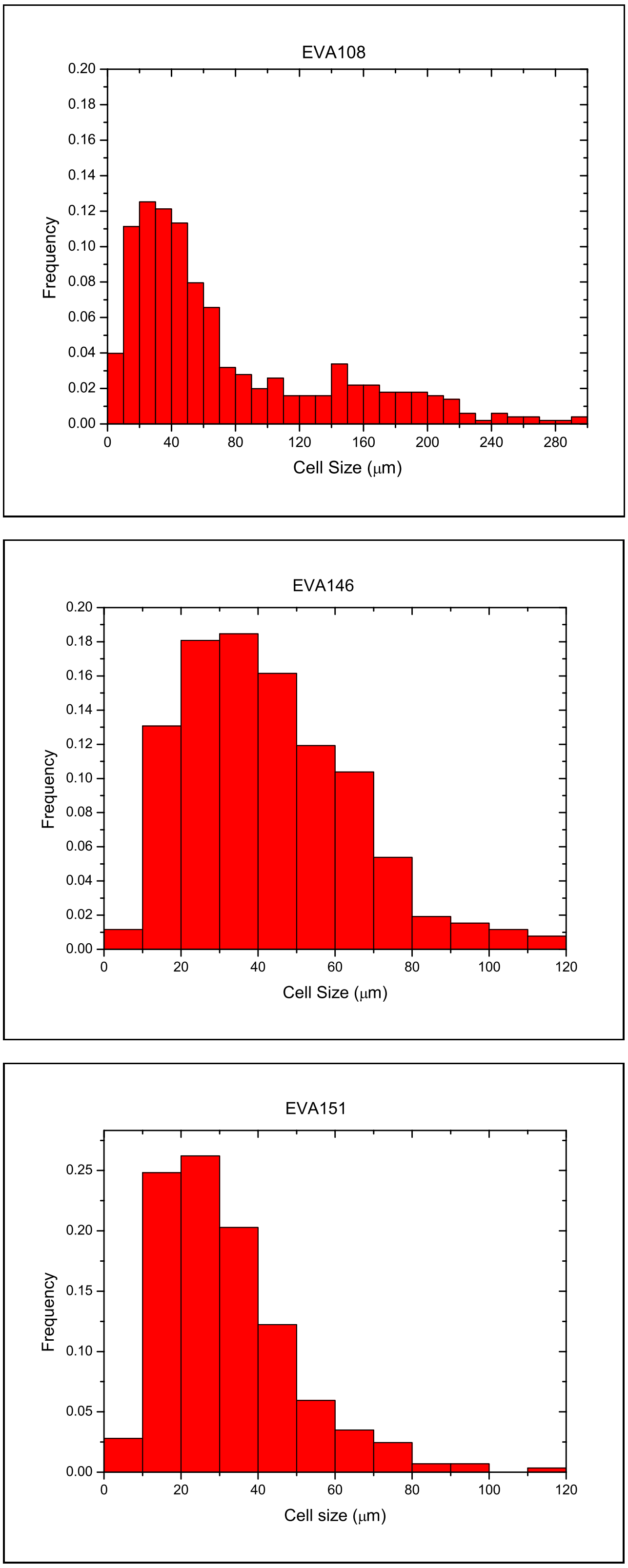

Figure 4.3: Cell size distribution of EVA108, EVA146 and EVA151.

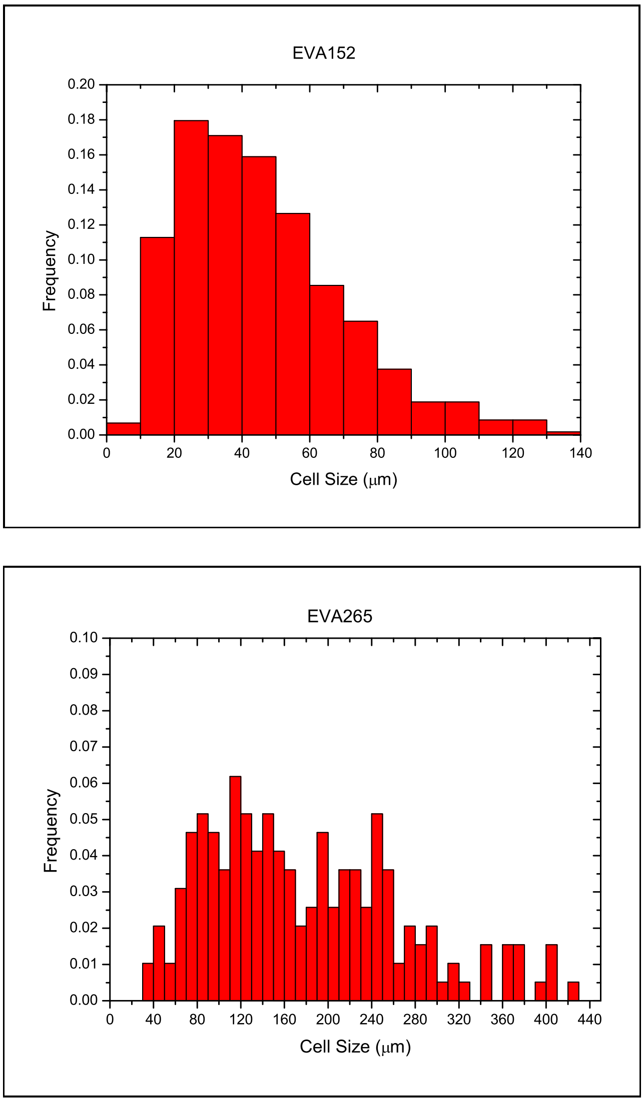

Figure 4.4: Cell size distribution of EVA152 and EVA265.

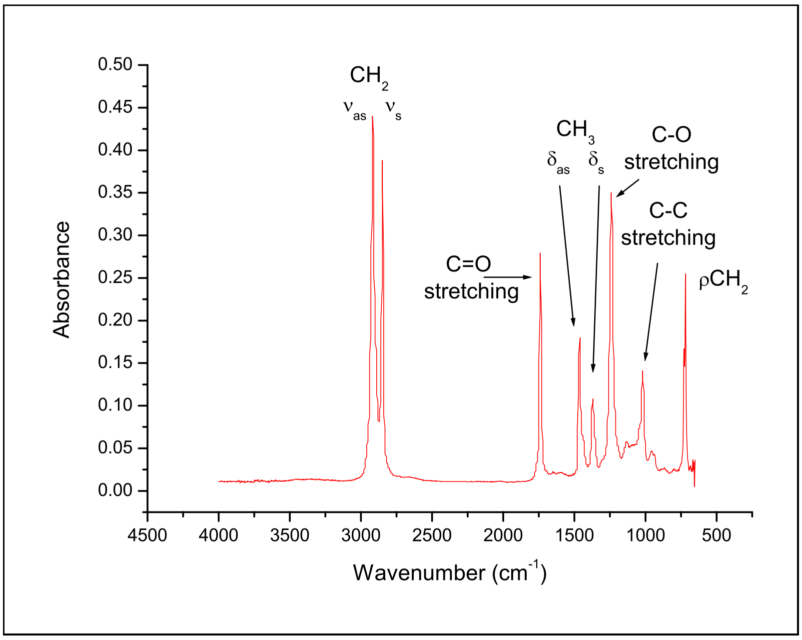

Figure 4.5: Typical IR spectrum of an EVA film. Film containing 12 % VA.

Wall thickness reveals the same tendency with density than does cell size due to the relationship between these parameters. For EVA108, wall thickness between both types of structures was calculated. Walls between large cells were very thin and, although the accelerating voltage beam was kept low (10 V), difficult to focus. Only a 30 % of the usual population were feasible to focus (Table 4.1). Wall thickness of EVA150 is very similar, slightly increasing with density, and as mentioned in the qualitative analysis, EVA265 has the thickest walls.

4.1.2 Polymer Matrix

Attenuated Total Reflectance (ATR)

A typical spectrum from the EVA films is shown in Figure 4.5. Each peak has been identified [Silverstein and Bassler (1967); Hsu (1997); Coates (2001)] and labelled accordingly (Table 4.3).

The selected representative groups for E and VA polymer were ν_{as}CH$_2$ - ν_sCH$_2$

Group	Wavelength (cm^{-1})
CH_2 stretching	2920 as
	2850 s*
C=O stretching	1740
CH_3 scissoring	1460 as
	1370 s
C-O stretching	1240
C-C stretching	1020
CH_2 rocking	719

Table 4.3: Vibrational groups and their position. * as and s stand for asymmetrical and symmetrical, respectively.

% VA	CH_3 Absorbance	CH_2 Absorbance
7.5 %	8.32	34.62
12.5 %	9.62	25.65
18 %	6.93	15.35
28 %	54.33	71.54

Table 4.4: Areas under the reference groups.

and $\delta_{as}CH_3$ - $\delta_{s}CH_3$, respectively. From Beer-Lambert's law (equation 3.1), the absorbance of the bands changes with the concentration of VA. Therefore, a calibration curve (Figure 4.6) was obtained by plotting the ratio of the absorbance areas as a function of the percentage of VA in the films (Table 4.4). The linear equation corresponded to,

$$\frac{\mathcal{A}_{CH_3}}{\mathcal{A}_{CH_2}} = \frac{e_{CH_3}}{e_{CH_2}} \times \frac{c_{CH_3}}{c_{CH_2}} \tag{4.1}$$

as both absorptions result from the same film, $b_{CH_3} = b_{CH_2}$. The linear fit of VA films is $\mathcal{A}_{CH_3}/\mathcal{A}_{CH_2} = 0.0272c_{CH_3}$ with correlation coefficient $R^2 = 0.98$.

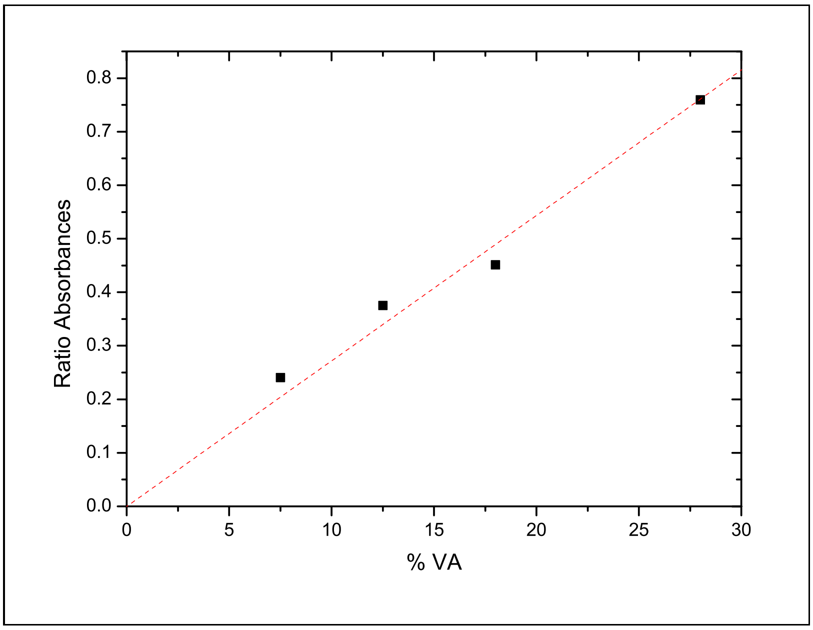

Figure 4.6: Calibration curve for ATR experiments.

Spectra (Figure 4.7) obtained from the two sets of experiments, horizontal clamp (h-ATR) and Golden Gate clamp (GG-ATR), are approximately the same. The h-ATR and GG-ATR spectra differ on the intensity and resolution of the absorption bands. These differences are likely to be due to variations of the degree of contact between the compressed foam-crystal system with respect to uncompressed foam-crystal system, due to the cellular structure of foams. Characteristic absorption bands at 3210 and 3390 cm^{-1} are resoluble with h-ATR but not with GG-ATR where they appear as a single broad band. Two more characteristic absorption bands at 1690 and 1590 cm^{-1} are clearly observed on h-ATR foams spectra. These peaks are present in the foam samples and cannot be observed in the film spectra. Therefore, these bands would be related to the presence of traces of blowing agent, as is the main difference between the EVA films and the foam samples.

Inserting the absorbance ratio of the foams in the linear equation, the amount of VA in the foam samples was obtained (Table 4.5). The mean average of the %

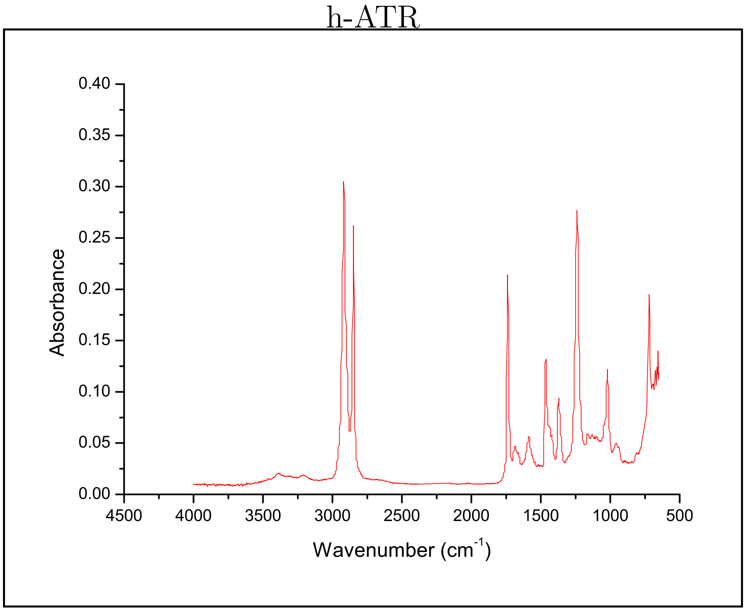

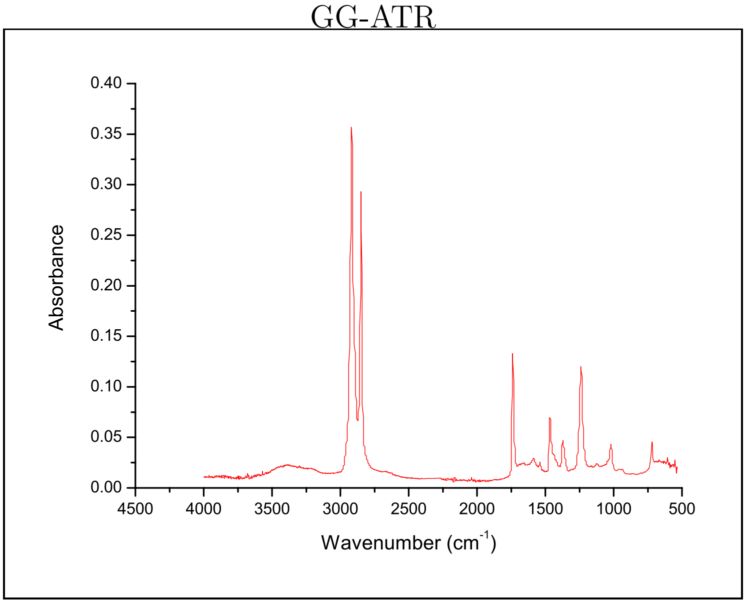

Figure 4.7: h-ATR and GG-ATR spectra of EVA152.

Foam	h-ATR % VA	GG-ATR % VA
EVA108	18.3	15.9
EVA146	18.9	15.4
EVA151	18.6	15.7
EVA152	19.0	16.5
EVA265	19.0	16.3

Table 4.5: % VA obtained from both h-ATR and GG-ATR experiments.

VA with the horizontal clamp (h-ATR) was 18.8 % with a standard deviation of 0.3, i.e. 18.8 ± 0.3 mol. %, whereas with the Golden Gate clamp (GG-ATR) was 15.8 ± 0.5 mol. %. The variation on the amount of VA is due to the differences on peak intensities observed in the spectra. The amount of VA obtained by h-ATR suggests a degree of crystallinity from 20 to 25 %.

Differential Scanning Calorimetry (DSC)

The melting point was taken to be the maximum of the power difference versus temperature curve and the melting enthalpy was calculated from the area under the second heat cycle curve (Table 4.6). The degree of crystallinity was calculated by dividing the measured enthalpy by the melting enthalpy of pure polyethylene (286.8 J/mol) [Brandrup and Immergut (1975)], assuming that only polyethylene sequences crystallised. In a typical thermogram (Figure 4.8), the following transitions are observed:

- 1st Heat cycle: Endothermic transition at a mean temperature of 90.6 °C. This is the melting point of the samples with the thermal history, showed as a small shoulder before the main peak.
- Cool cycle: Exothermic transition at a mean temperature of 70.4 °C. This corresponds to the main crystallisation.

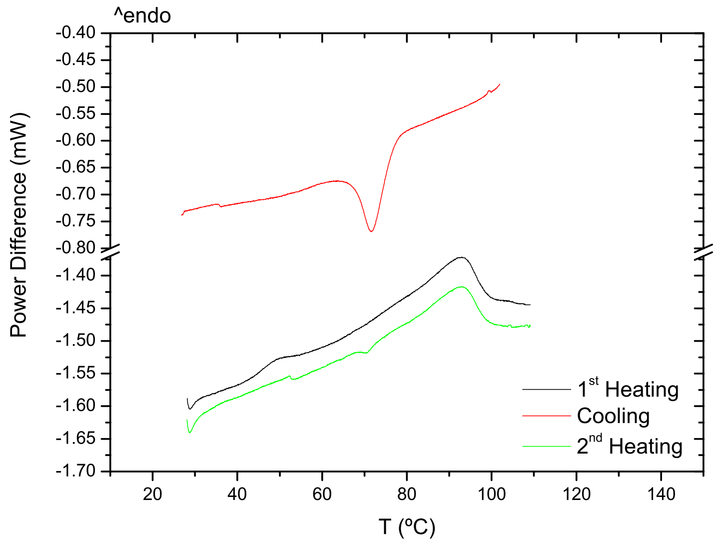

Figure 4.8: EVA152 thermogram with the three heating programs.

- 2^{nd} Heat cycle: Endothermic transition at a mean temperature of 92.6 °C. In this cycle, the samples showed a small increase in the heat flow with respect to the first cycle.

The experiment carried out from low temperature shows lower melting temperature and larger % of crystallinity (Figure 4.9). The temperature sifting could be due to the different equipment used. The degree of crystallinity is due to the temperature range, cooling the sample to −40 °C induces a small number of chains to crystallise. This can be observed in the thermogram, as the area under the cooling process from 30 °C to −20 °C. This crystallinity degree is similar to a previous study [Mills and Rodríguez-Pérez (2001)] on a running shoe midsole.

The differences in the amount of VA are not large enough to drastically change the degree of crystallinity. According to manufacturers [DuPont (1997); Samsung (1999)], the melting point and degree of crystallinity obtained indicate that the amount of VA in EVA is between 15 and 20 %. This result is in accordance with the ATR analysis mentioned above.

Foam	T_m (°C)	ΔH_m (J/g)	Crystallinity (%)
EVA108	90.2	63.27	22.06
EVA146	91.9	63.10	22.00
EVA151	94.6	64.05	22.33
EVA152	92.8	63.13	22.01
EVA152*	85.1	71.94	25.08
EVA265	93.3	62.99	21.96

Table 4.6: Melting temperature, enthalpy and degree of crystallinity. The results were corrected considering that there is a 17 % of inorganic material. * values obtained with larger temperature range.

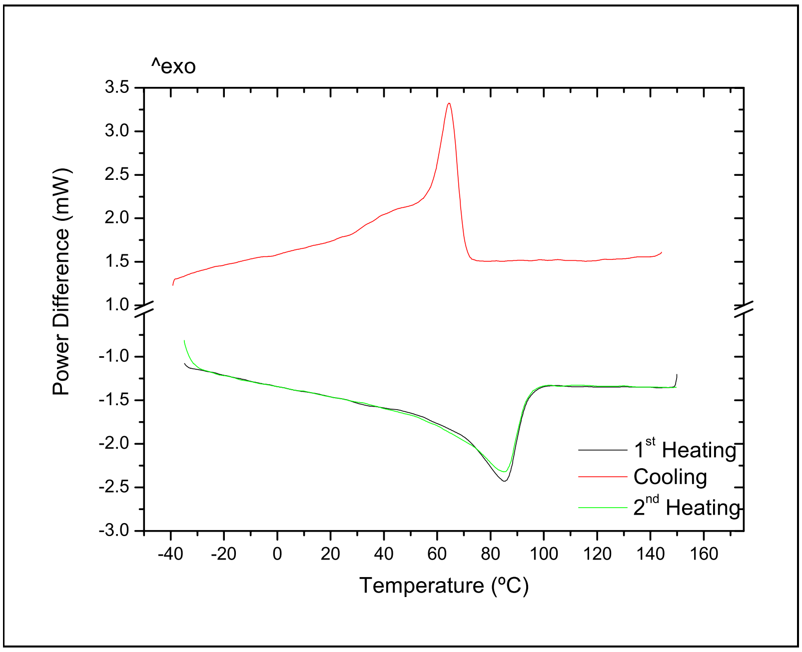

Figure 4.9: EVA152 thermogram with the three heating programs. (Large heating program).

Foam	% Mass loss
EVA108	17.4
EVA146	17.1
EVA151	17.7
EVA152	17.6
EVA265	17.6

Table 4.7: Percentage inorganic components present in the samples.

d-spacing (Å)	Relative Intensity (%)	Angle (°2Θ)
3.25	100	27.41
2.48	97.67	36.12
1.68	78.09	54.30
1.62	45.51	56.58
2.81	43.08	31.71
2.60	32.89	34.37
2.18	29.45	41.23
1.47	28.89	62.75

Table 4.8: Interplanar distance and relative intensity of sample EVA146.

X-Ray Diffraction

The amount of inorganic components present in the samples is on average 17.5 % (Table 4.7). The residues from each sample had the same X-Ray diffraction pattern (Figure 4.10), the largest differences of d-spacing and relative intensity with respect to the reported values (Table 4.8) were 0.003 Å and 8.9, respectively. The interplanar distance and relative intensity for 8 strongest lines were analysed following the Hanawalt method.

The first 3 strongest lines matched ASTM file number 21.1276 (Figure 4.12) corre-

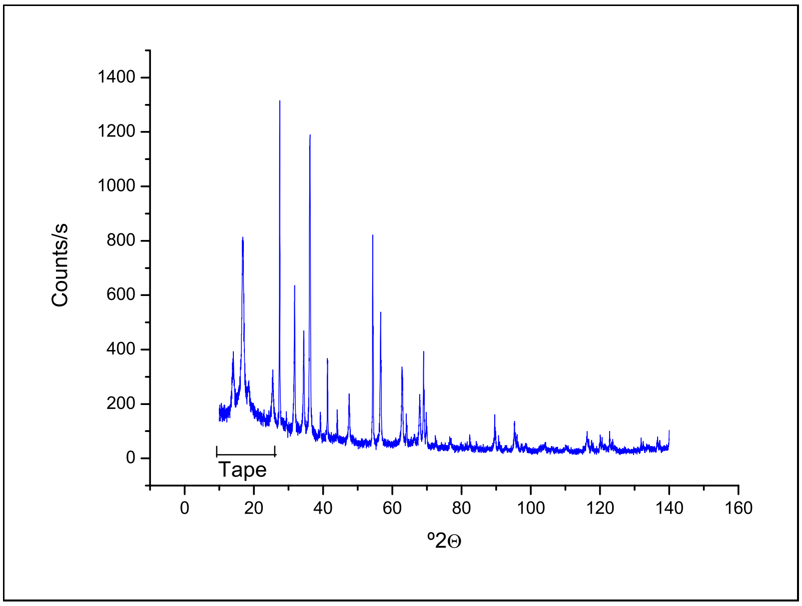

Figure 4.10: EVA108 X-Ray diffractogram.

sponding to titanium dioxide (TiO_2) but the presence of peaks at 31.71 ° and 34.37 ° not matching any TiO_2 peaks suggested the presence of more than one component. The displacement of the 2nd strongest line, and its relative intensity being higher than the ASTM pattern, insinuated the presence of two lines that had not been resolved. The second component was found by considering that line as its strongest line; the matching component is zinc oxide (ZnO), ASTM file numbers 36-1451 (Figure 4.12). Further analysis reveals a good agreement of the spectra with those two components (Figure 4.11).

Both Titanium dioxide and Zinc oxide are the most widely used white pigments. TiO_2 is used primarily to provide opacity, but can also have a significant effect on coating gloss and exterior durability. ZnO is been used as white pigment since end of 18th century and it is also used as a catalyst during the foaming process.

General available company information (Table 2.3) shows that EVA foam chemical formulation has 1 phr (grams of component per 100 g of dry resin) of ZnO,

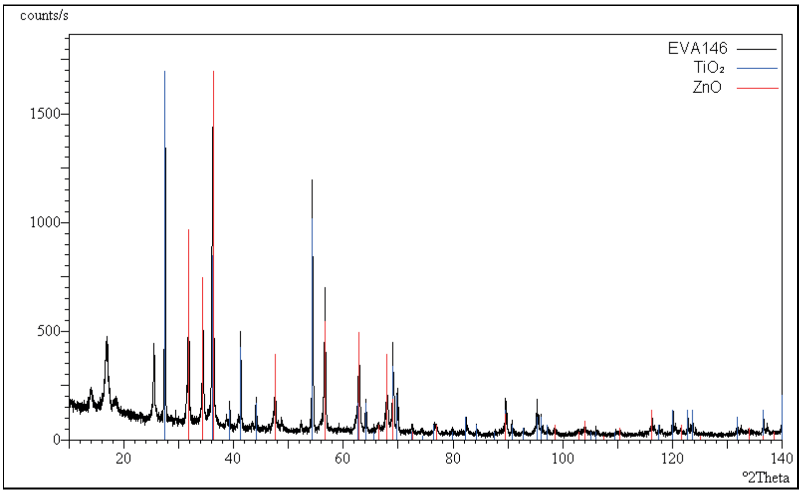

Figure 4.11: X Ray diffractogram of EVA146 and ASTM patterns of TiO_2 and ZnO.

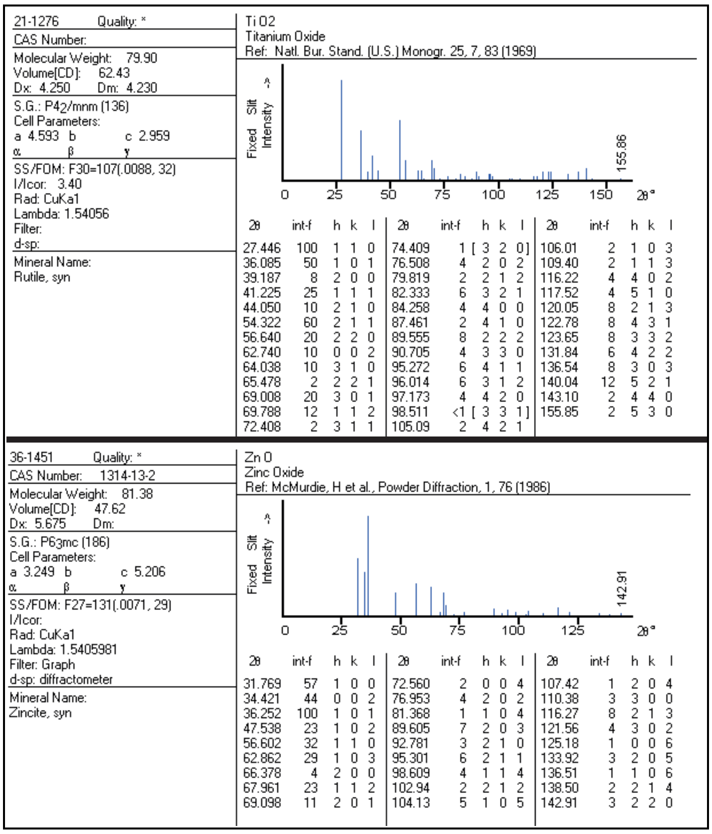

21-1276 Quality: *

CAS Number:

Molecular Weight: 79.90
Volume[CD]: 62.43
Dx: 4.250 Dm: 4.230

S.G.: $P4_2/mnm$ (136)
Cell Parameters:
a 4.593 b c 2.959
α β γ

SS/FOM: F30=107(.0088, 32)
I/Icor: 3.40
Rad: CuKa1
Lambda: 1.54056
Filter:
d-sp:

Mineral Name:
Rutile, syn

Ti O2
Titanium Oxide
Ref: Natl. Bur. Stand. (U.S.) Monogr. 25, 7, 83 (1969)

2θ	int-f	h	k	l	2θ	int-f	h	k	l	2θ	int-f	h	k	l
27.446	100	1	1	0	74.409	1	[3	2	0]	106.01	2	1	0	3
36.085	50	1	0	1	76.508	4	2	0	2	109.40	2	1	1	3
39.187	8	2	0	0	79.819	2	2	1	2	116.22	4	4	0	2
41.225	25	1	1	1	82.333	6	3	2	1	117.52	4	5	1	0
44.050	10	2	1	0	84.258	4	4	0	0	120.05	8	2	1	3
54.322	60	2	1	1	87.461	2	4	1	0	122.78	8	4	3	1
56.640	20	2	2	0	89.555	8	2	2	2	123.65	8	3	3	2
62.740	10	0	0	2	90.705	4	3	3	0	131.84	6	4	2	2
64.038	10	3	1	0	95.272	6	4	1	1	136.54	8	3	0	3
65.478	2	2	2	1	96.014	6	3	1	2	140.04	12	5	2	1
69.008	20	3	0	1	97.173	4	4	2	0	143.10	2	4	4	0
69.788	12	1	1	2	98.511	<1	[3	3	1]	155.85	2	5	3	0
72.408	2	3	1	1	105.09	2	4	2	1					

36-1451 Quality: *

CAS Number: 1314-13-2

Molecular Weight: 81.38
Volume[CD]: 47.62
Dx: 5.675 Dm:

S.G.: $P6_3mc$ (186)
Cell Parameters:
a 3.249 b c 5.206
α β γ

SS/FOM: F27=131(.0071, 29)
I/Icor:
Rad: CuKa1
Lambda: 1.5405981
Filter: Graph
d-sp: diffractometer

Mineral Name:
Zincite, syn

Zn O
Zinc Oxide
Ref: McMurdie, H et al., Powder Diffraction, 1, 76 (1986)

2θ	int-f	h	k	l	2θ	int-f	h	k	l	2θ	int-f	h	k	l
31.769	57	1	0	0	72.560	2	0	0	4	107.42	1	2	0	4
34.421	44	0	0	2	76.953	4	2	0	2	110.38	3	3	0	0
36.252	100	1	0	1	81.368	1	1	0	4	116.27	8	2	1	3
47.538	23	1	0	2	89.605	7	2	0	3	121.56	4	3	0	2
56.602	32	1	1	0	92.781	3	2	1	0	125.18	1	0	0	6
62.862	29	1	0	3	95.301	6	2	1	1	133.92	3	2	0	5
66.378	4	2	0	0	98.609	4	1	1	4	136.51	1	1	0	6
67.961	23	1	1	2	102.94	2	2	1	2	138.50	2	2	1	4
69.098	11	2	0	1	104.13	5	1	0	5	142.91	3	2	2	0

Figure 4.12: ASTM files of TiO_2 and ZnO.

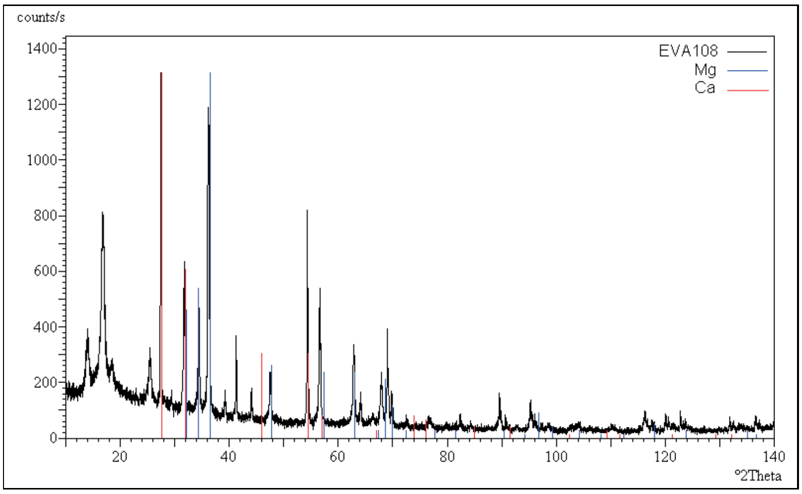

Figure 4.13: X Ray diffractogram of EVA108 and ASTM patterns of Mg and Ca.

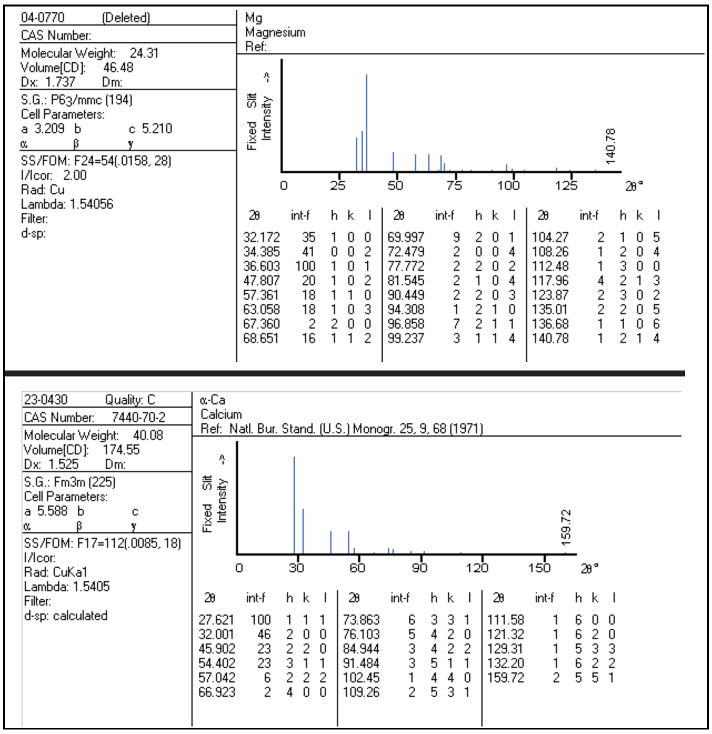

04-0770 (Deleted)
CAS Number:
Molecular Weight: 24.31
Volume[CD]: 46.48
Dx: 1.737 Dm:
S.G.: P63/mmc (194)
Cell Parameters:
a 3.209 b c 5.210
α β γ
SS/FOM: F24=54(.0158, 28)
I/Icor: 2.00
Rad: Cu
Lambda: 1.54056
Filter:
d-sp:

Mg
Magnesium
Ref:

2θ	int-f	h	k	l	2θ	int-f	h	k	l	2θ	int-f	h	k	l
32.172	35	1	0	0	69.997	9	2	0	1	104.27	2	1	0	5
34.385	41	0	0	2	72.479	2	0	0	4	108.26	1	2	0	4
36.603	100	1	0	1	77.772	2	2	0	2	112.48	1	3	0	0
47.807	20	1	0	2	81.545	2	1	0	4	117.96	4	2	1	3
57.361	18	1	1	0	90.449	2	2	0	3	123.87	2	3	0	2
63.058	18	1	0	3	94.308	1	2	1	0	135.01	2	2	0	5
67.360	2	2	0	0	96.858	7	2	1	1	136.68	1	1	0	6
68.651	16	1	1	2	99.237	3	1	1	4	140.78	1	2	1	4

23-0430 Quality: C
CAS Number: 7440-70-2
Molecular Weight: 40.08
Volume[CD]: 174.55
Dx: 1.525 Dm:
S.G.: Fm3m (225)
Cell Parameters:
a 5.588 b c
α β γ
SS/FOM: F17=112(.0085, 18)
I/Icor:
Rad: CuKa1
Lambda: 1.5405
Filter:
d-sp: calculated

α-Ca
Calcium
Ref: Natl. Bur. Stand. (U.S.) Monogr. 25, 9, 68 (1971)

2θ	int-f	h	k	l	2θ	int-f	h	k	l	2θ	int-f	h	k	l
27.621	100	1	1	1	73.863	6	3	3	1	111.58	1	6	0	0
32.001	46	2	0	0	76.103	5	4	2	0	121.32	1	6	2	0
45.902	23	2	2	0	84.944	3	4	2	2	129.31	1	5	3	3
54.402	23	3	1	1	91.484	3	5	1	1	132.20	1	6	2	2
57.042	6	2	2	2	102.45	1	4	4	0	159.72	2	5	5	1
66.923	2	4	0	0	109.26	2	5	3	1					

Figure 4.14: ASTM files of Mg and Ca.

Calcium Stearate and TiO_2 and 8 phr $MgCO_3$. Superimposing the $MgCO_3$ pattern to the foam residual spectrum does not reveal a match, neither does MgO. However, certain agreement was found between the spectra of the samples and Mg (Figure 4.13), ASTM file number 04-0770 (Figure 4.14). This could be due to the burning process where the CO_3 would decomposed. The Ca pattern was also checked and there was a reasonable match between the patterns with some Ca peak shift (Figure 4.13), ASTM file number 23-0430 (Figure 4.14).

To confirm the presence of Mg and Ca and to analyse if the burning process had altered the residues, one sample (EVA146) was analysed by Energy Dispersive X-ray (EDX) microanalysis. The sample was fractured at low temperature and introduced into an Environmental Scanning Electron Microscope (ESEM) with 5 % humidity. This equipment does not require the coating process for non-conducting samples and therefore the analysis is carried out in the sample without any additional layers. The analysis was firstly carried out on several particles present on the cell wall surfaces (Figure 4.15). The spectrum of these particles (Figure 4.15) shows the presence of sulphur (S), zinc (Zn), titanium (Ti) and oxygen (O). A further analysis was carried out of an area of $272.6 \times 204.1\ \mu m^2$ (Figure 4.16). The spectrum of this area shows the presence of S, Zn, Ti, O, calcium (Ca) and some silicon (Si) (Figure 4.16). Element maps (Figure 4.17) of the previous area show the location of the element within the scanned area, giving an idea of the element concentration. Regions with high concentration of sulphur correspond to regions in the SEM image where there are residues in the cell walls. There are some traces of Mg. The traces from Mg and Si could come from particles of talc ($Mg_3Si_4O_{10}$) meanwhile S and Ca could come from particles of gypsum ($CaSO_4$).

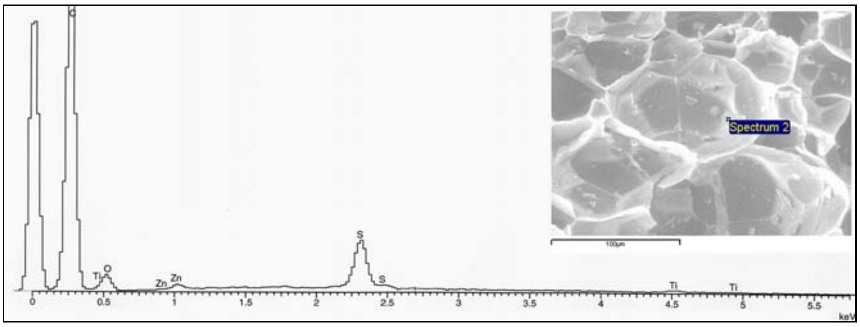

Figure 4.15: ESEM image and spectrum obtained from a residue on the cell walls.

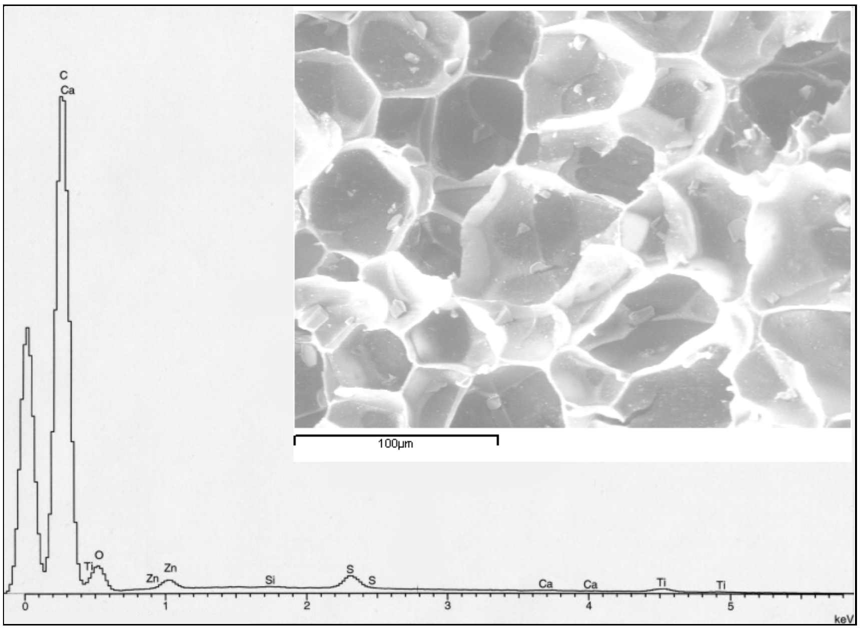

Figure 4.16: General ESEM image and spectrum obtained for EVA146.

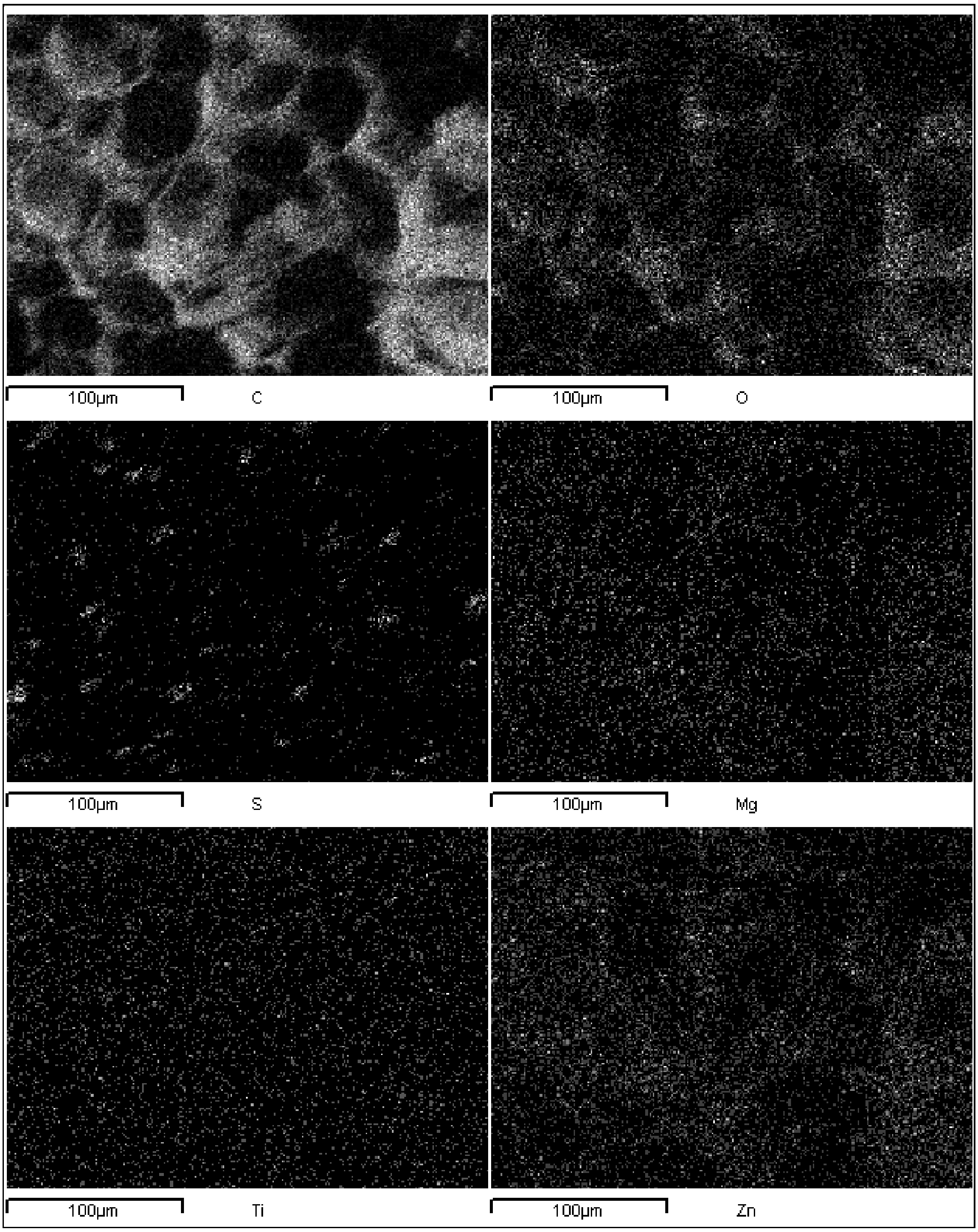

Figure 4.17: Maps showing traces of C, O, S, Mg, Ti and Zn in EVA146.

4.1.3 Discussion

Foam samples have been characterised in terms of their cellular structure and composition. ATR, DSC and X Ray diffraction results showed the same chemical composition in all samples. The foams had a 19 % VA content with 22 % crystallinity, in accordance with EVA literature. The introduction of VA limits the degree of crystallinity of the copolymer, which leads to changes in the mechanical properties such as Young's modulus, flexibility and hardness. Polymers with low degree of crystallinity have moderate to low hardness or compressive strength. Therefore, they have good cushioning properties, as their deformation, for a given stress, is larger than that of a higher modulus material, absorbing more energy.

The ATR spectra showed the presence of 4 absorption bands that were not present in EVA films, concluding they may be residues of the blowing agent. Further analysis could reveal the nature of these bands by comparing the spectra from foams with different type of blowing agent and peroxide. Such analysis is not intended in this study.

Earlier studies on midsoles [Mills and Rodríguez-Pérez (2001)] suggested that the presence of inorganic components in midsole foams could be related to improvements on stiffness, thermal resistance, or polymer degradation from UV light, however they do not reported type of filler or colour of the sample. X-Ray diffraction has revealed the presence of TiO_2, ZnO, Mg and Ca; which has been confirmed by EDX microanalysis. The microanalysis also revealed the presence of sulphur, which was not detected by X-Ray diffraction due to the burning process. Calcium sulphate ($CaSO_4$) are used as fillers in polymers because they reduce the manufacturing costs maintaining the physical properties.
A possible analysis of the effects of the inorganic fillers in this type of foams would consists on a study with and without such pigments. Also, the introduction of dif-

ferent types of filler might lead to an improve on the foam behaviour.

The cellular structure showed the presence of elongated cells close to the upper and lower layer of the samples. This anisotropic structure remained throughout the sample as the anisotropy coefficients of cells around the mid-thickness were larger that unity. This anisotropy would affect the mechanical properties of the samples. Samples had a different heterogeneity in the cell structure, EVA150 had large cells in the middle of the thickness whereas EVA108 and EVA265 exhibited two sets of cells.

4.2 Macroscopic characterisation

4.2.1 Density

This is one of the most important material characteristics of foam, because the mechanical properties are strongly influenced by it. From density measurements, the relative proportions of each phase in the material can be determinate. Density depends on the relative proportion, high density foams has lower percentage of gas inside it, and vice versa. The gas ratio is given by the equation [Glicksman (1994)]:

$$\Phi_{gas} = \frac{\rho_s - \rho_f}{\rho_s - \rho_g} \approx 1 - \frac{\rho_f}{\rho_s} \tag{4.2}$$

where ρ_s is the polymeric matrix density (941 kg/m^3 for EVA containing 18% VA) [Samsung (1999); Arsac et al. (2000)], ρ_g and ρ_f are the gas and foam densities. The hand right expression is valid if ρ_g (1.28 kg/m^3) is ignored with respect to ρ_s. Thus, the solid volume ratio is:

$$\Phi_{solid} \approx \frac{\rho_f}{\rho_s} \tag{4.3}$$

Density and standard deviation along side gas and solid ratio are presented in Table 4.9. Density measurements performed by Archimedes' principle can have experimental errors, due to air bubbles appearing on the surface of the foam, changing the

Foam	Density (kg/m^3)	Φ_{gas}	Φ_{solid}
EVA108	108 ± 1.5	0.88	0.12
EVA146	146 ± 1.3	0.84	0.16
EVA151	151 ± 1.3	0.84	0.16
EVA152	152 ± 1.4	0.84	0.16
EVA265	265 ± 1.4	0.72	0.28

Table 4.9: Density, standard deviation and relative proportions.

upthrust of the sample, and to water getting into the foam. Previous unpublished studies [Verdejo (2000-2001)] have shown a linear relationship between densities measured by Archimedes' principle and by dividing the mass by the volume, with approximately 10 % difference between them.

4.2.2 Dynamic Mechanic Thermal Analysis (DMTA)

The transitions of the samples have been identified (Figure 4.18). In all samples, the storage modulus (E') decreases sharply above 0 °C from glassy state to rubbery state followed by a rubbery plateau at 10^5 Pa and viscous flow after melting. On the overall temperature range, E' decreases with T, i.e. the samples becomes softer as they are heated, this is the consequence of the β transition. E' increases with density as higher density foams are harder to deform (Figure 4.19).

The glass transition temperature (T_g) was taken to be where tan δ has its maximum. There are no significant differences in the samples T_g values and tan δ peak heights (Table 4.10) as all samples have similar % VA. The average T_g in this study is -7.7 °C, whereas previous studies reported -25 °C [Nielsen (1960); Arsac et al. (2000)]. This difference, of 18 °C, is due to the equipment characteristics. The temperature at three different heights in the oven chamber was checked with K type thermocouples. These readings were compared with the one from the DMTA Pt

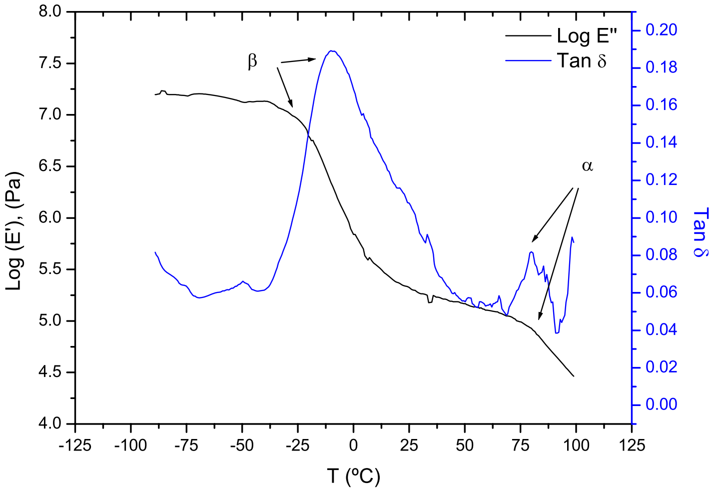

Figure 4.18: DMTA results for EVA152 where the main transitions have been identified.

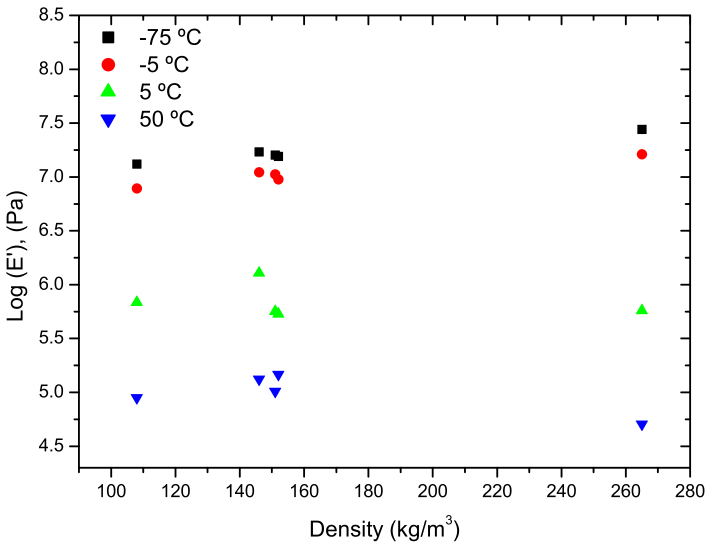

Figure 4.19: Storage modulus vs density at different temperatures.

Foam	T_g (°C)	tan δ
EVA108	-8.9	0.19
EVA146	-7.4	0.19
EVA151	-7.5	0.19
EVA152	-7.4	0.19
EVA265	-7.2	0.19

Table 4.10: T_g and maximum tan δ of foam samples.

resistance thermometer. The readings on the thermocouples of the top and bottom of the chamber were 10 °C to 30 °C different at 30 °C and 100 °C, respectively. The thermocouple at the middle recorded a temperature between the upper and bottom thermocouples, which was similar to that of the Pt thermometer.

4.2.3 Creep

The compressive creep experiments show the response of the foams to an applied stress over a 24 h period (Figure 4.20). The results are analysed in terms of the density and temperature.

The degree of deformation suffered by the samples for the same applied stress decreases with increasing density, i.e. lighter foams are softer than more dense foams. EVA265, at any temperature, deforms less than the rest of the foams whereas EVA108 suffers the highest deformation (Figure 4.21). Results also show that the higher the temperature, the higher the strain suffered by the samples (Figure 4.22).

Isochronous strain-stress curves have been obtained from the creep experiments (Figure 4.23). The effective gas pressure (p_0) in the cells and the initial yield stress (σ_0) as a function of time were calculated for all temperatures (Table 4.11). In general, p_0 decreases linearly with the logarithm of time, whereas σ_0 is practically constant except for the last two points at high stress levels, corresponding to long

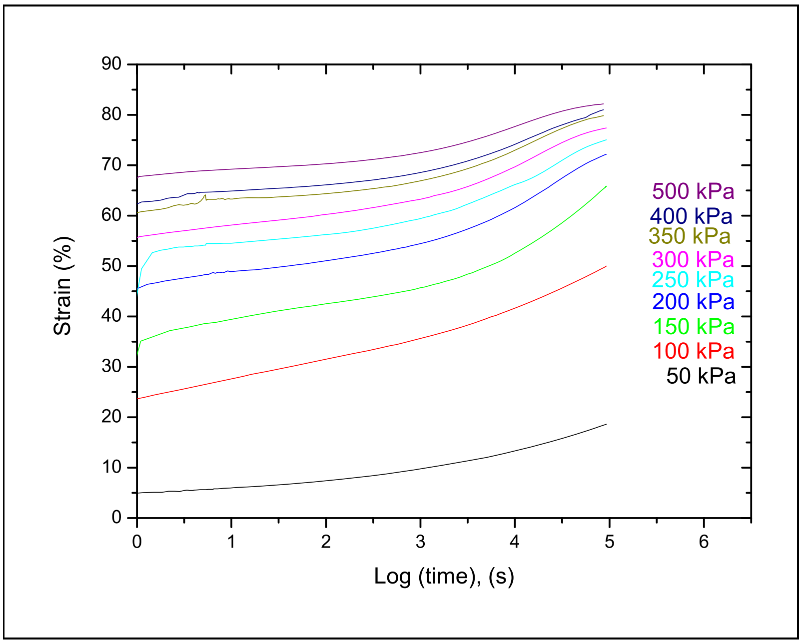

Figure 4.20: Creep response of EVA146 at 35 °C at a range of stresses.

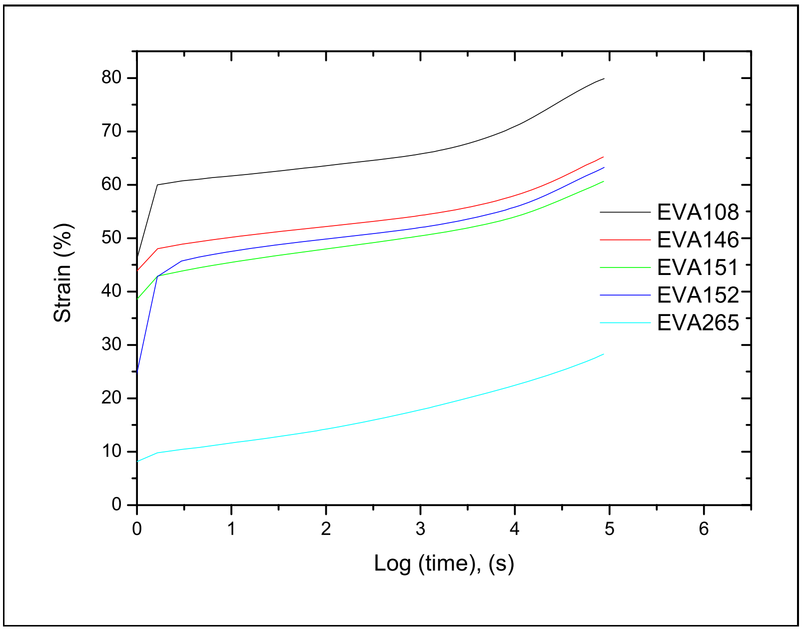

Figure 4.21: Creep response of all samples at 300 kPa and 20 °C

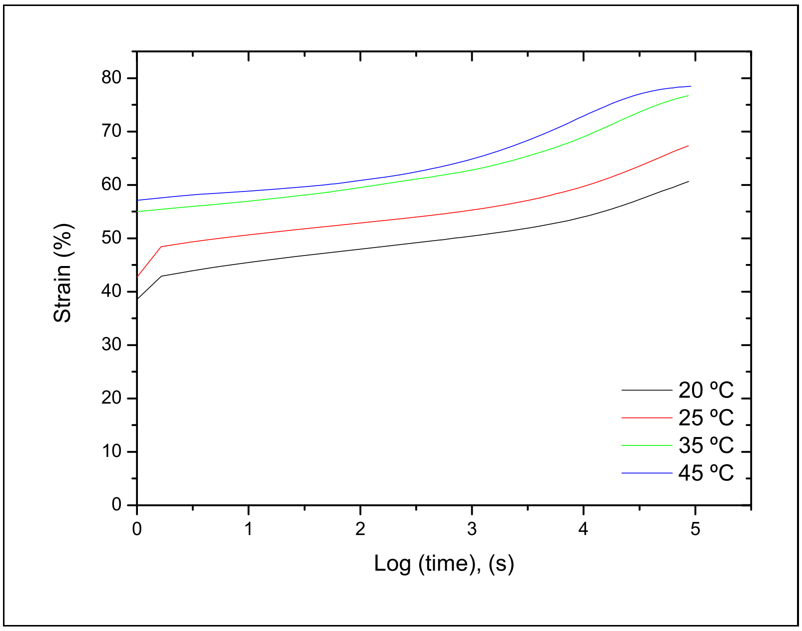

Figure 4.22: Creep response of EVA151 at 300 kPa and different temperatures.

times (> $10^{4.5}$ s) (Figures 4.24-4.25). This increase could be due to errors in the regression, as long times curves has the smallest correlation value. This effect can be observed in the creep curves where the strain, at high stress (> 300 kPa) and time (> $10^{4.5}$ s), shows a lower increase than before. The decrease of p_0 over the time is due to the diffusion of gas from the foam. The gas content inside the cells is higher at the beginning, given larger values of p_0, than at the end where the gas content has decrease. The values over atmospheric pressure, at creep times less than 500 s, suggest that this parameter is affected by the polymer matrix. This is supported by the fact that the p_0 increase with density (Figure 4.26).

Both gas pressure and collapse stress decrease with temperature (Figures 4.24-4.25), the σ_0 reduction is due to the softening of the polymeric matrix with temperature. The polymer contribution suggested above could explain the decrease of p_0. At a given stress, the foam strain increases with temperature (Figure 4.22) leading to a reduction of the cells volume, i.e. at a stress of 300 kPa, the strain at 20 °C is smaller than at 45 °C therefore the volume of the cells at 20 °C is larger

Creep	20 °C		25 °C		35 °C		45 °C	
time (s)	p_0 (kPa)	σ_0 (kPa)	p_0 (kPa)	σ_0 (kPa)	p_0 (kPa)	σ_0 (kPa)	p_0 (kPa)	σ_0(kPa)
EVA108								
10^1	109.3	50.2	104.7	45.7	85.3	56.7	79.35	48.3
$10^{1.5}$	104.5	49.7	100.4	44.8	82.3	55.3	76.1	46.8
$10^{2.5}$	93.2	48.4	90.6	42.0	70.8	56.7	63.7	45.6
$10^{3.5}$	77.8	47.6	66.2	44.5	42.2	75.4	24.7	74.1
$10^{4.5}$	41.7	53.0	25.9	54.4	–	–	–	–
10^5	26.4	53.4	19.9	51.3	–	–	–	–
EVA146								
10^1	149.9	69.8	143.8	100.9	104.7	43.5	100.9	41.7
$10^{1.5}$	145.1	67.3	136.2	100.1	102.2	40.9	96.1	41.6
$10^{2.5}$	134.8	63.6	127.9	96.9	90.7	39.4	78.9	44.8
$10^{3.5}$	117.9	61.9	109.3	96.8	64.4	48.0	40.2	67.7
$10^{4.5}$	82.1	65.6	69.5	104.5	22.0	85.4	11.5	97.0
10^5	64.9	65.4	52.8	107.4	12.7	92.5	8.0	108.9
EVA151								
10^1	180.1	73.5	146.4	62.6	106.2	66.4	101.9	42.3
$10^{1.5}$	172.0	71.2	140.3	60.4	102.7	65.0	96.1	43.0
$10^{2.5}$	158.2	66.2	127.5	57.1	90.6	61.2	78.1	47.5
$10^{3.5}$	141.2	61.5	107.1	55.7	67.5	63.7	40.0	74.1
$10^{4.5}$	105.1	60.5	67.2	61.6	29.1	80.4	5.6	144.5
10^5	87.5	58.6	53.3	57.5	19.3	83.0	2.0	170.2
EVA152								
10^1	161.1	70.9	134.3	68.6	120.7	33.7	100.3	50.8
$10^{1.5}$	154.7	68.8	146.6	60.2	116.2	32.2	96.6	49.1
$10^{2.5}$	142.6	66.2	136.3	54.0	105.3	29.6	81.5	50.3
$10^{3.5}$	124.2	65.1	115.4	52.3	79.5	33.0	45.7	67.3
$10^{4.5}$	86.5	68.2	70.8	60.0	37.4	47.5	11.5	104.4
10^5	69.7	67.0	48.7	65.0	28.03	36.9	8.0	111.7
EVA265								
10^1	618.4	148.8	504.2	121.4	161.1	143.5	283.7	78.5
$10^{1.5}$	634.7	122.6	462.5	121.8	151.5	143.4	285.0	63.2
$10^{2.5}$	578.0	105.7	394.8	121.6	127.1	142.7	255.1	55.8
$10^{3.5}$	490.5	101.7	343.0	119.4	101.8	142.3	213.4	47.8
$10^{4.5}$	401.9	97.8	282.0	115.8	66.5	144.4	158.0	39.7
10^5	357.9	96.2	250.2	112.8	49.4	145.8	145.0	32.2

Table 4.11: σ_0 and p_0 for creep experiments at 20, 25, 35, and 45 °C.

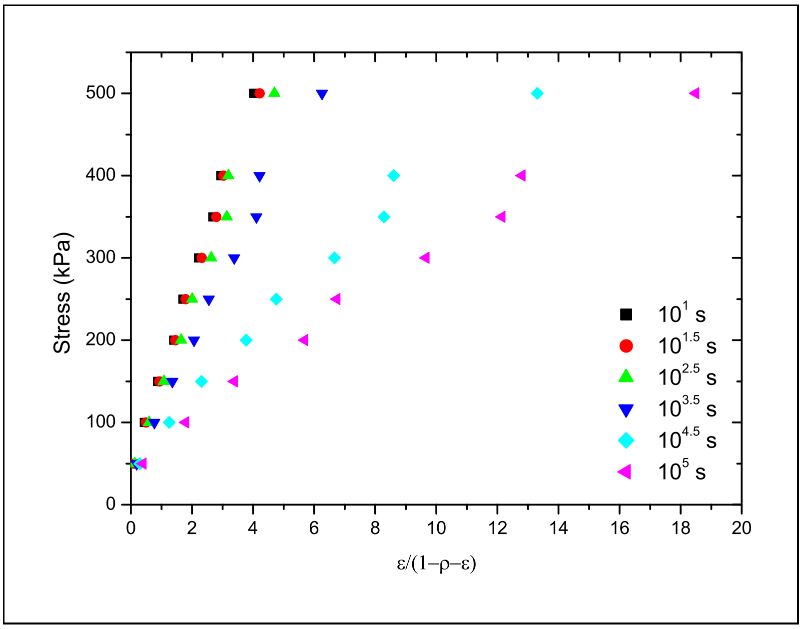

Figure 4.23: Typical isochronous stress vs gas volumetric strain graphs. (EVA152 at 35 °C).

than at 45 °C. The perfect gas law states that an increase of the temperature with a decrease of the volume occupied by the gas increases its pressure. However, as the matrix become softer with temperature the polymer contribution to p_0 decrease.

After creep tests at 400 and 500 kPa, creep recovery measurements were carried out. All samples present the same behaviour with a slow recovery process at the beginning and the main recovery starting at 10^3 s, this suggest that gas diffusion into the foam is the main factor (Figure 4.27) controlling the rate of recovery [Mills and Rodríguez-Pérez (2001)].

When comparing p_0 of EVA265 at 35 °C and that presented by Mills and Rodríguez-Pérez (2001) (Figure 4.28), EVA foam of 275 kg/m^3, it would appear that the diffusion process in EVA265 was quicker than the one reported, because EVA265 showed a steeper slope, but it has to be consider that the dimensions of both sam-

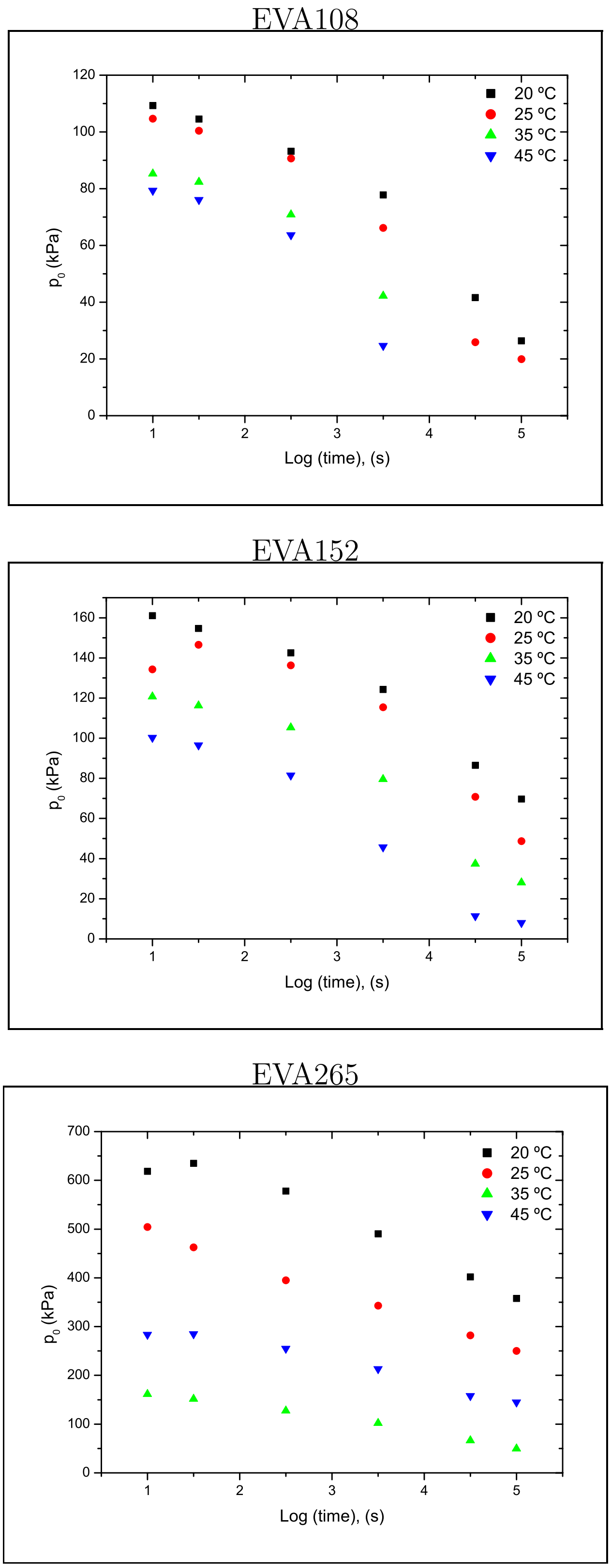

Figure 4.24: Effective gas pressure vs log creep time.

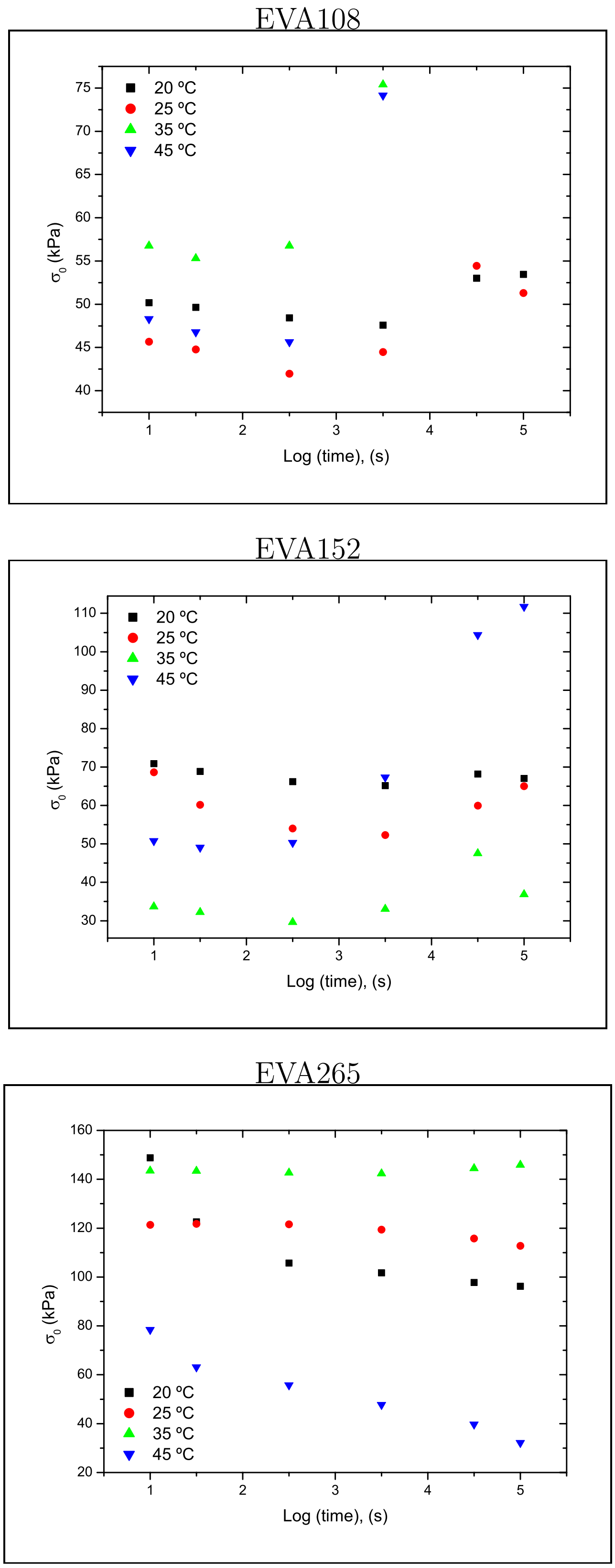

Figure 4.25: Initial collapse stress vs log creep time.

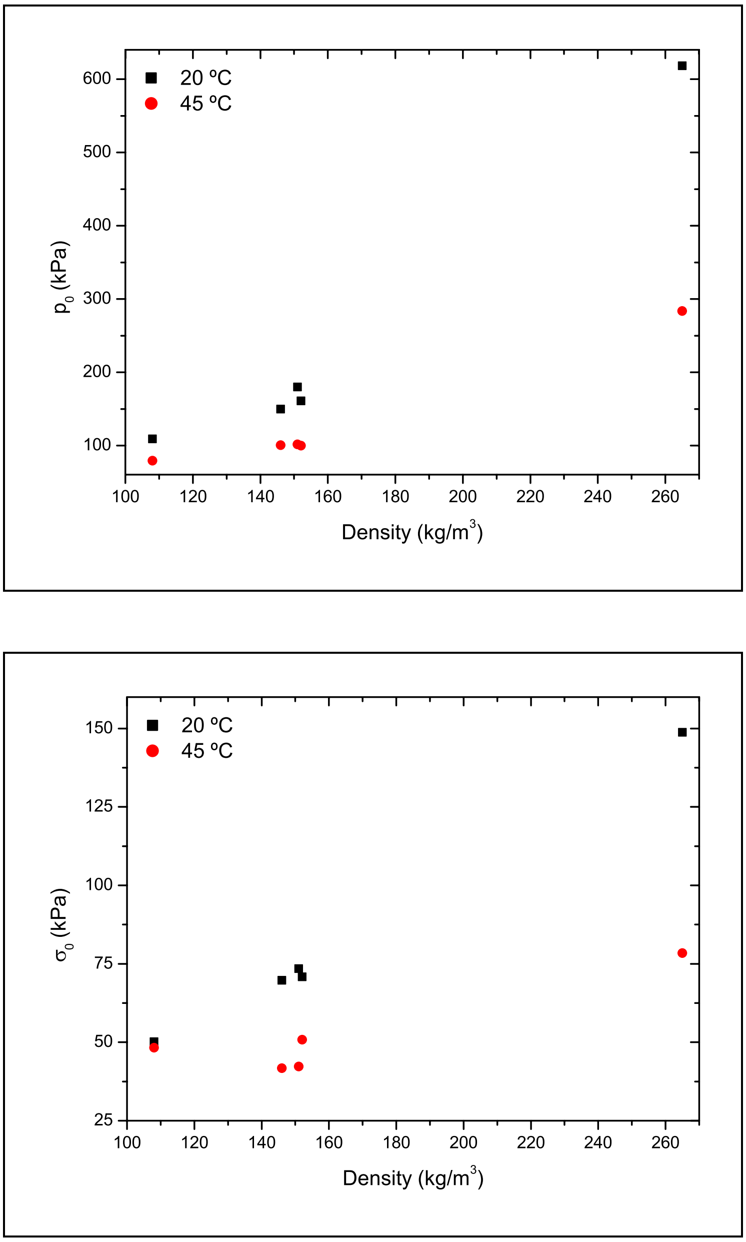

Figure 4.26: Effective gas pressures and initial collapse stress vs density at 10^1 s.

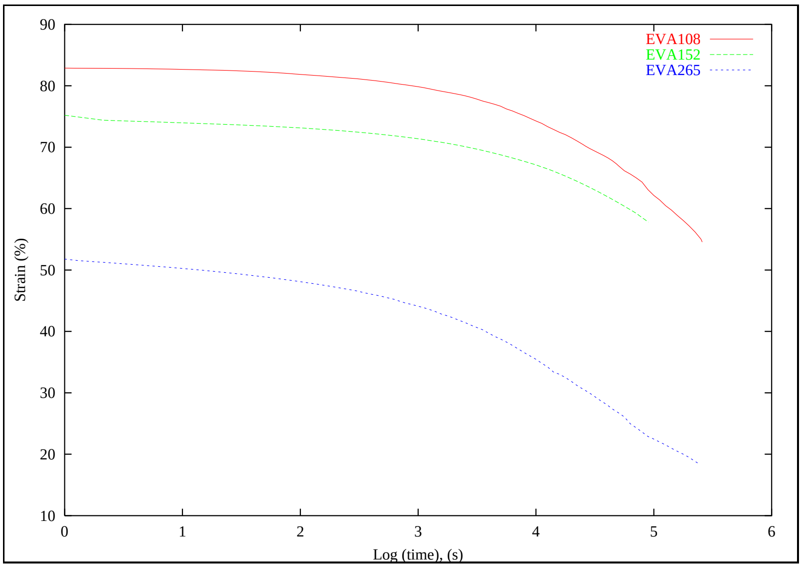

Figure 4.27: Recovery after creep vs time at 35 °C.

ples were different, EVA265 was 12 × 12 × 12 mm^3 whereas the sample of the paper was 16 × 16 × 20 mm^3. Diffusion occurs in a plane parallel to the applied stress [Mills and Rodríguez-Pérez (2001)], i.e. parallel to the foam thickness, therefore gas diffusion in thinner samples would be faster than in thicker samples.

4.2.4 Impact response

Repeat Impact based on ASTM F1614-99 Method

This test was design to measure shock absorption properties of athletic footwear midsole, and, although it is not a selection criterion, manufacturers uses this or similar tests [Knoerr and Rouiller (2002); Yu (2001)]. The results have been analysed as a function of the density and in terms of the number of impacts.

Density

Foam behaviour is largely dependent on the density, increasing the density increases Young's modulus, raises the plateau and reduces the strain at which densification

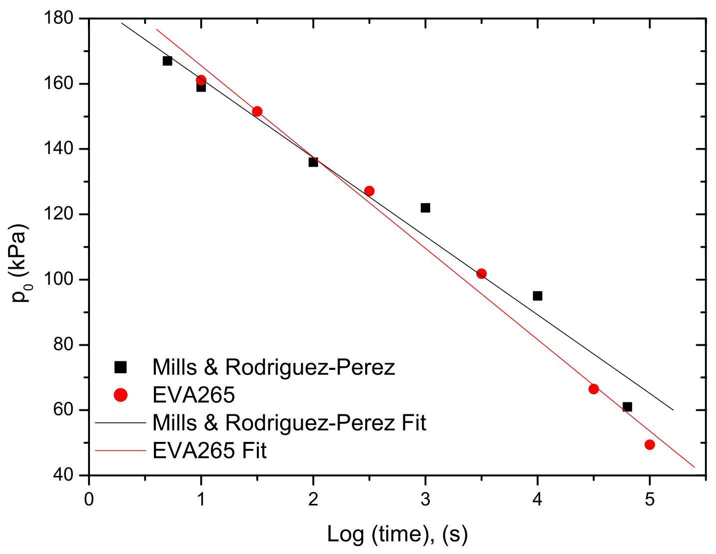

Figure 4.28: Effective gas pressures vs log time for EVA265 and Mills and Rodríguez-Pérez (2001) at 35 °C).

takes place [Gibson and Ashby (1997)]. All this three effects can be seen in these results (Figure 4.29),

- the slope of the linear region is steeper as the density increases,
- EVA150 largest yield point is nearly 0.4 kN (1st impact of EVA146 and EVA151), which is comparable to the smallest EVA265 yield point (100th impact), and
- the densification region on EVA265 starts around 5 mm (42 % strain) whilst EVA108 begins close to 8 mm (66 % strain), EVA150 being in the middle.

Comparing EVA150 foams (Figure 4.30) it can be see that in the first impact EVA146 and EVA151 behaves almost identically with their yield point slightly above that of EVA152 and their densification occurring at larger strain values. This implies that their peak force, for the same displacement, is lower than that of EVA152, absorbing more energy than EVA152. Therefore, these two foams are better shock absorbers

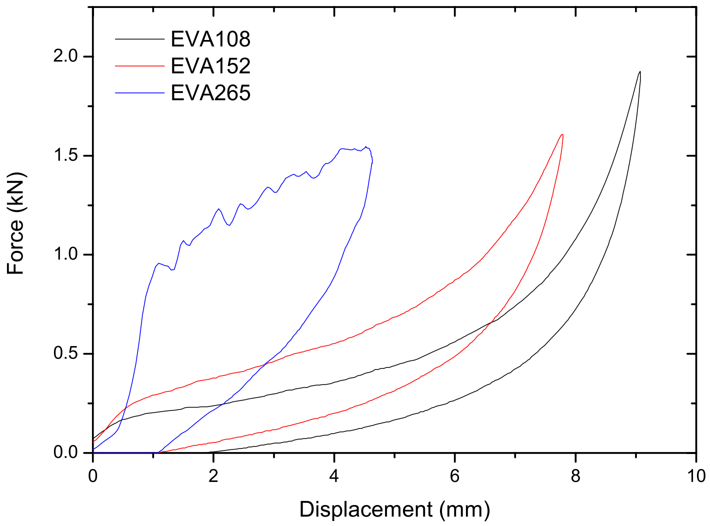

Figure 4.29: Force-displacement behaviour for the 1st impact for EVA108, 150 and 265.

than EVA152 and although, by the end of the experiment, they have suffered a larger variation of their peak force than that suffered by EVA152, their performance is better than EVA152 (Table 4.13). These differences may be related to the differences in the blowing agent and peroxide and in the cellular structure.

In general, the average absorbed energy (Table 4.12) increases with density. This is due to the increase of the compressive strength of polyolefin foams with increasing density [Park (1991)].

Number of Impact

Force-displacement curves of the samples show a distinctive change of the shape from the first to subsequent impacts, less noticeable in EVA108.

EVA108, due to its low density, deforms rapidly and more under low force. The

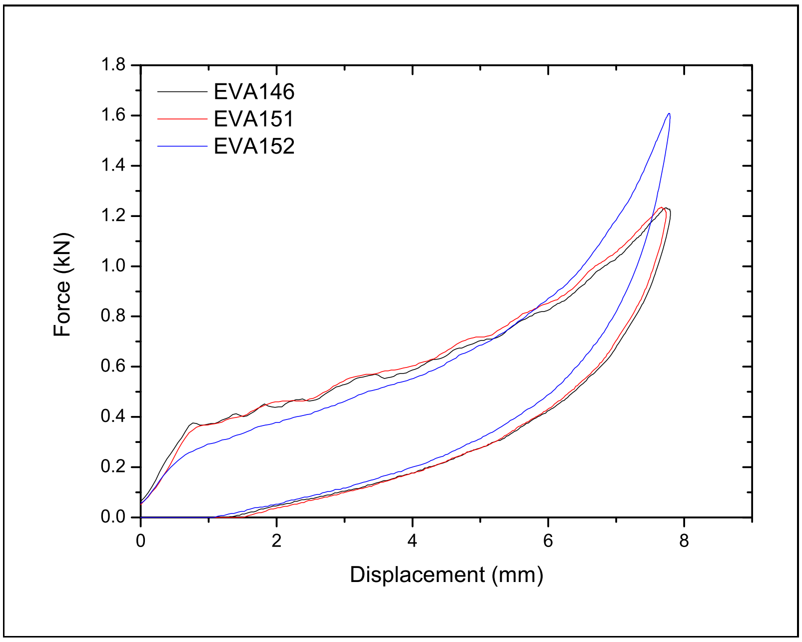

Figure 4.30: Force-displacement behaviour for the 1st impact for all three EVA150.

Foam	Average E_a (J)
EVA108	3.04 ± 0.23
EVA146	3.44 ± 0.10
EVA151	3.49 ± 0.12
EVA152	3.16 ± 0.10
EVA265	3.69 ± 0.17

Table 4.12: Average absorbed energy and standard deviation over the ASTM experiment.

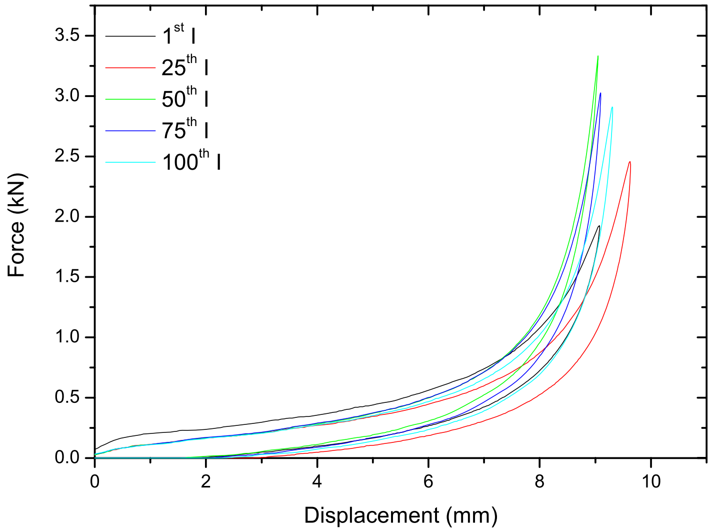

Figure 4.31: Force-displacement behaviour of EVA108 over the 100 impacts.

first impact shows a clear yield point followed by a region of plastic deformation. Such behaviour is not observed in the following impacts where there is no yield point present (Figure 4.31). The unloading curve is very close to the loading curve, hence absorbing little energy in the cycle. This is the most elastic behaviour of all the foams studied. The densification region increases with number of impacts, getting higher as the foam is subjected to repeated impacts. The displacement of the curves towards lower deflection with impact number is due to the indentation of the foam, reducing its thickness. This introduced an error as the thickness is used to assess the deflection of the top surface of the sample.

All three EVA150 foams change in behaviour during the experiment (Figure 4.32). The first impact curve shows a clear elastic region after which a constant slope of plastic deformation takes place. This type of curve is characteristic of viscoelastic foams. This behaviour is still observed in the following impacts but with a lower yield point. The frequency of the impacts does not allow the foam to recover, leading

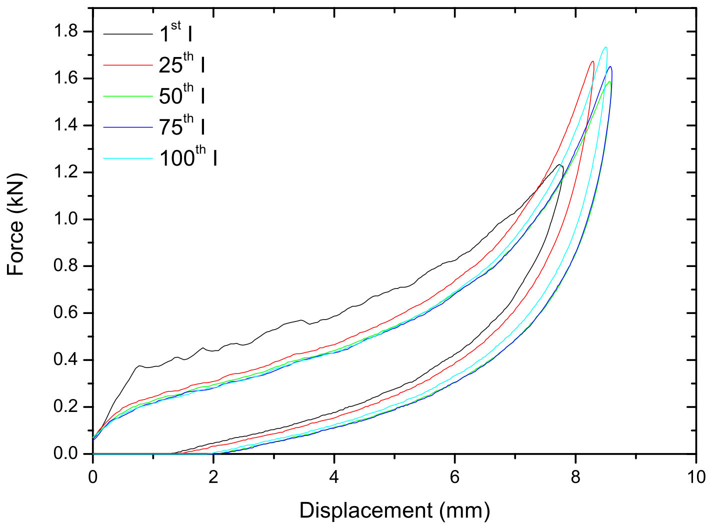

Figure 4.32: Force-displacement behaviour of EVA146 over the 100 impacts.

to such change. The behaviour seems to reach an "equilibrium" where curve shape, maximum force and displacement are practically the same. This could be because, during the first impact, some regions [Park (1991)] of the structure would have received damaged leading to a softening of the foam structure, such damage remains in the structure making the foams easier to deform. The term damage is used as a non-linear viscoelastic change in the cellular structure that could be reduced by leaving the sample to recover for a period of time.

Finally, EVA265 does have a large change of the initial yield point (Figure 4.33) but there is little change from 25^{th} impact on. That variation of the yield point, with the first being almost twice the following values, shows the softening of the structure mentioned above.

Although, all 5 foams have an increase of the peak deflection and force (Table 4.13) for the last compared with the first impact, there are some "random" variations for

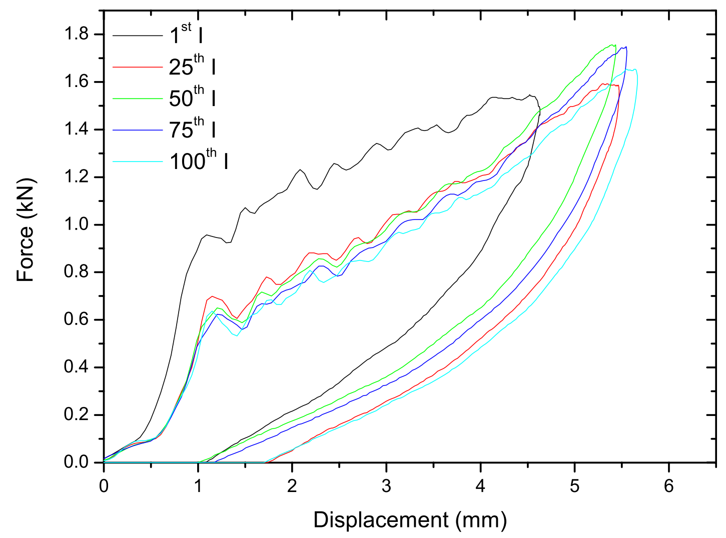

Figure 4.33: Force-displacement behaviour of EVA265 over the 100 impacts.

intermediate values. The energy absorbed (Table 4.14) in the loading-unloading cycle behaves similarly, with a slight decrease of the last with respect to the first value. A possible reason for this could be due to experimental errors occurred as result of variations on impact height, but the stop placed at the impact height did not move during the experiment and the height was visually checked before the data recording.

Although, the impacts cannot be considered as a uniaxial compression, because the dimensions of the sample were larger than the impacting area, the initial yield stress and gas pressure were calculated from the loading region of stress versus gas volumetric strain curve. The results are an approximation, but they give an idea of the relationship between mechanical behaviour and density. EVA108 regression for high impact number results on negative values of σ_0 due to its almost linear response mentioned above. Therefore, only the values for the first impact are reported. EVA265 values have to be carefully analysed as is a high density foam and equation 2.3 is not valid for this type of foams.

	Peak Force (kN)				
N Impact	EVA108	EVA146	EVA151	EVA152	EVA265
1	1.94	1.24	1.24	1.62	1.55
25	2.47	1.68	1.51	1.87	1.60
50	3.35	1.59	1.58	1.92	1.76
75	3.04	1.66	1.66	1.96	1.76
100	2.93	1.74	1.76	1.90	1.66

Table 4.13: Registered peak force over number of impacts.

	Absorbed Energy (J)				
N Impact	EVA108	EVA146	EVA151	EVA152	EVA265
1	3.23	3.55	3.61	3.30	3.84
25	3.27	3.30	3.54	3.10	3.85
50	2.69	3.45	3.56	3.12	3.48
75	2.96	3.49	3.43	3.07	3.52
100	3.02	3.39	3.30	3.22	3.74

Table 4.14: Absorbed energy over number of impacts.

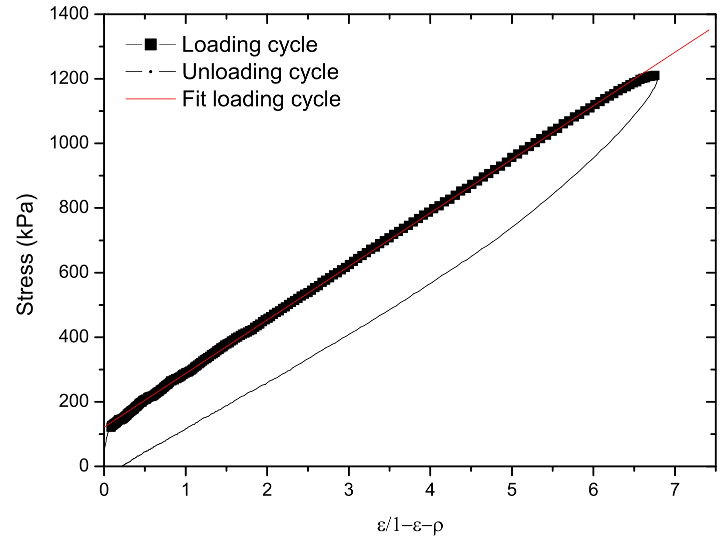

Figure 4.34: Stress vs gas volumetric strain for the 1st impact of EVA108.

All samples show a good agreement with equation 2.3 (Figure 4.34). The worse regression coefficient, 0.95, corresponds to the first impact of EVA265 due to its stiffness.

Initial inspection of p_0 (Table 4.15) reveals values of cell gas pressure higher than atmospheric pressure. Closer analysis of the first impact shows an increase of p_0 with density. These two facts suggest that the polymer contribution to the stress is not constant with strain, i.e. there could be cell face stresses contributing to the gas pressure, in accordance with creep results.

The collapse stress (σ_0) and gas pressure (p_0) inside the cells decrease and increase with number of impacts respectively (Figure 4.35). The softening of the foam structure causes the reduction of σ_0 values.

The increase of p_0 with impact number, whereas in creep experiments decreased with time, could be due to

1. the type of impact performed, as the compression is not uniaxial the region

1^{st} Impact

Foam	p_0 (kPa)	σ_0 (kPa)	R^2
EVA108	165.7	121.8	0.99
EVA146	209.8	241.3	0.99
EVA151	206.0	250.7	0.99
EVA152	300.6	161.4	0.99
EVA265	409.0	627.9	0.95

25^{th} Impact

Foam	p_0 (kPa)	σ_0 (kPa)	R^2
EVA108	–	–	–
EVA146	259.8	133.5	0.99
EVA151	220.6	162.6	0.99
EVA152	330.9	106.8	0.99
EVA265	441.7	379.3	0.98

50^{th} Impact

Foam	p_0 (kPa)	σ_0 (kPa)	R^2
EVA108	–	–	–
EVA146	214.9	144.3	0.99
EVA151	232.5	150.4	0.99
EVA152	334.0	94.99	0.99
EVA265	511.6	335.9	0.99

75^{th} Impact

Foam	p_0 (kPa)	σ_0 (kPa)	R^2
EVA108	–	–	–
EVA146	222.5	133.5	0.99
EVA151	254.4	136.9	0.99
EVA152	350.5	93.7	0.99
EVA265	485.5	325.6	0.99

100^{th} Impact

Foam	p_0 (kPa)	σ_0 (kPa)	R^2
EVA108	–	–	–
EVA146	245.7	118.5	0.99
EVA151	283.6	122.2	0.99
EVA152	317.3	99.0	0.99
EVA265	438.1	332.2	0.99

Table 4.15: σ_0, p_0 and correlation coefficient for ASTM impacts.

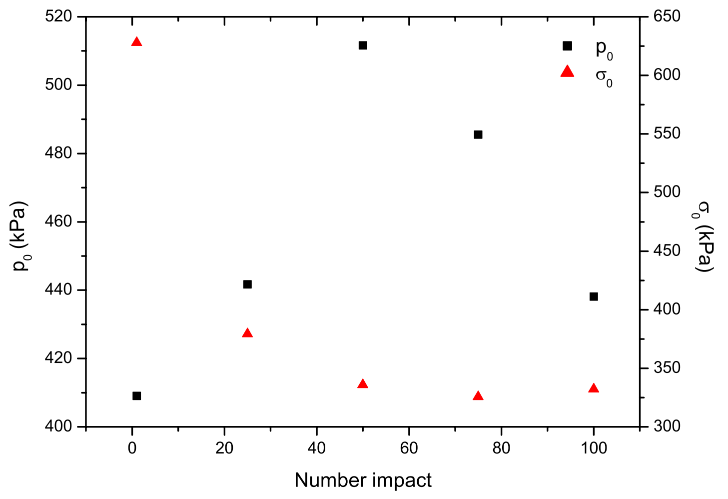

Figure 4.35: Effective gas pressure and initial yield stress vs impact number for EVA265.

of the foam that had not been compressed alters the response of that under compression. This introduces a complexity that it is not considered in equation 2.3. All foams, at the end of the experiment, were indented where the impact took place or

2. the different time scale of the experiments. Creep tests over a 24 h period allow gas diffusion to occur, which may not happen during a 20 ms impact.

Repeat Impact Machine

These experiments reveal the effects of mechanical ageing on the foam density, peak forces, peak pressures and absorbed energy. The displacement of the baseplate measured earlier affects the foam displacement during unloading. The correction for such effect preferably requires the use of a second laser extensometer. As that second laser was not available, the results presented have not been corrected for the displacement of the baseplate.

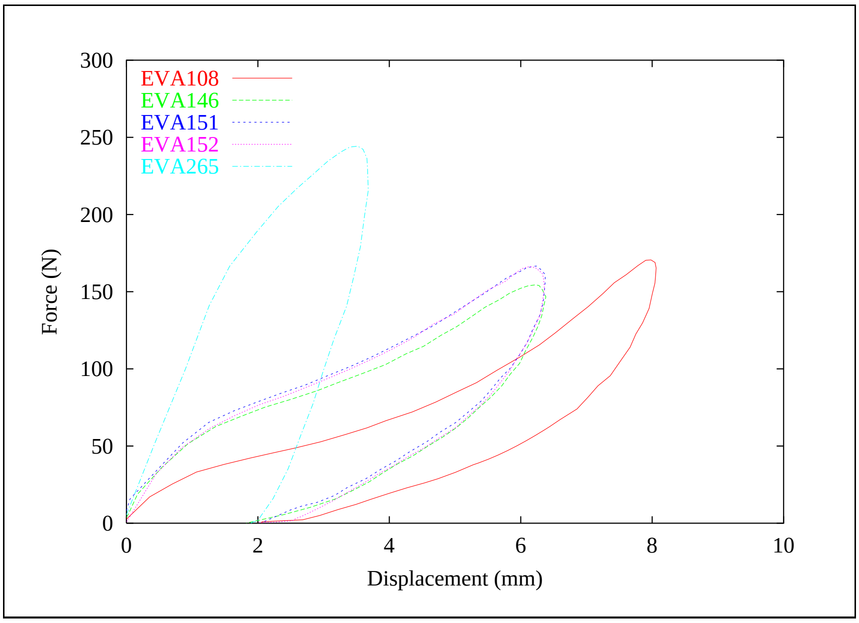

Figure 4.36: Force displacement graphs for 1st day 1st impact.

Overall, the effect of density on the force-displacement response (Figure 4.36) is similar to that already observed by ASTM impacts, although peak forces and displacements values differs as result of the different type of impact.

Run distance

This analysis informs about long term performance of the samples. Firstly, in this analysis, "run distance" and "experiment day" are equivalent. Run distance was calculated from the equipment velocity, see 3.2.4, multiply by run time. The prior day distance was added to following day run distance (Table 4.16).

Analysis of the five days experiment is carried out as a function of peak force and absorbed energy change, this informs about the short term performance of the samples. Afterwards, the long term experiment is analysed in terms of the density, total peak force and peak stress change and gas pressure and yield stress. The results of five days experiment on 5 samples are averaged for each foam. The magnitude of the

	Run distance (km)				
Run time (s)	day 1	day 2	day 3	day 4	day 5
0	0	54.0	108.0	162.0	216.0
1800	13.5	67.5	121.5	175.5	229.5
3600	27.0	81.0	135.0	189.0	243.0
5400	40.5	94.5	148.5	202.5	256.5
7200	54.0	108.0	162.0	216.0	270.0

Table 4.16: Machine run distance in 5 days experiment.

standard deviation varies with foam and day (Figure 4.37). In general, the standard deviation decreases with experiment day, i.e. the first day has the largest deviation whilst the fifth day has the smallest. The foam that suffers the largest deviation is EVA108 while EVA265 has the smallest. EVA108 first day first impact standard deviation is ± 20 N and ± 0.8 mm and EVA265 fifth day last impact standard deviation is ± 13 N and ± 0.6 mm. The possible reason for this reduction is that the polymer contribution to the stress is a function of foam microstructure, which may vary slightly from sample to sample. As the foam is fatigued, the polymer contribution reduces, while the cell air contribution remains constant. The latter should be constant from sample to sample.

5 Days Experiment

Initial inspection of force-displacement curves show a progressive change of the shape from the first to subsequent impacts, becoming less clear over the days (Figures 4.38-4.39). This progressive change is due to the foam resting time between sessions, which affects each foam differently. This gave a different degree of recovery, defined as the difference percentage between the peak force at the beginning of one session with respect to that presented at the end of the previous day session.

0 km of EVA108

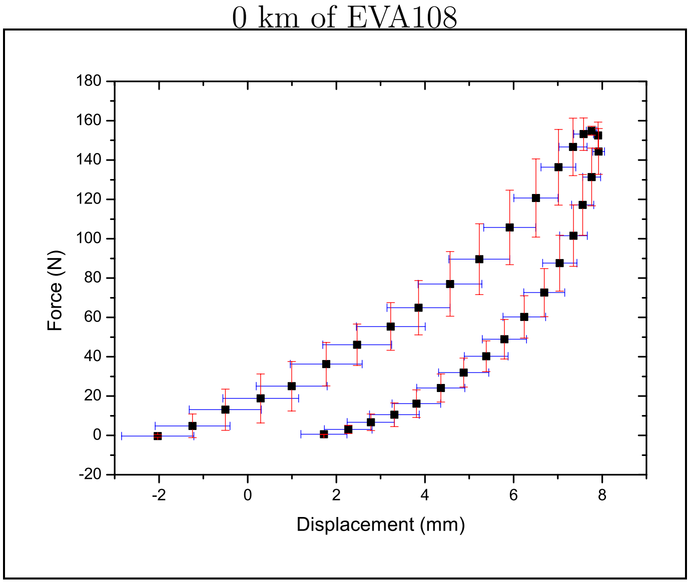

270 km of EVA265

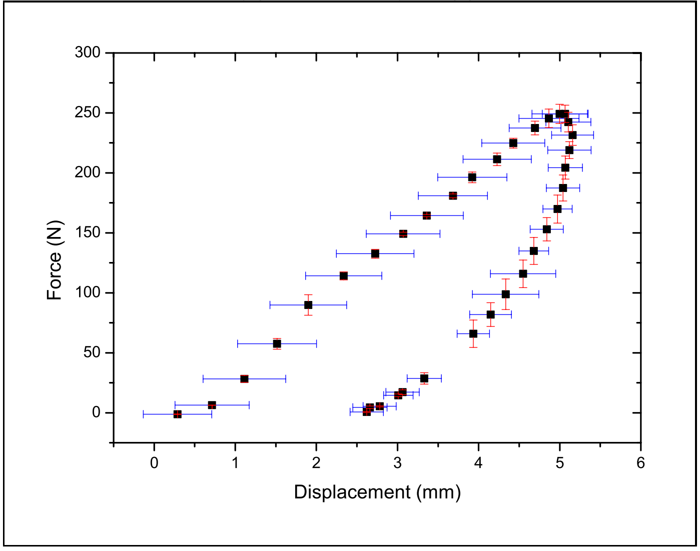

Figure 4.37: Mean and standard deviation of EVA108 first day first impact and EVA265 fifth day last impact. Graphs correspond to the smallest and largest standard deviation occured in repeat impact experiments.

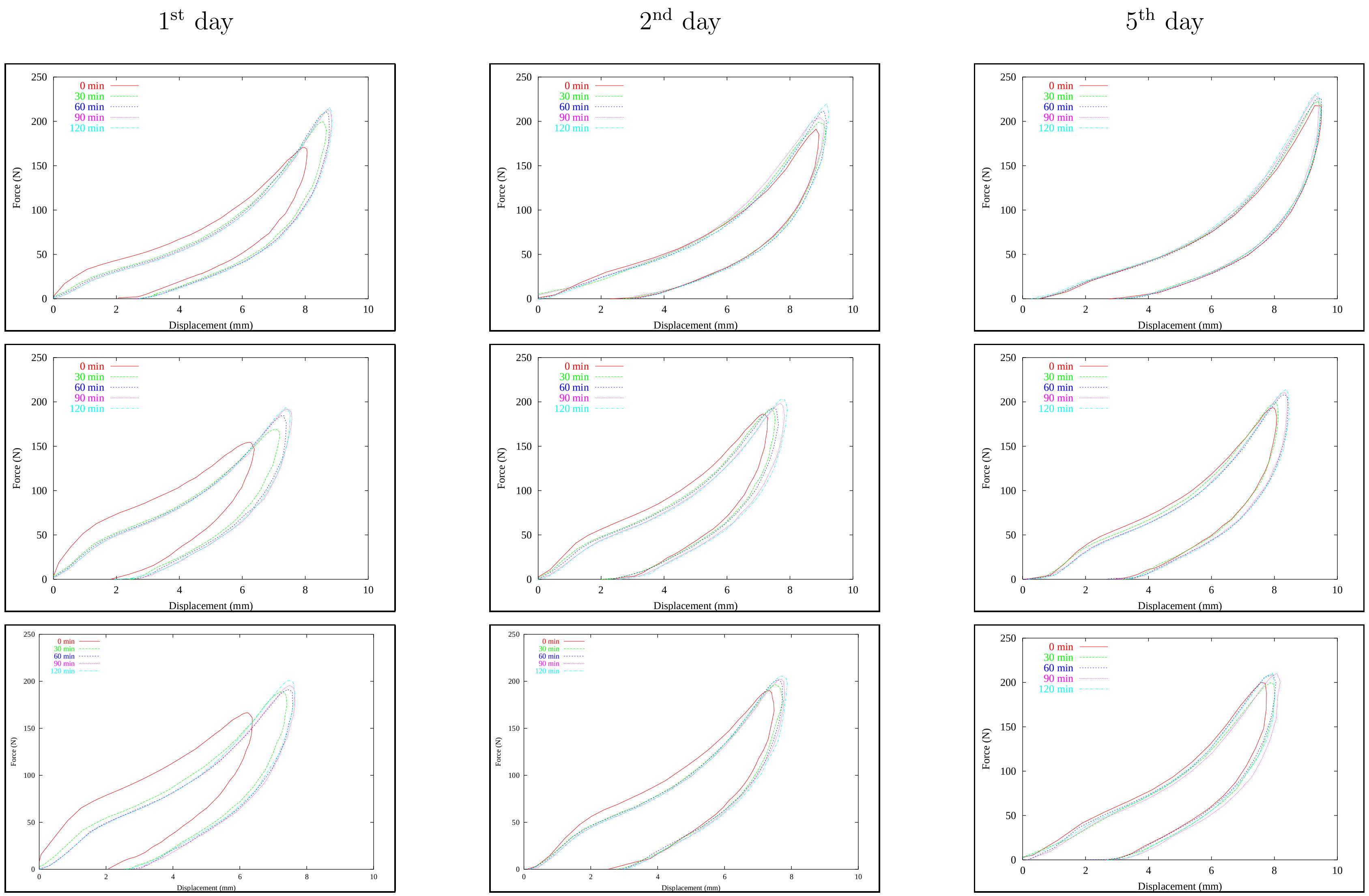

Figure 4.38: Force displacement behaviour of EVA108, 146 and 151 for 1st day, 2nd day and 5th day.

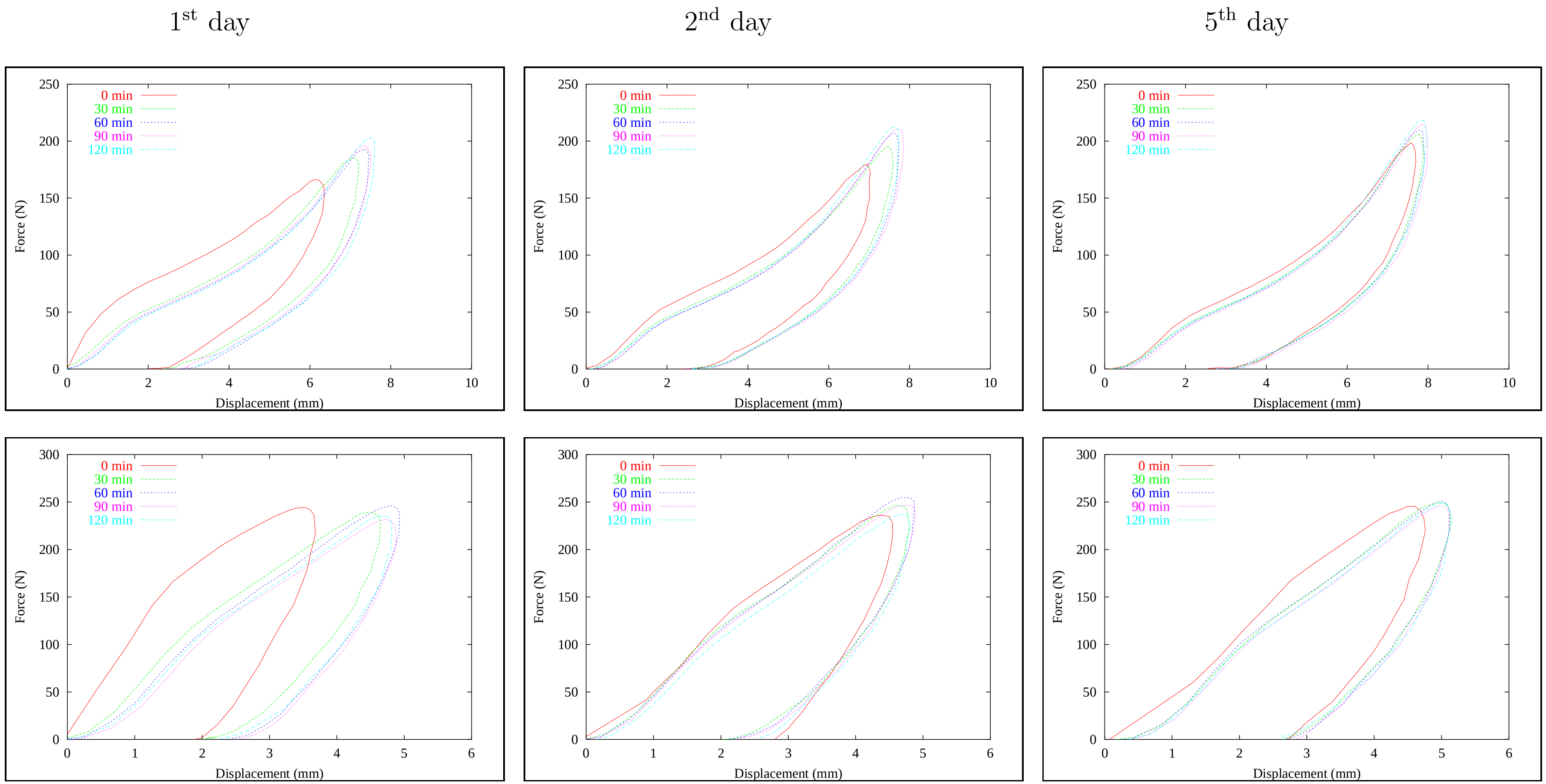

Figure 4.39: Force displacement behaviour of EVA152 and 265 for 1st day, 2nd day and 5th day.

The peak force (F_p) changes and degree of recovery suffered by the samples as a function of run distance (Table 4.17) are as follows,

- EVA108 has the largest change between the first and following impacts, with progressive reduction of its degree of recovery. The sample suffers a 33 % increase of its F_p from 0 km to 54 km (Figure 4.40). The final F_p value is 43 % larger with respect to 0 km.

  The degree of recovery for the first resting period is 10 %, i.e. the foam has recovered 10% of its compressive properties with respect to its behaviour at the end of the previous day. The degree of recovery for the last day is half this value.

- EVA150 have similar final peak force values although their initial value and increase pattern differs. EVA146 has the lowest initial peak force but it also has the largest 1st day (Figure 4.40) and total change of all EVA150. EVA146 F_p value at 270 km is 38 % larger than at 0 km, whereas for EVA151 and EVA152 is on average a 30 % larger.

  The degree of recovery of EVA146 and EVA151 stays almost constant through out the experiment, whilst the largest recovery percentage corresponds to EVA152 with 14 %.

- Finally, EVA265 has the lowest peak force change between 0 and 54 km, just a 3 % difference (Figure 4.40). The peak force is only 7 % larger at 270 km with respect to 0 km.

  Its degree of recovery is constant at 1 %, i.e. the foam does not recover its properties.

The absorbed energy increases almost linearly with density (Figure 4.41. a.) whereas it shows a decrease over run distance. On average, the samples have a 15 % difference (Figure 4.41. b.) in the absorbed energy over 270 km. EVA146 shows the

EVA108

	Peak Force (N)		Total	Recovery
Day	0 min	120 min	Diff. %	%
1st	162.28	215.25	33	
2nd	194.80	219.40	13	10
3rd	201.43	224.98	12	8
4th	213.75	228.71	7	5
5th	217.43	231.98	7	5

EVA146

	Peak Force (N)		Total	Recovery
Day	0 min	120 min	Diff. %	%
1st	154.98	193.42	25	
2nd	188.30	203.20	8	3
3rd	195.01	204.00	5	4
4th	197.10	209.68	6	3
5th	202.21	213.68	6	4

EVA151

	Peak Force (N)		Total	Recovery
Day	0 min	120 min	Diff. %	%
1st	165.20	199.17	21	
2nd	190.80	202.30	6	4
3rd	200.95	207.70	3	1
4th	201.40	213.85	6	3
5th	205.53	214.78	5	4

EVA152

	Peak Force (N)		Total	Recovery
Day	0 min	120 min	Diff. %	%
1st	166.62	201.52	21	
2nd	173.02	211.50	22	14
3rd	183.68	205.75	12	13
4th	191.45	214.52	12	7
5th	193.40	218.80	13	10

EVA265

	Peak Force (N)		Total	Recovery
Day	0 min	120 min	Diff. %	%
1st	246.01	254.10	3	
2nd	252.1	256.40	2	1
3rd	254.32	259.92	2	1
4th	258.41	261.81	1	1
5th	260.22	263.90	1	1

Table 4.17: Peak force and difference percentage at the start and end of each day session, and the recovery percentage of the samples after 22h resting period.

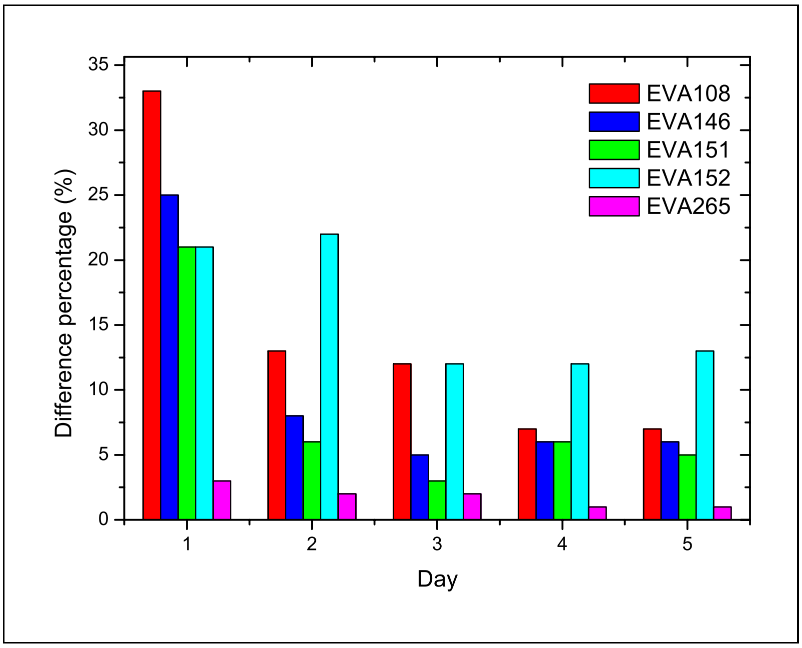

Figure 4.40: Difference percentage of the peak force at the beginning and end of each day session.

largest change meanwhile EVA152 has the smallest change.

The recovery process is also appreciable in the absorbed energy, EVA108 and EVA265 present a 7 and 3 % increase of absorbed energy at 54 km after the 22 h resting period. Again, the foam with the larger percentage of recovery is EVA152 with a 11 % increase at 54 km after the 22 h whilst that increase falls to 6 % for EVA151 and to 1 % for EVA146.

17 Days Experiment

All samples show a change in the density over the experiment (Figure 4.42.a.). There is a decrease in the volume, as result of a decrease in the height (Figure 4.42.b.) and a slight increase in the impacted area, with the mass remaining almost constant throughout the days.

For all the samples, the increase in the impacted area remains between 3 and 4 %. The larger density variation is observed in EVA108 with a 15% difference between

a. 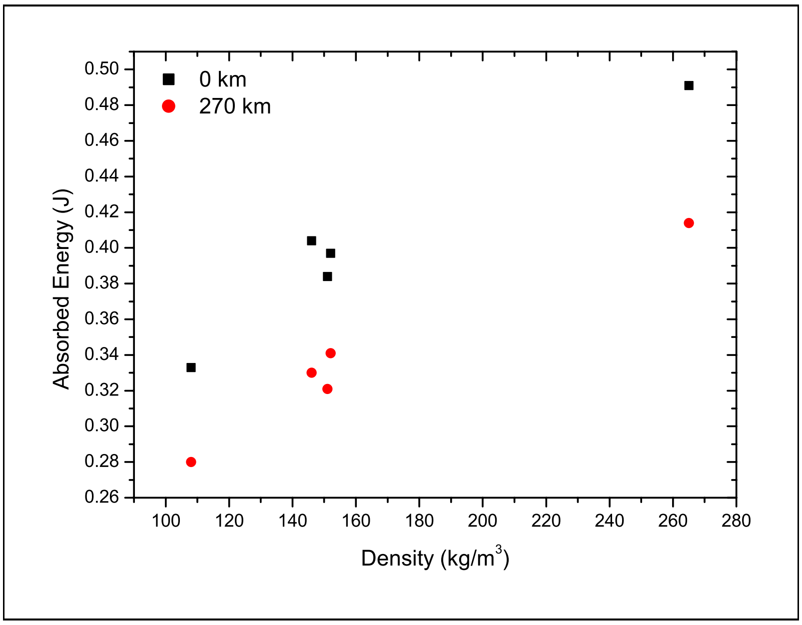

b. 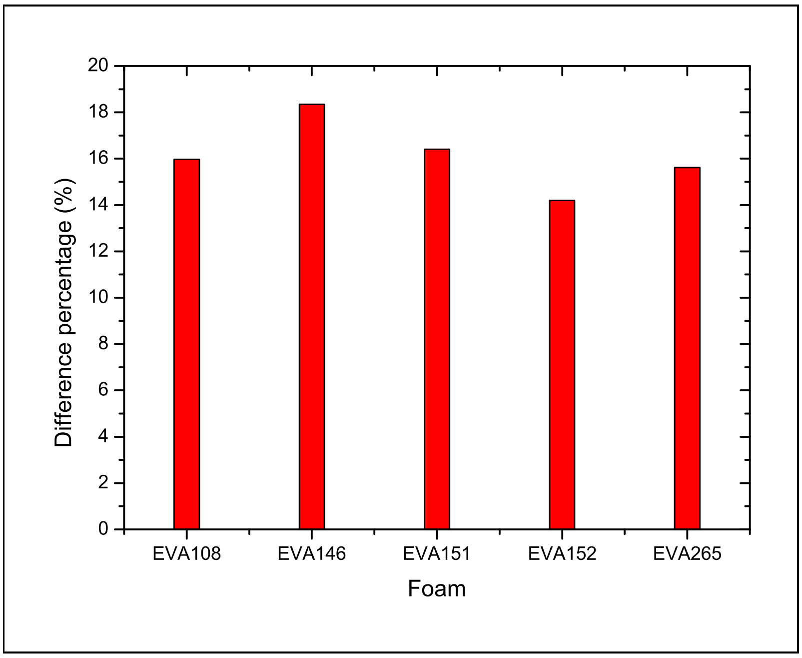

Figure 4.41: Absorbed energy and difference percentage as a function of density between 0 and 270 km.

0 and 1377 km with a height change of 16 %. EVA151 and EVA152 present similar density and height changes, around 9 % and 11 %, respectively. EVA146 shows the largest height reduction, 14 %, and a density change of 12 %. Finally, EVA265 has the lowest density change of 6 % although its 9 % height change is comparable to EVA151 and EVA152. Thus, both density and height difference percentage decrease with increasing density (Figure 4.43). The foam density increase is likely to be due to partly-viscoelastic changes in the polymer structure. Further recovery in the foam response occurs when the recovery time exceeded 22 hours and after 9 months the foam is not fully recovered.

All samples show a steady increase of the peak pressure with run distance (Figure 4.44). Such change for all the samples is smaller than 50 %. Considering that previous biomechanical studies [Cavanagh (1980)] has suggested a trainers' life of no more than 800 km, such change appears to be smaller than what could be expected after a 1377 km run. A reason for such small change could be that the tests were performed at an ambient temperature of 20 °C with a relatively small sample having good convection cooling from its surfaces. In real shoes there can be significant temperature rises [Kinoshita and Bates (1996)] which will reduce the polymer contribution to the compressive stress. A further study could analyse the effect of the temperature to the response of the foams under repeat impact.

Comparing the peak forces of 5 days and 17 days experiments has to be considered that the 5 days experimental results are average whereas, for each sample, there is a single 17 days experiment. The longer experiment (Figure 4.45) shows larger change in the last with respect to the 1^{st} impact. The difference percentage between the start and end of the experiments increases with decreasing density but, comparing this parameter at 1377 with respect to 270 km, the largest change corresponds to EVA265 and the smallest to EVA146.

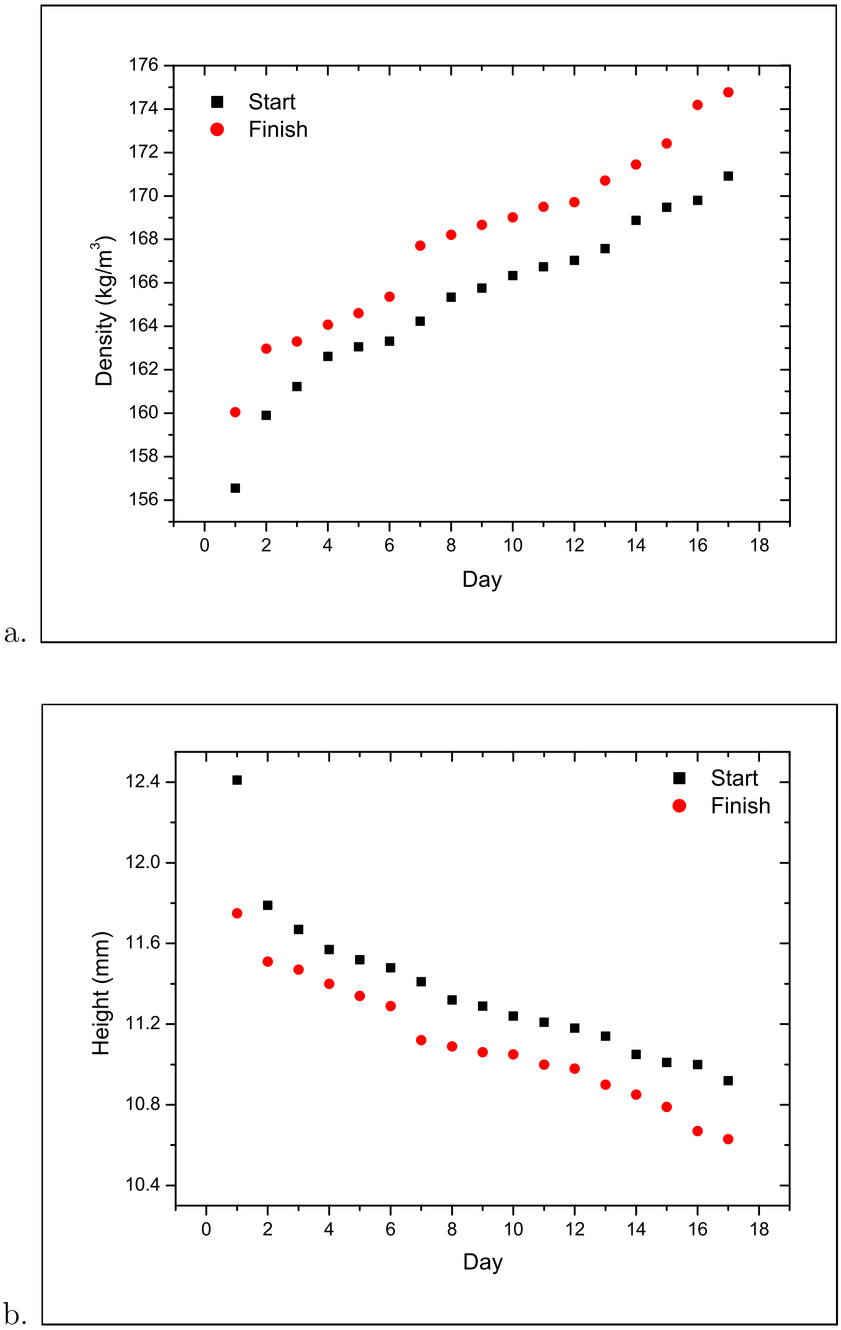

Figure 4.42: Density and height variation over 17 days experiment for EVA146.

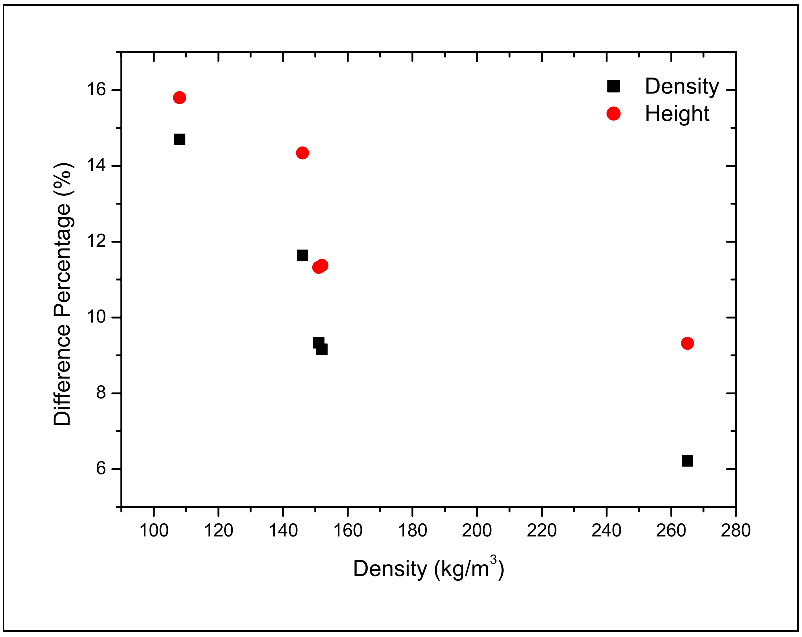

Figure 4.43: Difference percentage between 0 and 1377 km for density and height vs type of foam.

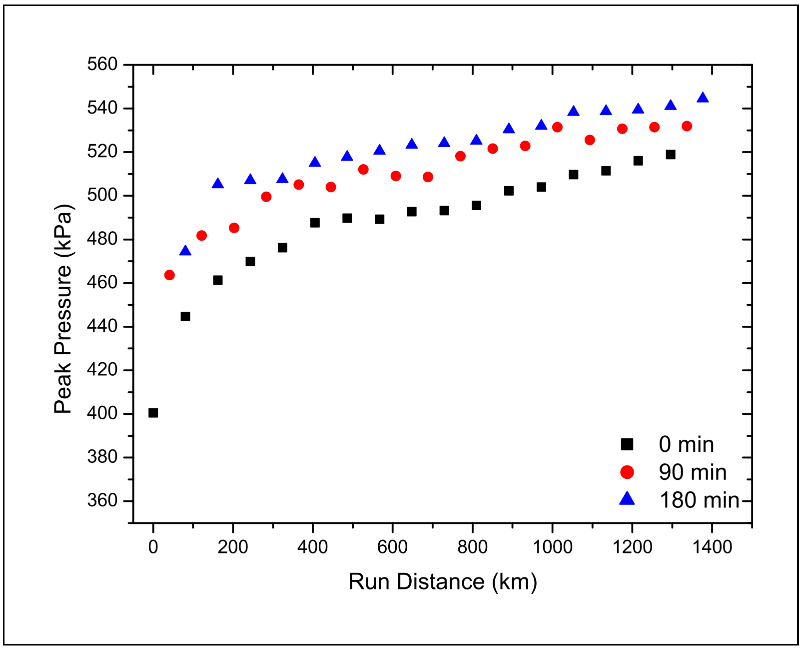

Figure 4.44: Peak pressure increase over run distance at the beginning, middle and end of each day for EVA151.

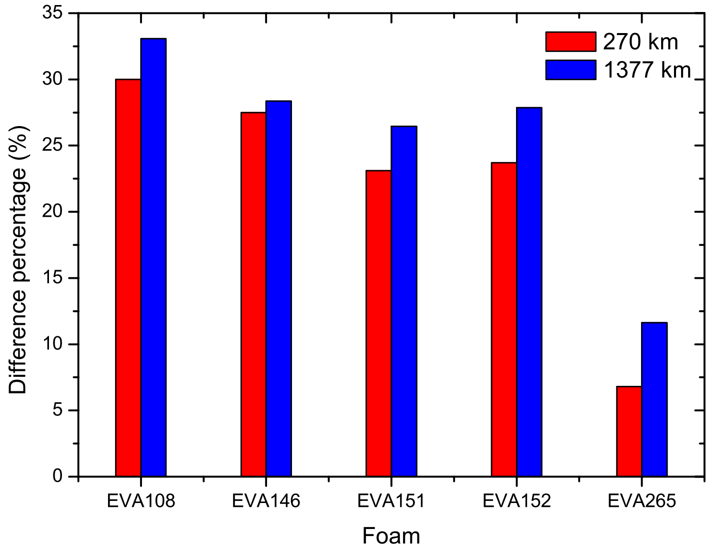

Figure 4.45: Comparison of the peak force difference percentage between 5 days and 17 days experiment.

The yield stress (σ_0) decreases over the experiment, the largest variation occurring in the first 30 min (Figure 4.46), EVA265 has the largest scatter due to its density. The gas pressure (p_0) values tend to vary around a mean value over the run distance, which increases almost linearly with density (Table 4.18). As the value is greater than 100 kPa, the polymer structure must contribute to the foam hardening. However, as the value does not change during the tests, it appears that the gas content of the foam cells remains constant.

The decrease of the yield stress reveals the softening of the material with run distance which suggests a decrease of the cushioning properties of the samples, as the lower the yield point, the easier a foam is to deform. Therefore, foam fatigue is produced as result of the softening of the material and it is not due to gas diffusion as suggested by Mills and Rodríguez-Pérez (2001).

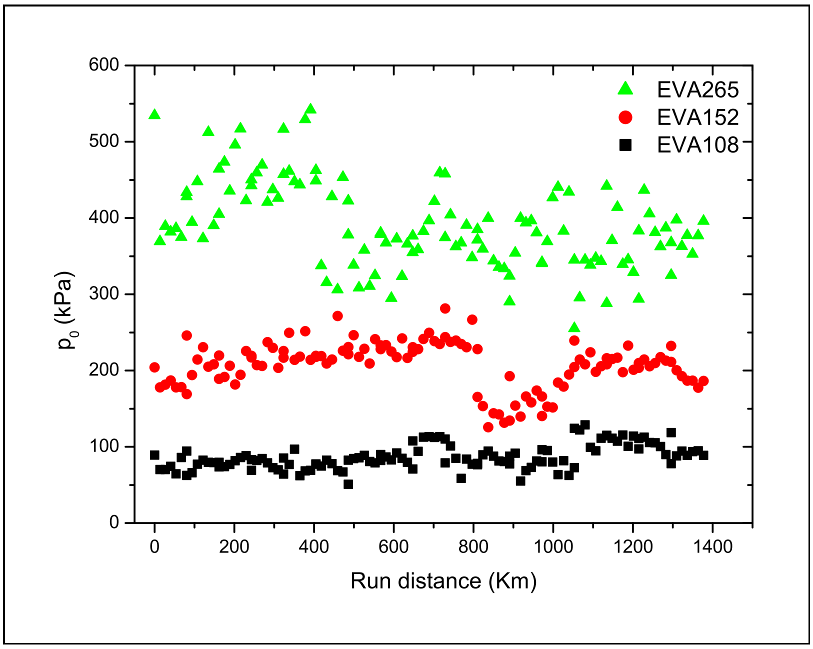

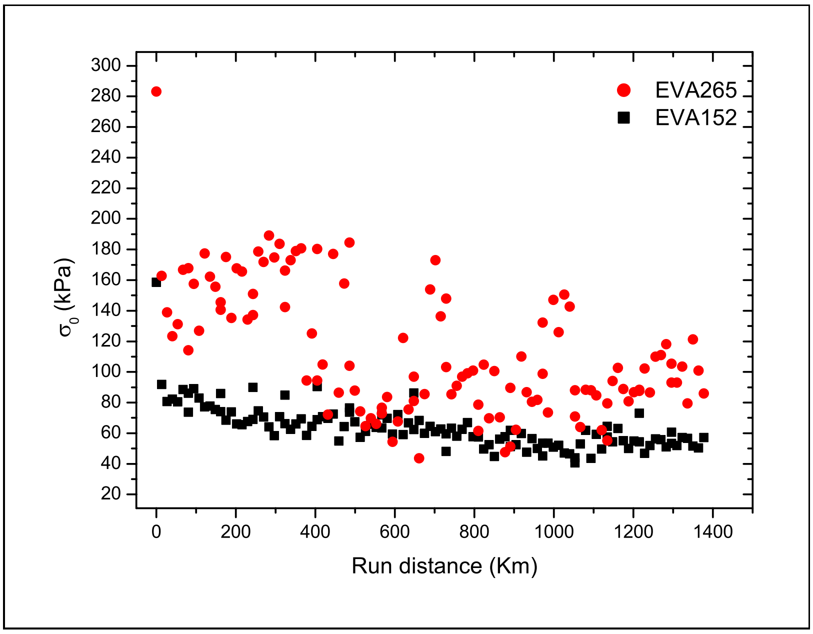

Figure 4.46: Initial gas pressure and initial yield stress as a function of run distance.

Foam	p_0 (kPa)
EVA108	85 ± 16
EVA146	146 ± 37
EVA151	178 ± 16
EVA152	207 ± 31
EVA265	390 ± 57

Table 4.18: Average and standard deviation of gas pressure over run distance.

4.2.5 Discussion

In this section, the mechanical properties of the foams have been studied under different compression tests.

DMTA was carried out in the linear region at low frequencies and low strain range. It showed typical thermoplastic behaviour, with a sharp transition from the glassy state to the rubbery state followed by a rubbery plateau and finally viscous flow. The stiffness of the samples increased with density, whereas the damping properties were not significantly affected by the density, because all samples had the same degree of crystallinity, i.e. they contain the same amount of amorphous material to which the damping properties are related.

Creep experiments showed the dependency of the compressive resistance on density and temperature. Denser foams are harder to deform that lighter foams, with the deformation increasing as the temperature is raised. The slow recovery process suggests that gas diffusion into the foam is the main factor controlling the rate of recovery.

Both sets of impact experiments, ASTM and repeat impact, showed a change of the mechanical properties with impact number and a distinctive modification of force-displacement shape. At high impact number, the behaviour seems to reach an “equilibrium” where curve shape, maximum force and displacement are practically the same. Foams structure softening is been related to the cause for such mechanical change. Initial impacts damage the structure and, due to the frequency of the impacts, the structure does not recover making foams easier to deform. However, ASTM experimental procedure did not exhibit homogeneous results, i.e. values did not follow any clear tendency. This could be due to the type of impact involved.

The repeat impact test method showed the significant recovery of the foam response after a daily ‘run’. This test has the following advantages compared with the ASTM method used to characterise midsole shock absorption:

- It applies a uniform stress to the foam, whereas the ASTM method, with a striker face area smaller than the foam upper surface, creates a non-uniform stress in the foam.
- It applies 300,000 impacts at 1.7 Hz, to simulate the typical life of a shoe, whereas the ASTM method only applies 30 impacts at a lower frequency.
- The impact duration is 100 ms, comparable with the heelstrike duration of 200 ms [Nigg (1986a)]. The slower ASTM loading time is 1 to 3 s, which change the response of the viscoelastic foam.
- Due to the uniaxial compression, it allows the results to be presented as the stress strain curve of the foam. This can be analysed in terms of microstructure parameters such as the cell gas pressure and the polymer initial yield stress.

The repeat impact experiments have showed a mechanical ageing as result of prior impacts. The changes observed in the foams are,

- an increase in the density over the experiment. The foam density increase is likely to be due to partly-viscoelastic changes in the polymer structure. Both density and height difference percentage decrease with increasing density,

- a decrease and an increase of the absorbed energy and peak force over run distance, and
- a steady increase of the peak pressure with run distance. However, the change appears to be smaller than what could be expected after a 1377 km run. A possible reason could be that the tests were performed at an ambient temperature with a small sample and good ventilation of its surfaces. In real shoes there can be significant temperature rises [Kinoshita and Bates (1996)] which will reduce the polymer contribution to the compressive stress.

The following work can be carried out in order to introduce improvements to the impact rig and extend the analysis of the effects of repeated impact in foams,

1. Introduce the signal from a second laser measuring the baseplate displacement or remove the antivibration feet and placing the equipment on an appropriate support which minimise vibration
2. Introduce the equipment in an environmental chamber to analyse temperature and humidity effects.
3. Analyse the change in the initial compressive collapse stress by creep or DMTA experiments.
4. Introduce a more realistic sample, e.g. a sample comprised of a layer of foam and a layer of rubber.

The gas pressure and initial yield stress showed the followed results,

- Gas pressure decreases with creep time suggesting a gas diffusion process during creep. However, repeat impact result showed that p_0 varied around a mean value over the run distance also ASTM result showed an increase of this value. Analysing this increase it was noted that its standard deviation was within the standard deviation reported in Table 4.18. Therefore, the impact experiments used show a similar response of the gas content with use. This difference between creep and impact response is associated with the strain rate of the experiments.

- Several factors of the gas pressure suggest that the polymer contribution to the stress is not constant with strain: values above the atmospheric pressure, values increasing with density and their dependency with temperature.
- Creep experiment showed a decrease of the collapse stress with temperature, as the temperature increases the crystallinity of the sample decreases and the foam becomes softer.
- The decrease of the yield stress with impact reveals a softening of the materials, which is related to a decrease of the cushioning properties of the samples. Therefore, foam fatigue is mainly produced as result of the softening of the material.

Finally, comparing the mechanical behaviour between the different foams, the absorbed energy values depend on density. The lighter the foam, the lower its shock absorption capabilities. However, EVA152 has a lower absorbed energy than both EVA146 and EVA151. Also, the mechanical ageing increase with decreasing density; EVA265 suffers the lowest change in its mechanical properties whereas EVA108 suffers the largest.

4.3 Conclusions

Foam samples have been characterised in terms of their cellular structure and composition. The cellular structure of the foams was anisotropic. Meanwhile, the foams were made of EVA copolymer with 19 % VA content and 22 % crystallinity also they showed presence of several inorganic fillers.

The increase of the gas pressure with density, values above the atmospheric pressure and the decrease of p_0 with temperature, indicate that this parameter is affected by the polymer matrix. Therefore, the polymer contribution to the stress is not constant with strain as suggested by Gibson and Ashby (1997).

Mechanical tests showed a change on the response of the midsole foams with use which leads to increases of the peak force and a reduction of the absorbed energy. Such effects will increase the force that is transmitted to the runner's body.
The softening of the material with run distance and the decrease in the cushioning properties are mainly due to a decrease in the initial compressive collapse stress, not to a change in the air content. Thus, the foam fatigue is due to the polymeric structure and not to the gas present in the foams.

The development of the repeat impact test rig for simulating the effects of long distance running has proved to have some advantages compared to the standard method used on running shoes. This test produced reproducible results with an impact duration comparable with the heelstrike duration.

Finally, the comparison of foams with similar density revealed a better performance of EVA146 and EVA151 than EVA152. This is related to differences in the cellular structure and composition of the samples.

Chapter 5

Gas Diffusion in Foams

Two major applications of closed cell foams are as thermal insulators and shock absorbers. However, ageing mechanics affect the thermal insulation properties of foams due to the outward diffusion of the low conductivity blowing agent and the inward diffusion of air constituents. Furthermore, it has been suggested by Mills and Gilchrist (1997a) and Mills and Rodríguez-Pérez (2001) that the diffusion process affects the creep behaviour of foams. Therefore, an analysis of the diffusion as a factor affecting the deterioration of foams under periodic impact loads was necessary.

The chapter is divided into two sections. In the first section, the empirical determination of diffusion coefficient is explained and in the second section, a theoretical approach to study the diffusing behaviour of the foams is developed. This second section analyses the findings from the model set out by Mills and Rodríguez-Pérez (2001) which studies the creep behaviour of foams taking into account the gas diffusion from the cells and an analysis considering a foam subjected to repeat impacts is suggested.

5.1 Empirical approach

5.1.1 Experimental procedure

The diffusion experiment was based on sorption techniques and consisted in measurements of the sample weight over time while the pressure and the temperature are controlled. This technique with similar equipment has been previously used with polymer films [Wang et al. (1994); Aubert (1998); von Solms et al. (submitted)], and with foams [Gunn et al. (1974)].

The experiments were carried out by a technician using Intelligent Gravimetric Analyser (IGA) (Hiden Analytical Ltd.) (Figure 5.1). This equipment is based on thermogravimetric analysis (TGA), which monitors the weight changes in a material as a function of temperature or time under a controlled atmosphere. The weighing mechanism of the IGA consists of a double-pan microbalance. A glass sample bulb with an aperture of 15 mm in diameter is suspended from one of the wire hangers inside a furnace. The pressure within the furnace tube is controlled by two stepper motors on the gas and vacuum lines. A microprocessor connected to a computer records the mass, temperature and pressure. The operating limits of the balance are temperatures ranging from liquid nitrogen ($-196\,^{\circ}$C) up to $1000\,^{\circ}$C [User Manual (2003)] and relative pressures between vacuum and 20 bars. The microbalance long term stability is $\pm 1\,\mu$g and its resolution is $\pm\,0.2\,\mu$g. For optimum measurements, the equipment needs a mass change $\geq$ 0.5 mg and a sample initial mass of 100 mg [Walton (2003)].

The experiment was carried out under vacuum conditions at $30\,^{\circ}$C and was monitored until the sample weight was stable (Figure 5.2). Immediately upon depressurisation, the mass apparently decreases. This is a buoyancy effect which is corrected using Archimedes' principle for the upthrust on an object. The buoyancy factor for

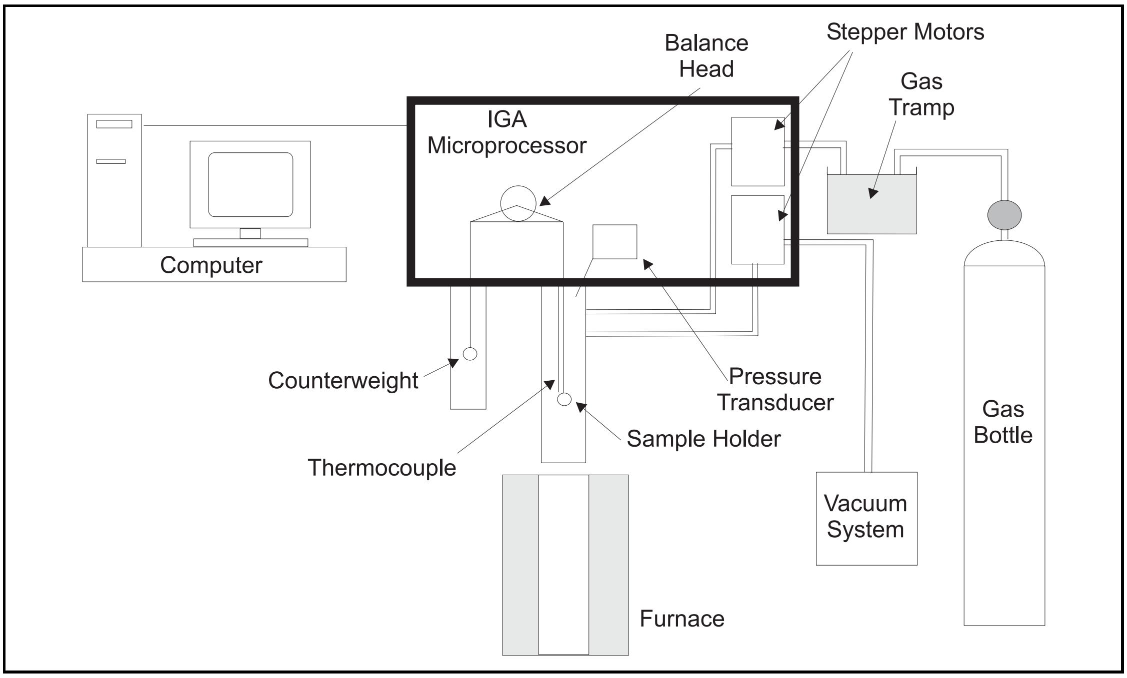

Figure 5.1: IGA microbalance diagram.

the IGA balance considers the presence of more than one object:

$$\Delta m^b = m_1 \frac{\rho_g}{\rho_1} + m_2 \frac{\rho_g}{\rho_2} - m_1' \frac{\rho_g'}{\rho_1'} \tag{5.1}$$

where m_1 and ρ_1 are the mass and density of the sample, m_2 and ρ_2 are the mass and density of the sample container, ρ_g is the gas density and m_1' and ρ_1' are the mass and density of the counterweight. The mass change is calculated by adding this correction (Δm^b) to the measured change.

The magnitude of mass change, the initial mass of the sample and the dimensions of the sample container limit the samples that are suitable for this experiment. Hence, some calculations were needed to identify those samples. Afterwards, the mass transfer equation was solved to estimate the length of the experiment.

Calculation to determine the suitable foams

The foam should have an initial mass of 100 mg and the change in its mass has to

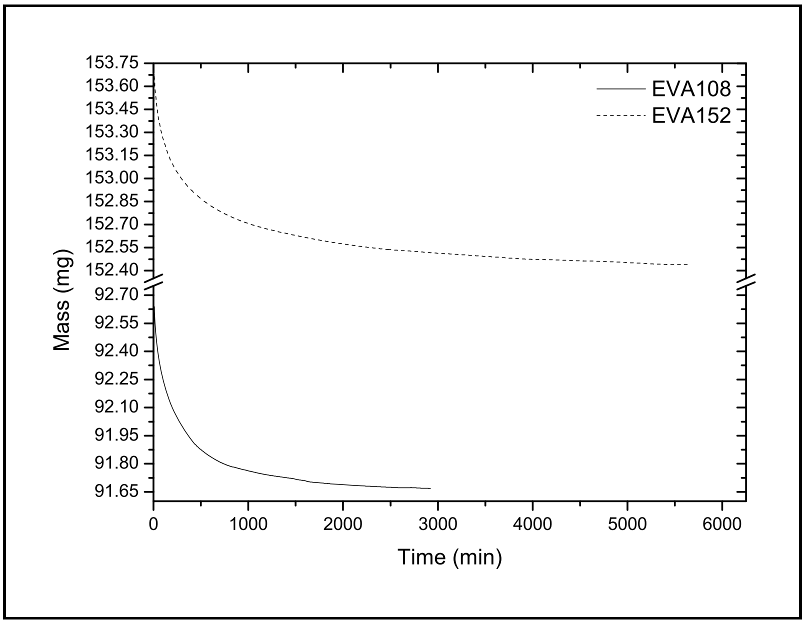

Figure 5.2: Weight measurements performed by IGA microbalance as a function of time.

be $\geq 500\,\mu$g, i.e. the amount of gas inside the foam has to be $> 500\,\mu$g. Also, the dimensions of the aperture of the glass bulb limit the sample dimensions to less than $15 \times 15 \times 15$ mm^3. An analysis of the density (ρ_f) and the fraction of total volume that is occupied by the gas (Φ_{gas}) (Table 4.9) will help establish the suitable foams for the experiment.

The initial gas and solid volume are calculated by multiplying the volume of a sample of 100 mg in weight by the fraction of gas and solid present in it (Table 5.1). Afterwards, the initial mass of gas and solid in the samples is obtained by multiplying their volume by the air and polymer density, respectively. Finally, the size of a cubic sample is calculated from the volume of foam. The analysis of these values (Table 5.1) revealed that the foams which can be used for this experiment are EVA108 and EVA150 because the amount of gas inside a 100 mg sample is larger than $500\,\mu g$ and their dimensions are within the sample limits.

Foam	Volume of 0.1 g (cm^3)	Volume of gas (cm^3)	Mass of gas (μg)	Mass of solid (μg)	Length cube side (mm)
EVA108	0.93	0.82	1049.0	98951.0	9.7
EVA146	0.68	0.58	740.5	99259.5	8.8
EVA151	0.66	0.56	711.5	99288.5	8.7
EVA152	0.66	0.55	705.9	99294.1	8.7
EVA265	0.38	0.27	346.8	99653.2	7.2

Table 5.1: Parameters used to establish the foams valid for the diffusion experiment.

Calculation to determine the change of mass

The mass change is predicted by solving the mass transfer equation and therefore an initial length of the experiment is obtained.

The mass transfer equation for diffusion is derived from the differential equation, determined by the principle of mass conservation [Luikov (1968); Incropera and DeWitt (1996)],

$$\frac{\partial \rho}{\partial t} = D\nabla^2 \rho \tag{5.2}$$

The solution of the partial differential equation for a parallelepiped with first kind boundary conditions ($\rho(s, \tau) = f(t)$, where $\rho(s, \tau)$ is the density at the point s of the body) is,

$$\theta = \frac{M(t) - M_0}{M_\infty - M_0} = \sum_{n=1}^{\infty} B_n exp\left(-\mu_n^2 Fo\right) \tag{5.3}$$

where

- $M(t)$ is the time-dependent mass, M_0 is the initial mass, M_∞ is the mass after an infinite time, B_n and μ_n are constants of the Fourier series given by,

$$B_n = \frac{2}{\mu_n^2} = \frac{8}{\pi^2(2n-1)^2} \tag{5.4}$$

Foam	Weight(g)	Dimension (mm^3)
EVA108	0.096	$10.08 \times 9.67 \times 9.10$
EVA152	0.146	$10.08 \times 10.05 \times 9.5$

Table 5.2: Samples weight and size dimensions used for the diffusion experiments.

- Fo is the Fourier number which is given by,

$$Fo = \frac{Dt}{L^2} \tag{5.5}$$

D is the diffusion coefficient and L is the length of the cube divided by $2\sqrt{3}$.

The series was summed from $n = 1$ to 10, assuming that after an infinity time all the gas escapes from the sample, i.e. M_∞ is the mass of the solid. Two sets of solution were calculated, one assuming the diffusion coefficient was $D_1 = 40 \times 10^{12}$ m^2/s [Marais et al. (2002)] and the other assuming the diffusion coefficient was $D_2 = 100 \times 10^{12}$ m^2/s [Mills and Rodríguez-Pérez (2001)]. The results show the change of mass (M(t)) as a function of time (Figure 5.3) over a 48 h experiment. The mass reaches an equilibrium point where the sample weight is almost constant with time. This equilibrium depends on the sample density and the diffusion coefficient. The equilibrium point of both EVA108 and EVA152 has not been reached for D_1 after 48 h, whereas for D_2, it has been achieved at 120×10^3 s ($\approx$ 33 h) for both EVA108 and EVA152.

Due to the heavy use of the equipment, only two experiments could be carried out. The foams selected for these experiments were EVA108 and EVA152.

5.1.2 Experimental results

The samples were cut, weighted using Oertling balance and measured using Mitotuyo calliper (Table 5.2). The values for the buoyancy correction (equation 5.1) are m_2

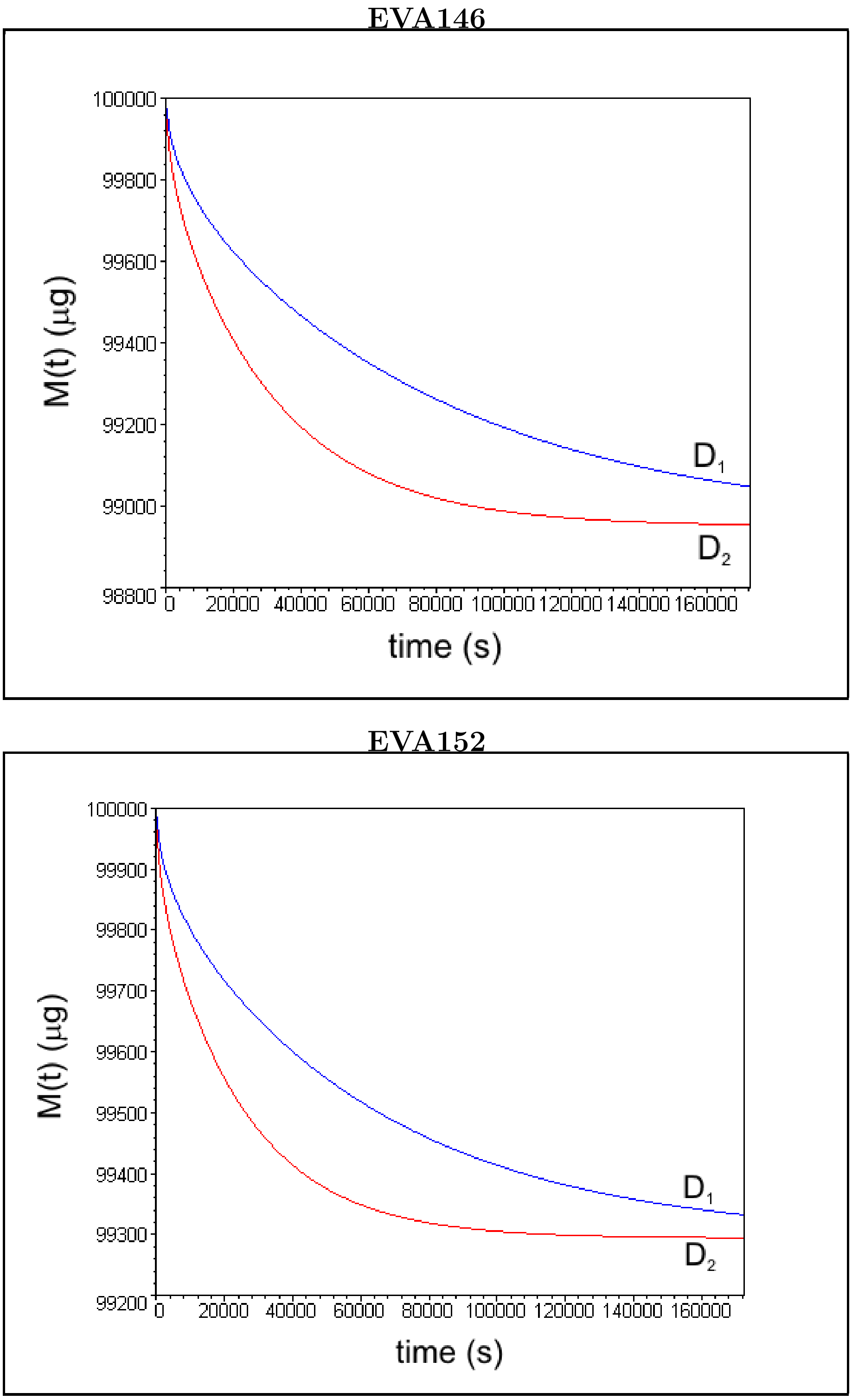

EVA146

EVA152

Figure 5.3: Evolution of the mass obtained from solving the mass transfer equation. Where $D_1 = 40 \times 10^{12}$ m^2/s and $D_2 = 100 \times 10^{12}$ m^2/s.

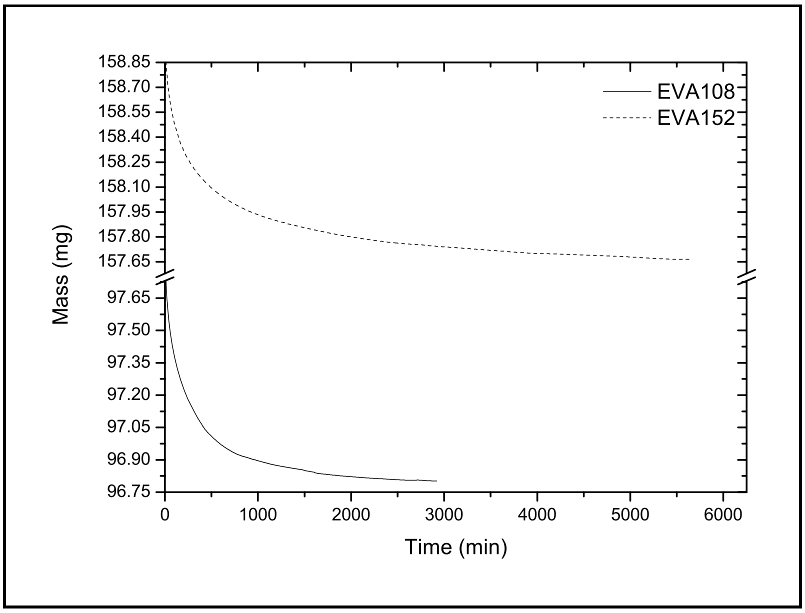

Figure 5.4: Results obtained from IGA microbalance as weight vs. time. Traces are corrected for buoyancy.

$= 0.5667$ g, $\rho_2 = 3$ g/cm^3, $m'_1 = 0.9422$ g, $\rho'_1 = 7.9$ g/cm^3 and $\rho_g = 0.00129$ g/cm^3, assuming the gas inside the chamber is air. Therefore, the buoyancy factor is

$$\Delta m^b_{EVA108} = 5.13 \text{ mg}$$
$$\Delta m^b_{EVA152} = 5.23 \text{ mg}$$

The change in mass was plotted as a function of time (Figure 5.4), where the traces have been corrected with the buoyancy factor. The equilibrium is attained at 140×10^3 s (≈ 40 h) for EVA108 and at 325×10^3 s (≈ 90 h) for EVA152. This result suggests that the diffusion coefficient of EVA108 is larger than that of EVA152.

The diffusion coefficient is obtained by fitting the experimental curve to a first order exponential decay curve (Figure 5.5).

$$y = y_0 + \alpha\, exp\,(-x/\beta) \tag{5.6}$$

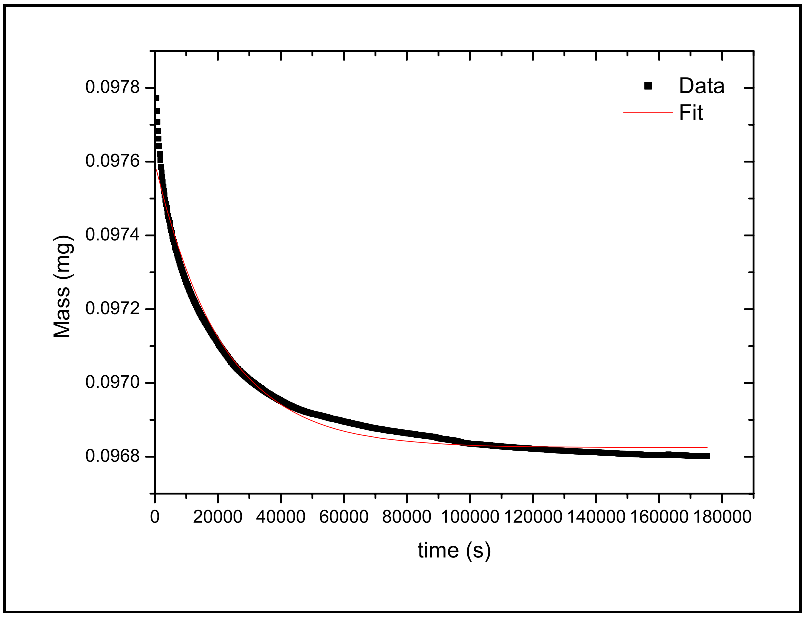

Figure 5.5: Experiment values fitted to a first order exponential decay for EVA108.

The theoretical mass variation (equation 5.3) for $n = 1$ is,

$$M(t) = M_0 + (M_\infty - M_0)\, exp\, (-\,\gamma\, D\, t) \tag{5.7}$$

with $\gamma = 8/(\pi^2 L^2)$. The experimental values of the initial (M_0) and final (M_∞) mass were introduced into equation 5.7 and the samples were assumed to be a cube of length L equal to the average of the sample dimensions.

The diffusion coefficient is calculated by identifying the two previous equations (5.6 and 5.7): $M_0 = y_0$, $M_\infty - M_0 = \alpha$ and $\gamma D = 1/\beta$. The results from both fitting operations are presented in Table 5.3.

The diffusion coefficients are $D_{EVA108} = 147 \times 10^{-12}$ m^2/s and $D_{EVA152} = 70 \times 10^{-12}$ m^2/s; hence, $D_{EVA108} \approx 2 D_{EVA152}$, i.e. diffusion process in EVA108 is twice as fast as in EVA152.

EVA108	Equation 5.6 y	Equation 5.7 M(t)	**EVA152**	Equation 5.6 y	Equation 5.7 M(t)
y_0 (g)	96.8×10^{-3}	96.8×10^{-3}	y_0 (g)	157.7×10^{-3}	157.7×10^{-3}
α (g)	7.7×10^{-4}	7.9×10^{-4}	α (g)	8.5×10^{-4}	9.9×10^{-4}
$1/\beta$	47.2×10^{-6}	$319941.7\,D$	$1/\beta$	21.3×10^{-6}	$303569.9\,D$
R^2	0.98		R^2	0.97	

Table 5.3: Parameters obtained from fitting the experimental results to an exponential decay and to equation 5.3. Where D is the diffusion coefficient.

5.2 Theoretical approach

5.2.1 Mills and Rodríguez-Pérez (2001) Model

The qualitative aspects of the model were briefly described in the literature review, see section 2.3.2. Therefore in this section, the assumptions and the computational sequence are described.

The gas diffusion across a cell face is considered to reach steady state within negligible time and, occurs in one direction. The foam is considered as a set of a unit cubic cells where the applied stress is constant throughout the foam, but the strain varies from cell to cell (Figure 5.6). The applied stress is considered to be shared between the polymer structure and the cell gas. The polymeric contribution is assumed to be constant in the compressive strain range 0.1 to 0.7 (Figure 5.7). The modelling factors are considered in sequence within a small time interval, and the interactions develop with the increase of time. Initially all the cells have a gas pressure equal to atmospheric pressure $p_{at} = 100$ kPa. The sequence of 6 steps is (the order is arbitrary):

- The absolute pressure p_{abs} applied is related to the creep time by

$$p_{abs} = \sigma + p_{at} - \sigma_{Y(t)} \tag{5.8}$$

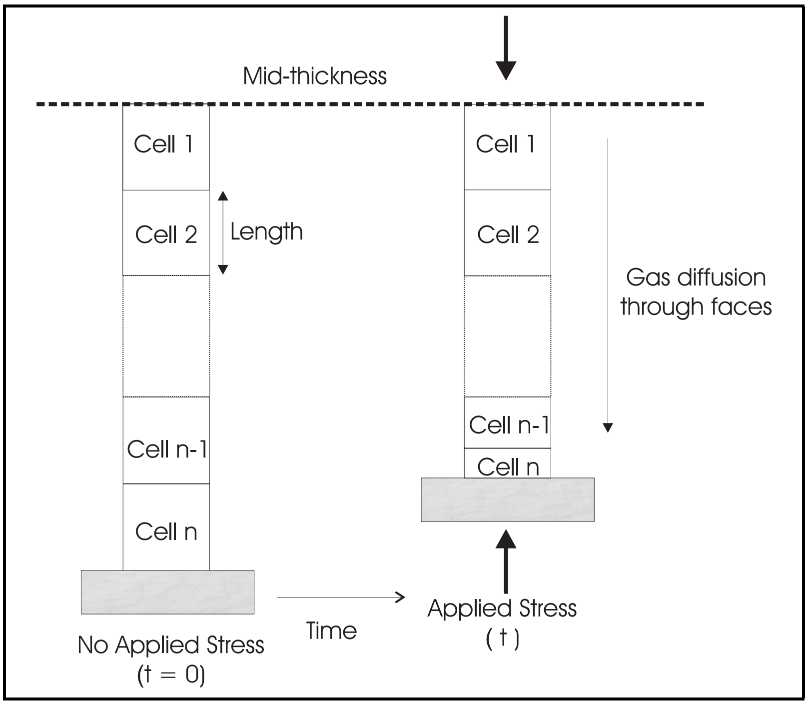

Figure 5.6: Diagram of the gas diffusion across cell faces, parallel to the applied stress axis.

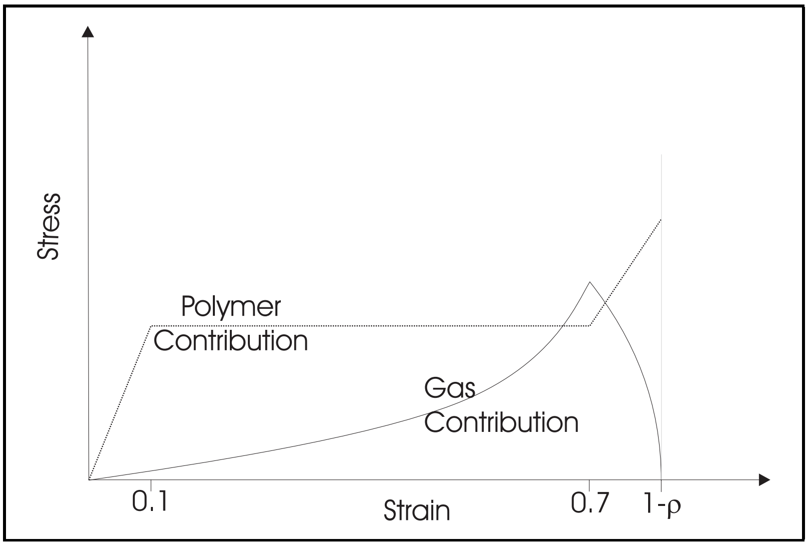

Figure 5.7: Assumed contributions to the creep stress from the polymeric structure and cell gas as a function of compressive strain.

where σ is the creep stress and $\sigma_{Y(t)}$ is the compressive yield stress of the polymeric structure of the foam given by

$$\sigma_{Y(t)} = \frac{\epsilon_Y}{C(1)} t^{-k} \tag{5.9}$$

where ϵ_Y is the constant yield strain of the foam (taken 0.1), k is a constant, and $C(1)$ is the creep compliance foam at 1 sec.

- The strain ϵ_i in each cell is given by,

  $$\epsilon_i = (1 - \rho_r)\left(1 - \frac{p_i}{p_{abs}}\right) \tag{5.10}$$

  where ρ_r is the relative density, p_i is the gas pressure inside the cell i.

- The explicit finite-difference equation used to calculate the new pressure in each cell after a time interval Δt, is

  $$p_i' = (1 - 2d)\, p_i + d\,(p_{i-1} + p_{i+1}) \tag{5.11}$$

  where p' is the new gas pressure inside the cell i and d is a constant given by

  $$d = \frac{P p_a \Delta t}{\delta L} \tag{5.12}$$

  where P is the polymer permeability, δ is the cell face thickness, and L is the diameter of the cells.

- The gas content of each cell p_i from the previous value is multiplied by p_i'/p_i.

- Once the foam strain exceeds a limit (taken as 0.7), the effect of cell face contact is considered. A face-touching factor F_t is used to multiply the absolute pressure of Equation 5.8, $p_i = F_t\, p_{abs}$. This factor is assumed to have a value 1 at strain 0.7 and 0 at strain (1-ρ_r), with a linear decrease in the interval.

- The foam is treated as a continuum, following Ostrogorsky et al. (1986), with a diffusion coefficient D_f and divided into layers of thickness Δx = L. The foam diffusion coefficient is related with the gas diffusion constant by

  $$D_f = d\frac{\Delta x^2}{\Delta t} = P p_a \frac{L}{\delta} \tag{5.13}$$

the hand right expression is obtained by substituting Δx = L and equation 5.12. Considering, for a cubic cell foam, the relationship L$/\delta = 3/f_s\rho_r$, where f_s is the fraction of polymer in the cell faces, and substituting it in equation 5.13

$$D_f = \frac{6Pp_a}{f_s\rho_r} \tag{5.14}$$

This equation is multiplied by 2 to consider the random orientation of cell faces. This equation connects the diffusivity to the relative density of the undeformed foam. The gas flow is impeded by the permeation through the cell faces, which do not change in thickness during compression as the faces wrinkle.

The parameters used to fit the experimental data for EVA150 are

Parameter	Value
Yield Stress	50 kPa
Yield Strain	0.10
Block half width	6 mm
Relative Density	0.16
1 s Compliance J(1)	600×10^9 Pa
Compliance Slope	0.06
Diffusivity	70×10^{-12} m^2/s

where the yield stress and strain are the average value of the experimental values of the initial yield stress (σ_0) and strain at 1 s at 35 °C of EVA150 group. The compliance at 1 s and the compliance slope were assumed to be those reported by Mills and Rodríguez-Pérez (2001).

The model predicts the average creep behaviour of the EVA150 foams, because the parameters used are the average values of the creep experimental response of EVA146, EVA151 and EVA152. A comparison of the creep response obtained by the model and that of the experiments is made. The predictions shows a reasonable fit with the experiments, with the best fit corresponding to EVA146 (Figure 5.8). The model predicts a change in the cell gas content which decreases from 100 kPa to about 20 kPa in the surface cells. Such reduction of the gas content leads to an increase in the strain suffered by the cells. As time passes, the changes in pressure and strain evolve reaching cells close to the mid-thickness (Figure 5.9).

The results obtained are similar to those predicted by Mills and Rodríguez-Pérez (2001) in their paper with a slight better fit of the creep response at stress range from 100 to 200 kPa. They concluded that the gas diffusion affecting the hardening of the foam after a creep period would affect in the same way a foam subjected to repeat impact.

5.2.2 Repeat impact diffusion model

One of the goals of this research was the analysis of the effects of gas diffusion in a foam subjected to periodic loads, in particular to midsole foams. Therefore, a mathematical model was needed in order to predict the foam behaviour under repeated compressions. The model would have to consider the changes in the foam response due to both the type of applied stress (compressive impacts separated by a recovery period) and the diffusion process. The applied stress could be considered as a sawtooth shape where the even teeth are missing (Figure 5.10).
However, prior to the development of this repeat impact model and because the gas pressure inside the cells remained almost constant as a function of run distance (see Table 4.18) the following initial analysis was carried out.

Effect of repeat impact on the gas pressure inside the cell

This initial analysis considers the gas diffusion process of a cubic cell subject to a cyclic load and it has the following assumptions:

1. The cubic cell has a closed cell structure with no face holes in it and has a

EVA146

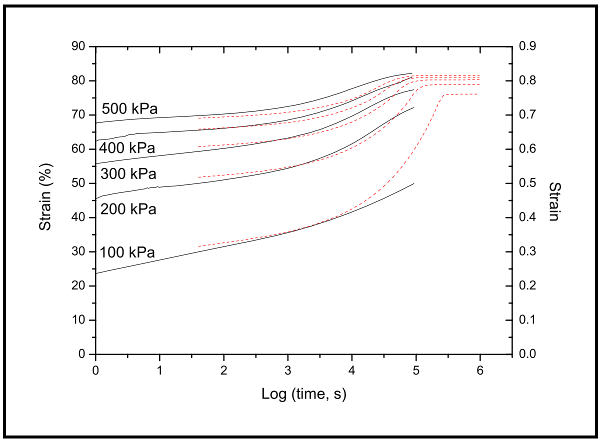

EVA151

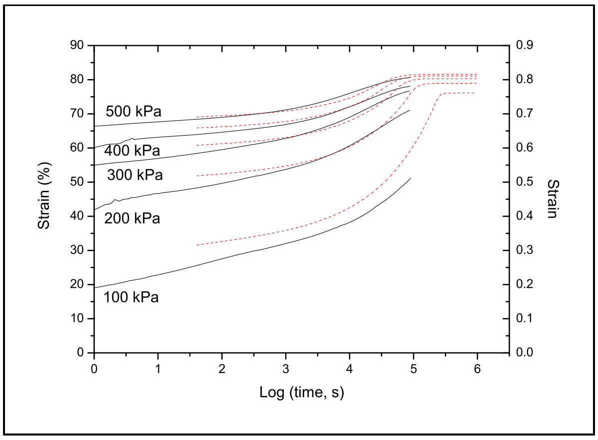

EVA152

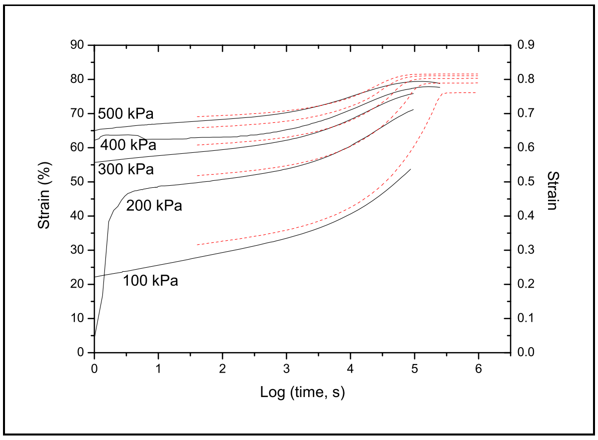

Figure 5.8: Comparison of the creep behaviour predicted by Mills & Rodríguez-Pérez model (red lines) and that of the experiments (black lines).

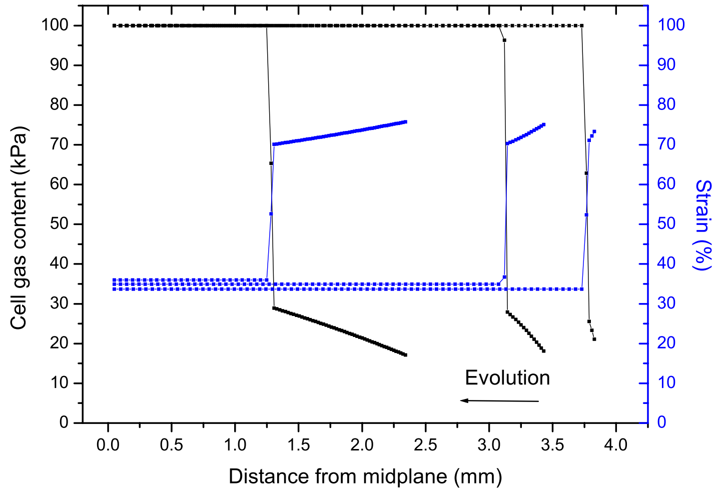

Figure 5.9: Cell gas content and layer strain predicted from Mills & Rodríguez-Pérez model.

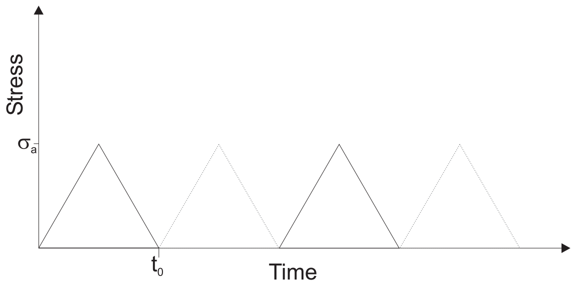

Figure 5.10: Shape of the stress applied in the repeated impact experiments. The applied stress has a sawtooth shape where the even teeth are missing.

side length of L = $50\,\mu$m.

2. The gas inside the cell behaves as an ideal gas.
3. Mass diffusion only occurs in one direction.
4. The initial pressure inside the cell is equal to the atmospheric pressure ($p_a =$ 100 kPa).
5. Henry's law is applicable,

$$c = Sp \tag{5.15}$$

   where c is the gas concentration in the polymer material, S is the solubility of the gas in the polymer and p is the pressure in the cell.

6. The diffusion process is defined by Fick's first law (equation 2.9),

$$\frac{\partial c}{\partial t} = D_{pol} \nabla c \tag{5.16}$$

7. The strain suffered by the cell due to the applied stress can be described as a viscoelastic behaviour where the cell recovers instantaneously on removing the applied stress but it does not completely recover its original volume after the impact (Figure 5.11), $V_1 > V_2$, $V_3 > V_2$ and $V_1 > V_3$.
8. The change in the volume is due to the change in the cell height,

$$\Delta V = A \Delta h \equiv V(t) = Ah(t) \tag{5.17}$$

9. The change in height of the cell is assumed to follow the same trend as the change in the foam height. Therefore, the height change of the cell over a 3 hour experiment is equal to the height change of the foam in the same period, i.e. as the foam height at 3 h is 6.4 % smaller than at 0 h ⇒ the cell height change in 3 h is assumed to be the same.
10. The foam deformation in each impact is ≈ 60 % ⇒ the cell deformation in each impact is ≈ 60 %.

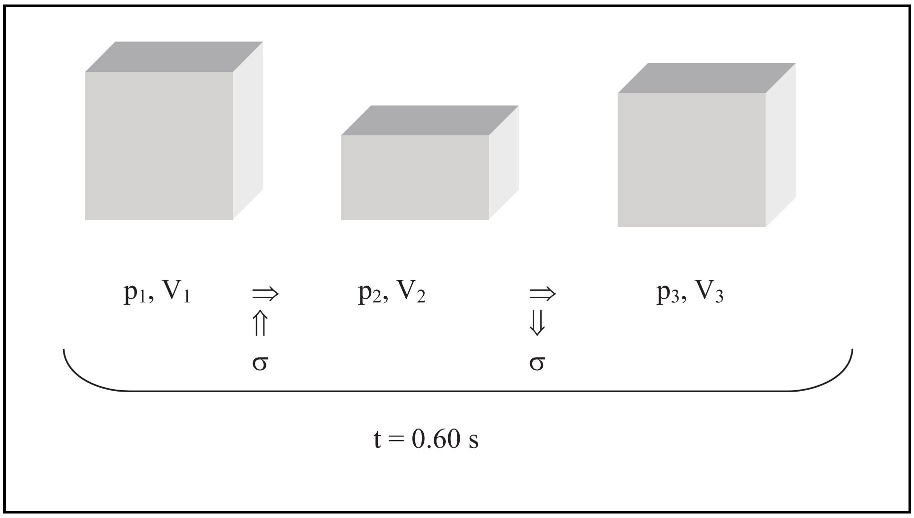

Figure 5.11: Cubic cell behaviour under compressive impacts.

The stationary mass flux (J) in the polymer through a membrane of thickness δ and area A with a pressure difference Δp across it is obtained by combining equations 5.15 and 5.16:

$$J = -D_{pol} S\, A \frac{\Delta p}{\delta} \tag{5.18}$$

Due to assumption number 2, the pressure and the volume during an isothermal compression [Burgess (1988); Mills and Gilchrist (1997b)] is

$$p_1 V_1 = p_2 V_2 = p_3 V_3 \tag{5.19}$$

as the initial pressure is equal to the atmospheric pressure (p_{at}) and the change in volume is given by equation 5.17 then

$$p_1 V_1 = p_{at} A h_0 \tag{5.20}$$

$$p_2 V_2 = p_3 V_3 = p(t) A h(t) \tag{5.21}$$

where h(t) represents the change in the height of the cell with time. Substituting these equations into 5.18

$$J = -D_{pol} S\, A \frac{p(t) - p_{at}}{\delta} = -\frac{D_{pol} S\, A}{\delta} \left(\frac{h_0 - h(t)}{h(t)} \right) \tag{5.22}$$

Coefficient	Value
a	1×10^{-6}
b	10.47
c	40×10^{-6}
d	1
f	6.8×10^{-6}

Table 5.4: Empirically determined values of h(t).

The function governing h(t) is assumed to be given by coupled functions, one considering the periodic stress, and hence strain, suffered by the cell and the other one considering the decrease of the height with time. In first approximation, the periodic load is assumed to follow a cosine shape and the height decrease is assumed to be linear (Figure 5.12). Thus,

$$h(t) = (a\,cos\,(bt) + c)\,(d - f\,t) \tag{5.23}$$

where a, b, c, d, f are empirically determined; firstly, the cosine function was fitted by considering a period of 0.6 s and the maximum and minimum values equal to $50\,\mu$m and $30\,\mu$m. Secondly, the linear decrease was fitted so that the h(t) curve passes through $46.8\,\mu$m (6.4% decrease) at t=10800 s. The obtained values are given in Table 5.4.

Substituting h(t) in equation 5.22 and integrating between 0 and 0.60 s, the amount of mass change for the 1st cycle is obtained where the integration was performed using the trapezoidal law dividing the total interval into 30 smaller intervals (Figure 5.13). The values of the gas diffusivity and solubility and the cell parameters are $D_{pol} = 70 \times 10^{-12}$ m^2/s, $S = 19 \times 10^{-10}$ kg/kg Pa [Briscoe and Savvas (1998)], $A = 250\,\mu\text{m}^2$, and $\delta = 0.2\,\mu$m, giving a value of 3×10^{-18} g mass loss for the 1st cycle. The total change of mass over the 3 h experiment is obtained by integrating between 0 and 10800, giving a value of 6×10^{-14} g mass loss. The mass of a $50\,\mu$m side cube filled with air is 1.61×10^{-10} g, which means that the amount of gas loss

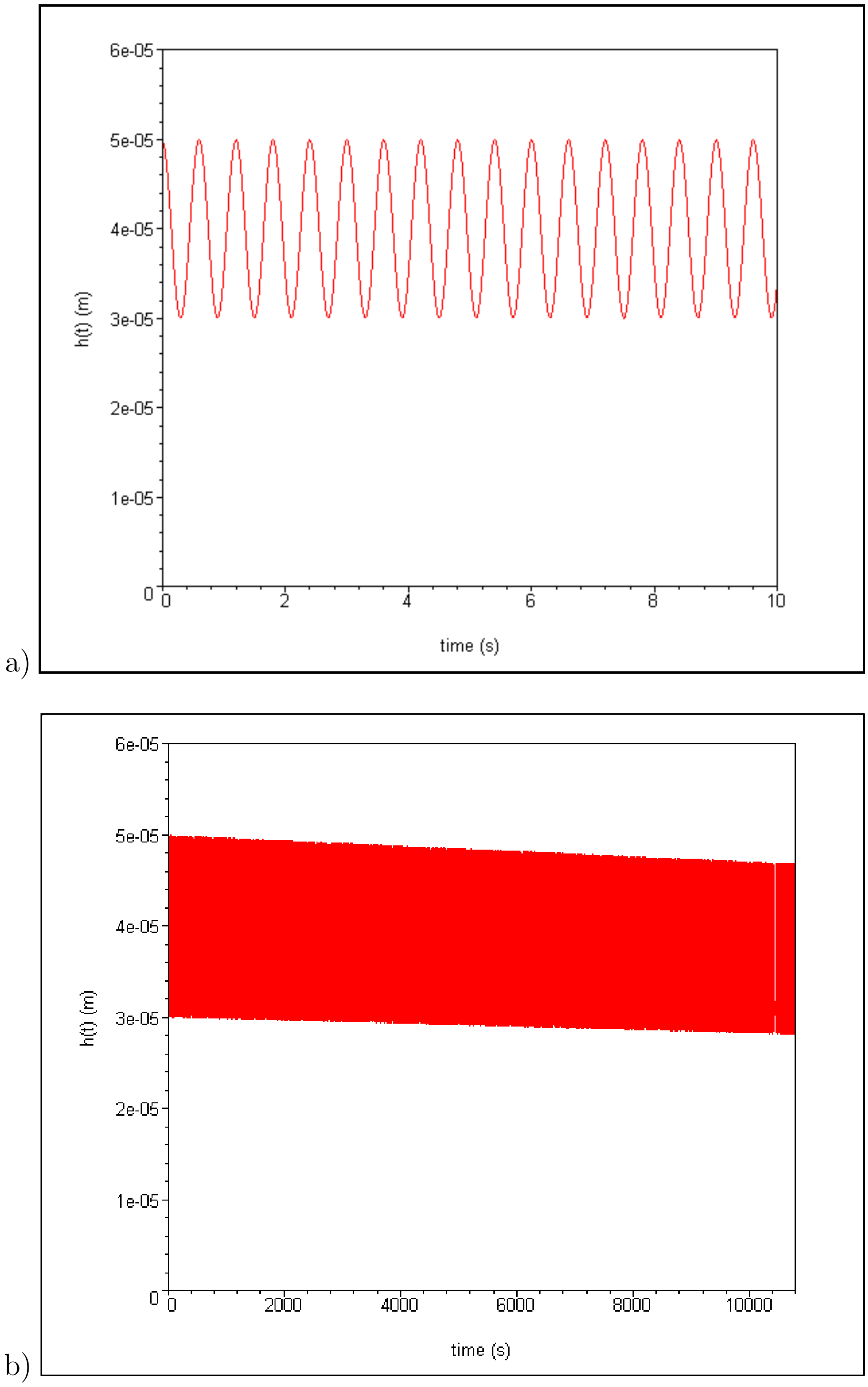

Figure 5.12: Graphic representation of h(t) as the product of a sinusoidal function and a linear decrease. The function is plotted both in a short a) and in a large b) time scale, in order to show the periodic and the decrease behaviour of the function.

over the 3 hours is 0.037%.

Assuming the foam consists of m cubic cells where all the cells suffer the same strain, so that the cells would lose the same amount of gas per impact. Although, creep experiments showed that the cells of the mid-thickness do not deform the same amount as the cells close to the surface (see Figure 2.13); this is the worse case scenario to calculate the total mass change in a foam. Thus, the mass loss of a foam with a volume of 4.8×10^{-6} m^3, which is the volume of the foam sample used in the repeat impact experiments, is in the order of 2×10^{-6} g, i.e. the mass loss is negligible.

Finally, assuming the same amount of gas loss each day, the overall change is 34×10^{-6} g which is a 5% of an initial mass of 720×10^{-6} g (Table 5.1).

Also, h(t) can be considered as a damped oscillator, due to the viscous behaviour of polymers. Repeating the process for the equation

$$h(t) \,=\, (a\, cos\,(b\,t) \,+\, c)\, exp\,(\,-\,f\,t) \tag{5.24}$$

where a, b and c have the same value as before and $f = 6.1 \times 10^{-6}$. Both the mass loss of the 1$^{\rm st}$ cycle and the total mass change are almost the same as the previous equation.

From this study, the mass loss in a cell with a change in volume of 6.4% is negligible. Taking into account that the perfect gas law in an isothermal process can be express as,

$$pV = \frac{m}{\nu} R\, T \tag{5.25}$$

where ν is the molar mass, then the change in pressure has to be also negligible.

Therefore, the deterioration of the foam can mainly be considered to be due to the plastic deformation of the polymer structure while the gas diffusion would be

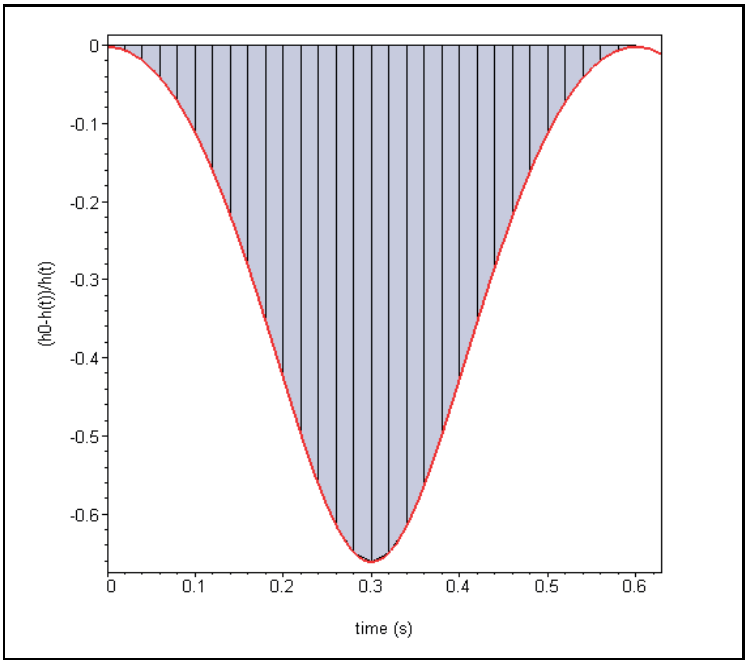

Figure 5.13: Graphic representation of one period of $(h_0 - h(t))/h(t)$ divided into 30 small intervals.

negligible. Models to describe the foam response to periodic compressions without considering the gas diffusion can be obtained from studies of polymer behaviour under cyclic stress [Nielsen (1962); Williams (1980)]. Williams (1980) analysed the strain response of polymers to a stress with a sawtooth shape obtaining,

$$\epsilon(t) = \frac{\sigma_a t^n}{(1+n)C_0}\left[\frac{t}{t_r} - \frac{t}{t_r}\left(1 - 2\frac{t_r}{t}\right)^{1+n} - \frac{2t}{t_r}\left(1 - \frac{t_r}{t}\right)^{1+n}\right] \tag{5.26}$$

where $t_r = \frac{1}{2}t_0$ and t_0 is the time of an impact (Figure 5.10), σ_a is the applied stress and the compliance of the polymer C is assumed to follow a power law $C = C_0\, t^n$.

5.3 Discussion

The diffusion coefficient of two EVA foams was obtained from the variation of the foam mass with time as the gas escapes. Due to limited equipment accessibility, there is a lack of information with regard to the experimental errors and reproducibility of the experiment. An obvious source of error is the control of the pressure, as fluctuations of the pressure will introduce errors into the measurements and into the upthrust suffered by the sample. Also, the buoyancy factor calculated for this experiment may not be completely accurate because the gas inside the chamber during the experiment is assumed to be air. To reduce these two possible sources of error, the experiment would have to be carried out in a controlled gas atmosphere, e.g. nitrogen. The equipment characteristics allow the introduction of a gas into the sample chamber from a gas bottle, hence a better control of the pressure by regulating the rate at which it is introduced.

Also, the method used to calculate the diffusion coefficients has a main uncertainty due to the dimensions of the samples and its shape, as it was assumed to be a cube of length the average value of the dimensions of a parallelepiped. This uncertainty may be reduced by using a foam where the cutting procedure does not produce large variations to the dimensions of the sample.

The experiments carried out can be considered as an initial approach to the diffusion characterisation. A critical analysis of the experiments would recommend the following work in this area:

1. The experiment will required a minimum of three samples for each foam in order to evaluate the reproducibility of the values and hence obtain the average value of the diffusion coefficient and percentage of error in this measure.

2. In order to properly analyse the effects of the density on the diffusion process of foams, the experiment should be carried out with all the EVA foams.

3. The effects of the composition will be analysed by comparing the results from all three EVA150 foams.

4. Due to the temperature changes to which the midsole foam is subjected, an analysis of the dependency of the diffusion coefficient with temperature should be carried out.

5. An analyse of any possible changes of the diffusion coefficient due to repeat impact should be carried out, by repeating the experiments with samples which have been subjected to repeated impacts.

Most diffusion theories [Ostrogorsky et al. (1986); Bart and du Cauzé de Nazelle (1993); Mills and Gilchrist (1997a)] predicts the diffusion coefficient to be inversely proportional to the relative density and independent of the cell size,

$$D_{foam} \propto \frac{1}{\rho_r} \tag{5.27}$$

because the diffusivity is a material property. From the experiment, the measured diffusion coefficient does vary with the density, D_{EVA108} being larger than D_{EVA152}. However, from the analysis of the following values,

Foam	D (m^2/s)	ρ_f (kg/m^3)	ϕ (μm)	K (ρ_f/ϕ)
EVA108	147×10^{-12}	108	120	0.9
EVA152	70×10^{-12}	152	75	2.03

the ratio D_{EVA108}/D_{EVA152} is equal to 2.1, which is very similar to K_{EVA152}/K_{EVA108} = 2.25. This result cannot be considered accurate because it has only two points, i.e. it could be a coincidence. However, if true it disagrees with the theories available at the moment as it relates the diffusion coefficient to the cell size. A detail study of the diffusion coefficient on foams with the same composition but different cell size would provide a better picture of the problem.

The model studied the creep behaviour where the diffusion process was taken into consideration as a mechanism for the changes in the foam compressive response. The prediction of the creep behaviour from the model set out by Mills and Rodríguez-Pérez is reasonably good with the parameters used. It predicts that under compression the cell gas content decreases, increasing the strain suffered by the cells. Based on this result, the authors suggest the same effect on foams under repeat compressions. However, no theoretical or experimental reasons are given apart from the one mentioned.

Prior to the development of a model where the gas diffusion is considered as a factor to the compressive response of foams, an analysis of the effects of repeat impact on the diffusion process was considered. Even though this analysis has the following simplifications

- the gas is treated as an ideal gas
- the gas diffusion is unidirectional
- Fick's and Henry's laws are applicable
- the change in volume is only due to the change in height and
- the applied stress follows a cosine function and the decrease in height is linear

it suggests a negligible gas loss due to diffusion; which is also in agreement with the experimental results where the gas pressure inside the cells remained almost constant irrespective of run distance.

5.4 Conclusions

The microbalance experiment has proved to be a straightforward technique which can be used with foams to characterise the diffusion process in them. Further work can be perform in this area in order to improve the accuracy and results obtained. From such research, a methodology to identify foam factors affecting the diffusion process in foams, and hence their ageing behaviour, may be achieved.

Although, the gas diffusion affects the creep behaviour of foams it seems as if it does not affect the compressive response under repeat impact in the same way. However, to be certain, a vacuum microbalance experiment is required to measure the air content after the simulated 1377 km of running. The different strain rate to which the foam is subjected is the reason for such difference. The slow strain rate of the creep experiments, compare to the high strain rate of the impact experiments, would allow the molecules of the gas to diffuse.

Chapter 6

Midsole Durability

6.1 Introduction

Running involves a series of heel-strikes on the ground. The midsole foams of running shoes, by absorbing energy, limit the peak impact force in the heel-strike. Soft cushioning systems increase the duration of footstrike impacts and spread the load across a larger area of the plantar surface [Shorten (2000)]. Pressure distributions have been measured across foot plantar surface for running using different shoe types [Hennig and Milani (1995); Chen et al. (1996); Shiang (1997); Hennig and Milani (2000)]; however, there is no information on how the pressure distribution changes with extended shoe use.

Most running shoe midsoles are made from the foamed copolymer of ethylene and vinyl acetate (EVA), of density in the range 150 to 250 kg m^{-3}. Footstrikes, repeated at approximately 1.5 Hz, may cause fatigue damage to the foam, hence may lead to the foam bottoming out, causing injuries. Prior research has used laboratory fatigue tests. Repeated, uniaxial rapid-compression tests on EVA foam, in which the stress did not vary with position in the foam [Misevich and Cavanagh (1984)] showed that the midsole force-deflection response changes with cycle number. They claimed there was an initially positive internal gas pressure in the foam cells, which declined during repeated loading. A prosthetic foot had been used to load the heel of the shoe [Cook et al. (1985)], tilted back by 15 °, from 0 to 1.5 kN at 2.5 Hz; this applies severe loads to the rear part of the heel. They only plotted the energy absorbed per cycle, and say that, after a number of cycles equivalent to 804.5 km (500 miles) of running, shoes maintained 55 ± 10 % of their initial energy absorption. They also tested shoes after 804.5 km of running by volunteers and say that 70 % of the initial energy absorption remained. As no details of the EVA densities were given, and foam types have changed in the last 17 years, it is unclear if the results still apply. The cell geometry in sectioned EVA midsoles, [Bartlett (1999)] showed that cells next to the outsole became flattened after 3200 km of running. Studies on diffusion in EVA foam [Mills and Rodríguez-Pérez (2001)] suggested that there is a reduction of the air content of the foam cells, reducing the cushioning.

The aim of this study is to assess the changes on running shoe midsoles. In-shoe pressure distribution and materials characterisation were used on the analysis. The materials characterisation of the running shoe has been carried out using DSC, SEM, ATR and ASTM F1416, standard method for shock attenuation. The results, when possible, will be compared with those already reported in Chapter 4.

6.2 Charaterisation Methods

6.2.1 Plantar pressure distribution

Three healthy male long distance runners (Table 6.1) ran at 2.69 ± 0.02 m/s for 10 min on a Quinton Instrument Co. 640 treadmill; this short experiment avoided fatigue, hence possible changes in foot loading [Edington et al. (1990)]. They were all rearfoot strikers, did not use orthotics, and reported no lower extremity injury for the past year. The University ethical committee approved the study and informed consent was obtained from the runners. They wore Reebok trainers that were new

	Age	Run distance (km)	Weight (kg)	Shoe size UK/EU	Av. Stride frequency (Hz)
Runner 1	49	500	62.9 ± 2.3	8/42	1.42
Runner 2	37	700	82.1 ± 1.4	9/43	1.37
Runner 3	34	725	91.4 ± 2.0	11/46	1.35

Table 6.1: Runners characteristics.

at the start of the experiment.

The plantar distribution of the runners was recorded using Tekscan F-Scan system. This consists of a flexible 0.18 mm thick plastic sole-shape having 960 pressure sensors, with spatial resolution of 5 mm (Figure 6.1). Pressure-sensitive ink is contained between 2 polymer-film substrates (Figure 6.2). The sensor resistance decreases with increased pressure applied normal to the substrate. The sensor has a long “handle”, the sensor tab, which is connected to the cuff unit. This unit is secured to the runner’s ankle with a Velcro band, its mission is to gather and process the data from the sensor, which are sent to the computer by a shielded cable of 9.1 m long (Figure 6.3). The cuff unit weight is 0.145 kg.

The sensor insole was trimmed to fit the subjects’ right shoe. Every session the sensors were calibrated by the known weight of the test subject, standing on one foot. Data were recorded at the beginning (once they had acquired their gait), middle and end of the 10 minute run at 150 Hz for 4 sec, which gave an average of 5 strikes per movie. According to runners’ judgement the system, the in-sole sensor plus the cuff unit, did not interfered with their gait. The subjects were asked to run on hard surfaces (track or roads), and to keep a running distance diary. Every 15 days the plantar pressure distribution was measured, waiting 24 hours since the last use to standardise the recovery time.

The results will be studied through the analysis of the forces and pressures recorded

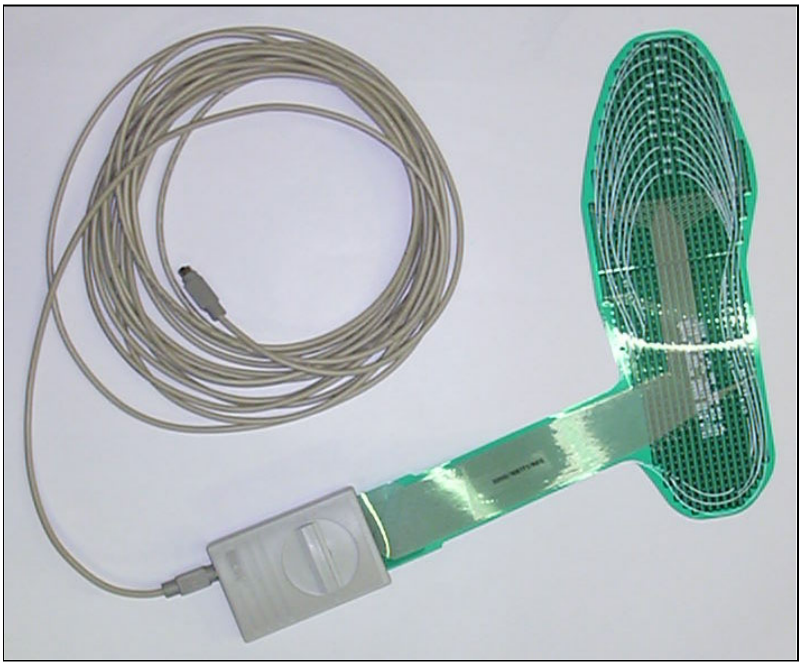

Figure 6.1: Photograph of the Tekscan sensor attached to the cuff unit and cable.

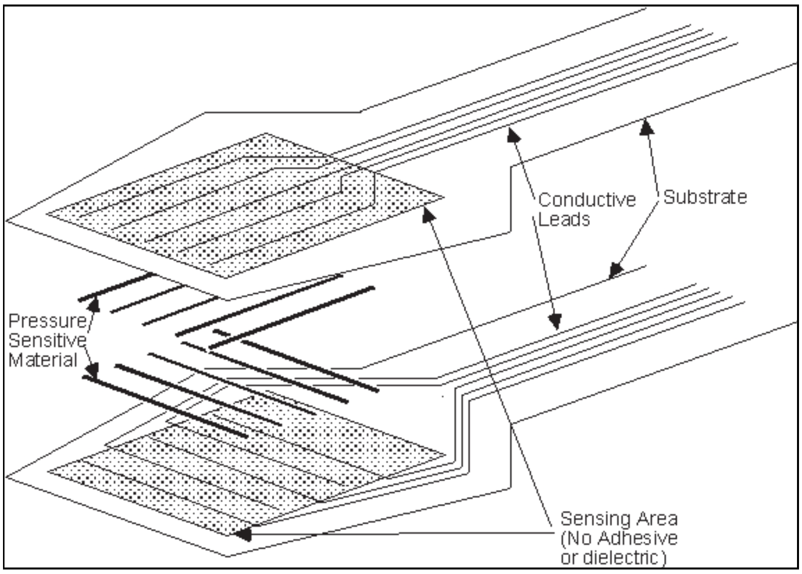

Figure 6.2: Tekscan sensor diagram. (Taken from manufacturer's information)

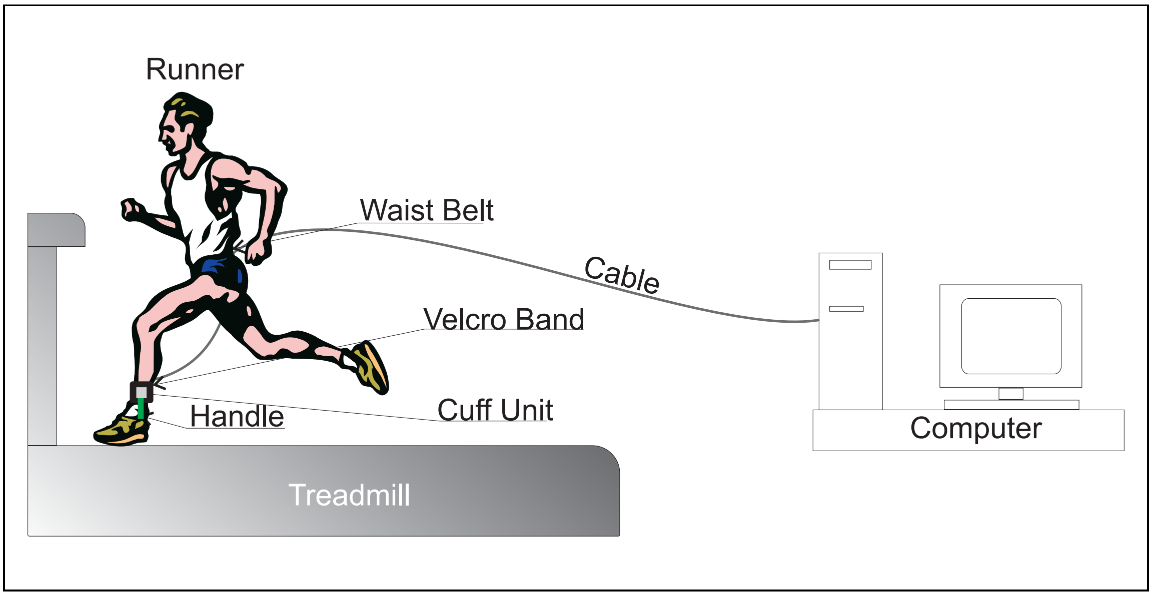

Figure 6.3: Diagram of the experiment set up.

during the experiments. They will be presented as colour coded maps and force/pressure-time graphs. The colour coded maps will be shown as single frames at a particular moment of the contact of the foot or as “composite maps” where all the frames during a foot contact have been added to form a combined map (Figure 6.4).

Reviews of the sensors [Mueller and Strube (1996); Ahroni et al. (1998)] showed contradictory results; while some researchers reported good reliability and reproducibility, others reported a decrease of sensor pressure output with time.
Although the sensor time-dependence was unknown at the start of the study, peak pressure measurements were similar to those reported on previous studies, allowing for differences in running speeds [Gross and Bunch (1989); Henning et al. (1990); Hennig and Milani (1995, 2000)].

To check the sensor linearity, an external calibration was performed over an area of 0.0079 m^2 in the forefoot region. The sensor was sandwiched between two 6 mm

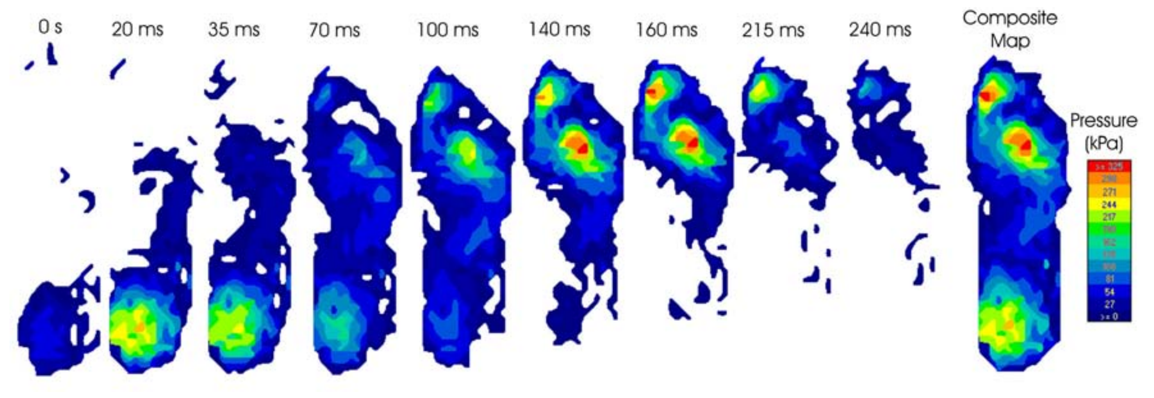

Figure 6.4: Composite map elaborated from single frames of a foot contact.

layers of soft closed-cell PVC foam (Airex 5230), then loaded in uniaxial compression between metal plates using an Instron machine. Constant pressures of 31, 36, 39, 155, 225, 329, 398 kPa were applied for a 20 s period, while data was recorded for 2 sec. The loading cycle was repeated 5 times. Tekscan values were taken from 15 different frames of each 300 frames 'movie'. The manufacturer suggested that

- a calibration curve was assigned to each sensing cell (but such software was not available),
- the 'weighted averaging' function was used, to reduce cell-to-cell variation (Figure 6.5).

This calibration was performed on 5 new and 3 used sensors (Figure 6.6). There is a linear relationship between pressures measured by the F-scan sensor and those applied by the Instron (Table 6.2). The calibrations with 'weighted averaging' and 'non-weighted averaging' are not significantly different. Although, sensor linearity did not seem to be largely affected with use, the slope was 11% larger than that for new sensors when the sensors were recalibrated. (Table 6.2)

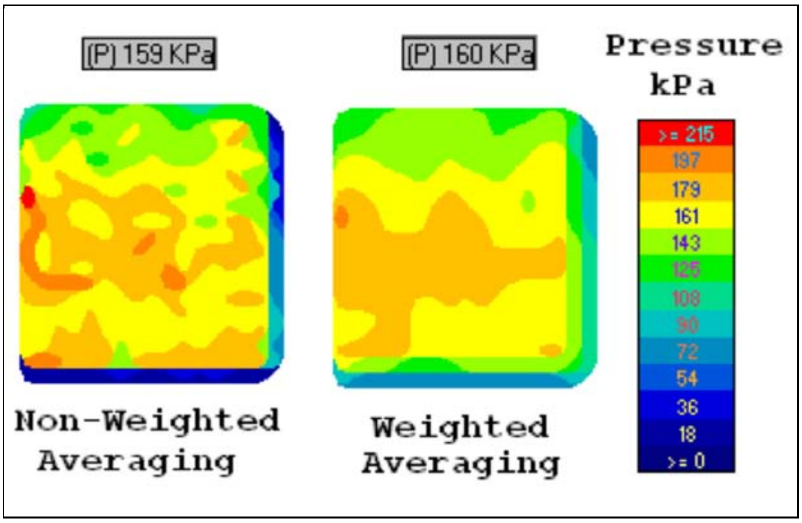

Figure 6.5: One tekscan frame for both non-weighted averaging and weighted averaging calibration procedure.

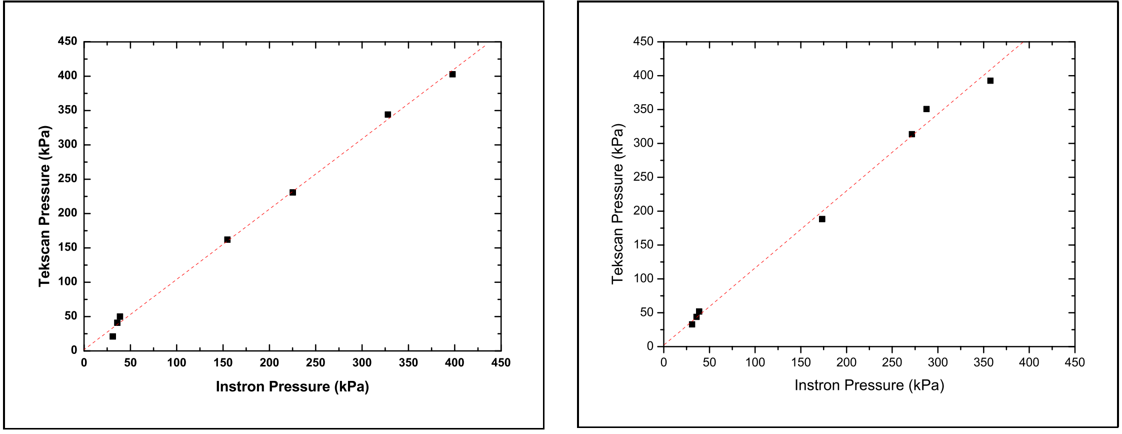

Procedure: 'non-weighted averaging', Data: Average of 5 new sensors.

Procedure: 'non-weighted averaging', Data: Average of 3 used sensors.

Figure 6.6: Calibration curve obtained with Instron machine for Tekscan sensors.

Sensor	Data Treatment	Intercept a (kPa)	Slope b	R^2
New	Non Average	1.02	1.3	0.99
New	Average	1.02	1.2	0.99
Used	Non Average	1.2	2.5	0.99

Table 6.2: Tekscan sensor calibration. Linear coefficients of average values for 5 new and 3 used sensors.

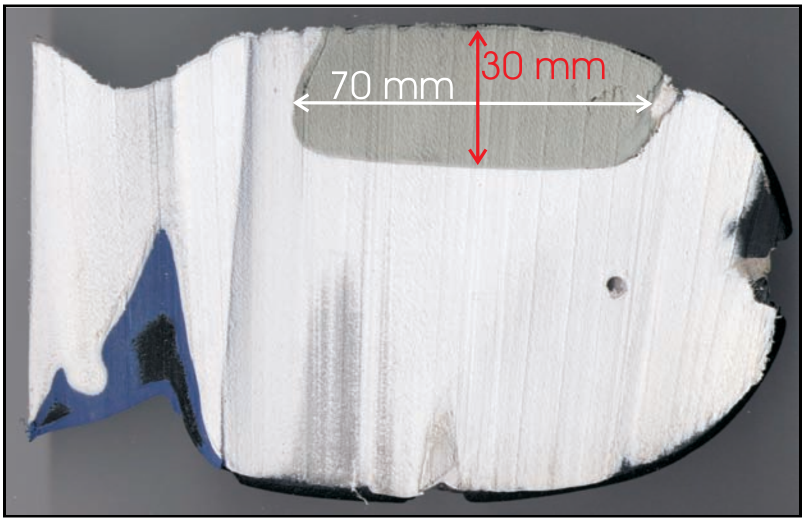

Figure 6.7: Photograph of the midsole at the heel region with grey and white foams. (Left foot).

6.2.2 Midsole foam characterisation

The midsole of Reebok Aztrek DMX shoes contained two foams: a section of area 30 mm by 70 mm on the lateral side of the heel was coloured grey, and the rest white (Figure 6.7). As midsole inserts are introduced to enhance the performance of trainers and can be made from different materials or same material but different densities [Reinschmidt and Nigg (2000)], material characterisation is required for both white and grey samples.

The densities, measured from 3 samples using an Electronic Densimeter (ED120T)

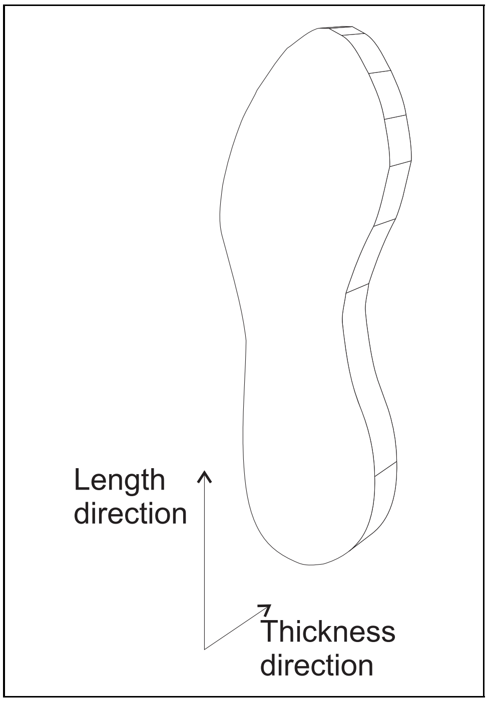

Figure 6.8: Midsole defined directions for SEM micrographs.

hydrostatic balance, were 170 and 173 kg/m^3 for the white and grey foams respectively, i.e. approximately the same.

Scanning Electron Microscopy (SEM)

The midsole structure was examined using a JEOL JSM 5410 scanning electron microscopy (SEM), to investigate changes in the foam structure. A cross-section of the midsole was fractured after being immersed in liquid nitrogen, then vacuum coated with gold. The midsole was fractured in a plane containing the thickness direction and the shoe length direction (Figure 6.8). Observations were made on foams from new and used trainers.

Attenuated Total Reflectance (ATR)

The samples were examined using Nicolet Nexus FT IR spectrometer with a Golden Gate clamp (see section 3.1.2). Sample collection was performed using the Omnic

ESPTM 1998 version software. Experiments were carried out between 4000 and 650 cm^{-1} with 100 iterations and 4 cm^{-1} of resolution. ATR correction was performed to increase the intensity of the absorbance of the bands toward the 4000 cm^{-1} end of the plot.

Differential Scanning Calorimetry (DSC)

The foams were analysed with Mettler Differential Scanning Calorimeter (DSC) 30. The weights of the white and grey samples were 3.24 and 3.29 mg, similar to previous DSC experiments. Experiments were performed with the heating programme corresponding to the large temperature range (see section 3.1.2):

1. Heat from $-40\,^{\circ}\text{C}$ to $200\,^{\circ}\text{C}$ at $10\,^{\circ}\text{C/min}$. The samples were maintained 5 min at the final temperature, to delete the thermal history.
2. Cool from $200\,^{\circ}\text{C}$ to $-40\,^{\circ}\text{C}$ at $10\,^{\circ}\text{C/min}$.
3. Heat from $-40\,^{\circ}\text{C}$ to $200\,^{\circ}\text{C}$ at $10\,^{\circ}\text{C/min}$.

The melting point and crystallinity were taken from the second heating. The melting point was taken to be the maximum of the power difference versus temperature curve and the melting enthalpy was calculated from the area under this curve. The degree of crystallinity was calculated by dividing the measured enthalpy by the melting enthalpy of pure polyethylene (286.8 J/mol) [Brandrup and Immergut (1975)], assuming that only polyethylene sequences crystallised.

Repeat Impact based on ASTM F$1614-99$ Method

The experiment was performed with the impact rig described on section 3.2.4. The outsole was removed from the heel giving a flat surface, which was fixed to a horizontal anvil. The midsole thickness was 20.1 mm. Data were collected from the first and the 26th impact. The sample was allowed to recover for 15 min, and 100 cycles

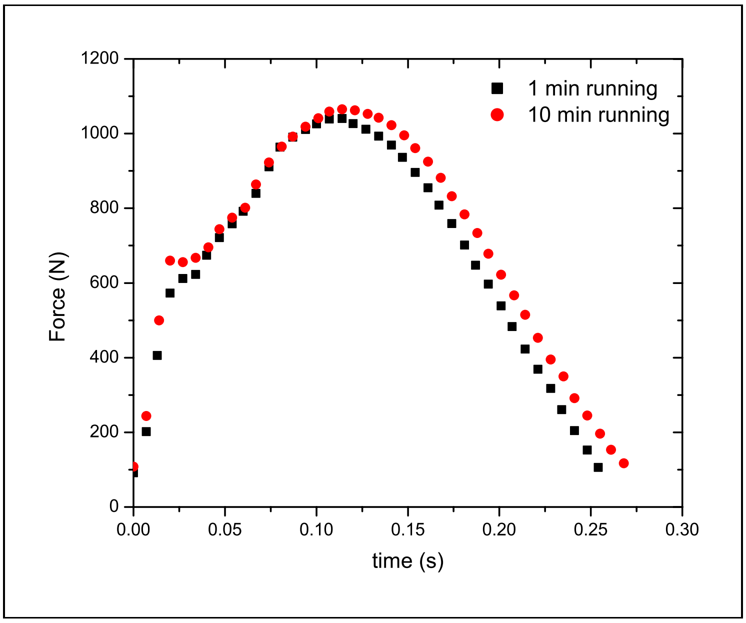

Figure 6.9: Vertical component of the ground reaction force of runner 1 as a function of foot contact time.

were performed on it, recording data every 25 cycles. To ensure the same impact height throughout the experiment, a stop was fixed to the vertical cables.

6.3 Results

6.3.1 Plantar pressure distribution

The runners' vertical force was examined as a function of foot contact (Figure 6.9). The curve shows an increase of the force with contact time, a small area where there is a constant force at around 0.025 s, followed by the "active" peak. The region of constant force is the region of the "passive" peak (section 2.4.1), which is not visible for velocities lower than 3.5 m/s [Nigg (1986a)] (Figure 2.19).

Runners have different pressure patterns [Shorten (1993); Rosenbaum and Becker (1997)] depending on various anthropometric and kinematic factors, such as gait dynamics, footshape, landing strategies among others (Figure 6.10). Therefore,

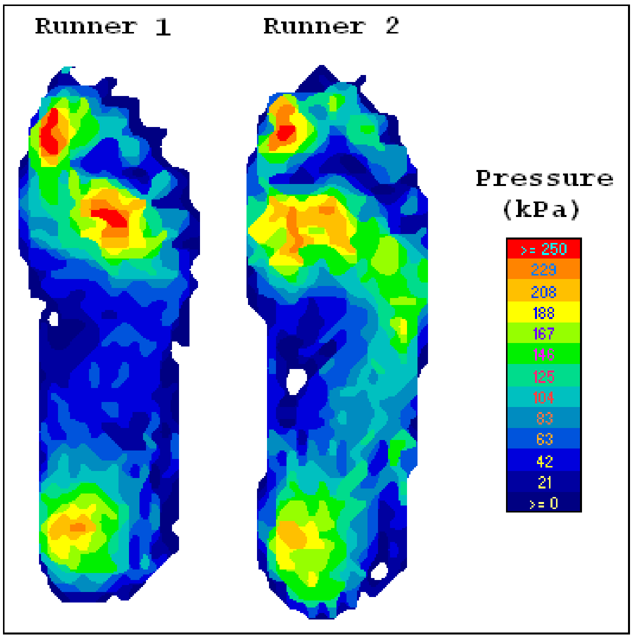

Figure 6.10: Composite maps over a footstrike for runner 1 and runner 2 showing the pressure distribution differences. Footstrikes at 1 min running and 0 km.

pressure distributions will only be graphically presented for runner 1, to be consistent throughout the section. Results, unless stated otherwise, will also have been observed in runners 2 and 3. Runners' peak pressure results will be presented as a function of run distance.

The analysis of pressure distributions, for the time in the footstrike when the peak pressure has a maximum in the heel region (Figure 6.11,) reveals an increase of the registered pressure and of the area over it is extended. Composite maps of the pressure distribution over a footstrike (Figure 6.12) also shows an increase of the pressures along the entire foot surface, hence the change occurs all over the midsole area with a large effect on the heel and forefoot regions. The isolated peaks at heel, forefoot and halux regions (Figure 6.13) almost have an axial symmetry, i.e. the peak values are near the centre of the heel, forefoot or halux contact area. Hence, the pressure distribution on the midsole upper surface is non-uniform. The change of the peak pressure and its area are evidence of a reduction in the cushioning prop-

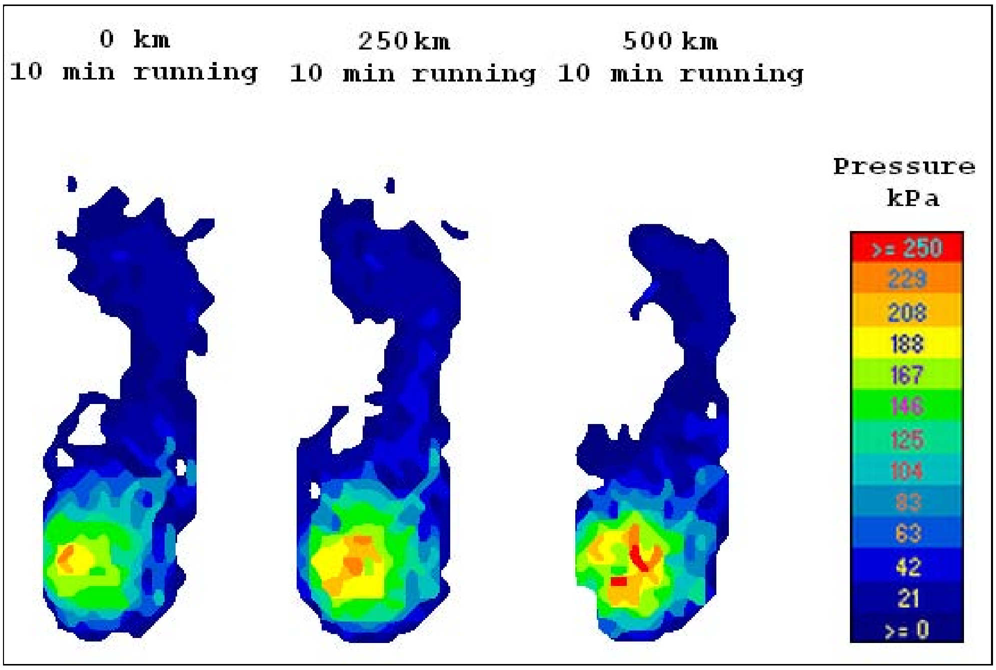

Figure 6.11: Runner 1 pressure distribution when the heel pressure has its maximum, for various distances run.

erties of the trainers.

The Tekscan measurements were analysed to produce in-shoe pressure distributions as a function of the running time and run distance. Peak pressures at the start of the experiment for all 3 runners are very similar, allowing for differences in runners' weight. Each session showed an increase of the peak pressures in the heel region with running time (Figures 6.14), with a greater increase in the second and subsequent sessions, when the trainers had been used for several 100 km. The decrease of runner's 1 peak pressure at 400 km is due to a longer resting time. Runner's 2 and 3 final peak pressure are more than twice the peak pressure registered at the start, the peak pressure increase is 117 % and 113 % for runner 2 and 3 respectively. The similarity of the increase is due to almost the same run distance of the subjects. Runner's 1 peak pressure does not show such large change due to the

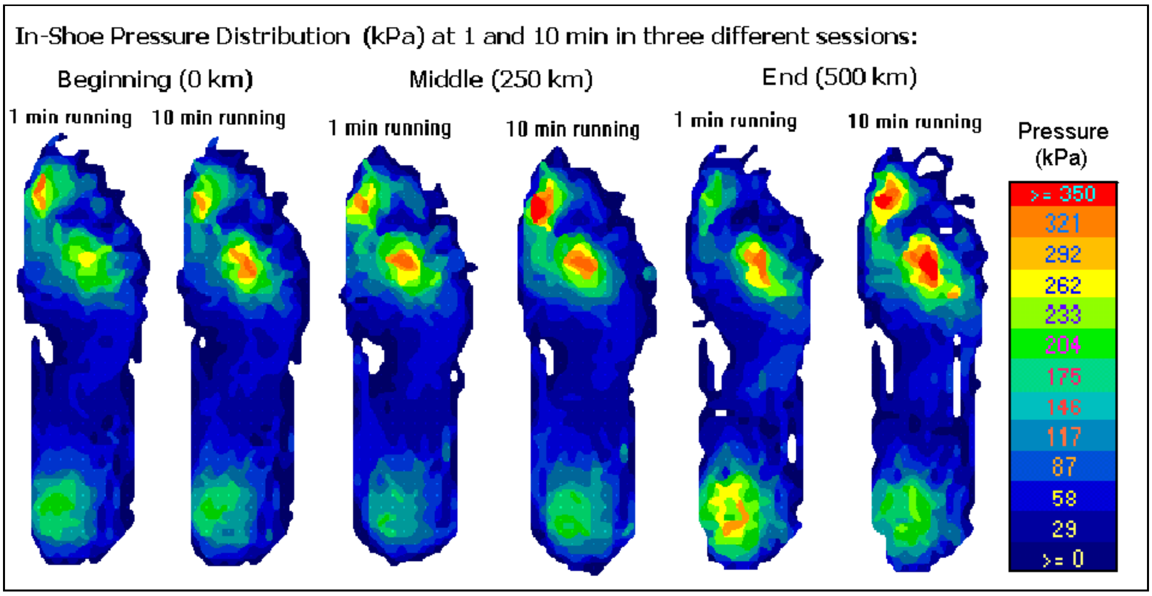

Figure 6.12: Composite maps for runner 1 of the pressure distribution at 1 and 10 min in three sessions: at the beginning, after 250 km and at the end of the experiment.

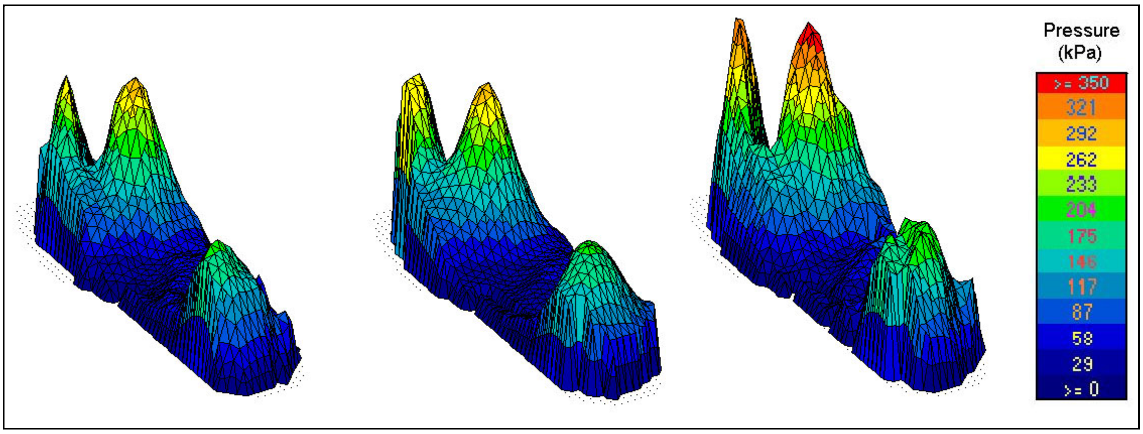

Figure 6.13: 3D composite maps for runner 1 of the pressure distribution at 10 min in three sessions: at the beginning, after 250 km and at the end of the experiment.

Runner	Shoe Size	Density (kg/m^3)
Runner 1	8	164.3 ± 4
Runner 2	9	167.8 ± 5
Runner 3	11	190.5 ± 3

Table 6.3: Foam density in used trainers.

different run distance and the longer resting period at 400 km. The peak pressure at 500 km has increased 72 % over its initial value.

Although, the magnitude of the impact force (or peak pressure) is been reported to be a cause for certain types of injuries [Miller (1990); James and Jones (1990)], there is no information on the limit magnitude that might cause the injury to occur [Frederick (1989)]. This experiment has shown that the peak pressure at the end of a 700 km run is more than twice that at the beginning.

6.3.2 Midsole foam characterisation

Larger shoe sizes often have higher foam density, in order to give extra support to the wearers, who are assumed to be heavier. Samples were cut from the arch region of each used running shoe, a region that is assumed to suffer little damage. The results (Table 6.3) show an increase of the density with shoe size.

Shoe size 8 and 9 can be considered to have the same density. The untested trainers were a UK size 8 and had an average density of 171.5 kg/m^3 at the beginning of the experiment. Midsole density between same size shoes varies due to manufacturing process. This result has to be considered on the analysis of the impact properties.

SEM

Micrographs of the foam from the new trainers (Figure 6.15) reveal the presence of flattened cells close to the lower (near to the outsole) and upper (near to the insole) surfaces, and cells slightly elongated along the shoe length direction. Midsole struc-

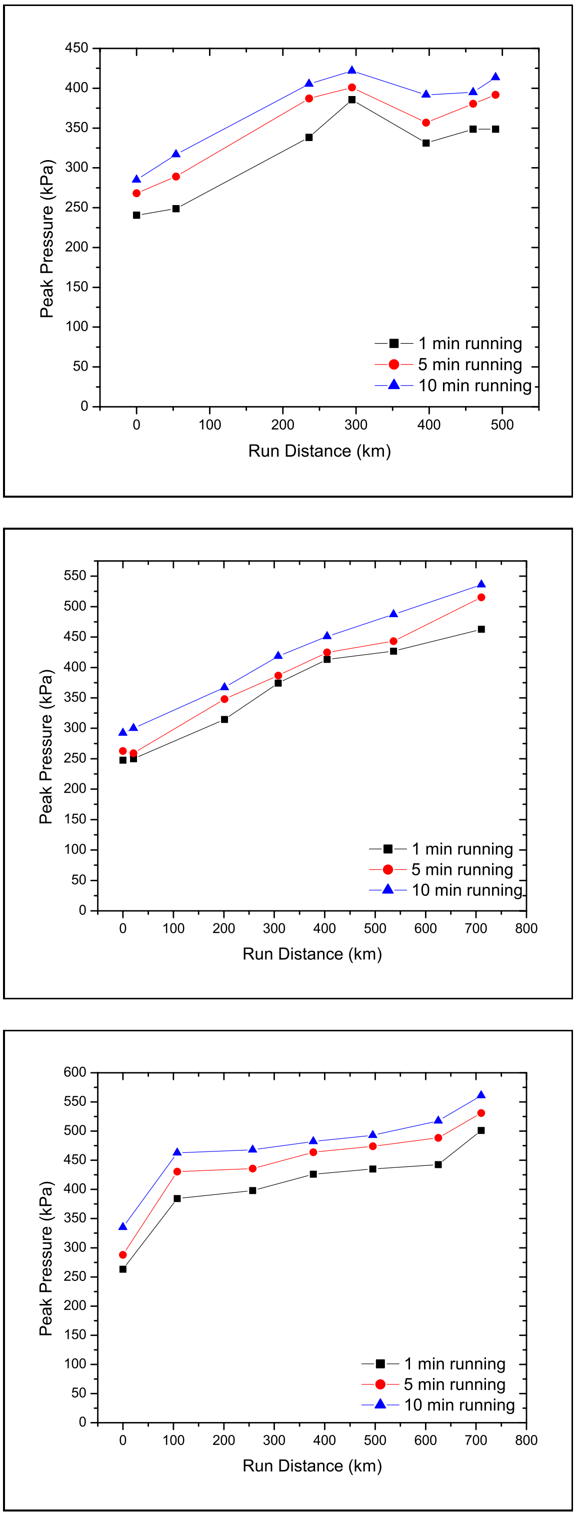

Figure 6.14: Peak pressure versus run distance for all three runners. Values have been modified with average calibration equation for new sensors.

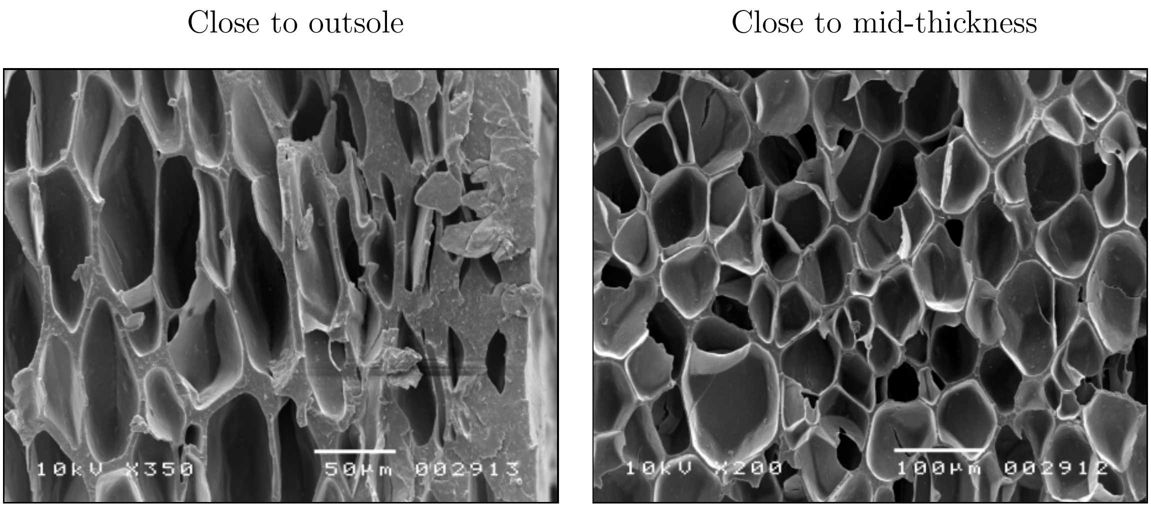
Close to outsole

Close to mid-thickness

Figure 6.15: Example of the new trainers cellular structure at the surface (left) and at the middle (right) of the samples. (Horizontal direction: Midsole thickness; Vertical direction: Shoe length)

ture has the same anisotropic structure as the foam slabs studied earlier. Hence Bartlett (1999) may have been incorrect in commenting that flattened cells near the midsole surface are evidence of foam fatigue. It is more likely that the flattened surface cells result from the moulding of the midsole into its final shape.

The used trainer micrographs (Figure 6.16) show the presence of permanent structural damage, with cell walls that have started to buckle. This type of damage is present on all three used trainers. More severe structural damage, such as cell-wall fractures, is present in the trainers of runners 2 and 3. Some fractured cell walls may be due to sample preparation; consequently it is difficult to quantify the percentage of cell faces that have fractured as result of use. Only "internal" fractures, i.e. those that can be seen on the internal faces of the cells, have been considered to be due to trainers use.

Cellular structure was not analysed by image analysis because the damage altered the cellular structure and its manual tracing was not possible to be carried out without introducing deviations from the contour of the cells, which will introduce

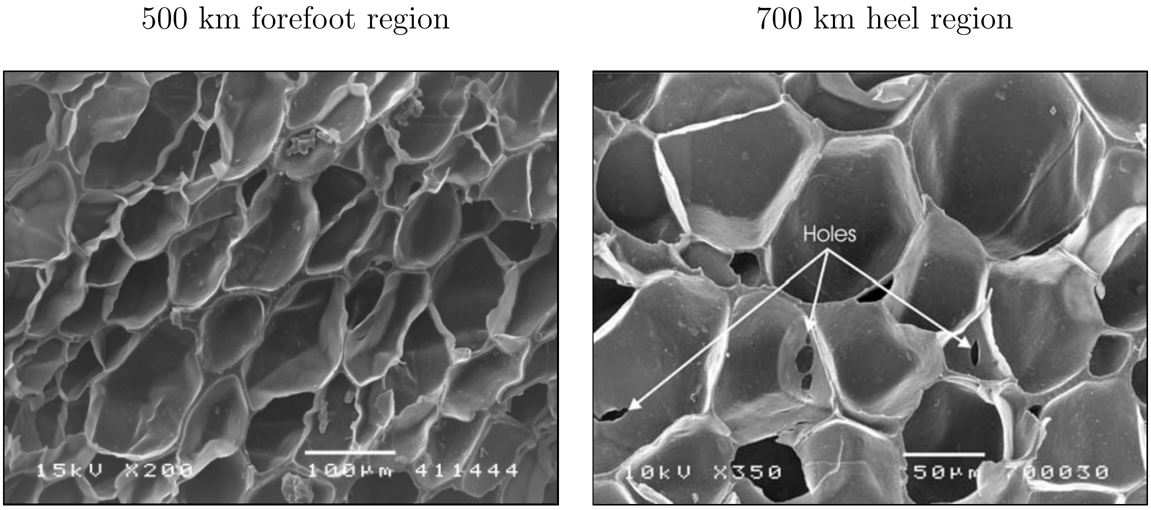
500 km forefoot region

700 km heel region

Figure 6.16: Example of the damage suffered by the cellular structure. Left: wrinkled cell faces. Right: holes in some internal cell faces. (Horizontal direction: Midsole thickness; Vertical direction: Shoe length)

large errors to the size and shape of the cells. Visual inspection of the new trainers suggests a mean cell size of 50 μm because there are two types of cell size in Figure 6.15: one larger and one smaller than the 100 μm scale. Thus, the midsole of the trainer may have a similar cell size as EVA150 foams.

ATR

ATR spectra of both white and grey (Figure 6.17) samples were compared to EVA films and foam spectra (Figures 4.5 and 4.7). It can be seen that they correspond to the same polymer, therefore it is concluded that white and grey foams are both made of EVA copolymer. Spectra also have the same undetermined broad bands seen on GG-ATR foam slabs spectra.

Applying the calibration curve obtained in section 4.1.2, the amount of VA was calculated. Both samples had 17.3 mol. % VA; this VA content is slightly higher than that already seen on Nike foam slabs.

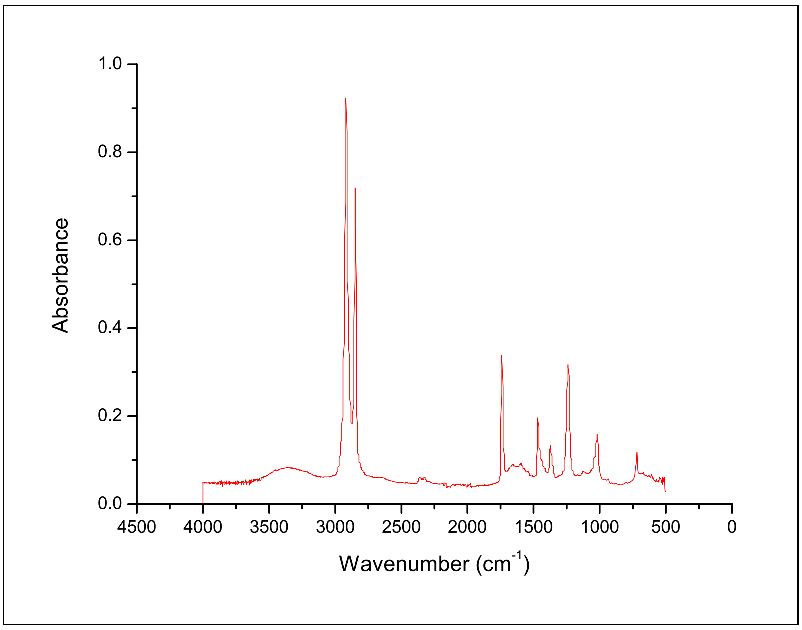

Figure 6.17: GG-ATR spectrum of grey sample.

DSC

The results for white and grey sample (Table 6.4) are similar. The midsole thermograms (Figure 6.18) has the following transitions,

- 1st Heat cycle: The melting point at a mean temperature of 80.4 °C. The thermal history is showed as a shoulder before the main peak.
- Cool cycle: The main crystallisation at a mean temperature of 56.4 °C.
- 2nd Heat cycle: The melting point at a mean temperature of 82.1 °C.

The degree of crystallinity is on average 7 % smaller than that of EVA152 with the same heating program. The midsole at room temperature will have a lower degree of crystallinity (see section 4.1.2). Furthermore, in the course of a run, the degree of crystallinity is expected to change as the midsole temperature rises during running. This introduces changes on the degree of crystallinity and therefore mechanical properties of running shoes, such as Young's modulus, flexibility and hardness.

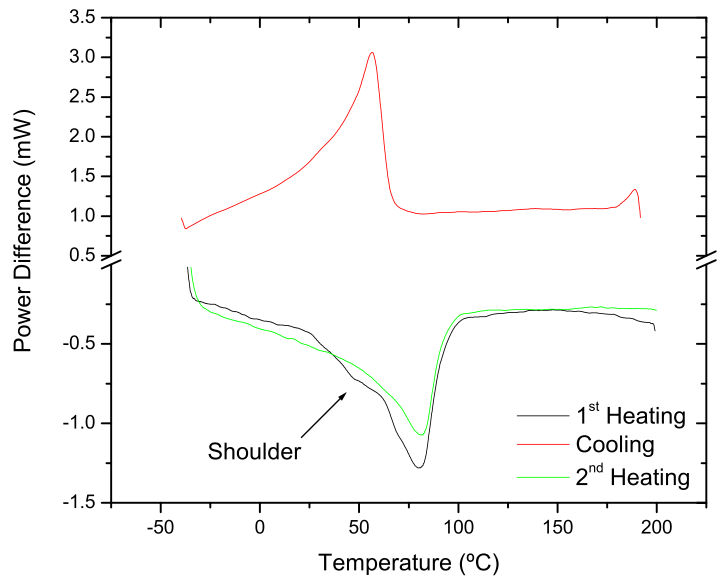

Figure 6.18: Thermogram of trainer's white foam.

Sample	Density (kg/m^3)	T_m (°C)	H_m (J/g)	Crystallinity (%)
White	170	82.2	56.7	19.8
Grey	173	82.0	53.6	18.7

Table 6.4: Characterisation of EVA foams in Reebok midsole.

From ATR and DSC results, it can be concluded that the presence of the grey foam is purely for aesthetic reasons. Both foams are made of EVA copolymer with density 171.5 kg/m^3 and 17.3 mol. % VA.

Repeat Impact based on ASTM F1614-99 Method

Force vs. deflection graphs for new midsoles (Figure 6.19) reveals the same two issues reported earlier (section 4.2.4). In the first session, there is a change in shape between the 1st and 26th impacts, as a result of the softening of the polymer structure.

In the second session the midsole behaviour appears to approach an "equilibrium" response when impact number is high. However, force-displacement curves of used trainers (Figure 6.20) do not show such change in shape; their behaviour is similar for all the impacts, i.e. curve shape, maximum force and displacement are practically the same.

The foam force-deflection response was studied as a function of impact number (Table 6.5). The new midsole has a peak force increase of 11 % whereas that for used trainers remains almost constant. The absorbed energy for each midsole decreases with impact number (Table 6.6). The largest change is 17 % for the new midsole. Neither the peak force nor absorbed energy values show a clear trend. The degree of recovery of the new midsole is 2 % whereas used trainers do not show any recovery.

Peak force values cannot be compared to previous ASTM experiments because the dimensions of the samples are different. The midsole is 20 mm thick, almost twice the foam slab thickness.

The peak pressure (Table 6.7) was calculated as the peak force divided by the area of the heel, i.e. peak pressure is the average value across the heel surface. These values are significantly higher than in the human trials.

Comparison of the behaviour of both absorbed energy and peak force with run distance (Figure 6.21), has to be carefully done as all four midsoles have different densities. If all 4 foams had the same density, peak force and absorbed energy are expected to increase and decrease respectively with run distance, due to prior use; result obtained with repeat impact experiments.

The average absorbed energy E_a(used) (Table 6.8) does decrease with run distance. However, even though the new trainers had a higher density than the trainers used for 500 and 700 km and that it is not been previously used, its E_a is lower than that

1st Session

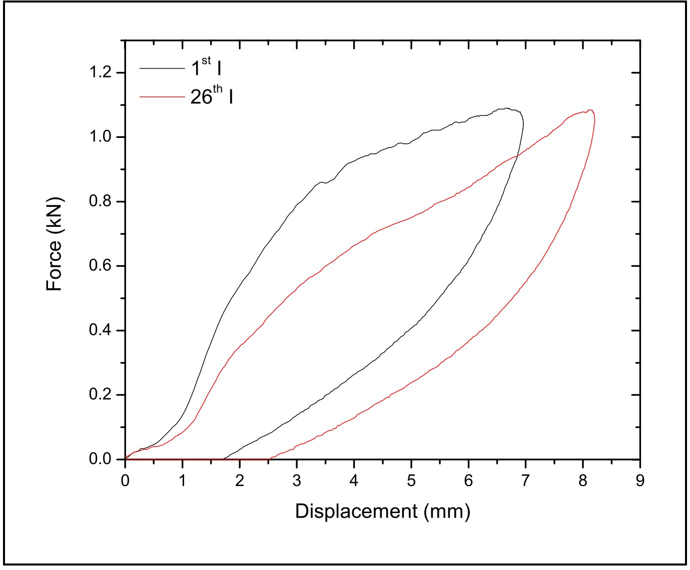

2nd Session

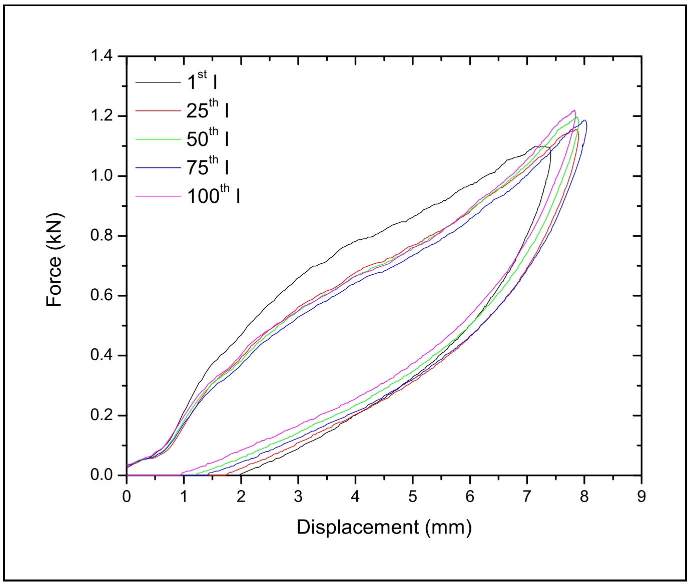

Figure 6.19: Force-displacement behaviour in session 1 and 2 of the new midsole.

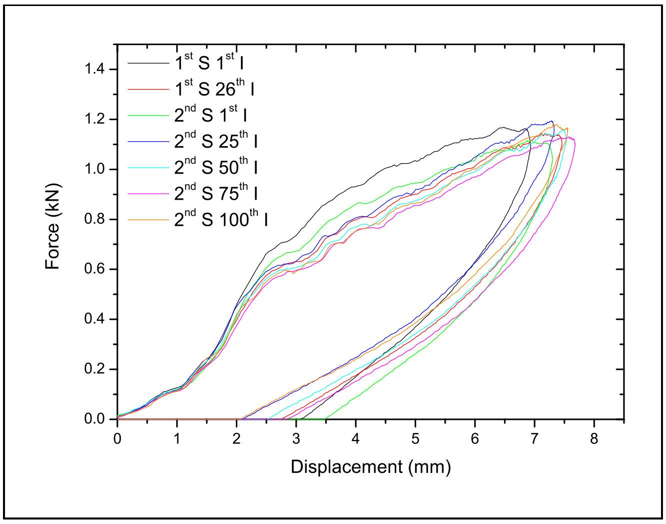

500 km

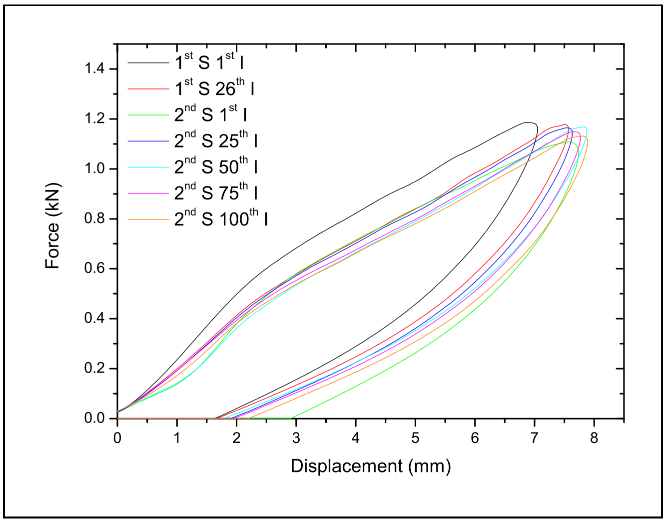

700 km

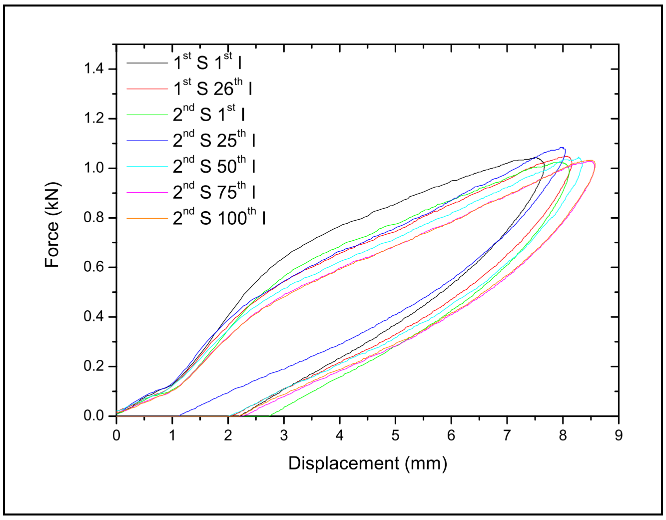

725 km

Figure 6.20: Force-displacement behaviour in session 1 and 2 of the used midsoles.

Session		Peak Force (kN) at run distance			
	I_n	0 km	500 km	700 km	725 km
1	1	1.10	1.17	1.19	1.05
1	26	1.09	1.14	1.18	1.05
2	1	1.10	1.12	1.11	1.03
2	25	1.16	1.20	1.17	1.09
2	50	1.20	1.16	1.17	1.05
2	75	1.19	1.14	1.15	1.03
2	100	1.23	1.19	1.14	1.04

Table 6.5: Peak force of ASTM test for both sessions on new and used midsoles.

Session		Absorbed Energy (J) at run distance			
	I_n	0 km	500 km	700 km	725 km
1	1	3.70	3.94	3.48	3.44
1	26	3.60	3.74	3.31	3.29
2	1	3.67	4.01	3.74	3.51
2	25	3.39	3.53	3.43	2.84
2	50	3.17	3.57	3.23	3.22
2	75	3.21	3.73	3.39	3.24
2	100	3.06	3.41	3.45	3.21

Table 6.6: Absorbed energy of ASTM test for both sessions on new and used midsoles.

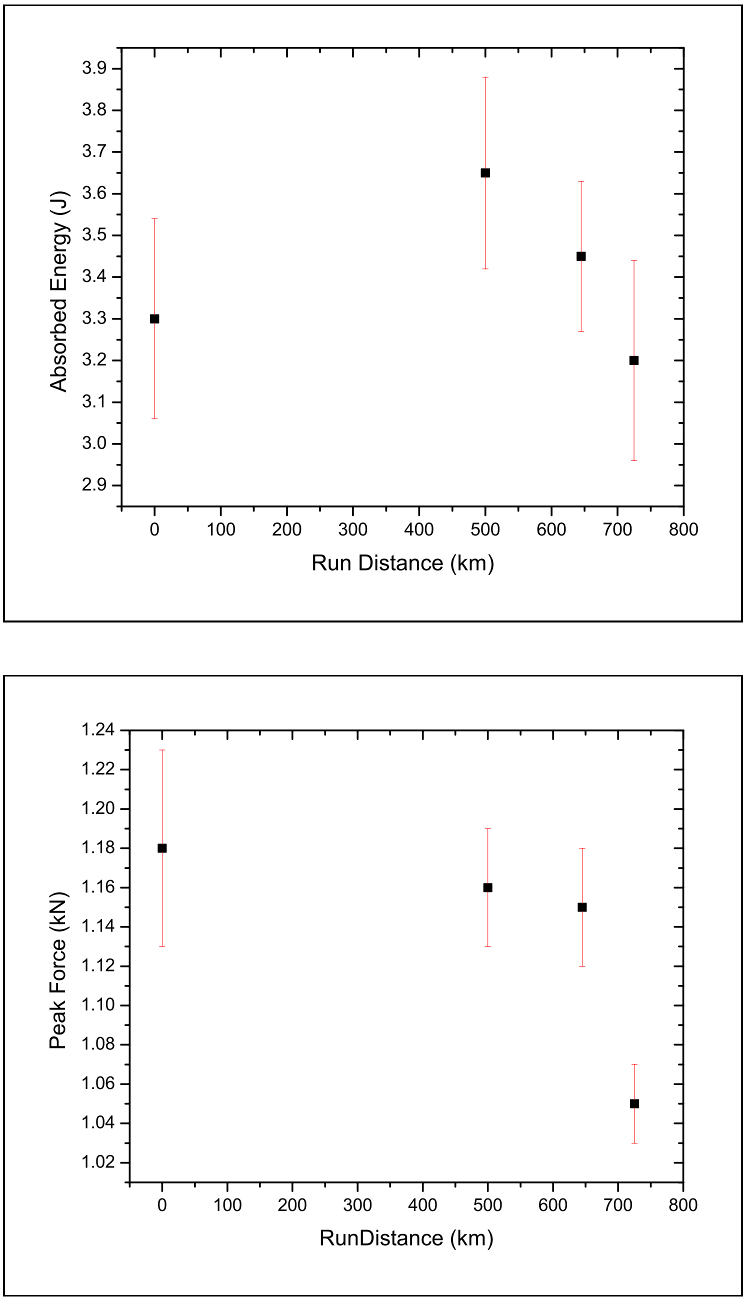

Figure 6.21: Average and standard deviation of absorbed energy and peak force of 2^{nd} session versus run distance.

Session	Peak Pressure (kPa)				
	I_n	0 km	500 km	700 km	725 km
1	1	691.64	735.65	748.22	660.20
1	26	685.35	716.79	741.94	660.20
2	1	691.64	704.21	697.92	647.62
2	25	729.36	754.51	735.65	685.35
2	50	754.51	729.36	735.65	660.20
2	75	748.22	716.79	723.07	647.62
2	100	773.38	748.22	716.79	653.91

Table 6.7: Calculated peak pressure across the heel area on new and used midsoles.

of the trainers used for 500 and 700 km. The repeat impact experiments showed that E_a increased with density and decreased with run distance (see Figure 4.41). Also, the average peak force (F_p) for new, 500 and 700 km old trainers is very similar whereas F_p(750 km) is significantly smaller. These results are inconsistent with the Tekscan and repeat impact results.

Possible reasons for this discrepancy are (1) experimental errors resulting from variations of impact height, (2) the ASTM heel geometry being inadequate for cushion-

	Average	
Run Distance (km)	F_p (kN)	E_a (J)
0	1.18 ± 0.05	3.30 ± 0.24
500	1.16 ± 0.03	3.65 ± 0.23
700	1.15 ± 0.03	3.45 ± 0.18
725	1.05 ± 0.02	3.30 ± 0.12

Table 6.8: Average value and standard deviation over the second session impacts for peak force and absorbed energy for all run distances.

ing testing. Special care was taken during the experimental procedure to ensure the same impacting height, nevertheless changes would have result on larger standard deviations. The ASTM striker geometry and material characteristics are very different from the human heel, which in turn affect the pressure distribution registered in the midsoles. Tekscan results showed pressures spreading over the midsole with the highest pressure registered underneath the heelbone. Whereas ASTM experiments suggest a different pressure pattern as, by the end, the midsoles exhibited a circular indentation where the edge of the heel impacted. Finite Element Analysis [Verdejo and Mills (2002)] confirms this different pressure distribution where there is a high stress close to the heel edge and an uniform strain around the middle of the heel area.

The gas pressure (p_0) and collapse stress (σ_0) were calculated for the second impact session (Table 6.9). The results for each trainer midsole show the same behaviour as previous results, i.e. σ_0 decreases and p_0 increases with the number of impacts.

As the initial yield stress of polymer foams strongly depends on the foams density [Mills (1994)], σ_0 values were corrected [Ankrah et al. (2002)] assuming that σ_0 is proportional to $\rho_r^{1.5}$, where ρ_r is the relative density. The correction coefficient is calculated as

$$CC = \frac{\rho_r^{1.5}}{\rho^{1.5}} \tag{6.1}$$

where ρ is the relative density of a reference foam. The selected density for the EVA reference foam was 150 kg/m^3, to compare the new trainer results with Nike foams. The average of the corrected initial yield stress (Table 6.10) do not have a clear trend for all 4 midsoles, however the result for the runners' trainers shows a decrease with run distance. This would suggest a decrease of the cushioning properties of the midsole. In polymeric foams, the lower the yield point, the easier it is to deform.

The same procedure was applied to EVA150 (Figure 6.22), with the correction coefficient being 0.96, 1.01 and 1.02 for EVA146, EVA151 and EVA152 respectively.

p_0 (kPa)

N Impact	0 km	500 km	700 km	725 km
1	329.1	367.0	386.4	294.7
25	367.0	452.5	452.4	355.9
50	415.1	388.7	413.61	304.7
75	400.4	376.7	421.4	292.5
100	439.7	446.3	395.04	293.6
Average	390.3	406.2	413.8	308.3

σ_0 (kPa)

N Impact	0 km	500 km	700 km	725 km
1	361.3	376.6	299.3	319.4
25	284.0	307.3	259.6	270.7
50	247.6	321.3	258.5	270.9
75	239.7	313.2	259.4	259.5
100	234.9	287.7	263.2	257.4
Average	273.5	321.2	268.0	275.6

Table 6.9: σ_0, p_0 and their average for ASTM impacts on midsole trainers as a function of run distance.

Run Distance (km)	CC	Average σ_0 (kPa)
0	1.22	223.7 ± 43.1
500	1.15	279.9 ± 29.1
700	1.18	265.5 ± 14.9
725	1.43	192.6 ± 17.7

Table 6.10: Correction coefficient and corrected σ_0 average and standard deviation values over the second session impacts for all run distances.

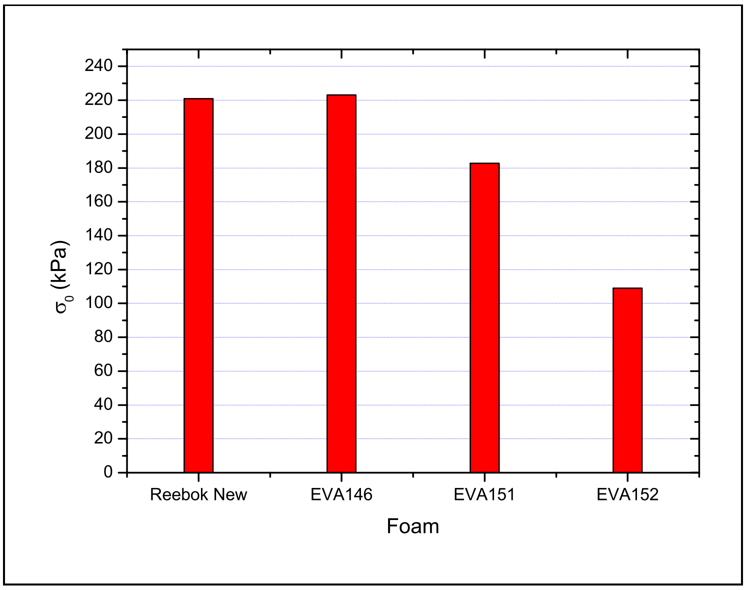

Figure 6.22: Initial yield stress for the new midsole and EVA150 foams (corrected to 150 kg/m^3).

The new Reebok midsole has similar initial yield point that EVA146 while EVA152 has the lowest value, thus being the easiest to deform.

6.4 Discussion

The aim was to analyse changes in running shoe midsoles with use. Although the linearity of Tekscan sensors decreased due to prior use, the effect is not large enough to invalidate pressure readings; since the change in pressure is an order of magnitude larger than the sensitivity change of Tekscan F-scan sensors. The experiments show an increase of peak pressures and changes in pressure distribution with the distance run in the heel and forefoot regions, with the peak pressure at the end of a 700 km run being more than twice the initial pressure. This indicates that changes have occurred in the midsole foam as a result of run distance. SEM analysis confirms these changes and shows that structural damage, such as cell wall buckling, has occurred at all three run distances. The severity of the structural damage is larger

in trainers used for 700 and 725 km, with internal fractures and holes.
A critical analysis of these experiments reveals aspects that could be improved in further studies, such as

1. use of new sensor in each session
2. Instron calibration of each sensor before and after the sessions (this calibration was done at the beginning and end of the experiment)
3. selecting a statistical number of runners, divided in trios, each trio running a certain distance
4. select runners with the same shoe size.

The ASTM test, used for shoe midsole testing, produces different pressure values and distribution than either those recorded in-shoe, or those predicted by ABAQUS Finite Element Analysis [Verdejo and Mills (2002, accepteda)] of the heelpad plus EVA foam. The peak forces in the ASTM test are probably too high, producing excessive pressures on the foam. The test probably causes a more rapid deterioration in the midsole response than does running.
The initial yield stress does decrease with run distance, although σ_0 of the new trainers was smaller than that of the used trainers. This confirms the change in the mechanical properties of running shoes with run distance. The midsole became softer with use as result of the softening of the polymeric matrix.
The differences in the mechanical properties of new and used trainers could be due to variations in the manufacturing process, suggested by the density differences between the same shoe size. A further chemical analysis of used trainers could reveal the presence of such changes.
The material characterisation of the midsole revealed a similar cellular structure and chemical composition to those already observed in the foam slabs.

6.5 Conclusions

Changes occurred in the midsole foam as a result of run distance have been analysed by different methods. (1) In-shoe pressures showed an increase in their peak values and a change in their distribution with run distance. (2) SEM inspection of the used trainers revealed structural damage occurred as result of use. (3) Impact tests show a decrease of the initial yield stress with run distance. These three methods confirm the deterioration of the midsole foam with use, hence affecting the durability of the running shoe.

Although changes have been shown in the shoe foam response, it is not easy to set limits to the peak pressures that represent an increased risk of a foot injury. Recent research [Taunton et al. (2003)] suggests that running shoe age contributes to running injuries. The deterioration of running shoe cushioning may be an important explanatory factor for such an effect.

Chapter 7

Conclusions

The main conclusions accomplished by this research are here presented and related to the aims and goals which started the study. A detailed summary was presented at the end of each chapter.

The main goal of this research was to identify the factors affecting the foam fatigue under repeated loads. Hence, the main conclusion achieved is that foam fatigue is due to the compression and recovery processes of the cellular structure and not to a change in the air content. This conclusion was drawn as a result of (1) the mechanical tests and (2) the theoretical analysis of gas diffusion in foams subjected to repeated impact.

1. From the mechanical tests it was concluded that the softening of the material with the distance run and the reduction in the cushioning properties are mainly due to a decline in the initial compressive collapse stress with the gas content remaining almost constant irrespective of run distance.
2. The theoretical analysis showed a negligible gas loss due to diffusion in foams under cyclic loads.

Therefore, and even though the gas diffusion affects the creep behaviour of foams, it does not affect the compressive response under repeated impact in the same way.

The different strain rate of these experiments is the reason for such difference.

The development of a new test rig provided information about the effects of repeated impact on polymeric foams. The test enables the simulation of the effects of long distance running on athletic shoes. Finally, the equipment is proved to have some advantages compared to the standard method used in running shoes and to produce reproducible results.

The microbalance experiment did prove to be a straightforward technique which can be used with foams to characterise the diffusion process in them. This technique can be used to achieve a deeper understanding of gas diffusion in foams.

The controlled running tests confirmed the deterioration of the midsole foam, with an increase of the peak pressure and structural damage in the foam after a long run. Although changes have been shown in the shoe foam response, it is not easy to set limits to the peak pressures which represent an increased risk of a foot injury. Recent research [Taunton et al. (2003)] suggests that running shoe age contributes to running injuries. The deterioration of running shoe cushioning may be an important explanatory factor for such an effect.

Chapter 8

Further Work

All three factors identified at the start of this research have been analysed. However, some further work can be carried out in order to provide a deeper understanding. Although most of this work has already been pointed out in the relevant chapter a summary may be of use.

1. Material characterisation
    - Analysis of the effects of the inorganic fillers for this type of application
    - Extension the analysis to other types of foam in order to improve the midsole selection
2. Gas Diffusion
    - Empirical approach
        a. Evaluating the reproducibility of the experiments
        b. Evaluating the material factors affecting the diffusion process, e.g. density, cellular structure, composition, etc.
        c. Evaluating the experimental conditions affecting the diffusion process, e.g. temperature, sample conditioning

- Theoretical approach
    a. Extension of the analysis by reducing the assumptions, e.g. non-ideal gas, non-stationary conditions, etc.

3. Durability
    - In lab durability tests
        a. Improvements to the repeat impact test rig developed for this research
        b. Analysis of the temperature and humidity effects
    - In field durability tests
        a. Improvements to the sensor data by calibrating the sensors before and after each run
        b. Selection of a statistical number of runners with the same shoe size, since foam density varies according to shoe size

From this suggested research two main improvements would be achieved

A methodology to identify foam factors affecting the diffusion process in foams, and hence their ageing behaviour

The identification of better foams for midsole performance and durability

Appendix A

Published Papers

Verdejo, R. & Mills, N. J. (2003, accepted) *Heel-shoe interactions and the durability of EVA foam running-shoe midsoles*, Journal of Biomechanics.

Verdejo, R. & Mills, N. J. (2003, accepted) *Simulating the effects of long distance running on shoe midsole foam*, Polymer Testing.

Mills, N. J., Fitzjerald, C., Verdejo, R., Gilchrist, A. (2003). *Polymer foams for personal protection: Cushions, shoes and helmets*, Composite Science and Technology, 63, 2389-2400.

Ankrah, S., Verdejo, R., Mills, N. J. (2002). *Ethylene - Styrene Interpolymer Foam Blends: Mechanical Properties and Sport Applications*, Cellular polymers, 21 n 4, 237-264.

Verdejo, R. & Mills, N. J. (2002). *Performance of EVA foam in running shoes*, The Engineering of Sport 4, Ujihashi, S. & Haake, S. J. (Ed.), pp 580-588.

List of References

Ahroni, J. H., Boyco, E. J., Forsberg, R., 1998. Reliability of F-Scan in-shoe measurements of plantar pressure. Foot and Ankle International 19, 668–673.

Alley, L., Nichols, G., 1999. Future technical challenges for the PU industry in athletic footwear production. Tech. rep., Nike Inc.

Alsoy, S., 1999. Modeling of diffusion in closed-cell polymeric foams. J. Cellular Plastics 35, 247–271.

Andrews, E. W., Gibson, L. J., Ashby, M. F., 1999. The creep of cellular solids. Acta materialia 47 (10), 2853–2863.

Andriachi, T. P., Alexander, E. J., 2000. Studies of human locomotion: past, present and future. Journal of Biomechanics 33, 1217–1224.

Ankrah, S., 2002. Protective materials for sporting applications - football shin guards. Ph.D. thesis, Metallurgy and Materials.

Ankrah, S., Verdejo, R., Mills, N. J., 2002. Ethylene-styrene interpolymer foam blends: mechanical properties and sport applications. Cellular Polymers 21 (4), 237–264.

Arsac, A., Carrot, C., Guillet, J., 2000. Determination of primary relaxation temperatures and melting points of ethylene vinyl acetate copolymers. J. Thermal Analysis and Calorimetry 61, 681–685.

Ashby, M. F., 1983. The mechanical properties of cellular solids. Metallurgical Transactions A 14A, 1755–1769.

ASTMD3576, 1994. Cell size of rigid cellular plastics. Tech. rep., American Society for Testing and Materials.

ASTMF1614-99, 1999. Test method F1614-99 standard test method for shock attenuating properties of materials systems for athletic footwear. Tech. rep., American Society for Testing and Materials.

ASTMF1976-99, 1999. Test method F1976-99 standard test method for cushioning properties of athletic shoes using an impact test. Tech. rep., American Society for Testing and Materials.

Atwater, A. E., 1990. Gender differences in distance running. In: Cavanagh, P. R. (Ed.), Biomechanics of Distance Running. Human Kinetics, pp. 321–362.

Aubert, J. A., 1998. Solubility of carbon dioxide in polymers by quartz crystal microbalance technique. J. Supercritical fluids 11, 163–172.

Bart, G. C. J., du Cauzé de Nazelle, G. M. R., 1993. Certification of thermal conductivity aging of PUR foam. J. Cellular Plastics 29, 29–42.

Bartlett, R., 1999. Sports biomechanics: reducing injury and improving performance. E and FN Spon.

Brady, G. S., Clauser, H. R., Vaccari, J. A., 1997. Material Handbook, 14^{th} Edition. McGraw-Hill, Inc., pp. 374–377.

Brandreth, D. A., 1991. Insulation foam ageing-a review of the relevant physical phenomena. In: Brandreth, D. A. (Ed.), Improved thermal insulation: problems and perspectives. Technomic Publishing Co., pp. 165–173.

Brandrup, J., Immergut, E. H., 1975. Polymer Handbook, 2^{nd} Edition. Wiley Interscience Publication.

Briscoe, B. J., Savvas, T., 1998. Gas diffusion in dense poly(ethylene) foams. Advances in Polymer Technology 17 (2), 87–106.

Brodt, K. H., Bart, G. C. J., 1993. The Delft sorption set-up as an instrument to determine the intrinsic solubility and diffusion coefficient of gases in plastics. J. Cellular Plastics 29, 478–491.

Burgess, G. J., 1988. Some thermodynamic observations on the mechanical properties of cushion. J. Cellular Plastics 24, 56–69.

Cavanagh, P. R., 1980. The running shoe book. Anderson World, Mountain View. CA.

Cavanagh, P. R., 1989. The biomechanics of running and running shoe problems. In: Segesser, B., Pförringer, W. (Eds.), The shoe in sport. Year book medical publishers, Inc., pp. 3–15.

Cavanagh, P. R., 1990. Biomechanics of Distance Running. Human Kinetics.

Cavanagh, P. R., Kram, R., 1990. Stride length in distance running: velocity, body dimensions, and added mass effects. In: Cavanagh, P. R. (Ed.), Biomechanics of Distance Running. Human Kinetics, pp. 35–63.

Cavanagh, P. R., Lafortune, M. A., 1980. Ground reaction forces in distance running. Journal of Biomechanics 13, 397–406.

Cavanagh, P. R., Valiant, G. A., Misevich, K. W., 1984. Biological aspects of modelling shoe/foot interaction during running. In: Frederick, E. C. (Ed.), Sports shoes and playing surfaces. Human Kinetics, pp. 24–46.

Charrier, J.-M., 1990. Polymeric Materials and Processing: Plastics, Elastomers, and Composites. Oxford University Press.

Chen, H., Nigg, B. M., de Köning, J., 1996. Relationship between plantar pressure distribution under the foot and the insole comfort. Clinical Biomechanics 9 (6), 335–341.

Cheskin, M. P., Sherkin, K. J., Bates, B. T., 1987. The complete handbook of athletic footwear. Fairchild Publications.

Clarke, T. E., Frederick, E. C., Cooper, L. B., 1983. Effects of shoe cushioning upon ground reaction forces during running. Int. J. Sports Medicine 4, 247–251.

Clarke, T. E., Frederick, E. C., Hamil, C., 1984. The study of rearfoot movement in running. In: Frederick, E. C. (Ed.), Sports shoes and playing surfaces. Human Kinetics, pp. 166–189.

Coates, J., 2001. Interpretation of infrared spectra, a practical approach. In: Meyers, R. A. (Ed.), Encyclopedia of Analytical Chemistry. John Wiley and Sons, pp. 1–23.

Cocks, A. C. F., Ashby, M. F., 2000. Creep-buckling of cellular solids. Acta materialia 48, 3395–3400.

Cook, S. D., Kester, M. A., 1985. Biomechanics of running shoe performance. Clinics in Sports Medicine 4, 619–626.

Cook, S. D., Kester, M. A., Brunet, M. E., 1985. Shock absorption characteristics of running shoes. American Journal of Sports Medicine 13, 248–253.

Covill, D., Guan, Z., Pope, D., Bailey, M., 2002. The effect of shoe fit on subjective responses, temperature and relative humidity levels. In: Ujihashi, S., Haake, S. (Eds.), The Engineering of Sport 4. pp. 588–594.

Crank, J., Park, G. S., 1968. Diffusion in Polymers. Academic Press.

Craver, C. D., 1983. Polymer characterisation-Spectroscopic, chromatographic and physical instrumental methods. American chemical society.

Cullity, B. D., 1956. Elements of X-Ray diffraction. Addison-Wesley.

Cunningham, A., Hilyard, N. C., 1994. Physical behaviour of polymeric foams-an overview. In: Hilyard, N. C., Cunningham, A. (Eds.), Low Density Cellular Plastics - Physical basis of behaviour. Chapman and Hall, Ch. 1, pp. 1–21.

Cussler, E. L., 1975. Diffusion, mass transfer in fluids systems, 2^{nd} Edition. Clarendon Press.

Diffraction Manual, P., 1976. Powder diffraction file: Search Manual-Inorganic compounds Hanawalt Method.

Dodd, J. W., Tonge, K. H., 1987. Thermal Methods. John Wiley and Sons, pp. 100–169.

Donaghue, V. M., Veves, A., 1997. Foot pressure measurement. Orth. Phys. Therapy Clinics of North America 6 (1), 1–16.

Dubois, R., Karande, S., Wright, D. P., Martinez, F., 2002. The use of ethylene/styrene interpolymers in crosslinked foams for the footwear industry. Cellular Polymers 38, 149–161.

DuPont, 1997. Thermal properties of Elvax. http://www.dupont.com/industrial-polymers/elvax/E-54514.html.

Edelmann-Nusser, J., Ganter, N., Witte, K., Geisrt, C., 2002. Short term estimation of abrasion in running shoes. In: Ujihashi, S., Haake, S. (Eds.), The Engineering of Sport 4. pp. 573–579.

Edington, C. J., Frederick, E. C., Cavanagh, P. R., 1990. Rearfoot motion in distance running. In: Cavanagh, P. R. (Ed.), Biomechanics of Distance Running. Human Kinetics, pp. 135–162.

Ewing, G. W., 1975. Instrumental methods of chemical analysis, 4^{th} Edition. McGraw-Hill, Inc.

FootSolutions, O., 1999. Foot health. http://www.ohiofootsolutions.com/foothealth.html.

Frederick, E. C., 1984. Sports shoes and playing surfaces. Human Kinetics.

Frederick, E. C., 1989. The running shoe: Dilemmas and dichotomies in design. In: Segesser, B., Pförringer, W. (Eds.), The shoe in sport. Year book medical publishers, Inc., pp. 26–35.

Frederick, E. C., Hagy, J. L., 1986. Factors affecting peak vertical ground reaction forces in running. Intern. J. of Sport Biomechanics 2, 41–49.

Gefen, Y., Aharony, A., Mandelbrot, B. B., Kirkpatrick, S., 1981. Solvable fractal family and its possible relation to the backbone at percolation. Physical Review Letters 47, 1771–1773.

Gibson, L. J., Ashby, M. F., 1997. Cellular Solids: Structure and Properties, 2^{nd} Edition. Cambridge University Press.

Glicksman, L. R., 1994. Heat transfer in foams. In: Hilyard, N. C., Cunningham, A. (Eds.), Low Density Cellular Plastics - Physical basis of behaviour. Chapman and Hall, Ch. 5, pp. 104–152.

Gonzalez, R. C., Woods, R. E., 2002. Digital image processing, 2^{nd} Edition. Prentice Hall.

Gross, T. S., Bunch, R. P., 1989. Discrete normal plantar stress variations with running speed. Journal of Biomechanics 22, 699–703.

Gunn, D. J., Moores, D. R., Thomas, W. J., Wardle, A. P., 1974. Sorption of water vapour into polyurethane foams. Chemical Engineering Science 29, 549–559.

Hennig, E. M., 2002. Human foot during locomotion- applied research for footwear. Lecture at The Chinese University of Hong Kong, http://www.cuhk.edu.hk/puo/weilun/Hennig/Prof

Hennig, E. M., Milani, T. L., 1995. In-shoe pressure distribution for running in various types of footwear. Journal of Applied Biomechanics 11, 299–310.

Hennig, E. M., Milani, T. L., 2000. Pressure distribution measurements for evaluation of running shoe properties. Sportverletzung/Sportschaden 14, 90–97.

Henning, E. M., Rosenbaum, D., Milani, T. L., 1990. Pressure distribution measurements in comparative shoe testing. In: Biennial Conference of Canadian Soc. Of Biomechanics. pp. 105–106.

Hoogendoorn, C. J., 1994. Thermal ageing. In: Hilyard, N. C., Cunningham, A. (Eds.), Low Density Cellular Plastics - Physical basis of behaviour. Chapman and Hall, Ch. 6, pp. 153–186.

Hsu, C.-P. S., 1997. Infrared spectroscopy. In: Settle, F. A. (Ed.), Handbook of Instrumental Techniques for Analytical Chemistry. Prentice Hall, pp. 247–283.

Iannace, F., Iannace, S., Caprina, G., Nicolais, L., 2001. Prediction of impact properties of polyolefin foams. Polymer Testing 20, 643–647.

Incropera, F. P., DeWitt, D. P., 1996. Fundamentals of heat and mass transfer, 4^{th} Edition. John Wiley and Sons.

Indesteege, J., Camargo, R. E., Mackey, P. W., 1998. Considerations on the selection of polyurethane systems for midsole wedges in athletic footwear application. J. Cellular Plastics 34, 329–347.

Ingle, J. D., Crouch, S. R., 1988. Spectrochemical Analysis. Prentice-Hall International, Inc., pp. 404–437.

James, S. L., Jones, D. C., 1990. Biomechanical aspects of distance running injuries. In: Cavanagh, P. R. (Ed.), Biomechanics of Distance Running. Human Kinetics, pp. 249–270.

Kaelble, E. F., 1967. Handbook of X-Rays: For diffraction, emission, absorption and microscopy. McGraw-Hill, Inc.

Kimball, J., Frisch, H. L., 1991. Diffusion through foams and fractal-like cellular solids. Physical Review A 43 (6), 1840–1848.

Kinoshita, H., Bates, B. T., 1996. The effect of environmental temperature on the properties of running shoes. Journal of Applied Biomechanics 12, 258–268.

Klempner, D., Frisch, K. C., 1991. Handbook of polymeric foams and foam technology. Hanser Publishers.

Knoerr, K., Rouiller, V., 2002. Integrating high performance PU-materials in sportsshoe's. In: Polyurethanes expo 2002. pp. 533–537.

Kraynik, A. M., Warren, W. E., 1994. The elastic behavior of low-density cellular plastics. In: Hilyard, N. C., Cunningham, A. (Eds.), Low Density Cellular Plastics - Physical basis of behaviour. Chapman and Hall, Ch. 7, pp. 187–225.

Lemmon, D., Shiang, T. Y., Hashmi, A., Ulbrecht, J. S., Cavanagh, P. R., 1996. The effect of insoles in therapeutic footwear a finite element approach. Journal of Biomechanics 30, 615–620.

Liu, W., Nigg, B. M., 2000. A mechanical model to determinate the influence of masses and mass distribution on the impact force during running. Journal of Biomechanics 33, 219–224.

Luikov, A. V., 1968. Analytical heat diffusion theory. Academic Press.

Mackenzie, B., 2002. private communication, athletics senior performance coach. http://www.brianmac.demon.co.uk/.

Mahapatro, A., Mills, N. J., Sims, G. L. A., 1998. Experiments and modelling of the expansion of crosslinked polyethylene foams. J. Cellular Polymers 17 (4), 252–270.

Maiti, S. K., Gibson, L. J., Ashby, M. F., 1984. Deformation and energy absorption diagrams for cellular solids. Acta Metall. 32 (11), 1963–1975.

Marais, S., Saiter, J. M., Devallencourt, C., Nguyen, Q. T., Metayer, M., 2002. Study of transport of small molecules through ethylene-co-vinyl acetate copolymers films. part B: CO_2 and O_2 gases. Polymer Testing 21, 425–431.

Masaro, L., Zhu, X. X., 1999. Physical models of diffusion for polymer solutions, gels and solids. Progress in Polymer Science 24, 731–775.

Milani, T. L., Hennig, E. M., Lafortune, M. A., 1997. Perceptual and biomechanical variables for running in identical shoe constructions with varying midsole hardness. Clinical Biomechanics 12 (5), 294–300.

Miller, D. I., 1990. Ground reaction forces in distance running. In: Cavanagh, P. R. (Ed.), Biomechanics of Distance Running. Human Kinetics, pp. 203–224.

Milliron, M. J., Cavanagh, P. R., 1990. Saggital plane kinematics of the lower extremity during distance running. In: Cavanagh, P. R. (Ed.), Biomechanics of Distance Running. Human Kinetics, pp. 65–106.

Mills, N. J., 1993. Plastics-Microstructure and engineering applications, 2^{nd} Edition. Edward Arnold.

Mills, N. J., 1994. Impact response. In: Hilyard, N. C., Cunningham, A. (Eds.), Low Density Cellular Plastics - Physical basis of behaviour. Chapman and Hall, Ch. 9, pp. 270–318.

Mills, N. J., 1997. Time dependence of compressive response of polypropylene bead foam. Cellular Polymers 16, 194–215.

Mills, N. J., 2000. Micromechanics of polymeric foams. In: 3^{rd} Nordic Meeting on Materials and Mechanics. pp. 45–76.

Mills, N. J., Fitzgerald, C., Gilchrist, A., Verdejo, R., 2003. Polymer foams for personal protection: cushions, shoes and helmets. Composites science and technology 63, 2389–2400.

Mills, N. J., Gilchrist, A., 1997a. Creep and recovery of polyolefin foams- deformation mechanisms. J. Cellular Plastics 33, 264–292.

Mills, N. J., Gilchrist, A., 1997b. The effect of heat transfer and Poisson's ratio on the compressive response of closed-cell polymer foams. Cellular Polymer 16, 87–119.

Mills, N. J., Hwang, A. M. H., 1989. The multiple-impact performance of high-density polyethylene foam. Cellular Polymers 8, 259–276.

Mills, N. J., Rodríguez-Pérez, M. A., 2001. Modelling the gas loss creep mechanism in eva foam from running shoes. Cellular Polymers 20, 79–100.

Miltz, J., Ramon, O., 1990. Energy absorption characteristics of polymeric foams used as cushioning materials. Polymer Engineering and Science 30 (2), 129–133.

Mirabella, F. M., 1992. Principles, theory, and practice of internal reflection spectroscopy. In: Mirabella, F. M. (Ed.), Internal Reflection Spectroscopy, Theory and Applications. Marcel Dekker, Inc., pp. 17–52.

Misevich, K. W., Cavanagh, P. R., 1984. Material aspects of modeling shoe/foot interaction. In: Frederick, E. C. (Ed.), Sports shoes and playing surfaces. Human Kinetics, pp. 47–75.

Mueller, M. J., Strube, M. J., 1996. Generalizability of in-shoe peak pressure measures using f-scan system. Clinical Biomechanics 11, 159–164.

Nielsen, L. E., 1960. Transitions in ethylene polymers. J. Polymer Science 62, 357–366.

Nielsen, L. E., 1962. Mechanical properties of polymers. Chapman and Hall.

Nigg, B. M., 1986a. Biomechanical aspects of running. In: Nigg, B. M. (Ed.), Biomechanics of running shoes. Human Kinetics, pp. 1–26.

Nigg, B. M., 1986b. Biomechanics of running shoes. Human Kinetics.

Nigg, B. M., 1986c. Experimental techniques used in running shoe research. In: M., N. B. (Ed.), Biomechanics of running shoes. Human Kinetics, pp. 27–61.

Nigg, B. M., Anton, M., 1995. Energy aspects for elastic and viscous shoe soles and playing surfaces. Official Journal of the American College of Sports Medicine, 92–96.

Nigg, B. M., Kerr, B. A. (Eds.), 1983. Biomechanical aspects of sport shoes and playing surfaces.

Nigg, B. M., Liu, W., 1999. The effect of muscle stiffness and damping on simulated impact force peaks during running. Journal of Biomechanics 32, 849–856.

Nurses Association, C., 2003. Foot anatomy–Bone structure of the foot. http://www.nefca.ca/find-ft-nurse/ftanatomy.asp.

Orlin, M. N., McPoil, T. G., 2000. Plantar pressure assessment. Physical Therapy 80 (4), 399–409.

Ostrogorsky, A. G., Glicksman, L. R., 1988. Rapid, steady-state measurement of the effective diffusion coefficient of gases in closed-cell foams. J. of Heat Transfer 110, 500–506.

Ostrogorsky, A. G., Glicksman, L. R., Reitz, D. W., 1986. Ageing of polyurethane foams. Intern. J. of Heat and Mass Transfer 29, 1169–1196.

Park, C. P., 1991. Polyolefin foam. In: Klempner, D., Frisch, K. C. (Eds.), Handbook of polymeric foams and foam technology. Hanser Publishers, pp. 187–242.

Pilon, L., Fedorov, A. G., Viskanta, R., 2000. Gas diffusion in closed-cell foams. J. Cellular Plastics 36, 451–474.

Potts, W. J., 1963. Chemical infrared spectroscopy. John Wiley and Sons, pp. 155–203.

Powell, P. C., 1983. Engineering with polymers. Chapman and Hall.

Pribut, S., 2002. Dr. Pribut's sports page. http://www.drpribut.com/sports/sportframe.html.

Rabek, J. F., 1980. Experimental Methods in Polymer Chemistry- Physical Principles and Applications. John Wiley and Sons, pp. 606–615.

Reinschmidt, C., Nigg, B. M., 2000. Current issues in the design of running and court shoes. Sportverletzung/Sportschaden 14, 71–81.

Rhodes, M. B., 1994. Characterizations of polymeric cellular structures. In: Hilyard, N. C., Cunningham, A. (Eds.), Low Density Cellular Plastics - Physical basis of behaviour. Chapman and Hall, Ch. 3, pp. 56–77.

Richardson, M. O. W., Al-Hassani, A. H. M., 1987a. Shock mitigation foams, 1. structure and property relationships. Cellular Polymers 6, 1–15.

Richardson, M. O. W., Al-Hassani, A. H. M., 1987b. Shock mitigation foams, 2. static/dynamic characteristics. Cellular Polymers 6, 39–60.

Richardson, M. O. W., Nandra, D. S., 1985. Shock mitigation foams - the basic parameters. J. Cellular Plastics 4, 279–287.

Robbins, S., Waked, E., 1997. Balance and vertical impact in sports: Role of shoe sole materials. Arch. Phys. Med. Rehabil. 78, 463–467.

Rodríguez-Pérez, M. A., Almanza, O., del Valle, J. L., González, A., de Saja, J. A., 2001. Improvement of the measurement process used for the dynamic mechanical characterisation of polyolefin foams in compression. J. Applied Polymer Science 20, 253–267.

Rodríguez-Pérez, M. A., de Saja, J. A., 2000. Dynamic mechanical analysis applied to the characterisation of closed cell polyolefin foams. Polymer Testing 19, 831–848.

Rodríguez-Pérez, M. A., Velasco, J. I., Arencón, D., Almanza, O., de Saja, J. A., 2000. Mechanical characterisation of closed cell polyolefin foams. J. Applied Polymer Science 75, 155–166.

Rosenbaum, D., Becker, H.-P., 1997. Plantar pressure distribution measurements: Technical background and clinical applications. Foot and Ankle Surgery 3, 1–14.

Rosenfeld, A., 2001. From image analysis to computer vision: An annotated bibliography, 1955-1979. Computer Vision and Image Understanding 84, 298–324.

Running Magazine, R., 2003. Runner's world. http://www.runnersworld.com/.

Rusch, K. C., 1969. Load-compression behavior of flexible foams. J. Applied Polymer Science 13, 2297–2311.

Rusch, K. C., 1970a. Energy-absorbing characteristics of foamed polymers. J. Applied Polymer Science 14, 1433–1447.

Rusch, K. C., 1970b. Load-compression behavior of brittle foams. J. Applied Polymer Science 14, 1263–1276.

Samsung, 1999. Technical literature for EVA foams. Tech. rep., Samsung.

Saunders, J. H., 1991. Fundamentals of foam formation. In: Klempner, D., Frisch, K. C. (Eds.), Handbook of polymeric foams and foam technology. Hanser Publishers, pp. 5–16.

Sawai, M., Miyamoto, K., Takemura, K., Mori, M., Kiuchi, K., 2000. Super low density polyurethane systems for sports shoes. J. Cellular Plastics 36, 286–291.

Sawyer, L. C., Grubb, D. T., 1996. Polymer Microscopy, 2^{nd} Edition. Chapman and Hall.

Schwaber, D. M., Meinecke, E. A., 1971. Energy absorption in polymeric foams, II. prediction of impact behaviour from instron data for foams with rate-dependent modulus. J. Applied Polymer Science 15, 2381–2393.

Segesser, B., Nigg, B. M., 1993. Sport shoe construction: Orthopaedic and biomechanical concepts. In: F., P. A. (Ed.), Sports Injuries: basic principles of prevention and care (Encyclopaedia of sports medicine). Vol. 4. Blackwell Scientific, pp. 398–416.

Shiang, T.-Y., 1997. The non linear finite element analysis and plantar pressure measurements for various shoe soles in heel region. Proceedings National Science Council, ROC, Part B: Life Sciences 21 (4), 168–174.

Shorten, M. R., 1993. The energetics of running and running shoes. Journal of Biomechanics 26 (1), 41–51.

Shorten, M. R., 2000. Running shoe design: protection and performance. In: Pedoe, T. (Ed.), Marathon Medicine. Royal Society of Medicine, London, pp. 159–169.

Shorten, M. R., 2002. Keynote-The myth of running shoe cushioning. In: Ujihashi, S., Haake, S. (Eds.), The Book of the 4^{th} Int. Conference on the engineering of sport. The engineering of sport, pp. 25–29.

Shutov, F. A., 1991a. Blowing agents for polymer foams. In: Klempner, D., Frisch, K. C. (Eds.), Handbook of polymeric foams and foam technology. Hanser Publishers, pp. 375–408.

Shutov, F. A., 1991b. Cellular structure and properties of foamed polymers. In: Klempner, D., Frisch, K. C. (Eds.), Handbook of polymeric foams and foam technology. Hanser Publishers, pp. 17–46.

Silverstein, R. M., Bassler, G. C., 1967. Spectrometric identification of organic compounds. John Wiley and Sons, pp. 64–109.

Sims, G. L. A., Khunniteekool, C., 1994. Cell size measurement of polymeric foams. Cellular Polymers 13, 137–146.

Stefanyshyn, D. J., Nigg, B. M., 2000. Energy aspects associated with sport shoes. Sportverletzung/Sportschaden 14 (3), 82–89.

Stewart, J. E., 1970. Infrared spectroscopy: Experimental Methods and Techniques. Marcel Dekker.

Svanström, M., Ramnäs, O., 1995. A method for analysing the gas phase in polyurethane foam. J. Cellular Plastics 31, 375–388.

Svanström, M., Ramnäs, O., Olsson, M., Jarfelt, V., 1997. Determination of effective diffusion coefficients in rigid polyurethane foam. J. Cellular Polymers 16, 182–193.

Taunton, J. E., Ryan, M. B., Clement, D. B., McKenzie, D. C., Lloyd-Smith, D. R., Zumbo, B. D., 2003. A prospective study of running injuries. British Journal of Sports Medicine 37, 239–244.

Throne, J. L., Proglhof, R. C., 1985. Closed-cell foam behavior under dynamic loading ii: Loading dynamics of low density foams. J. Cellular Plastics, 43–50.

Tortora, G. J., Grabowski, S. R., 1996. Principles of anatomy and physiology, 8th Edition. Addison Wesley Longman, Inc.

Urry, S., 1999. Plantar pressure-measurement sensors. Measurement Science and Technology 10, 15–32.

User Manual, G., 2001. MKII Golden Gate single reflection ATR System. Nicolet Nexus.

User Manual, I., 2003. Gravimetric analysers for the characterisation of the sorption properties of materials. Hiden Analytica.

Verdejo, R., 2000-2001. Last year project, University of Valladolid (Spain), 1^{st} year project, School of Metallurgy and Materials (Birmingham), Degree Report and School Internal Report.

Verdejo, R., Mills, N. J., 2002. Performance of EVA foam in running shoes. In: Ujihashi, S., Haake, S. J. (Eds.), The Engineering of Sport 4. pp. 580–587.

Verdejo, R., Mills, N. J., accepteda. Heel-shoe interactions and the durability of EVA foam running-shoe midsoles. Journal of Biomechanics.

Verdejo, R., Mills, N. J., acceptedb. Simulating the effects of long distance running on shoe midsole foam. Polymer Testing.

Vieth, W. R., 1990. Diffusion in and through polymers, principles and applications. Hanser Publishers.

von Solms, N., Nielsen, J. K., Hassager, O., Rubin, A. Dandekar, A. Y., Andersen, S. I. Stenby, E. H., submitted. Direct measurements of gas solubilities in polymers using a high-pressure microbalance. J. Applied Polymer Science.

Walton, A., 2003. private communication.

Wang, N. H., Takishima, S., Masuoka, H., 1994. Measurements and correlation of solubility of a high-pressure gas in a polymer by piezoelectric quartz sorption-CO_2+PVAc and CO_2+PBME systems. Int. Chemical Engineering 34 (2), 255.

Williams, J. G., 1980. Stress analysis of polymers, 2^{nd} Edition. John Wiley and Sons.

Young, R. J., Lovell, P. A., 1991. Introduction to Polymers. Chapman and Hall.

Yu, J., 2001. private communication company.